Design and control contributions to high efficiency Ferrite-PMSM drives for small compressors

Teză destinată obţinerii
titlului ştiinţific de doctor inginer
la
Universitatea Politehnica Timişoara
în domeniul Inginerie Electrica
de către

Andy-Sorin Isfănuţi

Conducător ştiinţific:	prof.univ.dr.ing. Ion Boldea
Referenţi ştiinţifici:	prof.univ.dr. Mircea M. Rădulescu
	prof.univ.dr.ing. Iulian M. Tudor Birou
	conf.univ.dr.ing. Octavian Cornea

Ziua susţinerii tezei: 12.02.2021

Preface

This thesis proposes and analyzes the performance of several new Ferrite based permanent magnet synchronous motor topologies for use in driving low power compressors (30 to 100W), as well as their close loop control strategies. FEM-only/FEA assisted optimal design methodologies are developed and applied to optimize the for high efficiency (88% or above) and reduced material cost.

In addition, two sensorless control strategies are investigated for use in driving a 3-phase ferrite permanent magnet synchronous motor: standard field-oriented control versus V/f scalar control enhanced with two stabilizing loops, both strategies using the active flux observer for rotor position estimation. The two control strategies are thoroughly analyzed by digital simulation and experimental tests on a 1 kW 4.5krpm spoke-IPMSM prototype motor.

The results show feasible motor solution and control strategies for being employed in driving reciprocating compressor for energy and cost saving refrigerator applications.

Acknowledgement

This PhD thesis was elaborated during my research activity at the Department of Electric Machines and Drives from Politehnica University of Timisoara.

I would first like to express my gratitude to my supervisor, Professor Ion Boldea for the opportunity to do research under his supervision and for his continuous support and guidance during the past years. Secondly, I want to thank Professor Lucian Tutelea for his valuable technical inputs and advices on the optimization and numerical methods topics used in this thesis.

I want to additionally thank Professor Gheorghe Andreescu and Associate Professor Codruta Ancuți for their support and advices on the experimental part of the thesis.

Furthermore, I would also like to thank Professor Lucian Tutelea, Professor Gheorghe Andreescu and Professor Nicolae Muntean for being part of the guidance committee, for their advices and their contribution to my technical education.

Not least, I want to thank my family for the support, encouragement and understanding they offered me during this period.

Timişoara, 12.2020 Andy-Sorin Isfanuti

Isfănuți, Andy-Sorin

DESIGN AND CONTROL CONTRIBUTIONS TO HIGH EFFICIENCY FERRITE-PMSM DRIVES FOR SMALL COMPRESSORS

176 pages, 119 figures, 25 tables.

Keywords:
optimal design, permanent magnet synchrohous motor, finite element analysis, single phase motors, reciprocating compressors, scalar control, stablilizing loops

Abstract:
This thesis presents and investigates several new motor topologies, candidates for driving small compressor applications for home appliances, for ratings: 35-1000W, 1600-4500rpm. Their operation principles, main characteristics and advantages are investigated and discussed. FEA assisted or full FEA optimal design methodologies are developed with the design target of maximize the efficiency and minimize the motor cost. The optimized motors are validated via finite element analysis and simulation of the dinamic operation under proposed close loop control simple strategies.

This work is also focused on investigating sensorless control strategies for 3 phase permanent magnet synchonous motors applicable for compressor applications. The V/f scalar control with active power variation and MTPA operation based stablilizing loops is investigated and compared against the classic sensorless field oriented control strategy, via experimental and digital simulation. Active flux model-based observer is employed for rotor position and speed estimation. The target is proving that the scalar control is suitable for being used in home appliances applications.

Table of content

NOMENCLATURE

Abbreviations

AC	Alternative current
AFO	Active flux observer
API	Application programable interface
BEMF	Back-electromotive force
BLAC	Brushless alternative current motor
BLDC	Brushless direct current motor
COM	Component objects
DC	Direct current
DTC	Direct torque control
EEMFO	Extended EMF observer
EMF	Electromotive force
ENC	Encoder based calculation
FEA	Finite element analysis
FEM	Finite element method
FOC	Field oriented control
HPF	High pass filter
HVAC	Heat, ventilation, and air conditioning
IPMSM	Interior permanent magnet synchronous motor
MMF	Magnetomotive force
PI	Proportional integrator
PM	Permanent magnet
PMSM	Permanent magnet synchronous motor
PV	Pressure – volume
RMS	Root mean square
SPMSM	Surface permanent magnet synchronous motor
SVM	Space vector modulation
VCRS	Vapor compression refrigeration systems
VSI	Voltage source inverter

Subscripts

s	stator quantities
a	active flux

Superscripts

s	stator coordinates
r	rotor coordinates
*	reference value or conjugate of a complex value
^	estimated

List of Figures

List of tables

CHAPTER 1. INTRODUCTION

Abstract

This chapter presents the motivation behind the research subject, continues with a presentation of the refrigerator system, followed by the types of compressors used in home refrigerators systems and types of electric drives and motors employed in driving a reciprocating compressor and the requirements on motor side for such applications. The thesis structure is presented at the end together with a list of author's publications related to this topic.

1.1 Motivation in choosing the subject and objectives

Studies promoted by the European Commission and US Department of Energy (DOE) show that electric motors account for a major part of the total energy utilized in homes [1] [2], being present as pumps in HVAC systems, washing machines, refrigerator systems etc.

Up to last decades the single-phase line start induction machine was the primary choice for home appliances due to its robustness, low cost [3]. Initially being used mainly as generator and as drive-in constant speed applications, the synchronous machine has gained importance, and use in variable speed applications with the development of the power electronics and the permanent magnet materials.

For medium and small power application, permanent magnet excitation is preferred over the electromagnetic because of the benefits [4]:

- simplified construction and maintenance
- increase in reliability due to slip rings absence
- no need for supplementary DC power source
- increase of efficiency due to elimination of joule losses
- higher power density per volume unity

The characteristics of PMSM and their topology strongly depend on the properties of the permanent magnets used for excitation. The main types of permanent magnets used for excitations are AlNiCo, sintered Ferrites, SmCo and NdFeB.

NdFeB magnets (as SmCo magnets) are "rare earth" permanent magnets. The use of rare earth elements in their composition confers them exceptionally good magnetic properties, but also high cost, due to "rare earth" materials scarcity. The NdFeB permanent magnet synchronous machines are generally used in applications that require high performance and high-power density per volume unit [3].

Ferrite permanent magnet synchronous machines, on the other hand, are generally used in lower performance applications. Their main advantage is the low price (up to one order of magnitude smaller) compared to the price of the NdFeB magnets. Other notable advantages are the high resistivity and the high operating temperature.

In the light of the "rare earth" PMs increase price during latest years, the aim of the present research is to identify and study topologies of permanent magnet synchronous machines which using Ferrites magnets could achieve good performance in household applications, particularly in gas compressing applications.

To make the Ferrite magnets a good candidate, special topologies of machines must be adopted. Ferrites have low value for magnetic energy product; therefore, a higher volume of magnet must be used to achieve the desired magnetic energy. Also due to low remanent flux density value, they must be placed inside the rotor, to avoid demagnetization. Low remanent flux density requires a higher active surface, therefore special displacement configurations must be used, which can enable radial and axial flux concentration [5].

The refrigerator and air conditioning compressors are among the main household applications energy consumers [6]. They constitute an important share of the load. It was estimated in 2010 that the domestic freezers consume 6% of the energy produced worldwide. Therefore, continuous efforts have been made along the time to improve their efficiency. Although there are many factors which impact the energy consumption of a refrigerator system, e.g., ambient temperature and humidity [7], thermostat setting, compartment thermal insulation quality [8], the efficiency of the compressor motor represents an important component which has been subject of improvements across the time.

Taking all these aspects into consideration it is believed that cost effective solutions using ferrite PMSM can be designed with acceptable performance, benefiting of Ferrite material low cost and high availability. The research objectives are to study and design several new Ferrite based PMSM topologies candidates for compressor drive applications. The design target is high efficiency (above 88% for powers below 100W), low material cost and meeting the application constraints (requirements for starting torque, torque pulsations, protection against demagnetization, etc.).

1.2 Refrigeration compressor applications - overview

1.2.1 Vapor compression refrigeration system (VCRS)

The refrigeration systems (used by refrigerators, air conditioning systems, heat pumps) make use of the Joule Thomson effect to extract heat from a certain closed environment. This is achieved by cyclically changing the phase of a gas (refrigerant) through modification of its properties (volume, pressure) to force it to exchange heat with the environment. One of the most widely used systems are the vapor compression refrigeration systems (VCRS). A generic one compression stage system is shown in Fig. 1.1 [1].

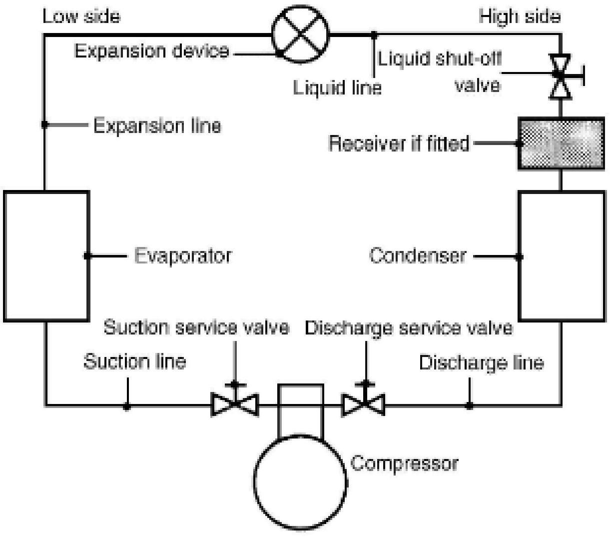

Fig. 1.1 Single stage vapor compression system [1]

The main components of this system are: the compressor, the expansion valve, the condenser and the evaporator. The compressor uses mechanical work to raise the pressure of the gas and, at constant volume, the gas temperature. The high-pressure gas is pushed through the condenser (heat releasing component) where it transmits its high temperature to the environment. The heat releasing causes the change of the refrigerant state from gas to liquid. Next, the refrigerator is pushed through the expansion valve, which causes a decrease in its pressure, which determine a decrease in its temperature too. In this low temperature state, the refrigerant is circulated through the evaporator component where it absorbs the environmental temperature and changes its state from liquid to gas.

The changes in the refrigerant parameters during a VCRS cycle is shown in the PV diagram from Fig. 1.2 (representative for a reciprocating compressor).

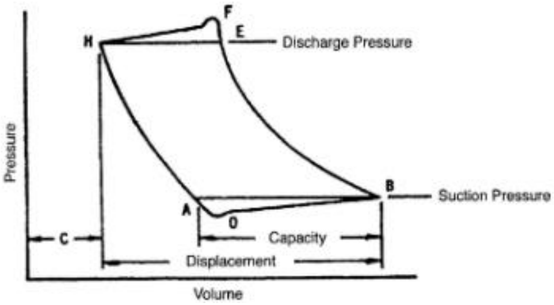

Fig. 1.2 The PV diagram for a reciprocating compressor [9]

The compressor role in vapor refrigeration system is to compress the gas and circulate it through the closed circuit. To do so it requires mechanical work input which, for small power home appliance systems, is delivered by electric machines [10]. A generic refrigerator circuit with its components is shown in Fig. 1.3, using a single refrigeration circuit. The capillary tube plays the role of the expansion valve. The standard refrigerator usually uses two refrigeration circuits: one for fresh food compartment (R) and one for freezer compartment (F).

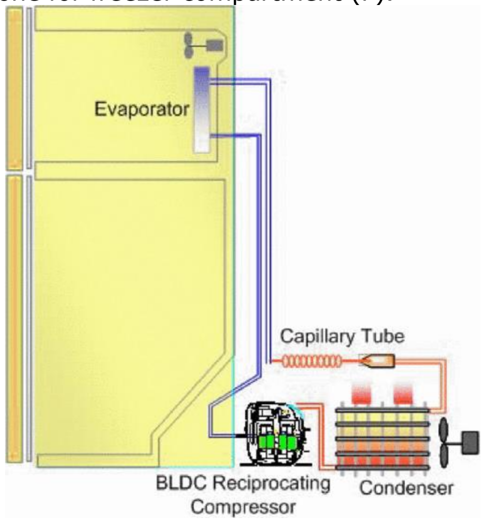

Fig. 1.3 Refrigerator system [8]

There are several types of compressors used in refrigerator systems, each having its benefits and particularities: reciprocating compressors, centrifugal compressors, scroll compressors etc. Because of its wide used, the reciprocating compressors (positive displacement compressor), is used in the present study as load during the dynamic operation study of PMSM. Its operation and mathematical model will be presented in detail in Chapter 2.

1.2.2 Motor drives in refrigerator compressor applications

Initially, the compressors were simply controlled by electromechanically switches (relays) based on the desired temperature (thermostat controlled) [11] as shown in Fig. 1.4. While having the advantages of being less sensitive to voltage disturbances, they have the disadvantages of low switching frequency, higher power consumption (lowers the total efficiency) and the presence of sparks during commutation.

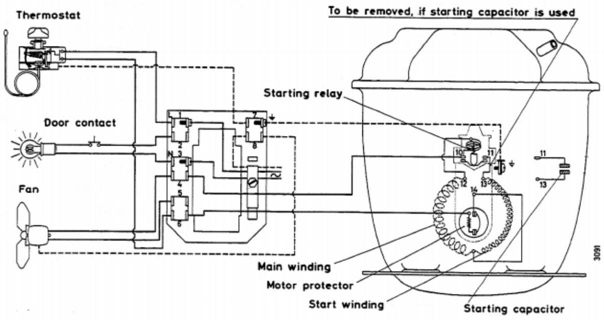

Fig. 1.4 Old refrigerator system drive [12]

An improvement step was the introduction of electronic thermostat. This allowed the possibility of implementing of more precise temperature conditions, better protection features and the benefit of increased reliability and number of off-on cycles (brought by the replacement of mechanical switches with solid state switches).

The next major improvement is the introduction of variable speed drives (Fig. 1.5). They allow the operation at variable speed (which improves the efficiency and reduces the inrush currents associated with starting, reduces the needed motor power, increases maximum speed past the speed associated with grid frequency, which also beneficially impacts the motor size and efficiency in operation) Through acquisition of the temperature sensors information, multiple temperature control profiles can be specified and better temperature control can be realized digitally, also allowing for configuration through user input interface.

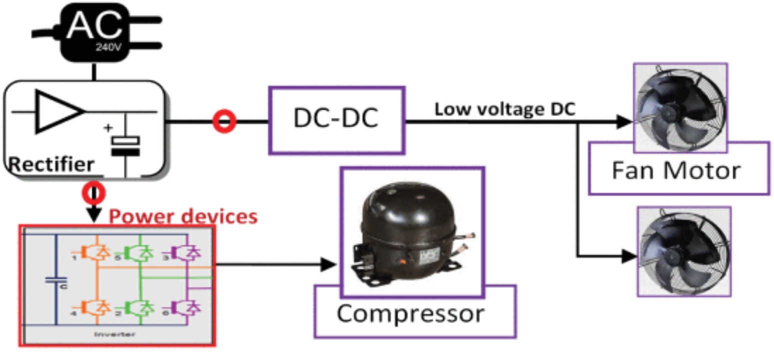

Fig. 1.5 VSC based refrigerator – main component [7]

1.2.3 Electric motors used in compressor application

There are various solutions of electric machines employed for driving the compressor. The particularity depends on the compressor type. E.g., for a centrifugal compressor which operates at high speeds of tens or hundreds of rotations per minute, a high-speed motor is required. The overview below targets the reciprocating compressors, commonly used by household refrigerators.

The widely used solution in the refrigerators up to several decades ago was the single-phase line start induction machine [13], its advantages being simple structure, low production cost and easy maintenance. It is usually built to run at single speed and consists of a main winding (so-called RUN winding) and an auxiliary winding (so-called START winding). Depending on how the auxiliary winding is used, this motor falls into several categories [14]:

- Resistance start/Induction run (RSIR)
- Capacitor Start/Induction run (CSIR)
- Permanent split capacitor (PSC) – use a capacitor in series with the auxiliary winding, the auxiliary winding being also used during motor run.

Fig. 1.6 show a Danfoss solution used in the past - a single phase, two poles IM squirrel cage [12].

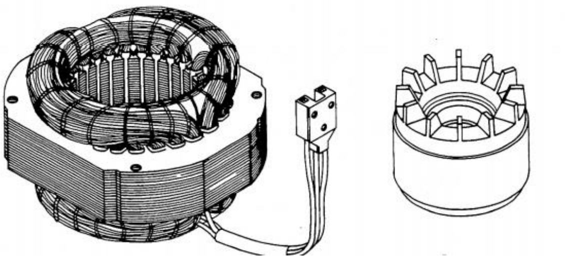

Fig. 1.6 Danfoss single phase induction motor for refrigerator compressor [12]

As the trend in home appliance applications became oriented towards higher efficiency, performance, energy conservation and environment protection products, the single-phase induction machine's low efficiency (60-70%), poor power factor and small flexibility in speed variation [15] led the industry into seeking other solutions.

Adding of permanent magnets in rotor, below the cage, for excitation brings important advantages for the one phase induction machine, such as higher power density and higher efficiency, but at the cost of increased material cost and starting difficulties (due to PM braking) [16] [17]. In [18] it is shown that adding PMs in special configuration can increase the efficiency of the one phase motor (up to 87%) and increases the general motor performance. Also, in ref. [19] a 2/4-pole split-phase capacitor motor is presented which, through use of PMs, reaches 87% efficiency when running in synchronism.

The relative recent introduction of variable speed drives in compressor applications [15] [20], allowed the use of synchronous single-phase motors: synchronous reluctance motors/switched reluctance motors [21] and permanent magnet synchronous motors. While the 2nd category has a smaller cost associated with non-use of permanent magnets (smaller material cost and easier manufacturing process), the permanent magnet synchronous motor benefits of higher efficiency and power factor.

Variable speed drives also allowed the introduction of the three phase motors in compressor applications. Different topologies were proposed, studied, and optimized as candidates for home appliances such as exterior rotor [13], surface permanent magnet [22] and interior permanent machines [15] [23] [24]. Switch reluctance motors were also proposed as cost-effectives candidates for pump applications [17].

Literature studies have been done for the use of linear permanent magnet oscillatory machines to drive the piston pumps [25]. They show lower friction and copper losses and better performance than single phase induction machines [26].

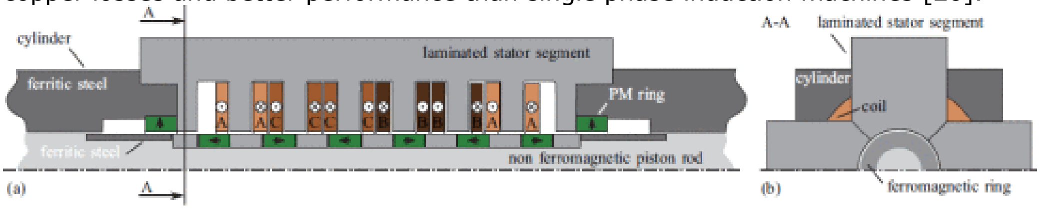

Fig. 1.7 Linear motor proposed for in compressor applications [23]

1.2.4 Main requirements for a motor driving a compressor

There are several aspects which needs to be considered in the design of the motors used for driving a compressor [27]:

- Rated power, operating speed range and supply voltage – dependent on the refrigerator capacity, refrigerant properties etc.
- Starting performance (sufficiency large starting torque to secure the starting under load)
- Noise and vibration (limitation/minimization of torque ripples) [23]
- Efficiency and power factor [23] [24]
- Material and manufacturing cost

Additional constraints are represented by physical dimensions restrictions (the motor must fit the compressor housing), manufacturing technological limitations (minimum airgap, minimum stator slot opening, etc.).

1.3 Thesis contributions and outline

Within the present thesis, several Ferrite permanent magnet synchronous motors are designed and studied together with closed loop control strategies, to be employed for driving low power compressors, targeting high efficiency during operation and low material cost. An outline of the thesis is presented below:

- Chapter 2 presents a few introductory elements related to the properties of the materials used in the motor design chapters, the FEA analysis procedure, the optimal design procedure, and the reciprocating compressor model.
- Chapter 3 presents a two-stator two rotor poles doubly salient flux reversal single phase synchronous motor topology. The motor electromagnetic characteristics and operation principles are presented using magnetostatic finite element analysis, with an emphasis on the motor starting challenges. A FEA based optimal design methodology is built, which optimizes the moor geometry targeting the material cost minimization, efficiency increase and ensure a minimum electromagnetic torque value for secure starting. The optimal design is deployed for a case study of a 35 W, 1600 rpm motor case study (mobile small refrigerator compressor case). The optimal design results are validated through detailed FEA analysis and dynamic operation simulation on a speed-current cascade closed loop control strategy. Preliminary experimental results on a built prototype are presented at the end.
- Chapter 4 presents a similar analysis done on a four-stator pole four rotor pole poles doubly salient flux reversal single phase synchronous motor topology. Developed based on the two-stator pole motor topology presented in chapter 2, the new motor topology brings the benefit of better use of the stator PMs

and higher torque density. As in the previous chapter an optimal design methodology is built and deployed on an 85 W, 3000 rpm test case. The design results are validated through FEA and digital simulation results.

- Chapter 5 introduces a new topology of four stator poles four rotor poles single phase permanent magnet motor and analyzes its performance against the performance of the motor presented in Chapter 4 for the same case study. The particularity of the new motor topology is the placement of the permanent magnets in the rotor and the use of additional PMs in stator for parking/starting. Same performance is obtained for a smaller overall material cost (mainly due to reduced copper use). FEA validation and dynamic operation simulation are also included.
- Chapter 6 presents the design of an external rotor 3 phase synchronous motor intended also for driving a compressor. An optimal design routine is built around an analytic design model, which is iteratively corrected by FEA coefficients throughout the optimization process. The optimal design methodology is used for designing a 1kW, 4500 rpm motor. FEA analysis and preliminary tests on a built prototype validate the design methodology.
- Chapter 7 is focused on experimental study of two control strategies which can be employed on 3 phase PMSM motors driving compressors through a 3-phase voltage source inverter. A scalar V/f sensorless control strategy using correction loops for reference voltage amplitude and phase is proposed and compared against the standard sensorless field-oriented control strategy. The motor under test is represented by a 3 phase 6/8 spoke PMSM motor prototype Through detailed experimental tests, the scalar control strategy is proved effective for being used in compressor control applications.

1.4 Author publications related to the thesis subjects:

The following papers were published during the author’s doctoral program (in order of appearance):

1. F. J. H. Kalluf, A. S. Isfănuţi, L. N. Tutelea, A. Moldovan-Popa and I. Boldea, "1-kW 2000–4500 r/min Ferrite PMSM Drive: Comprehensive Characterization and Two Sensorless Control Options," in IEEE Transactions on Industry Applications, vol. 52, no. 5, pp. 3980-3989, Sept.-Oct. 2016, doi: 10.1109/TIA.2016.2574776.
2. A. S. Isfanuti et al., "Small single-phase two pole Ferrite-PM-stator double-saliency motor: Optimal design and experimental characterization," 2016 XXII International Conference on Electrical Machines (ICEM), Lausanne, 2016, pp. 2492-2497, doi: 10.1109/ICELMACH.2016.7732871.
3. A. Isfanuti, L. N. Tutelea, I. Boldea and T. Staudt, "Small-power 4 stator-pole stator-ferrite PMSM single-phase self-starting motor drive: FEM-based optimal design and controlled dynamics," 2017 International Conference on Optimization of Electrical and Electronic Equipment (OPTIM) & 2017 Intl Aegean Conference on Electrical Machines and Power Electronics (ACEMP), Brasov, 2017, pp. 517-522, doi: 10.1109/OPTIM.2017.7975020.
4. A. Isfanuti, M. Paicu, L. Tutelea, T. Staudt and I. Boldea, "V/f with stabilizing loops versus FOC of Spoke-PM rotor SM drive: control with experiments," 2018 IEEE 18th International Power Electronics and Motion Control Conference (PEMC), Budapest, 2018, pp. 629-636, doi: 10.1109/EPEPEMC.2018.8521862.
5. A. Isfanuti, L. N. Tutelea, I. Boldea, T. Staudt and P. Ely da Silva, "Outer-Ferrite-PM-Rotor BLAC Motor Characterization: FEM Assisted Optimal Design," 2018

XIII International Conference on Electrical Machines (ICEM), Alexandroupoli, 2018, pp. 345-350, doi: 10.1109/ICELMACH.2018.8507079.

6. A. Isfanuti, L. N. Tutelea, I. Boldea, T. Staudt and P. E. da Silva, "Outer Ferrite-PM-Rotor BLAC Motor Characterization: FEM-Assisted Optimal Design and Preliminary Experiments," in IEEE Transactions on Industry Applications, vol. 56, no. 3, pp. 2580-2589, May-June 2020, doi: 10.1109/TIA.2020.2979672.

7. Andy Isfanuti , Mihaela-Codruta Paicu , Gheorghe-Daniel Andreescu , Lucian Nicolae Tutelea , Tiago Staudt & Ion Boldea (2020): V/f with Stabilizing Loops and MTPA versus Sensorless FOC for PMSM Drives, Electric Power Components and Systems, DOI: 10.1080/15325008.2020.1836072

CHAPTER 2. GENERAL INTRODUCTORY ELEMENTS

Abstract

This chapter introduces several concepts used thorough the thesis, from theoretical point of view. General information on finite element analysis together with the methodology used for creating models and extracting relevant information are presented, followed by a detailed explanation of the Hooke Jeeves optimization algorithm. The reciprocating compressor operation principles and mathematical model for its digital simulation are also included.

2.1 FEA analysis

Although very highly computationally intensive with respect to the analytic methods, the finite element method allows obtaining highly accurate solutions to magnetostatics problems, often difficult to express or to solve analytically.

The finite element analysis within this thesis is carried out using the free SW package FEMM 4.2, which allows defining and solving 2D magnetostatics nonlinear planar/axisymmetric problems [28]. The integrated Lua scripting language provides the feature to programmatically carry out of the preprocessing, analysis and postprocessing phases. COM APIs are available and make possible calling FEMM4.2 via MATLAB, SciLab, Mathematica or Microsoft Windows PowerShell. This offers the possibility to automate the model creation, analysis and results extraction, a necessary feature in the context of motor optimization.

The FEMM4.2 magnetostatics solver uses the Maxwell equations to calculate the magnetic field vector in each mesh point, using the equation

$$\nabla \times \left(\frac{1}{\mu(B)} \nabla \times \bar{A} \right) = \bar{J} \tag{2.1}$$

where ∇ represents the differential rotor operation, μ represents the material magnetic permeability (which can be non-linear, commonly the case of the core materials in electric machines), B represents the magnetic induction, $\bar{A}$ represents the magnetic potential vector and $\bar{J}$ represents the current density vector. The problem solution $\bar{A}$ is used in the postprocessing phase for various magnetic field properties extraction or calculations, as will be shown in the following paragraphs.

2.1.1 FEA pre-processing

The preprocessor stage in finite element method consists of:

- magnetostatic problem and solver settings definition (maximum number of iterations, mesh refinement, solution global error)
- boundary conditions, material properties and circuit properties definition
- machine geometry drawing
- applying the boundary conditions, setting the magnetic field sources

The planar symmetry was used, the FEA models representing a cross section of the machine, with the depth dimension being set to the core stack length.

2.1.1.1 Material properties

The material properties used in analytic/FEA models of the motor are listed below.

- *Laminated steel*

0.18mm thick non-oriented laminated steel material was used to model the laminated part of the motor core [29]. The magnetization curve is shown in the Fig. 2.1 and the material properties are presented in Table 2.1.

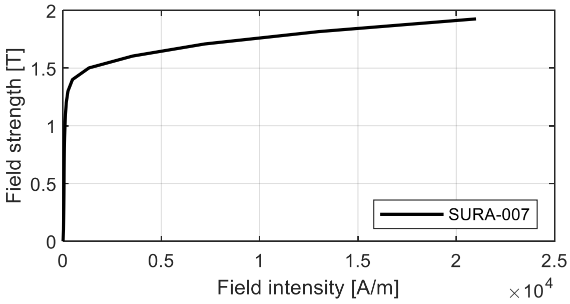

Fig. 2.1 Magnetization curve for laminated steel material

Table 2.1 Laminated steel properties

Property	Value
Density [kg/m3]	7650
Resistivity [Ω/m]	$0.52 \cdot 10^{-6}$
Sheet thickness [mm]	0.178
Lamination filling factor [%]	0.95
Specific losses at 400Hz and 1T [W/m3]	14.3
Cost [$/kg]	1.7

- *Non-laminated steel*

Pure iron material properties are used thorough the thesis for modelling the non-laminated part of the core (e.g., shaft), taken from the FEMM4.2 material library. The material magnetization curve is presented in Fig. 2.2 and the material properties are listed in Table 2.2.

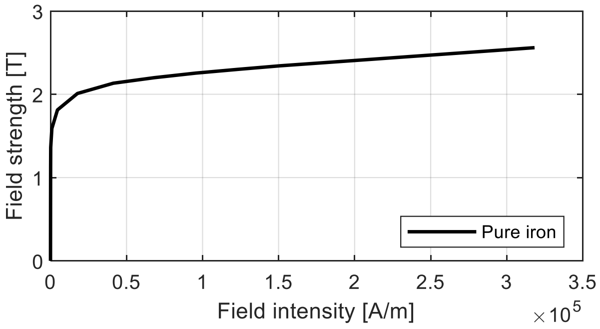

Fig. 2.2 Magnetization curve for non-laminated core material

Table 2.2 Non-laminated core material properties

Property	Value
Density [kg/m3]	8050
Resistivity [Ω/m]	10^{-7}
Cost [$/kg]	1

- *Copper*

Regular copper was used, having the properties listed in Table 2.3.

Table 2.3 Copper material properties

Property	Value
Density [kg/m3]	8930
Conductivity [S·m]	35.46
Cost [$/kg]	10

- *Permanent magnet material*

Sintered Ferrite material, with properties shown in Table 2.4 was used for modeling the permanent magnet. Different remanence values, corresponding to different quality PMs were used for different machines design.

Table 2.4 Ferrite permanent magnet properties

Property	Value
Density [kg/m3]	4930
Remanence [T]	0.33 / 0.42 / 0.45
Relative permeability [-]	1.5
Cost [$/kg]	6

2.1.2 Boundary conditions

The boundary conditions can be also seen as problem initial values, defining the solution or the magnetic field properties in the boundaries surrounding the model and in certain boundaries separating the model regions. The boundary conditions used in FEA analysis are:

- ***Dirichlet boundary condition A = 0*** – is set on the boundary between stator core and surrounding region or outer rotor and surrounding region, to keep the magnetic flux lines confined within the core region. It is also used at the boundary between rotor axle and rotor to simulate a non-magnetic rotor shaft Fig. 2.3).
- ***Periodic boundary conditions*** - used when simulating only one part of the model (comprising an integer number of pole pairs). This allows setting same values on the boundaries which share same periodic boundary condition (Fig. 2.3). The green boundary condition line is divided into multiple separate pairs of periodic boundaries, symmetrically displaced.

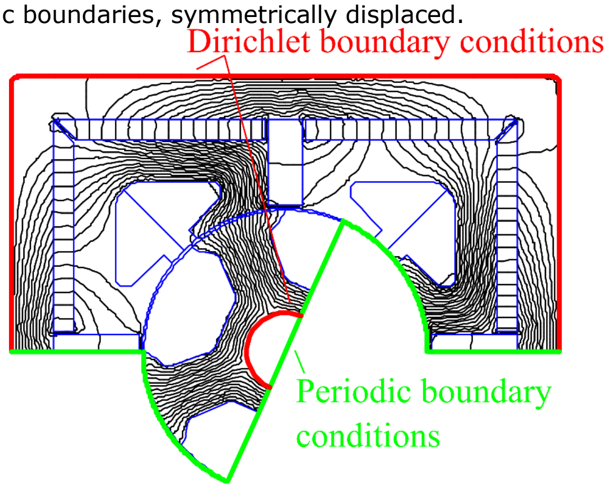

Fig. 2.3 Dirichlet and periodic boundary conditions used in modeling the single-phase synchronous motor (Chapter 4)

2.1.3 Airgap air layers and meshing settings

To accurately simulate the electromagnetic phenomena in the airgap (the region where the power conversion takes place, being characterized by the highest values for magnetic field intensity), the airgap is divided into three layers of air (Fig. 2.4).

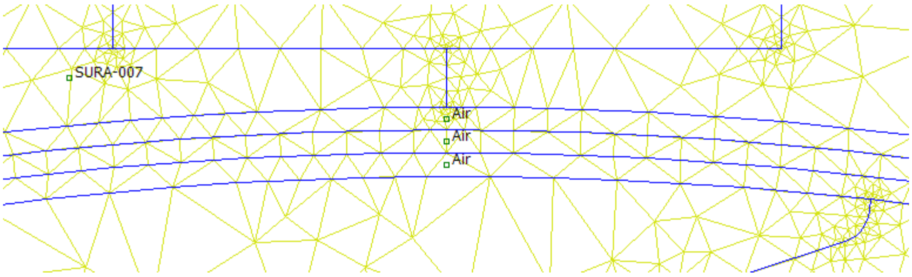

Fig. 2.4 Airgap layers

2.2 Analysis

FEMM4.2 does not include a circuit model or the possibility to perform transient analysis. To simulate the motor operation, it is necessary to update the rotor position at each analysis step prior to the analysis. Additionally, the load operation is simulated by directly prescribing the current amplitude within the coil turn.

For determining the PMSM's magnetic characteristics and performance, two sets of FEA analysis are performed for successive rotor positions:

- **No load analysis**: this analysis simulates the open load generator steady state operation mode at rated speed. The current amplitude in the winding material region is set to 0 prior to the analysis and the rotor position is changed successively over an electric period for each analysis step.
- **Load analysis**: this analysis simulates the motor steady state operation at rated speed and load. The analysis is also performed for successive rotor positions over an electric period, the phase current amplitude value being updated for each rotor position prior to the analysis.

There is a list of FEA analysis limitations and simplifications used in this thesis:

- the end coil influence and its leakage flux are not considered
- the skin effect is not considered in copper losses
- the 3D path of the magnetic flux is neglected
- the phase voltage necessary to produce the simulated current amplitude variation is not considered.

2.3 FEA post-processing

During no-load / load analysis for successive rotor positions, the winding flux density, the torque acting on the rotor with reference to (0,0) point and the core losses are recorded for each rotor position. The winding magnetic linkage flux density is extracted from the winding circuit properties (calculated by FEMM4.2). Alternatively, it can be obtained as the difference in the magnetic potential vector A amplitude values over the sides of a stator tooth (flux linkage for one turn), multiplied by the number of turns per coil and the number of coils per phase. The EMF value versus rotor position is calculated by differentiating the flux linkage:

$$E_{emf} = -\frac{d\lambda}{dt} = -\frac{d\lambda}{d\theta_r}\cdot\frac{d\theta_r}{dt} = -\frac{d\lambda}{d\theta_r}\cdot\omega_r = -\frac{d\lambda}{d\theta_r}\cdot\frac{2\cdot\pi\cdot p}{60}\cdot n_N \tag{2.2}$$

where λ is the flux linkage, $d\theta_r$ is the rotor step between two successive analyzed positions, n_N represents the rated motor speed. The BEMF coefficient is calculated using the same formula, but for one turn per coil winding.

The torque acting on the rotor is obtained using the torque via weighted stress tensor method [28], which is a volume integral of the force via Maxwell stress tensor over the region where the torque calculation is needed (rotor block), about the (0.0) point. The no load analysis provides the cogging torque (produced by the interaction between the PM flux and core material), while the load analysis provides the total torque, which includes both the cogging torque and the electromagnetic torque (the interaction torque between the winding mmf and the PM flux). The segregation of the torque components is done by subtracting the cogging torque from the total torque.

2.3.1 Iron losses calculation

The iron core is calculated only for the laminated core material using one of the two approaches below:

The first approach uses a simplified version of Steinmetz formula, which accounts for eddy losses only and uses the specific core losses material information from datasheet:

$$p_{fe} = k_{p_{fe}} \cdot p_{fe_{1T\,400Hz}} \cdot \left(B_s \cdot \frac{f}{400}\right)^2 \cdot m_{fe} \tag{2.3}$$

where $k_{p_{fe}}$ represents a safety coefficient added to consider the mechanical processing losses, $p_{fe_{1T\,400Hz}}$, represents the material specific losses for 400 Hz frequency and 1T magnetic loading, provided in the material datasheet (Table 2.1), B_s represents the average flux density in the core region where the losses are calculated and m_{fe} represents the mass of the core material. The formula approximates the core losses and can be applied for the entire core material, a core region or even for a FEA mesh element.

The second method is also based on Steinmets formula [30] [31], but accounts for both eddy and hysteresis core losses [32] [33]:

$$p_{fe_k} = \left(k_h \cdot f^{fHysExp} \cdot B_k^{BHysExp} + \frac{\pi^2 \cdot f^{fEddyExp} \cdot B_k^{BEddyExp} \cdot lam_{th}^{lamThkExp}}{6 \cdot \rho_{fe}}\right) \cdot V_k \tag{2.4}$$

where V_k represents the core block volume, ρ_{fe} – the iron conductivity, B_k is the flux density for the core block k, f is the frequency of the stator currents main harmonic and lam_{th} is the stack lamination sheet thickness. The exponent coefficients are material specific. Table 2.5 lists their values (for SURA-007 material).

Table 2.5 Iron core exponent coefficients for SURA-007

Description	Name	Value
Hysteresis loss coefficient	k_h	175
Hysteresis loss frequency exponent	fHysExp	1
Hysteresis loss flux density exponent	BHysExp	2
Eddy loss frequency exponent	fEddyExp	2
Eddy loss flux density exponent	BEddyExp	2
Eddy loss lamination thickness exponent	lamThkExp	2

The expression (2.4) is applied during FEA routine, for each mesh element. To reduce the calculation effort which is significant for regular discretization meshes which contain tens of thousands of elements, the analysis in Chapter 3 used a less fine discretization applied over a quarter of stator core (Fig. 2.5), the core losses being calculated considering the average value of flux density B_k in each region. The final value of the stator core losses is calculated as:

$$p_{fe} = 4 \cdot \sum_{k=1}^{n} p_{fe_k} \tag{2.5}$$

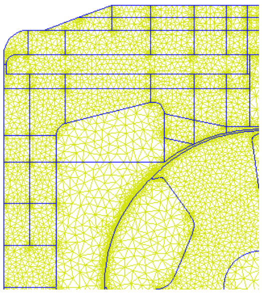

Fig. 2.5 Quarter of the stator core, divided into sub-regions used for core loss calculations

where n represents the number of core regions (elements). Because the considered core region becomes active only half of an electric period, the above method does not reflect very accurately the core losses for the entire stator core. Fig. 2.6 shows a comparison between stator core losses calculation with this method (block regions) versus the calculation in each mesh element with. The latter method, while it may be more accurate, is less feasible for being used in an optimization routine due to the high amount of calculation resources required.

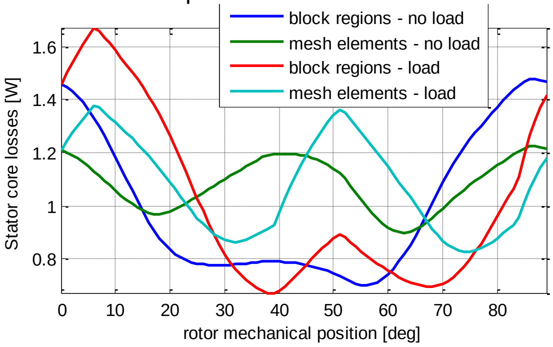

Fig. 2.6 Comparison between block regions versus element stator core loss calculations under load and at no load

The "block region" calculated values, for both load and no-load cases, are higher when the considered quarter stator core is active, and lower on the other half of electrical period (Fig. 2.6). As it is expected both "block region" and "core mesh" values match in the neutral rotor position when both sides of stator pole have approximately same magnetic load.

For additional reduction of the calculation effort, the rotor core losses are calculated based on the stator core losses, assuming that the core losses are proportional with the core volume:

$$p_{fe_R} = p_{fe_S} \frac{V_{rotor}}{V_{stator}} \tag{2.6}$$

The maximum value of the stator plus rotor iron losses values recorded over an electric position is considered as the final core losses value and it is used for efficiency calculation.

2.3.2 Stator phase inductance calculation

- ***Single phase permanent magnet synchronous motor***

The inductance variation with rotor position $L_s(\theta_r)$ represents an important motor parameter, used in the study of the dynamic motor performance via dynamic simulation. Both no load and load analyses are necessary for calculating the winding inductance variation with rotor position. In no load operation mode, the PM magnetic flux linkage crossing the stator winding coils versus rotor position is recorded: $\lambda_{PM}(\theta_r)$. The load analysis provides the stator flux linkage value: $\lambda_s(\theta_r)$ which consists of both PM linkage flux and armature magnetic flux.

$$\lambda_s(\theta_r) = \lambda_{PM}(\theta_r) + L_s(\theta_r) \cdot i_s(\theta_r) \tag{2.7}$$

From (1.7), the stator winding inductance variation with rotor position is extracted:

$$L_s(\theta_r) = \frac{\lambda_s(\theta_r) - \lambda_{PM}(\theta_r)}{i_s(\theta_r)} \tag{2.8}$$

This calculation method is feasible only if the machine operates in non-saturated region during load.

- ***Three phase permanent magnet synchronous motor***

The stator synchronous inductances L_d and L_q are determined in a similar way, but only for a given rotor position, considering that the inductance dependance to rotor position is removed by translation to rotating reference frame:

- d-axis inductance: two FEA are done for the rotor having the d-axis aligned with the phase a stator winding, one at no load generator mode (where λ_{PM} is recorded, assuming that the PM is placed in the d-axis) and one at rated load motor mode (where λ_s is recorded). The d-axis synchronous inductance is calculated using an expression like (2.9):

$$L_d = \frac{\lambda_s - \lambda_{PM}}{i_s} \tag{2.9}$$

- q-axis inductance: a single FEA analysis is performed for motor operation at rated load and the q axis aligned with the phase a axis. With the stator winding linkage and stator current recorded and the assumption that the PM is placed in the d-axis, the q-axis inductance yields:

$$L_q = \frac{\lambda_s}{i_s} \tag{2.10}$$

2.3.3 Demagnetization check

The risk of demagnetization is assessed by running a FEA analysis at 1.5 times rated load (1.5 times the rated current) by recording the minimum value of the normal flux density along a contour defined in the middle of the PM height, perpendicular to the magnetization direction (the red contour in Fig. 2.7).

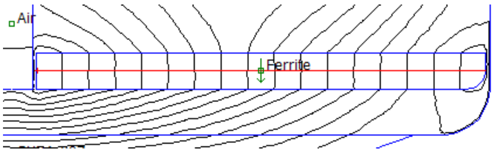

Fig. 2.7 Contour for checking the PM flux density

2.4 Hooke Jeeves algorithm

The optimization process done using Hooke-Jeeves deterministic pattern search algorithm (Fig. 2.8) [34] which is a simple, straightforward, optimization algorithm employed for optimization problems which require finding of the closest local minimum solution [35].

The implementation is based on an adapted version of the algorithm [36], whose diagram is shown below:

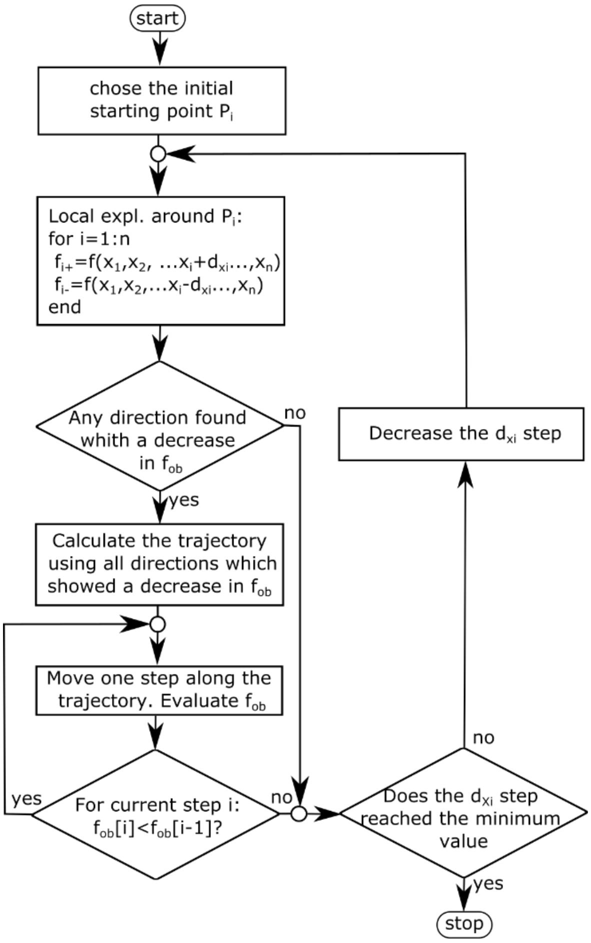

Fig. 2.8 Modified Hooke Jeeves algorithm diagram

The adapted version of the algorithm is presented shortly below. Here, *current point* means the currently evaluated candidate solution, the set of values for the optimal design variables values corresponding to the currently evaluated candidate represent the coordinates of a point in the multidimensional exploration space. These coordinates uniquely describe a single-phase machine. Presented as a state machine (Fig. 2.9), the algorithm can be briefly described as follows:

2.4.1 Exploration phase:

- In this state, the surroundings of the current point are explored along each dimension, successively, by taking two steps: one in the direction of increasing the coordinate value along the respective direction and one in the opposite direction. The total number of objective function evaluation is 2n, where n is the number of exploration space dimensions (number of optimal design variables)
- The step size along each dimension is initially selected according to the interval size (e.g., selected as 10%) and can vary during optimization process (e.g., reduced during step reduction phase to refine the search or set to 0 along a dimension when the limit of the search space is reached).
- In the original version of this algorithm [34], if the movement in one of the two directions lead to a better candidate, the position of the current point was updated and the exploration movements along the remaining directions to be explored were carried out from this new point. The authors of [3] updated the algorithm to preserve the initial same position throughout the exploration phase and use the information on the surroundings to calculate the descending gradient
- In both variants, the objective function variation along each searched dimension is stored at the end of the exploration phase before the algorithm state is changed to *gradient calculation phase*

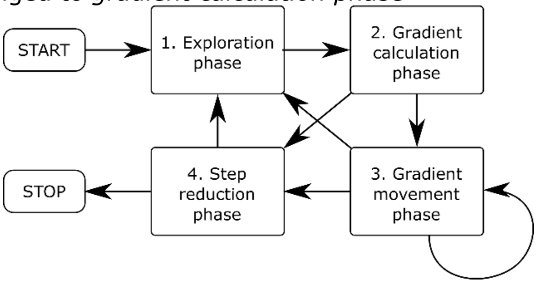

Fig. 2.9 Hooke Jeeves algorithm state machine diagram

2.4.2 Gradient calculation phase

- In this phase the previous exploration steps where the objective function showed a decrease in value (compared to the objective function of the starting point) are selected and combined into a movement direction in the n-dimensional space.
- If the objective function showed no decrease in the objective function during the exploration step movements in either direction for a given dimension, no movement is done along the respective dimension (step size for gradient movement is set to 0)
- If the objective function showed no decrease in its value for any of the exploration steps, the algorithm transitions to the *step reduction phase*, otherwise, the next algorithm state is set to *gradient movement phase.*

2.4.3 Gradient movement (or pattern movement) phase

- In the gradient movement phase, the movement direction and step size calculated during *gradient calculation phase* is successively applied for as long as it shows a decrease in the objective function. The current point is updated after each step.

- The same gradient movement direction and step size is used for all successive descending steps, except for the cases mentioned below, where the initially calculated gradient direction is altered:
    - If the current point reaches the vicinity of the search space and no further movement is possible along one or more directions, the movement along the direction(s) where the exploration interval was reached is limited as to not exceed the interval.
    - If not a single successful gradient movement took place, instead of reducing the movement step and re-running the exploration phase, a gradient movement is started along the direction which showed the largest reduction in objective function in the previous exploration phase, only (with same step size used in the respective exploration step). This gradient change is applied only for modified version of the exploration phase [36] to reduce the computation effort taken to rerun the exploration space, in the context of highly resource demanding FEM-based-only objective function evaluation, and still take advantage of the results of the previous exploration phase.
- If at least one single successful gradient movement took place, but after one or more steps the objective function does not show any more a decrease in the objective function, the algorithm transitions to the exploration phase, to explore the area of the new current point.
- If the current point reached the limits of the search space and it is not possible to step further along **any** direction, the current point is saved and algorithm transitions to the *step reduction phase* state, to reduce the movement step and allow a refined search in the area surrounding the current point.

2.4.4 Step reduction phase

- This algorithm state reduces the movement step with a predefined rate (usually set to 2) and changes the algorithm state to exploration phase. The last "good" optimization point found before enabling the step reduction phase is saved and used as starting point for the next exploration phase.
- A minimum movement step is defined before the algorithm starts, considering the minimum resolution for the optimal design variables (e.g., from technological manufacturing point of view, in case of geometric dimensions). In case the current movement step is already the minimum movement step and no further step reduction is possible along any direction, the optimization process is ended, and the last point is considered as optimum solution.

The Hooke Jeeves algorithm is known to not to ensure the finding of the global optimum solution. To be able to cover the entire exploration space, the algorithm must be deployed several times, from different initial starting positions (starting points) which can either be equidistantly distributed or randomly selected (as applied in Chapter 6).

2.5 Compressor model

The compressor model is a standard model for a reciprocating air compressor, whose PV cycle diagram is shown in Fig. 2.10. The compressor's cylinder is connected through valves to two pressure systems:

- Lower pressure system: P_s (suction pressure) – intake path
- Higher pressure system P_d (discharge pressure) – exhaust path

The operation of the compressor can be divided in 4 stages: expansion, suction, compression, and discharge. This corresponds to a complete piston trip from V_m (top dead center) to V_{max} (bottom dead center) and back.

The minimum cylinder volume V_m is a manufacturing parameter, whereas the maximum cylinder volume V_{max} can be calculated based on current crankshaft position (electric motor rotor’s position), piston surface and rod length as:

$$V_{max} = \left(1 + \cos\left(\theta_r + \frac{\pi}{6}\right)\right) \cdot R_{ex} \cdot S_{piston} + V_m \tag{2.11}$$

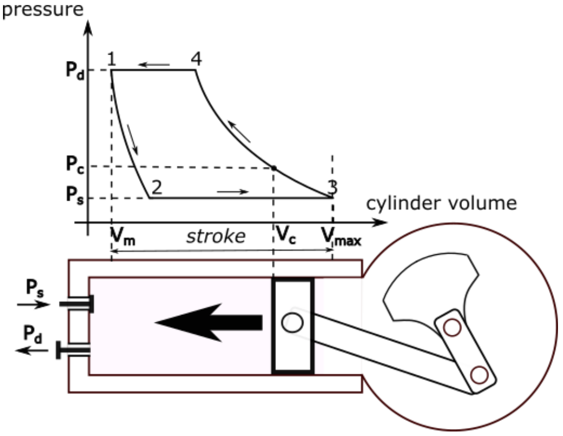

Fig. 2.10 Reciprocating compressor pv diagram and scheme (with current operating point during Compression phase)

1. Expansion: phase 1-2

This represents an adiabatic transformation characterized by the equation (2.17), where P_c and V_c characterize the current operating point, for current piston position (moving from 1 to 2, in Fig. 2.10):

$$P_d V_m^{n_{gas}} = P_c V_c^{n_{gas}} \tag{2.12}$$

The n_{gas} represents the refrigerant gas constant. The set of conditions characterizing this phase are:

$$\begin{cases} \dfrac{dV_c}{dt} > 0 \\ P_c > P_s \end{cases} \tag{2.13}$$

2. Suction: phase 2-3

This part is characterized by piston movement to bottom dead center, under constant suction pressure P_s. The intake valve is open, and gas fills the cylinder under piston movement. The conditions characterizing this phase are:

$$\begin{cases} V_c \le V_{max} \\ P_c = P_s \end{cases} \tag{2.14}$$

3. Compression: phase 3-4

During this phase, the piston starts moving from the bottom dead center back to top dead center, compressing the gas. This phase is characterized by the adiabatic law:

$$P_s V_{max}^{n_{gas}} = P_c V_c^{n_{gas}} \tag{2.15}$$

This phase is characterized by the conditions:

$$\begin{cases} \dfrac{dV_c}{dt} \le 0 \\ P_c \le P_d \end{cases} \tag{2.16}$$

4. Discharge: phase 4-1

During this last phase, the compressed gas is discharged through the exhaust valve, under constant P_d pressure, while the piston is moving towards the top dead center. The phase is characterized by the conditions:

$$\begin{cases} V_c \ge V_m \\ P_c = P_d \end{cases} \tag{2.17}$$

Knowing the pressure in the cylinder chamber, the torque acting on crankshaft (load torque for the electric motor) can be calculated as:

$$T_c(\theta_r) = \sin\left(\theta_r + \frac{\pi}{6}\right) \cdot R_{exc} \cdot S_{pist} + V_m \tag{2.18}$$

The compressor parameters used here for simulation are presented in Table 2.6.

Table 2.6 Reciprocating compressor parameters

Parameter	Value	Description
R_{exc} [m]	10×10^{-3}	Axis eccentricity
S_{pist} [m^2]	0.45×10^{-3}	Piston surface
V_m [m^3]	120×10^{-9}	Cylinder dead volume
P_d [bar]	5.3	Discharge pressure
P_s [bar]	0.3	Suction pressure
n_{gas} [-]	1.1	refrigerator gas constant

Fig. 2.11 presents the Simulink implementation of the reciprocating compressor model.

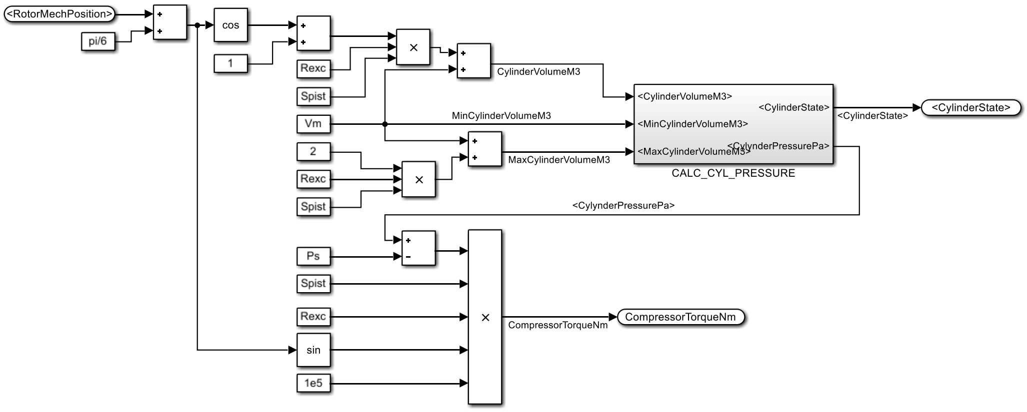

a)

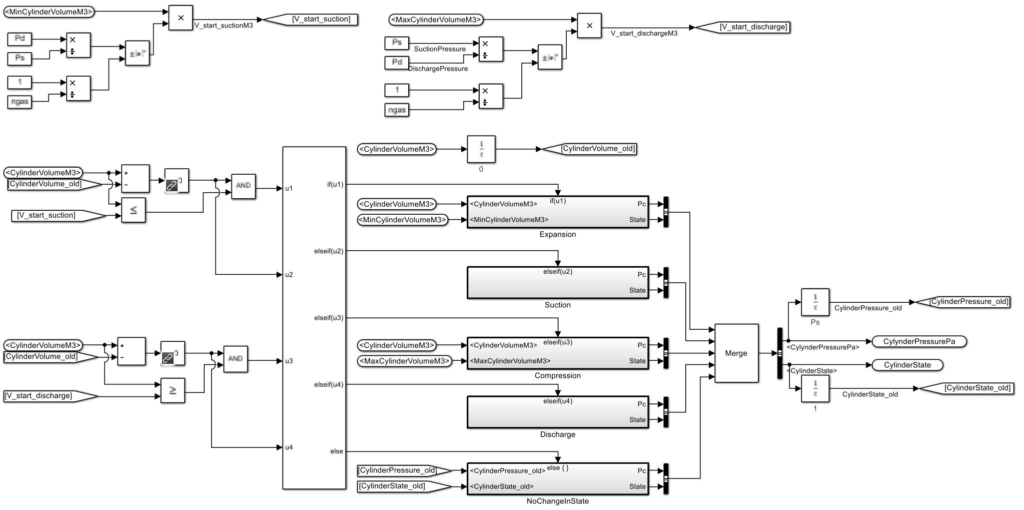

b)

Fig. 2.11 Reciprocating compressor model: a) cylinder volume and torque calculation; b) cylinder pressure calculation

Fig. 2.12 shows the simulation results for 2 cycles of operation (two crankshaft revolutions). The load torque is highly pulsatory, reaching 1 Nm peak during the start of discharge phase (when the gas compression reaches the maximum value P_d). This represents an ideal case of the compressor operation, at constant angular velocity. In reality, the rotating speed is not constant, and the discharge and suction pressures are also not constant.

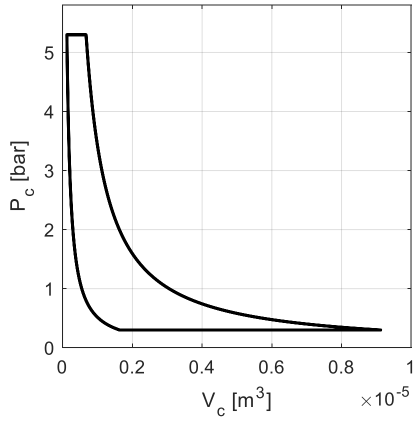

a)

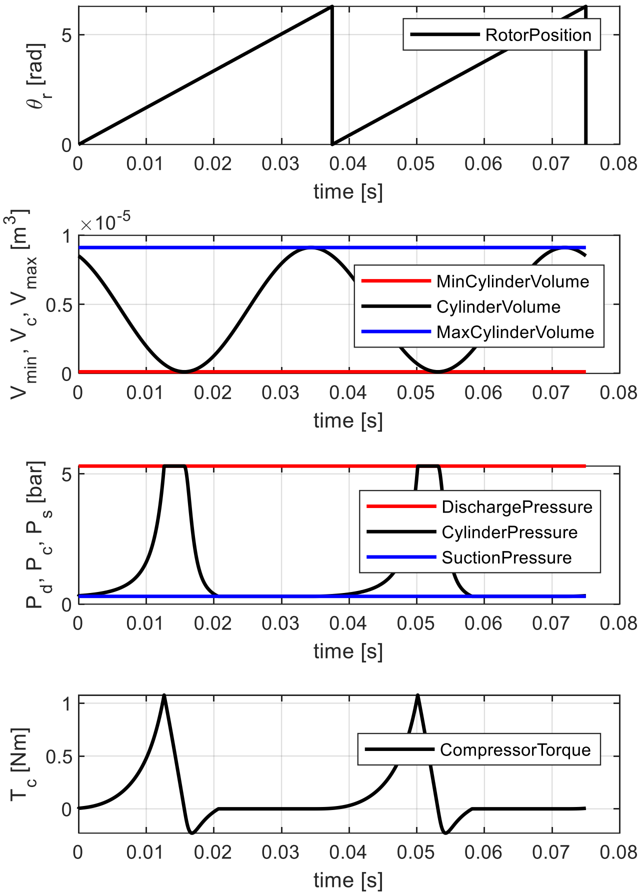

b)

Fig. 2.12 Simulation results for the reciprocating compressor operation for two crankshaft revolutions a) P-V diagram, b) variation of the cylinder volume, pressure, and compressor torque with time

CHAPTER 3. DESIGN AND ANALYSIS OF SINGLE PHASE TWO STATOR POLES FERRITE PM DOUBLE SALIENCY SM

Abstract

This chapter presents the study and design of a new single-phase motor topology. The chapter starts with an overview of the single-phase synchronous motors, introduces the new topology, and explains its operation with the aid of finite element analysis. After introducing a FEA based optimal design methodology, a case study is done for a 35W, 1600rpm motor, corresponding to the demands of a small mobile refrigerator compressor. The main optimization targets are increasing the motor rated efficiency to 88% and minimize the motor cost material cost. Optimal design results are presented, followed by FEA and digital dynamic simulation under close loop speed and current control validations. A few test results on a built prototype are presented at the end.

3.1 Introduction

Permanent magnet synchronous motors offer many advantages, in terms of high-power density, high efficiency and fast dynamic response.

The most widespread configurations use permanent magnets placed on the rotor (active rotor). While these configurations provide several merits, they also have drawbacks, such as: weaken the rotor structure and robustness (preventing operation at high speeds), difficulties in fixating the PMs, for surface placed PMS. Less spread configurations use magnets placed on stator, where they assist the armature magnetomotive force.

Placing the PM on the stator can overcome the above-mentioned difficulties and, due to passive and robust rotor, allow for operation at high speeds (for low power targeted applications as tools, compressors, etc.)

The stator PM synchronous machines can be classified into the following categories [37] [38]:

- **Doubly salient permanent magnet machines (DSPMM)** – their main characteristic is having unipolar stator coil magnetic flux. They resemble the switch reluctance machines, with additional assistance from the permanent magnets. They can be used as either BLDC (step commutation), or with additional mechanical changes (rotor skewing [39]) as BLAC.
- **Flux reversal permanent magnet machines (FRPMM)–**their main characteristic (which also gives their name) is that the PM flux direction through the stator coil changes with rotor position. This occurs by having the rotor tooth aligned successively with PMs of alternate polarity placed under a stator tooth surface. From control strategy point of view, they can also be treated as BLDC or BLAC (with rotor skewed).
- **Flux switching machines (FSPMM) -** contain an inset PM magnet, placed under a stator pole which has a winding coil wrapped around it. The PM magnetization direction perpendicular to the tooth coil axis, therefore the magnetic flux through the coil "switches" polarity as the rotor tooth change its position and transitions from facing one side of the permanent magnet flux to facing the other side.

Due to this transition, the PM magnetic flux variation through the coil is inherently sinusoidal. A flux concentration effect is also employed, which increases the EMF for same number of turns per coil but can also increase the magnetic saturation level.

Cheng et. al provides a comparison of these categories of stator PM brushless machines (Fig. 3.1):

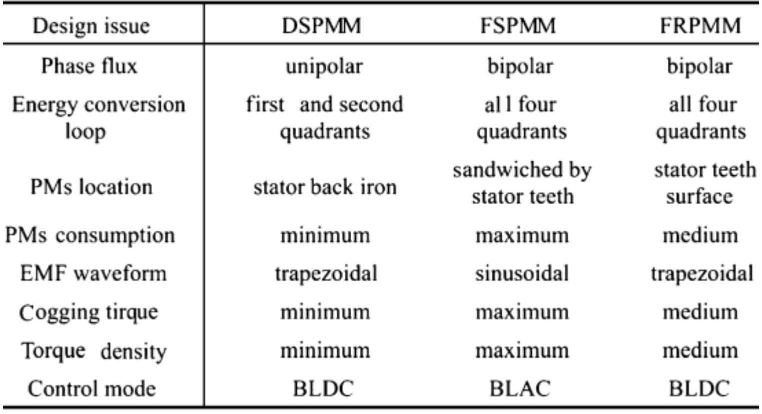

Design issue	DSPMM	FSPMM	FRPMM
Phase flux	unipolar	bipolar	bipolar
Energy conversion loop	first and second quadrants	al l four quadrants	all four quadrants
PMs location	stator back iron	sandwiched by stator teeth	stator teeth surface
PMs consumption	minimum	maximum	medium
EMF waveform	trapezoidal	sinusoidal	trapezoidal
Cogging tirque	minimum	maximum	medium
Torque density	minimum	maximum	medium
Control mode	BLDC	BLAC	BLDC

Fig. 3.1 Comparison of stator PM synchronous machines from several operation/design characteristics point of view [39]

Single phase synchronous motors are suitable for use at lower powers as they are easier to manufacture and more reliable (the use of a single-phase winding reduces the chances of failure).

They do have disadvantages, like requiring a reduced airgap and exhibiting higher noise due to non-cylindrical rotor shape and the starting challenges they pose. From this point of view, there are two types of strategies (types of motors):

- line start single phase motors: start is performed asynchronous, with the support of a rotor cage winding.
- Geometric/magnetic anisotropy start based on the existence of a non-zero electromagnetic torque in the stop position. Once started, the rotor will align to one of the rotating magnetic fields produced by the stator coil. This second type of machine will be addressed here.

The present chapter characterizes a single phase two-pole Ferrite-PM stator double saliency, **flux reversal motor**, in terms of optimal design, controlled dynamics and preliminary experimental validation.

The next paragraph expands on the flux reversal permanent magnet machines.

3.1.1 Topologies of flux reversal machines

The flux reversal motors are double salient permanent magnet synchronous motors which have the magnetic flux sources placed on the stator and magnetically passive rotors. Their main advantages are simplicity and fault tolerance. At lower powers they are more efficient than the induction motors, simpler and more cost effective in terms of power electronics drive and control than 3 phase PMSM or BLDC drives.

The first flux reversal machine was proposed by Binder, in 1948 [40]. Since then, many other topologies were proposed and investigated. Deodhar et al [37] proposed single phase a topology with two stator poles and three rotor poles, designed for use as a high-speed generator (Fig. 3.2). Its claimed advantages were robustness, fault tolerance and high-speed capability. This topology was investigated also by Jang et al. [41], for an application of a vacuum cleaner (with a target speed of 30krpm).

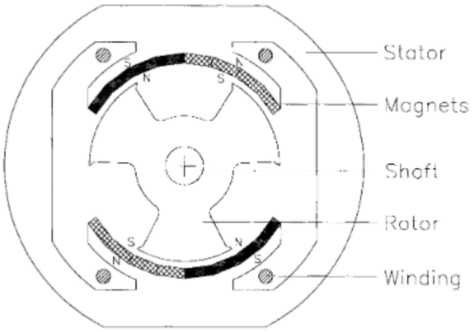

Fig. 3.2 Flux reversal machine according to [37]

Building on this configuration, Prakht and al. [42] proposed a single-phase topology containing 4 stator poles and four rotor poles, for an angle grinder application, claiming that this topology improves the use of the stator iron, thus increasing the efficiency and reducing the radial forces (Fig. 3.3).

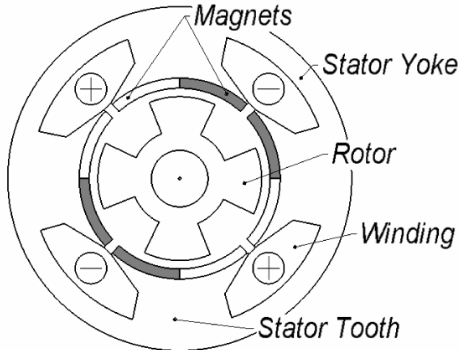

Fig. 3.3 Single phase flux reversal PM machine with four stator poles configuration [20]

Flux reversal machines have also been studies for 3 phase configurations with inner rotor [43] [44] and outer rotor [45], as small power small speed wind generator.

3.1.2 The proposed concept

Starting from the conventional flux reversal PM motor, some modifications are proposed here to reduce the size and cost of the motor (Fig. 3.4):

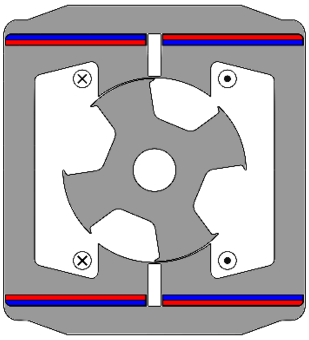

Fig. 3.4 Proposed single phase motor topology

- use magnets buried in the stator instead of placing them on the stator tooth surface: this modification allows the use of larger magnet blocks, the increasing of the magnetization flux and reducing the necessary winding mmf, resulting in smaller number of turns per coil. This leads to a decrease in either the copper use (cost reduction) or in larger room available for thicker wire diameter (lower copper losses). The magnets are better fixed and protected against radial forces and less exposed to demagnetization risk.
- Use a stator flux barrier to prevent "short-circuit" of the PM magnetic flux

The rotor poles are shaped to introduce a variable airgap, which secures the motor starting. The two sides of the stator poles are active successively, when they become aligned with the rotor teeth. However, as it can be observed in Fig. 3.5, all four magnets are active for each rotor position. Fig. 3.5 shows in a simplified manner (neglecting leakage magnetic flux) the main magnetic flux paths produced by the stator PM for successive rotor positions. The 2nd and 4th rotor positions correspond to 0 stator coil PM flux, the PM flux being "short-circuited" (this is also the position for maximum EMF value).

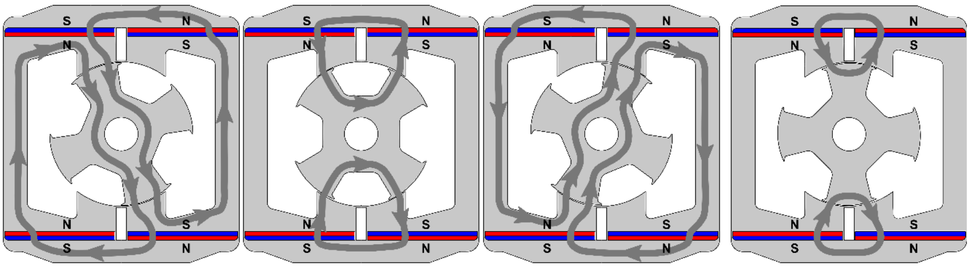

Fig. 3.5 Permanent magnet flux path for different rotor positions

Fort this motor, the ideal emf variation in time (with rotor position) with rotor position is a square wave (or sharp trapezoidal shape) as shown in Fig. 3.6. To obtain a constant output power value, the prescribed current should also follow a trapezoidal shape. The electromagnetic torque variation with time follows in this case a shape like the power P(t), with zero values corresponding to the current or linkage flux zero crossing. Ideally, these torque gaps are compensated by cogging torque values, which is achievable through proper geometry shaping of the motor.

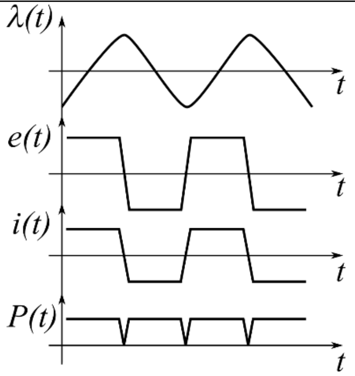

Fig. 3.6 Ideal variation of linkage flux, electromotive force, stator current and electromagnetic power for single phase flux reversal machine

The current shape (rise and fall slope) and phase-shift with respect to the EMF are influenced by the winding inductance. Special phase advance control techniques are needed to compensate for the current rise and fall delay and at the same time avoid high dv/dt voltage gradient value, which poses risks for the power converter.

Fig. 3.7 a shows PM magnetic flux path for three successive rotor positions and the corresponding airgap flux density along the stator interior diameter circumference obtained by FEA. The airgap flux density shows that a rather small portion of the rotor is magnetically active at any time and used for torque producing. Additionally, the approx. 0.6T maximum airgap flux density value is acceptable for Ferrite PMs.

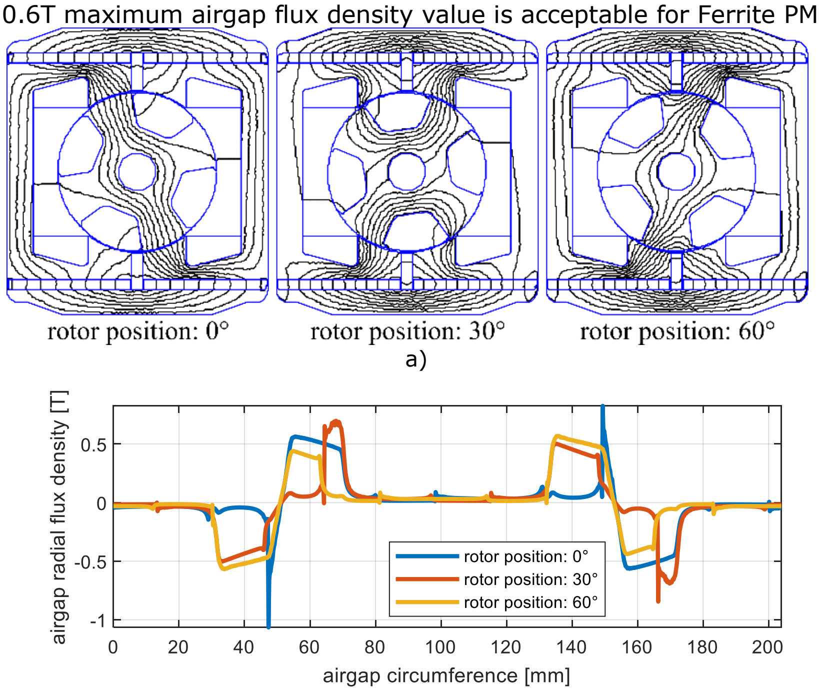

a)

b)

Fig. 3.7 PM magnetic flux distribution versus several rotor positions a) and airgap flux density distribution b)

Explanatory for the machine operation, below is presented a FEM analysis for no load and load operation (of the FEA model shown in Fig. 3.7 a). The FEM analysis simulated the rotor movement over an electric period (90 mechanical degrees) in anti-clockwise rotation.

The operation under open load generator mode analysis (no load analysis) results are listed in Fig. 3.8 a. The PM magnetic flux linkage amplitude crossing the stator winding coils variation with rotor position is not symmetric (due to geometry structure and airgap tapering) and deviates from the ideal triangular shape. This causes the EMF shape to deviate from the trapezoidal waveform.

The operation under load analysis is simulated by setting a phase coil current which has a trapezoidal variation with the rotor position and has same phase as the emf waveform (Fig. 3.8 b). The torque produced by the motor extracted from load analysis (Fig. 3.8 c blue line) can be split into two main components: electromagnetic torque (torque produced by the interaction between the winding current and the PM flux) and cogging torque (generated by the interaction between the PM flux and the rotor core iron – determined during no load analysis).

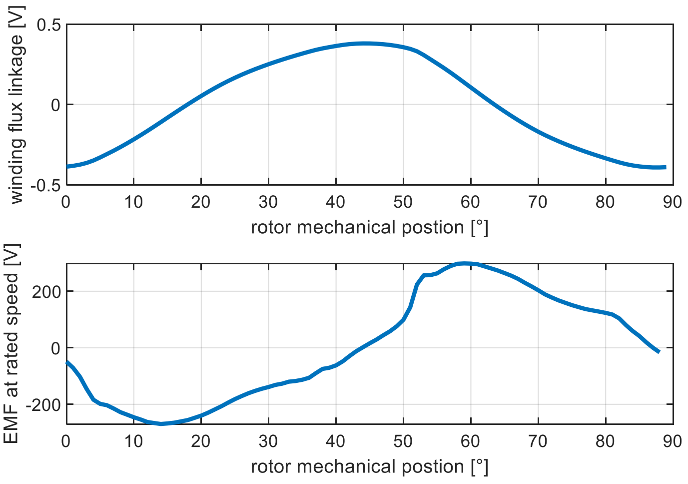

a)

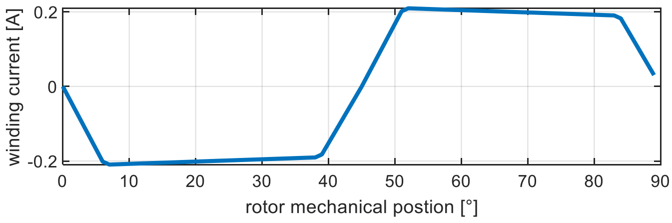

b)

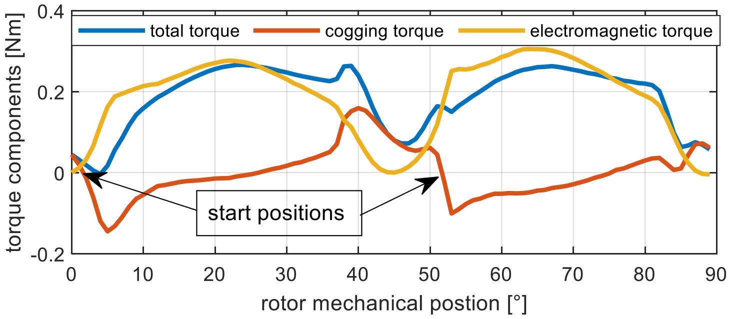

c)

Fig. 3.8 FEM analysis of operation of a single-phase synchronous machine: a) stator winding flux linkage versus rotor position and EMF at rated (1600rpm) speed, b) load prescribed current (assuming operation under closed loop current control), c) torque components

To obtain a non-negative electromagnetic torque, the stator current variation should be in phase with the EMF.

Ideally, the shape of cogging torque should compensate the gaps in electromagnetic torque (caused by current zero crossing, during polarity change – occurring at 45 deg, in Fig. 3.8) and smoothen its shape. The cogging torque shape depends on the geometric shape of the stator/rotor teeth and the airgap profile and can be, therefore, subject to optimization during machine design.

Another important information provided by the cogging torque waveform is the rotor stop positions – the position where rotor will halt after the winding is not energized anymore. The stop positions are identified as the positions where the cogging torque changes its sign from positive to negative values (positions marked in Fig. 3.8 c). The real stop position is a region, rather than a fixed point, being dependent on the air and bearings friction torque and the friction torque characteristic of the load (reciprocating piston crankshaft, in this case)

To secure a safe start, the electromagnetic torque value should be as high as possible in this region. Fig. 3.8 c shows a bad stop position (around 5° degrees) and a good stop position (at approx. 45° mechanical degrees).

3.2 FEM-analytic model co-simulation routine for the optimal design process

The motor design algorithm combines analytic and FEA calculations. The flux distribution, iron losses and torque calculations are based on FEA simulations, while all other performance data is analytically calculated. Fig. 3.9 shows a diagram of the design algorithm, where load and no-load finite element method calculations are iteratively run for successive rotor positions over an electric period.

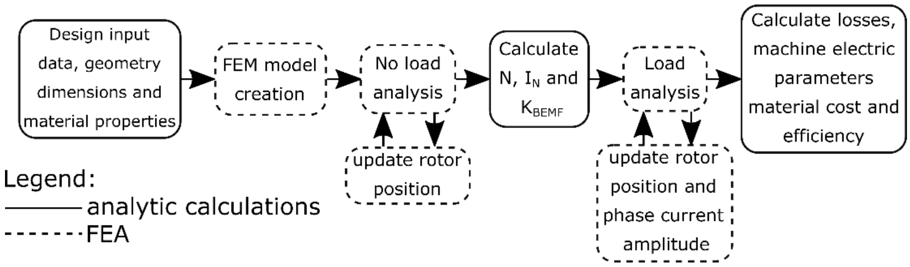

Fig. 3.9 Motor design calculation routine

- **Data definition** – consists of defining the design requirements which constitutes the input data for the design process, defining the initial values for the main geometric motor dimensions necessary for machine CAD drawing, listed in Table 3.1 and Fig. 3.10 and the parametrization of the optimal design algorithm

Table 3.1 Primary single phase motor geometry parameters

Geometry parameters	Description
s_{Do}	Stator outer diameter sDo [mm]
s_{Di}	Stator inner diameter sDi [mm]
s_{hy}	Stator yoke height shy [mm]
s_{hy1}	Stator yoke height shy1 [mm]
α_{ST}	Stator tooth span α_{ST} [rad]
l_{stack}	Stack length [mm]
h_{pm}	PM height
h_{ag}	Smaller airgap part h_{ag} [mm]
h_{ag1}	Larger airgap height h_{ag1} [mm]
r_{hy}	Rotor yoke height
α_{RT}	Rotor pole span coefficient α_{RT} [p.u.]

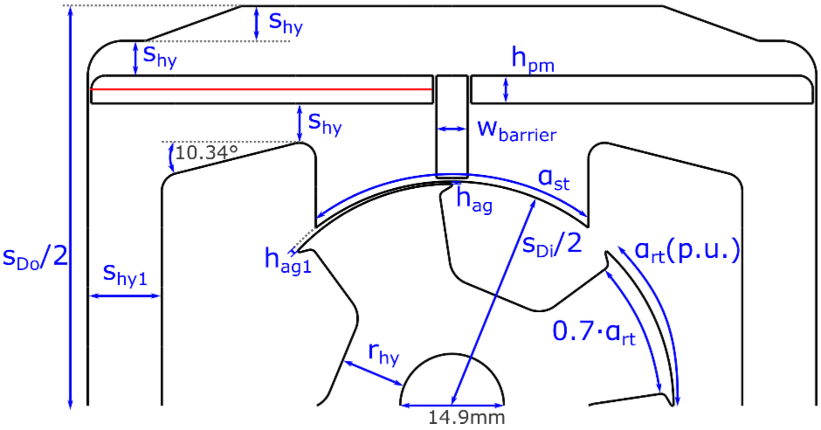

Fig. 3.10 Machine geometry including the primary geometry dimensions

- **Create the FEM model** - uses the FEMM 4.2 preprocess phase to draw the machine geometry, set the material properties, winding material circuit and boundary conditions.
- **No load analysis** - represents an iterative process of solving the FEA model for successive rotor positions covering one electric period. No load analysis is simulated by imposing a 0 A current within the machine windings. Using FEA postprocess stage, cogging torque value T_{cogg} (computed Maxwell stress tensor), winding flux linkage Φ_S (for a single turn per coil) are recorded for each rotor position.
- The no load analysis results are used for estimation of the necessary number of turns per coil and rated current amplitude. First, the EMF per

one coil turn, also called emf coefficient k_e is calculated for rated speed ω_r as:

$$\begin{aligned} E_{emf/turn}(\theta_r) = k_e(\theta_r) &= -\frac{d\Phi(\theta_r)}{dt} \\ &= -\frac{d\Phi(\theta_r)}{d\theta_r}\frac{d\theta_r}{dt} \\ &= -\frac{d\Phi(\theta_r)}{d\theta_r}\cdot\omega_r \\ &= -\frac{d\Phi(\theta_r)}{d\theta_r}\cdot\frac{2\cdot\pi\cdot n_N\cdot p}{60} \end{aligned} \tag{3.1}$$

where $d\theta_r$ represents the rotor step between two no load analysis (electric angle), n_N represents the rated speed and p represents the rotor pole pairs. The k_e shape is similar to the EMF shape shown in Fig. 2.8 a. Next, a rough estimation of the number of turns per coil N is done by assuming that BEMF covers 70% of the DC voltage at rated speed (30% reserve of the DC voltage is considered, to cover also the voltage drop on the resistive and inductive components of the stator winding):

$$N = round\left(\frac{0.7V_{DC}}{max\left(k_e(\theta_r)\right)}\right) \tag{3.2}$$

The $max(k_e)$ value represents the EMF constant, which is the proportionality factor between both stator current/electromagnetic torque and EMF/electric rotor speed.

$$K_e = N\cdot max(k_e) \tag{3.3}$$

The rated output mechanical torque can be calculated based on design input rated power and rated speed:

$$T_e = \frac{P_N}{2\cdot\pi\cdot p\cdot n_N/60} \tag{3.4}$$

By neglecting the mechanical losses and rotor iron losses, it can be assumed the electromagnetic torque equals the output mechanical torque. With this simplification, the winding magnetomotive force (mmf) is calculated as:

$$mmf = \frac{T_e}{\frac{\Phi_1}{\sqrt{2}}\cdot p} \tag{3.5}$$

where Φ_1 is the first space harmonic of the flux linkage measured during no load analysis.

Finally, the rms value of the current amplitude results from:

$$I_N = \frac{mmf}{N} \tag{3.6}$$

- **Load analysis** – after updating the FEA model winding number of turns per coil to N, a second analysis for successive rotor positions spanning one electric pole pair is ran, having a position dependent trapezoidal shape current (Fig. 2.8b) of amplitude I_N imposed to the stator winding. The torque acting on rotor, phase magnetic flux linkage and flux density variation in mesh element block region are measured. Using FEM extracted measurements; the efficiency is calculated as:

$$\eta = \frac{T_m \cdot \omega_N}{T_m \cdot \omega_N + p_{co} + p_{fe} + p_{mec}} \tag{3.7}$$

where T_m represents the total torque mean value, extracted from FEM, p_{co} – are the copper losses, p_{fe} represent the core losses and p_{mec} are the mechanical losses.

The mechanical losses are considered as 1.5 % of the mechanical output power, while copper losses are calculated using Ohm law, for a winding resistance determined based on number of turns per coil, fitting the available stator slot area.

For the iron loss calculation, both hysteresis and eddy loss components are considered, determined from FEA as presented in Chapter 2.

3.2.1 Optimal design routine using FEA analysis

Having the electric machine design routine established, the optimization process is further defined, to ensure that the design result represents the best compromise result in terms of performance and cost [3]. The setup consists in defining the variables to be optimized, the range for each variable (search domain) and their initial values as well as the objective function.

Design variables

The primary geometry dimensions which define the machine already presented in Table 3.1 are selected as optimization variables. The search range and initial values are presented in Table 3.2.

Table 3.2 Single phase motor optimal design variables

Parameter	Initial value	Min values	Max values	Minimum variation step
s_{Do}	105	90	115	0.5
s_{Di}	64.54	50	68	0.5
s_{hy}	5	4	10	0.2
s_{hy1}	10.67	3	10	0.2
α_{ST}	75·pi/180	45·pi/180	81·pi/180	0.01
l_{stack}	30	25	40	0.4
h_{pm}	4	3	8	0.1
$w_{barrier}$	4.5	3	8	0.1
h_{ag}	0.35	0.35	0.6	0.01
h_{ag1}	0.77	0.65	1	0.01
r_{hy}	9.6	6	10	0.1
α_{RT}	0.5	0.4	0.65	0.05

To reduce the resource consumption, the no load FEA (together with the calculation of the number of turns per coil and rated current) is ran only once at the beginning of the optimization process. During the optimization process, only the load FEA and objective function evaluation are calculated for each candidate and optimization step. This means that same current amplitude is used throughout the entire optimization process, as well as for the final candidate. While this reduces the optimization time to half, it also affects the optimization process, by e.g., introducing the risk for the optimum solution to not have enough voltage reserve to develop rated torque at rated speed (caused by not updating the number of turns per coil according to the change in magnetic circuit, produced by the update of the design variables). Additionally, the load FEA is performed for successive rotor positions in steps of 12 electrical degrees (30 steps per electric period), for safety.

Objective function

The objective function f_{ob} is a cost function consisting of total material cost plus penalty costs (all expressed in $).

$$f_{ob} = C_{mat} + c_{T_{min}} + c_{T_{avg}} + c_{\eta} + c_{demag} \tag{3.8}$$

The first cost component C_{mat} represents the motor material cost. It includes the stator lamination cost, PM cost, copper and rotor iron core cost and passive material cost (which accounts for frame cost, insulation material cost etc.). Each cost was calculated as material cost (defined in $/kg) multiplied by quantity of material used to fabricate the motor (expressed in kg). The meaning of the penalty costs is:

$c_{T_{min}}$ represents the minimum torque penalty cost. It is applied only if the minimum toque at nominal load decreases under a minimum prescribed value T_{min}. It is expressed as the sum of all the FEA analysis extracted torque values T_k (within an electrical period) which fall under the minimum threshold, multiplied by a weighting coefficient $k_{T_{min}}$.

$$c_{T_{min}} = k_{T_{min}} \cdot C_{mat} \cdot \sum_{k=1}^{n} max\left(T_{min} - T_k, 0\right) \tag{3.9}$$

where n is the number of iterative FEA analysis steps over an electric period. The purpose of this penalty cost is to reduce the torque pulsations and prevent negative minimum torque values during operation. It directly impacts the optimal design variables which shape the cogging torque and changes it in such way as to compensate for the electromagnetic torque 0 values (present during current sign switch).

$c_{T_{avg}}$ represents the average torque penalty cost. It is applied only if the average torque value T_{avg} falls under the rated torque value and varies linearly with the material cost multiplied by the average torque reduction ratio multiplied by a weighting factor $k_{T_{avg}}$.

$$\begin{aligned} c_{T_{avg}} &= k_{T_{avg}} \frac{max\left(T_N - T_{avg}, 0\right)}{T_N} \cdot C_{mat} \\ T_{avg} &= \frac{\sum_{k=1}^{n} T_k}{n} \end{aligned} \tag{3.10}$$

c_{η} represents the efficiency non-realization penalty cost. It is expressed as energy consumption by operating at rated power, below a minimum imposed efficiency threshold η_{min}, weighted by a factor k_{η}:

$$c_{\eta} = \begin{cases} k_{\eta} \cdot c_{energy} \cdot \left(\frac{1}{\eta} - \frac{1}{\eta_{min}}\right) \cdot P_N \cdot h_{work}, \eta < \eta_{min} \\ 0, \eta \geq \eta_{min} \end{cases} \tag{3.11}$$

where c_{energy} represents the energy cost ($/kWh), P_N represents the rated motor power and h_{work} represents the motor operation lifetime (hours). This penalty cost ensures that the efficiency of the optimum solution, calculated using (3.7), does not decreases under η_{min}.

Last, c_{demag} represents the demagnetization penalty function, applied if the radial component of the PM flux density decreases below a minimum imposed value $B_{PM_{min}}$, for an overload current of $1.5 \cdot I_N$. The red lines in Fig. 2.7 and Fig. 3.10 denote the contours used for measuring the normal flux density for demagnetization check (the minimum flux density value $B_{\Gamma_{min}}$ along the red contour Γ was considered).

$$c_{demag} = k_{demag} \cdot C_{mat} \cdot \frac{min\left(B_{PM_{min}} - B_{\Gamma_{min}}, 0\right)}{B_{PM_r}} \tag{3.12}$$

were B_{PM_r} represents the PM remanent flux and k_{demag} is a weighting factor. This penalty cost ensures that the resulted PMs thickness is large enough to avoid demagnetization during motor overload.

For the case study below, the objective function parameter values were selected as shown in Table 3.3.

Table 3.3 Single phase motor objective function parameters values

Parameter	Value [unit]
k_{Tmin}	1 [-]
T_{min}	0.1 [T]
k_{Tavg}	1 [-]
k_{η}	1 [-]
c_{energy}	0.5
h_{work}	36500 [h]
η_{min}	0.88 [-]
k_{demag}	10 [-]
B_{PMmin}	0.2 [T]

3.3 Optimal design: case-study

The presented optimal design procedure was applied for a case study of a small power motor, intended for small, mobile refrigeration systems. The design input requirements and optimization results are presented below.

Design requirements.

The requirements are to design a low power motor single phase motor having the following rating:

- output mechanical power: 35W
- rated speed: 1600rpm
- minimum efficiency for operation at rated speed and torque: 88%
- immune to demagnetization risk during operation at 1.5 times the rated load
- a minimum torque ripple value of 0.1 Nm during rated load (approx. 50% of the rated torque value)

Optimization results

The optimal design was started from the initial point defined by the optimal design variables in Table 3.2. An optimal solution was found after 5 Hooks Jeeves algorithm steps, the entire optimization process taking 23 hours. Fig. 3.11 presents the evolution of the main electric/geometry parameters during the optimization process, while Table 3.4 presents a comparison of the performance of the initial candidate versus the optimum result.

The optimization processes reduced the objective function value with more that 40 \$ to a final value of 16 \$ (Fig. 3.11 a) which represents the motor material costs (Fig. 3.11 c), all the penalty costs being reduced to 0 $ (Fig. 3.11 b). Even if the objective function value was minimized, the total material cost for the final motor increased with 4 $, from the initial cost of 12.04 $. This outcome was generated by the high weighting of the minimum torque and efficiency penalty cost in the objective function, which overcome the motor materials cost.

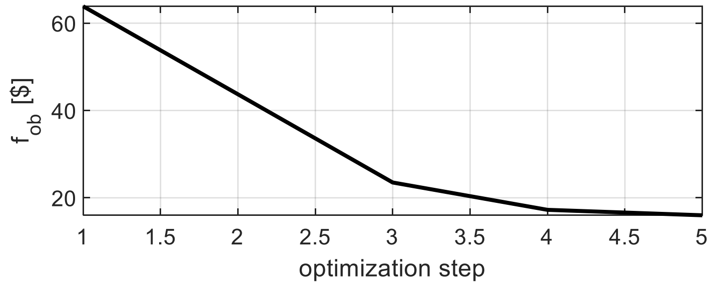

a)

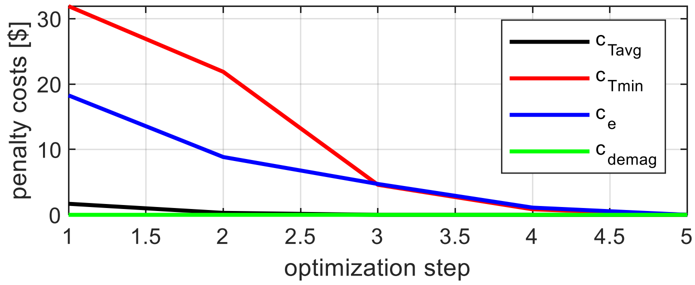

b)

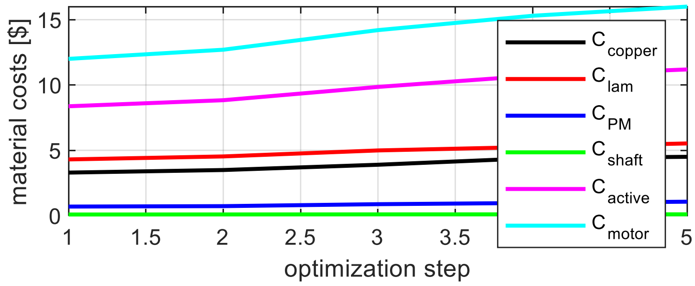

c)

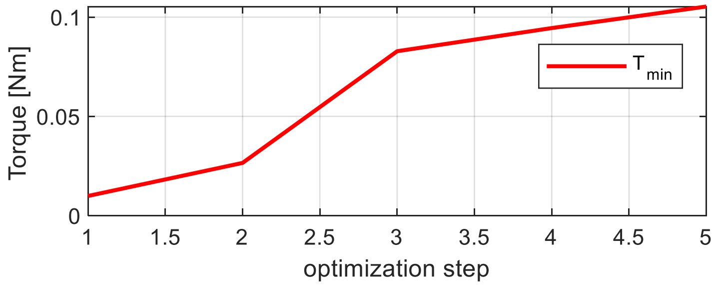

d)

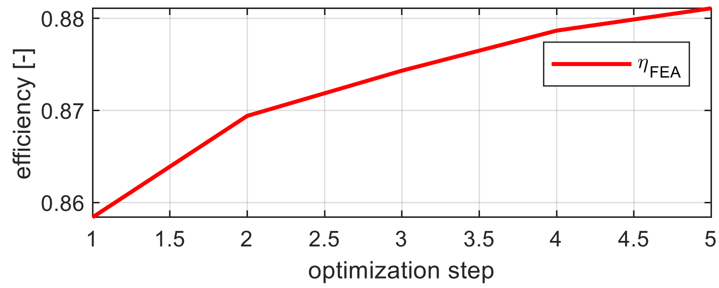
efficiency [-]
0.88
0.87
0.86
η_{FEA}
1
1.5
2
2.5
3
3.5
4
4.5
5
optimization step

e)

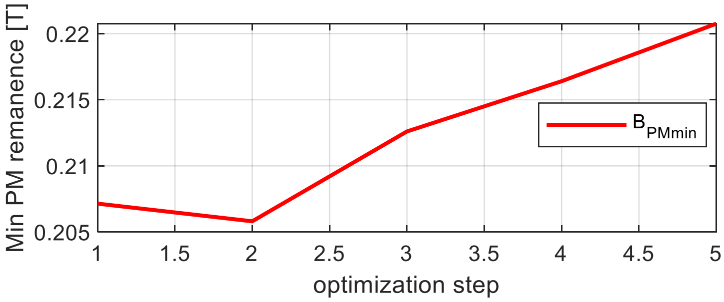
Min PM remanence [T]
0.22
0.215
0.21
0.205
B_{PMmin}
1
1.5
2
2.5
3
3.5
4
4.5
5
optimization step

f)

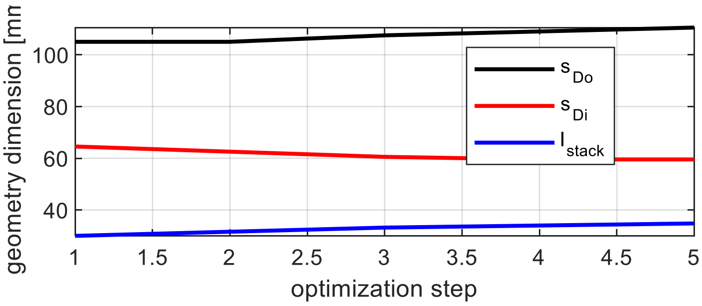
geometry dimension [mn
100
80
60
40
s_{Do}
s_{Di}
l_{stack}
1
1.5
2
2.5
3
3.5
4
4.5
5
optimization step

g)

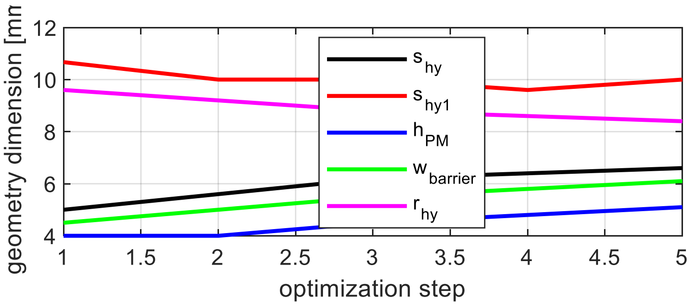
geometry dimension [mn
12
10
8
6
4
s_{hy}
s_{hy1}
h_{PM}
$w_{barrier}$
r_{hy}
1
1.5
2
2.5
3
3.5
4
4.5
5
optimization step

h)

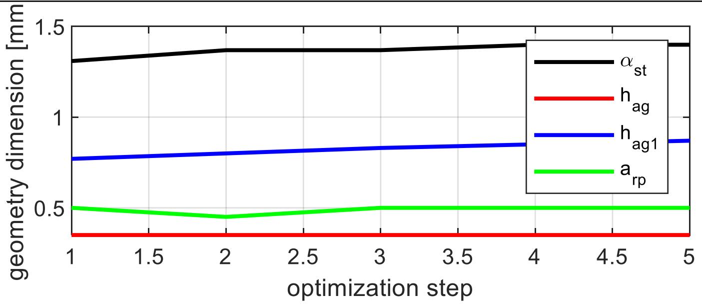

i)

Fig. 3.11 Evolution during the optimization process of: a) objective function, b) penalty costs, c) material costs, d) minimum torque value over an electric period, e) efficiency, f) minimum PM normal flux density component at 1.5 rated current overload, g, h, i) optimal design variables

The motor efficiency at rated operation is indeed improved from 85% to 88% (Fig. 3.11 e), while the minimum torque value during rated load operation is also increased from 0 Nm to 0.1Nm (Fig. 3.11 d).

A detailed comparison of the optimal design results versus the initial motor is presented in Table 3.4. The motor material cost increase is mainly caused by the increase in rotor stack length, outer diameter, PM height and winding cross-section (for same number of turns per coil). For same mmf value, the PM flux increase was necessary to be able to produce the required output power of 35W.

The efficiency improvement also impacted the material cost, the copper losses reduction being done at the expense of increasing the copper use. While the iron losses value increased during optimization results, the increase in the output power at the same load current improved the net efficiency value.

Table 3.4 Single phase motor: initial vs optimum results comparison

Parameter	Initial result	Optimum results
Mechanical output power [W]	30	40.3
Number of turns per coil [-]	451	451
Rated phase current [A]	0.28	0.28
Average torque value for rated load [Nm]	0.17	0.24
Minimum torque value for rated load [Nm]	0.01	0.10
Efficiency [-]	0.85	0.88
Copper losses [W]	2.24	1.89
Stator iron losses [W]	1.68	2.39
Rotor core iron losses [W]	0.57	0.56
Motor mass [kg]	2.16	2.82
Copper material cost [$]	3.29	4.5
Lamination material cost [$]	4.3	5.52
PM material cost [$]	0.69	1.06
Rotor shaft material cost [&]	0.08	0.1
Active material cost [$]	8.37	11.19
Total motor cost [$]	12.04	16
Stator outer diameter sDo [mm]	105	110.5
Stator inner diameter sDi [mm]	64.54	59.54
Stator yoke height shy [mm]	5	6.6

Stator yoke height shy1 [mm]	10.67	10
Stator tooth span α_{ST} [rad]	75·pi/180	80.15·pi/180
Stack length [mm]	30	34.8
PM height	4	5.1
Smaller airgap part h_{ag} [mm]	0.35	0.35
Larger airgap height h_{ag1} [mm]	0.77	0.87
Rotor yoke height	9.6	8.4
Rotor pole span coefficient α_{RT} [p.u.]	0.5	0.5
Winding wire resistance [Ω]	27.8	23.4
Winding conductor diameter [mm]	0.5	0.56

To get a better understanding of the performance improvements for the optimal design result, Fig. 3.12 shows a FEA comparison between optimization starting point versus the final result.

The cogging torque shape for the optimum solution became closer to the ideal shape (Fig. 3.12 a - maximum positive values at 0 and 45 deg and flat negative values in between). This improvement is also seen in the total output torque at rated load, which, while exhibiting ripples of approx. same amplitude, does not show a decrease to 0Nm during current zero-cross. The two stop positions: 5 deg and 49 deg show now a secure starting torque: above 0.1 Nm.

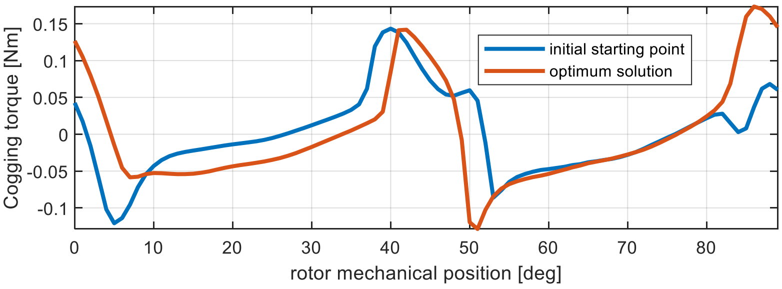

a)

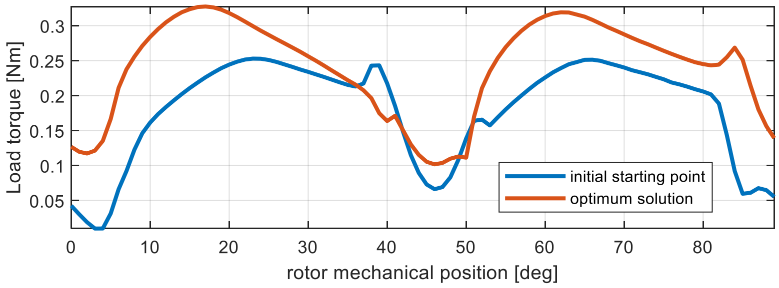

b)

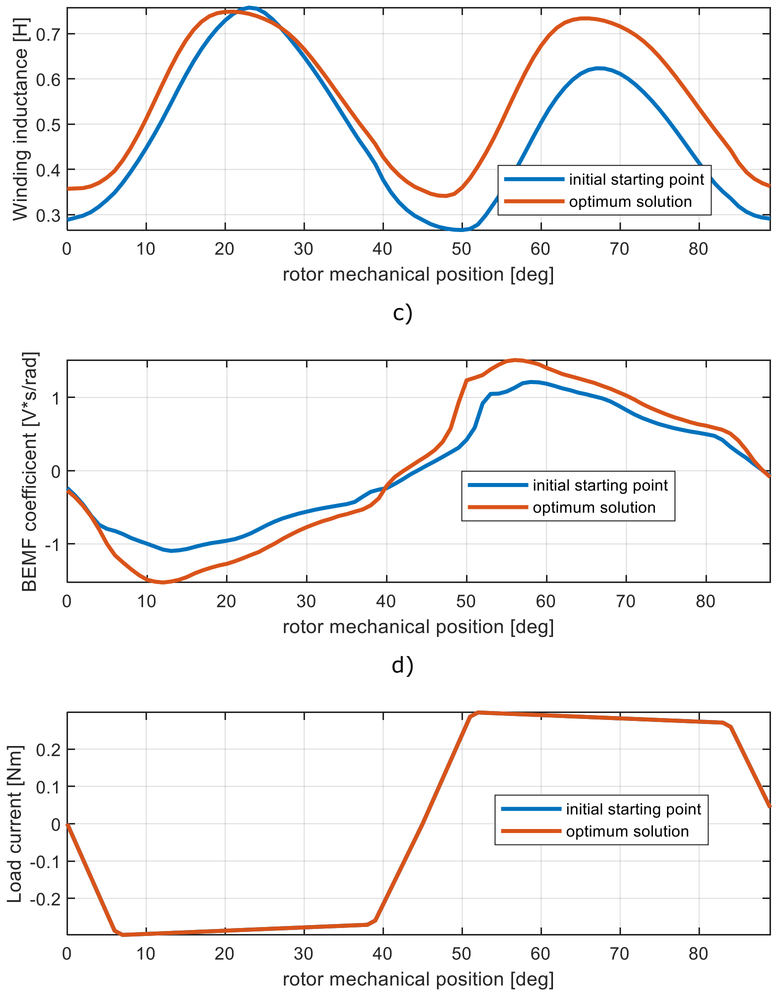

c)

d)

e)

Fig. 3.12 Comparison between starting optimization point and final optimum result: a) cogging torque; b) load torque; c) winding inductance; d) k_{BEMF} coefficient; e) load analysis current

The FEA based performance comparison is further expanded with analysis for the operation at different loads, presented in Fig. 3.13. The analysis was performed for values of current amplitude between (0.5 – 2)·I_N. The improvement in efficiency is visible mainly at higher loads.

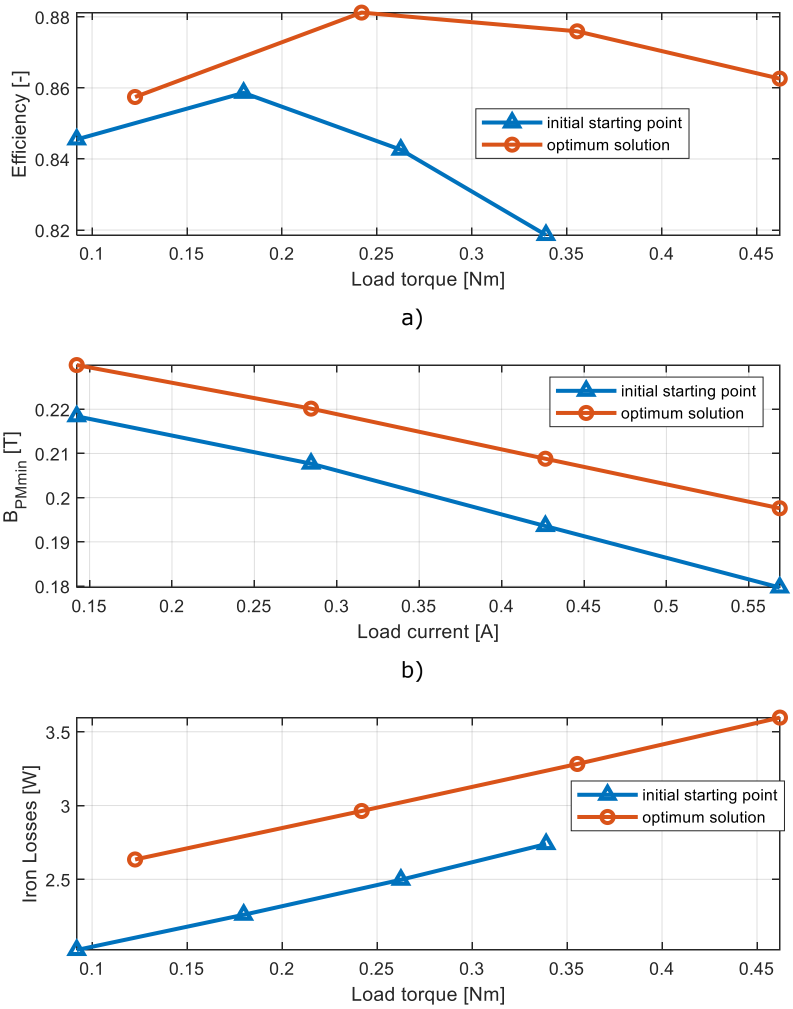

a)

b)

c)

Fig. 3.13 Initial starting point versus optimum solution: a) efficiency versus load torque, b) normal component of PM flux density versus load current, c) iron losses versus load torque

3.4 Controlled dynamics

To better asses the motor performance, the dynamic operation is checked in this section via digital simulation, using a machine dynamic model which combines analytic equations with FEA extracted parameters. The motor is tested under a speed – current cascaded control loops strategy to verify the capability to produce the rated power at rated speed.

3.4.1 Machine dynamic model

The simplified state space model of the single-phase machine is presented in (2.8). The state variables are stator current and rotor mechanical speed. The EMF constant $k_e(\theta_r)$ and stator inductance $L_a(\theta_r)$ are varying with rotor position θ_r. Additional, mechanical equation includes the speed dependent load, through fictitious load coefficient B and cogging torque, also dependent on rotor position $T_{cogg(\theta_r)}$, R_s represents the stator winding load and T_{load} represents the mechanical load torque, applied at motor shaft.

$$\begin{bmatrix} \dfrac{di_s(t)}{dt} \\ \dfrac{d\omega_r(t)}{dt} \end{bmatrix} = \begin{bmatrix} -\dfrac{R_s}{L_s(\theta_r)} & \dfrac{k_e(\theta_r)}{L_s(\theta_r)} \\ \dfrac{k_e(\theta_r)}{J} & \dfrac{B}{J} \end{bmatrix} \begin{bmatrix} i_s(t) \\ \omega_r(t) \end{bmatrix} + \begin{bmatrix} \dfrac{1}{L_s(\theta_r)} & 0 \\ 0 & \dfrac{1}{J} \end{bmatrix} \begin{bmatrix} V_s(t) \\ T_{cogg}(\theta_r) - T_{load} \end{bmatrix} \quad (3.13)$$

The rotor position is defined as integral of the rotor speed, also considering the initial position (start position).

$$\theta_r(t) = \int \omega_r(t) \cdot dt + \theta_{r\,ini} \quad (3.14)$$

Same as for the DC motor, the EMF constant represents the proportionality factor between both stator current/electromagnetic torque and rotor speed/electromotive force (emf)

$$T_e(t) = k_e(t) \cdot i_s(t) \quad (3.15)$$

$$emf(t) = k_e(\theta_r) \cdot \omega_r(t) \quad (3.16)$$

A diagram of the motor model is shown in Fig. 3.14, while Table 3.5 presents the model parameters values. To enable accurate representation of the motor parameters, the inductance, the emf constant and the cogging torque variation with position information are extracted from FEM.

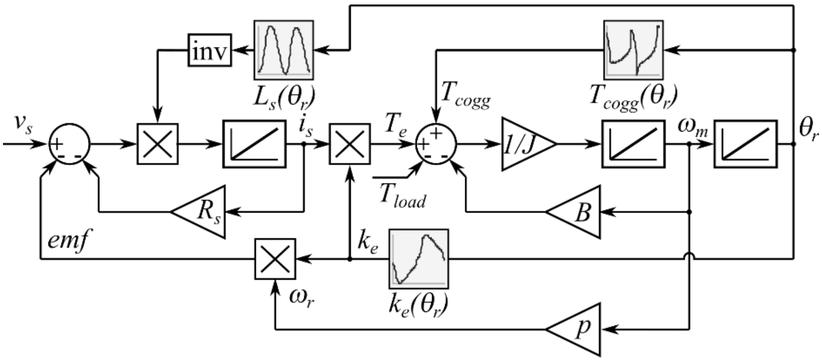

Fig. 3.14 Motor model diagram

Table 3.5 Single phase motor model parameters

Parameter	Value
V_{DC} (rated DC voltage [V]):	280
P_N (rated power [W]):	40.3
n_N (rated speed [rpm]):	1600
R_s (phase resistance [Ω]):	40.57
J (inertia constant [kg·m^2]):	4.78x10^{-4}
p (number of pole pairs):	4
B (friction coefficient)	2 x10^{-4}

3.4.2 Simulation model and results

The generic control system is shown in Fig. 3.15. It consists of a speed PI controller followed by a hysteresis current controller. The speed controller outputs the current reference amplitude, while the current shape is imposed through a rotor position dependent lookup table. The output of the hysteresis controller is the duty cycle of the PWM command for the single-phase inverter (full h-bridge inverter). The reference speed and position are acquired with an encoder/resolver.

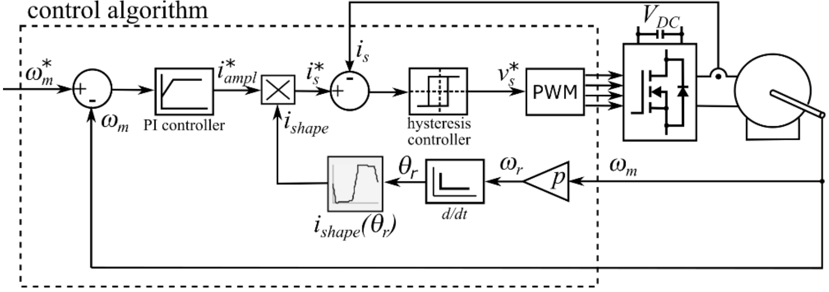

Fig. 3.15 The control system

The coefficients used for the PI speed controller were set to: k_p=1.1, k_i=0.4, while the hysteresis band for the current hysteresis controller was set to 0.05. Additionally, the reference current amplitude prescribed by the speed regulator, was limited to a maximum value of 4 times the rated current rms value.

Fig. 3.16 shows the Simulink model of the single-phase motor control system. The control calculations are executed at 10kHz frequency, while the plant model calculations (inverter, motor, and reciprocating compressor models) are executed at 100kHz frequency.

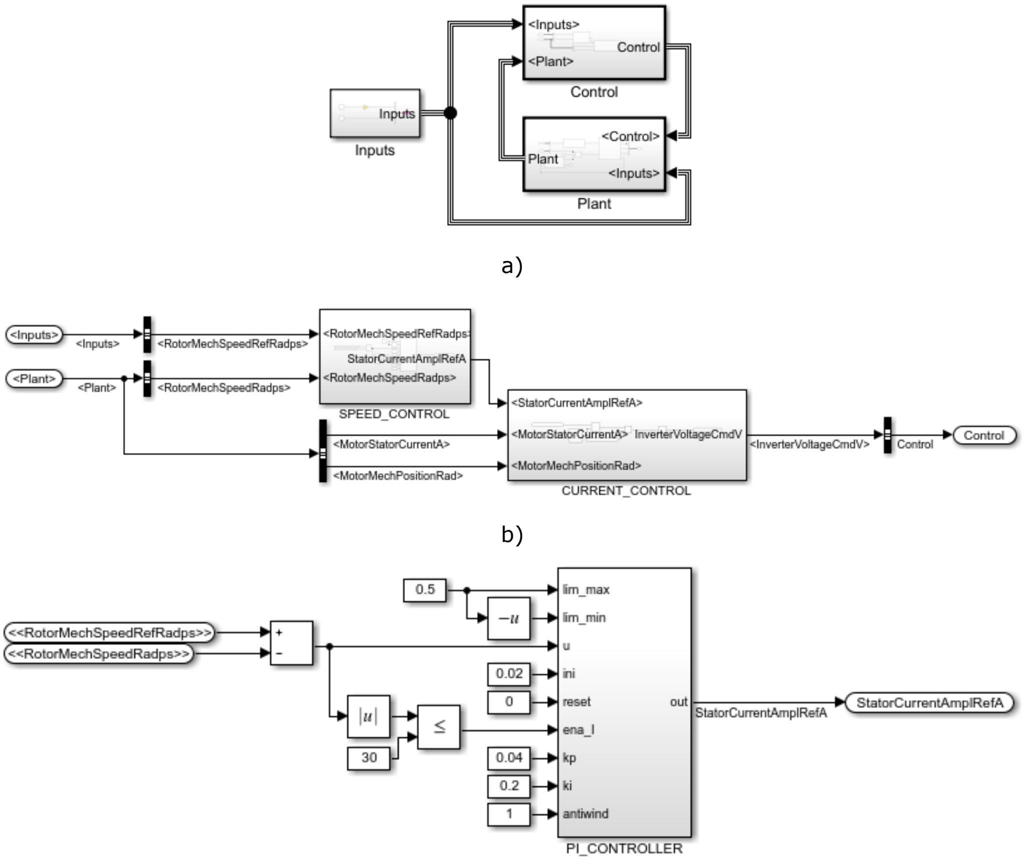

a)

b)

c)

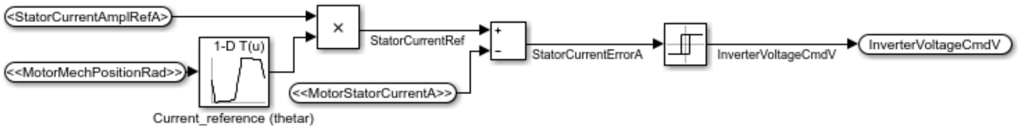

d)

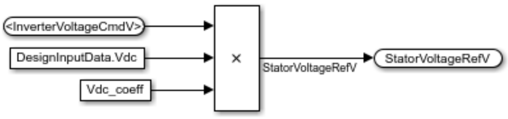

e)

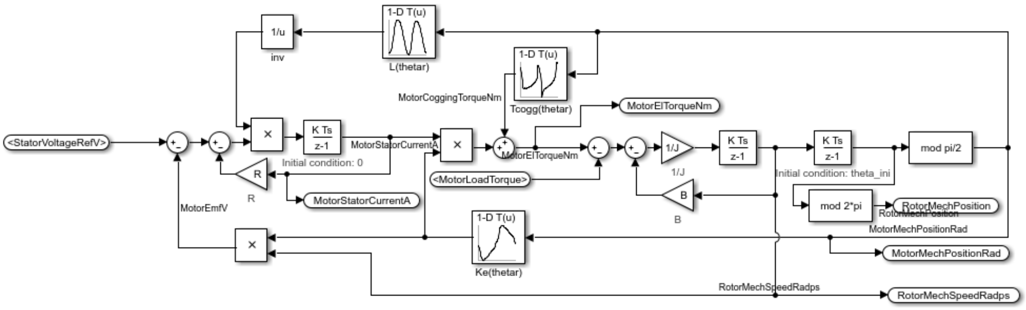

f)

Fig. 3.16 Simulink close loop control simulation model: a) simulation model; b) the control part of the simulation model; c) the speed controller; d) the current controller; e) the voltage source inverter; f) the single-phase motor dynamic model

3.4.2.1 2.4.3.1 Simulation with compressor load

The first simulation set verifies the startup and acceleration to rated speed under compressor load. A step reference speed to rated 1600 rpm value was prescribed. The simulation results show that the motor is capable to drive a reciprocating compressor to rated speed, although with relative high speed pulsation amplitudes of approx. 250 rpm.

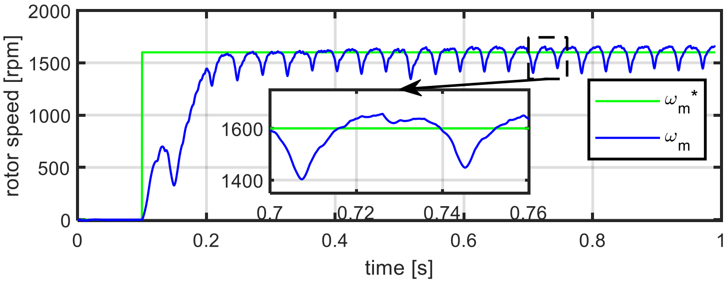

a)

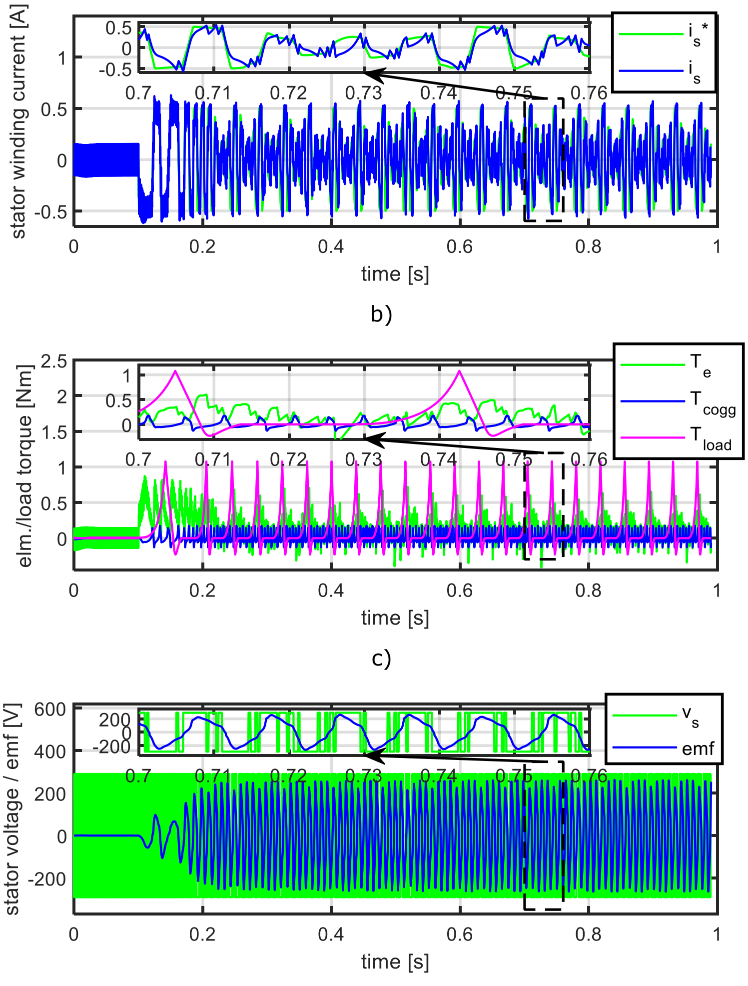

b)

c)

d)

Fig. 3.17 Simulation results for acceleration to rated speed under reciprocating compressor load: a) reference rotor speed vs measured value, b) reference stator current reference vs. measured value, c) electromagnetic torque, compressor load torque and cogging torque, d) stator voltage vs. motor emf

3.4.2.2 2.4.3.2 Simulation with step load

The second simulation set verifies the startup and acceleration to rated speed. A step reference speed to rated 1600 rpm value was prescribed at 0.1s, followed by a reverse to -1600 rpm command at t=1s. A step load of 0.2Nm, was applied within t = 0.4-0.8 s and t = 1.5 – 1.9 s time intervals. The simulations results prove the motor capable to operate close to the rated speed at rated load.

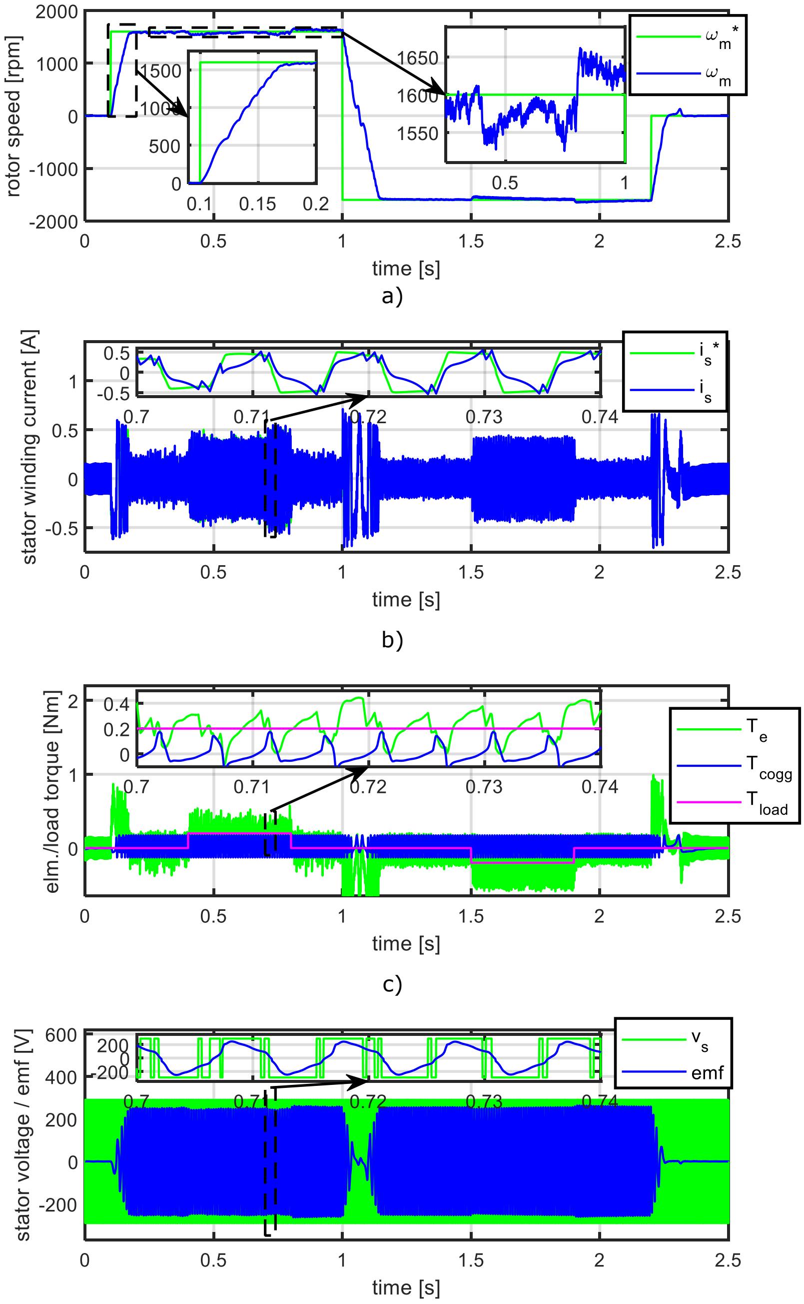

Fig. 3.18 Simulation results for acceleration to rated speed followed by step load: a) rotor speed reference and controlled value, b) stator current reference and controlled value, c) electromagnetic torque, compressor load torque and cogging torque, d) stator voltage and motor EMF

3.5 Experimental results

Because no experimental results are available for the above designed motor, a set of experimental data for a prototype built on an optimally previous design attempt is presented in what follows. The results are extracted from [46].

No load voltage (Back-EMF) measurements

The single-phase motor was mechanically coupled to a primary motor and run as open loop generator. Using an oscilloscope, the EMF waveform was measured. Fig. 2.26 a) illustrates the test bench setup, while measurement results for 1000 rpm operation are shown in Fig. 2.26 b).

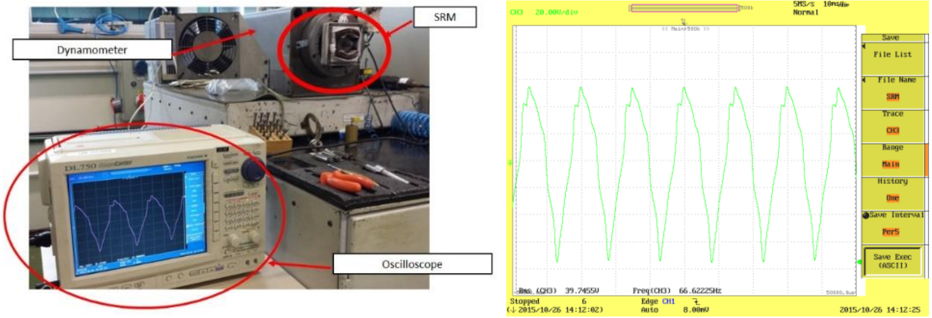

a) b)

Fig. 3.19 a) Test bench used for measuring the motor EMF, b) back-EMF at 1000 rpm

Efficiency determination

The test rig used for efficiency tests is presented in Fig. 3.20. The single-phase motor is mechanically connected to an electromagnetic brake through a torque transducer and flexible couplings. The input power is determined from the motor feed voltage, current ratings, while the output power is calculated using speed and torque measured by the torque transducer.

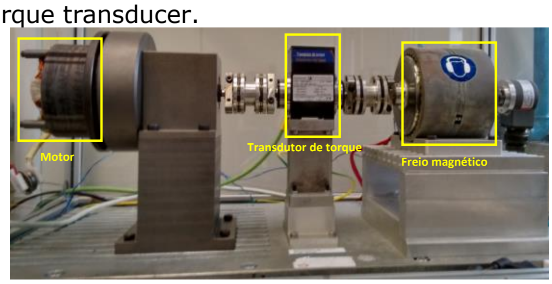

Fig. 3.20 The motor coupling to the torque transducer and magnetic brake for efficiency determination

Fig. 3.21 shows a comparison between measured efficiency and FEA based calculation, expressed in per-unit (values normalized to the maximum calculated value) for operation under few load points at constant speed of 2000 rpm.

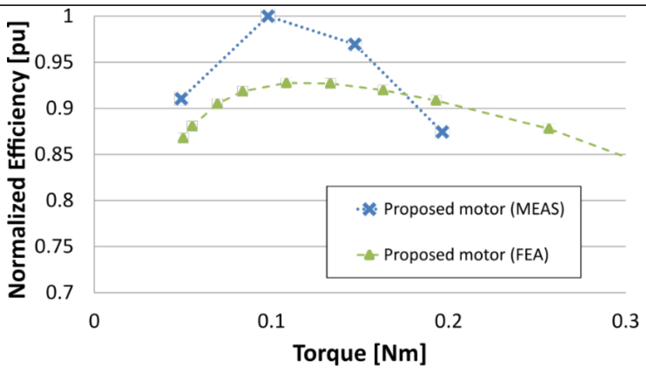

Fig. 3.21 Comparison between experimental data and simulation for calculating the efficiency of 2000 rpm

The difference between calculated and simulated values are attributed to iron loss calculation limitations in FEA analysis, uncertainties regarding actual material parameters and temperature influence.

3.6 Conclusions

This chapter studied a small power one phase 2-pole ferrite-PM-stator double saliency (flux reversal). A set of case study requirements of 35W and 1600 rpm were selected for design. A new optimal design methodology was introduced, aimed to fix the self-starting issue, caused by the total negative torque value [47] [46], maximize efficiency (above 88%) and minimize the material cost, all targets being achieved.

A close loop control strategy was also investigated via digital simulation, using a FEA-analytic combined dynamic motor model. The motor proved capable of developing the rated torque at rated speed.

CHAPTER 4. DESIGN AND ANALYSIS OF SINGLE PHASE 4 STATOR POLES FERRITE PM DOUBLE SALIENCY SM

Abstract

Continuing the study in Chapter 3, this chapter analyses a new single-phase motor topology, which uses 4 stator poles (4 stator teeth). The two additional poles are expected to increase the torque density, as they will render all the rotor poles active at any time. The operating principle is presented, followed by setting up the design methodology. A case study is selected for design and the optimization results are presented. The results are verified via FEA and close loop control digital simulation.

4.1 Introduction

A cross-section of the proposed motor is shown in the Fig. 4.1. The four coils are connected in series. The used PM quantity is doubled in this configuration, the four vertically placed additional PMs being oriented to exhibit same inward/outward magnetization direction as the neighbor upper/lower side PMs.

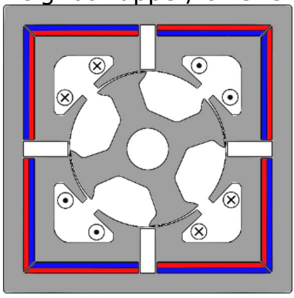

Fig. 4.1 Proposed motor topology

By neglecting the leakage flux, a simplified PM flux path through the iron core for 4 rotor positions within an electric period in shown in Fig. 4.2.

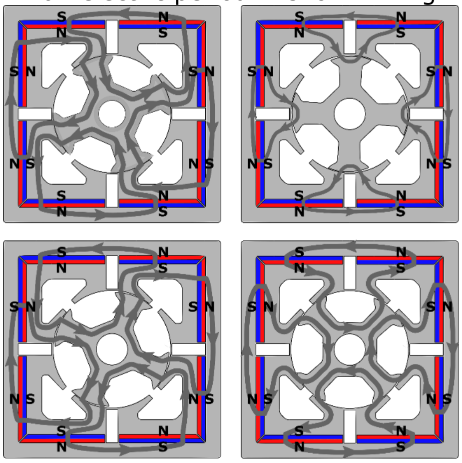

Fig. 4.2 PM flux density path for four rotor positions (anticlockwise rotor movement: 0deg, 22.5deg, 45deg, 67.5 deg)

Same as for the two-stator pole machine presented in the previous chapter, there are two rotor positions where the rotor is likely to stop: the positions where the magnetic flux of the two magnets belonging to the same stator tooth is short-circuited through the rotor pole(s). Although all four PMs are active at each moment, only one side of the stator pole actively participates in torque production at any time.

For a better understanding of this new topology's specific characteristics, brief finite element analysis results are presented below. The full 2D FEA model is shown in Fig. 4.3.

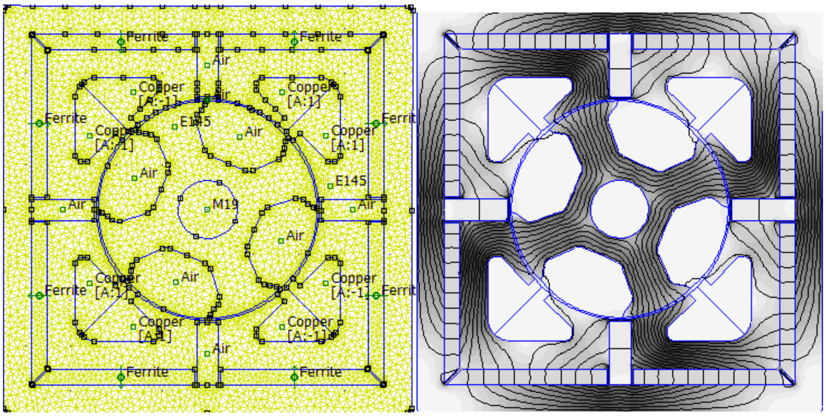

a) b)

Fig. 4.3 FEA model: a) preprocess phase, b) post process phase for no load analysis

Because the geometry and electromagnetic phenomena are symmetric, only a half of the stator and the rotor is modeled, using periodic boundary conditions. This reduces the simulation effort to half, providing sufficient accuracy for the results.

To get the correct results, the model reduction is accounted by multiplying the FEA extracted quantities such as: phase flux linkage value and torque via Maxwell stress tensor value with the factor of 2.

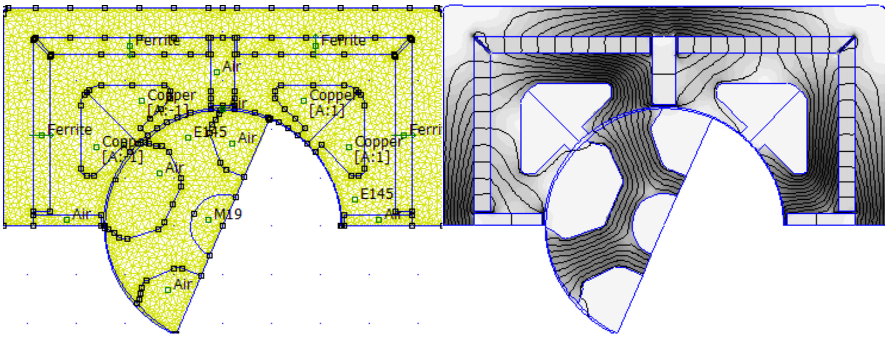

Fig. 4.4 FEA model of half of the machine: a) preprocess phase, b) post-process phase

The periodic boundary conditions are shown in Fig. 4.5. Only the boundary conditions on the right side of the model are listed in the Fig. 4.5, but they were symmetrically applied also on the left side of the model. The periodic conditions are: three stator periodic boundary conditions (denoted by "st"), two airgap boundary conditions ("ag") and 3 rotor periodic boundary conditions ("rt"). The alternating red/blue colors are used only for distinguishing the adjacent boundaries.

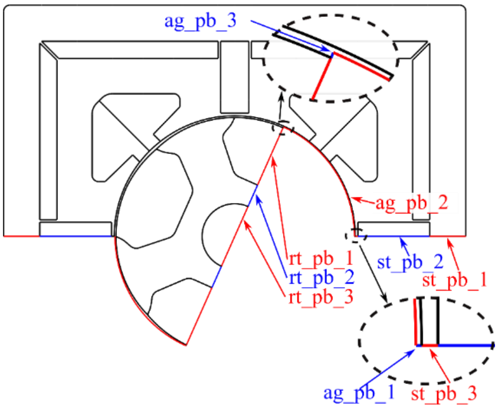

Fig. 4.5 Periodic boundary conditions (for the model right half side)

First, the normal component of the airgap flux density, for half of the airgap length, below upper and left stator teeth (anti-clockwise direction) is shown in Fig. 3.6. The maximum amplitude reaches 0.7 T, the shape being influenced by the tapered airgap. The tapered airgap [48] [49] [50] also affects the EMF shape, which is not trapezoidal, as expected for this topology of single-phase BLDC.

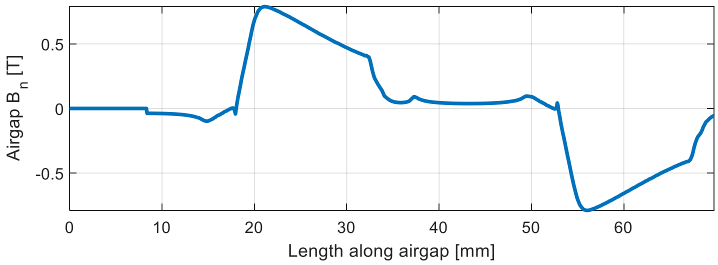

a)

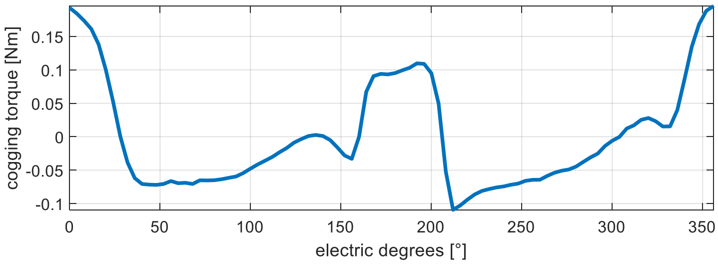

b)

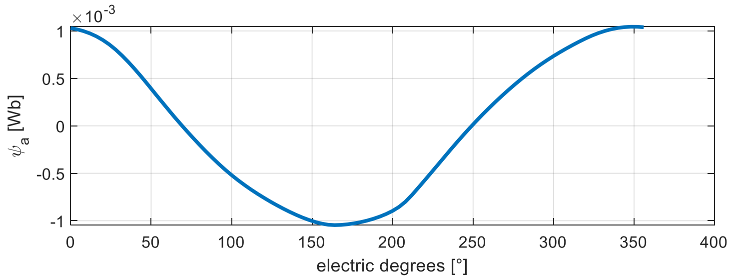

c)

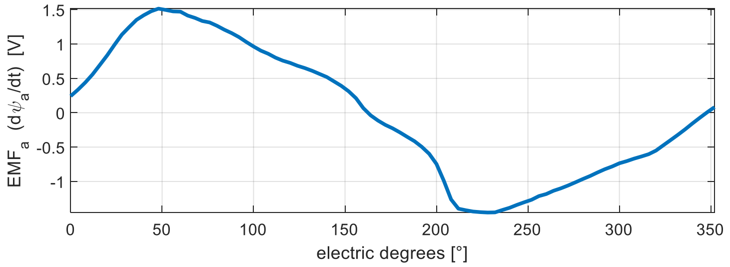

d)

Fig. 4.6 No load FEA results

The EMF for open load generator operation at rated speed (Fig. 4.6 d) changes polarity at 160°/340° electric rotor positions. To obtain an all-positive electromagnetic torque and power, the motor fed alternating stator current, must be in phase with the EMF. As discussed in Chapter 3, to reduce the total torque pulsations amplitude and their minimum value, the cogging torque should be shaped to exhibit positive values in these regions, compensating for the null electromagnetic torque. Fig. 4.6 b, shows that this is not the case here, also visible in Fig. 4.7 b.

Because the PM flux linkage changes polarity, feeding the motor with a bipolar current is suitable for operation. The current waveform (Fig. 4.7 a) can be shaped in such way to compensate the EMF departure from a trapezoidal shape, to obtain a smoother and rather constant electromagnetic power and torque (Fig. 4.7 b). Shaping the cogging torque and reducing the total torque pulsations will be a topic for the optimization process.

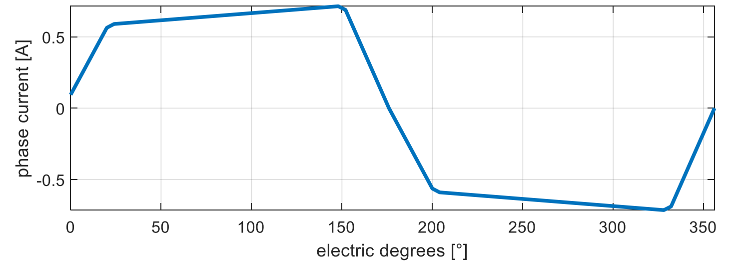

a)

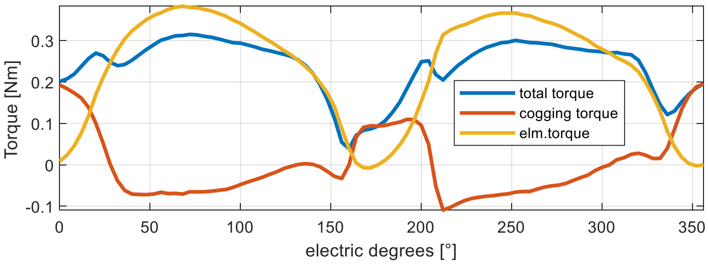

b)

Fig. 4.7 Load analysis

The next sections will focus on design requirements definition and optimal design results.

4.2 Optimization algorithm

A FEA based similar routine to the one developed in Chapter 3 (Fig. 3.9) was applied for motor design and it is briefly presented here. Starting from the design input data (design requirements, given values for the optimal design variables and material properties), the FEA model is built. The first analysis routine is the finite element no load analysis, performed for successive rotor positions over an electric period (with 0 current density in the stator winding and one turn per coil stator winding). The FEA extracted winding flux density is used for calculation of the number of turns per coil and, the magnetomotive force and the rated current amplitude. The FEA model is updated with this information and the load finite element analysis is deployed, again for successive rotor positions. Finally, using the torque, flux density, flux linkage and several additional values extracted during analysis, the machine performance, cost, and weight are calculated.

As opposed to the implementation in Chapter 3 (and [51]), the no load analysis is performed for each objective function evaluation (and not only for the objective function evaluation of the initial starting point). Although the computation effort and analysis time increase notably, it ensures better accuracy for the final optimization result and avoids the risk of insufficient voltage reserve for running at rated speed and load [51].

Fig. 4.8 presents the design optimization variables, all being geometry dimensions (Table 4.1), selected based on the following criteria:

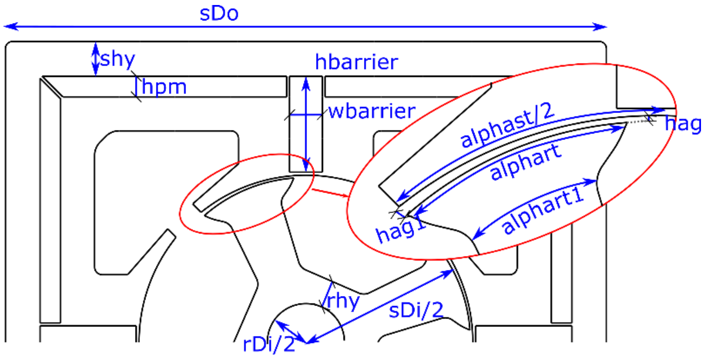

Fig. 4.8 Optimal design variables

- The design variable should have a direct impact in the objective function value
- The optimal design variables should not be interdependent (the values set on one design variable should not directly influence the other design variables)

An important phase in optimal design preparation is the setting of the exploration phase limits. The limits can be imposed by the application constraints (e.g., a limit of the outer stator diameter or the stack length is imposed by the volume the motor should fit in). Other limits, such as the minimum airgap height or minimum PM height are set by the technological manufacturing limitation. Other search intervals limitations are set based on designer experience, which represents a preoptimization process itself. Choosing a large interval could make the search exhaustive, while choosing a minimum interval could limit the chance of finding the global optimum.

Following the above considerations and given the rated mechanical power of the motor, the search space limits chosen for the optimization process are presented in Table 4.1.

Table 4.1 Four stator poles single phase motor: optimal design variables

Parameter	Optimization start point	Min values	Max values	Minimum step
sDo	107	90	110	1
sDi	57	30	65	1
shy	7.8	5	8	0.2
shy1	5.6	3	7	0.2
αst	1.0996	0.7 π/2	0.95 π/2	0.02 π/2
lstack	35.5	30	37	0.5
hpm	6.6	3	7	0.2
wbarrier	6	4	7	0.2
hag	0.45	0.35	0.5	0.02
swp	22.2	20	23	0.2
hag1	0.7	0.6	0.9	0.02
αrt	0.53	0.4	0.6	0.01

Same objective function as in Chapter 3 is used. The objective function comprises the total cost of the machine materials. Additional penalty costs are minimum and average torque, efficiency, and PM demagnetization avoidance.

4.3 Optimal design - case study

A case study for a slightly larger power compressor pump application is selected. The main design requirements are:

- Rated power: P_N=85W
- Rated DC voltage supply for the single-phase inverter feeding the single-phase motor V_{DC}=290V
- Rated mechanical speed n_N=3000 rpm
- Reduced material quantity
- Minimum efficiency at rated speed and torque: 88%
- 0.1Nm minimum torque values during operation under rated load
- no risk of PM demagnetization at 1.5 times rated current overload

4.3.1 Optimization results

The optimization process was started from an initial random point (listed in Table 4.1 as *Optimization start point*) and reached the optimum solution after 54 steps (consisting of 12 local exploration phases and several gradient-descend steps), over the course of 13 hours and 16 minutes. Table 4.2 compares the optimization start point versus the optimum point in terms of performance indexes, geometry values and geometry dimensions.

The optimum solution's output power calculated as the rated speed multiplied by the rated torque represents 84.7% of the output power design requirement (0.27 Nm for 85W and 3000rpm). As the average torque penalty function should have ensured that the FEA average torque value for rated load T_{FEM} meets the rated torque value T_N, this smaller output power value is attributed to the conflict between the objective function's components objectives. As result, the final penalty cost value for average torque is 1.8$.

Table 4.2 Four stator poles single phase motor: initial point versus optimum point versus optimum point

Parameter	Initial result	Optimum results
Mechanical output power [W]	72.44	72.01
Number of turns per coil [-]	87	142
Rated phase current [A]	0.9	0.67
Average torque value for rated load [Nm]	0.23	0.23
Minimum torque value for rated load [Nm]	-0.42	0.1
Efficiency [-]	0.85	0.878
Copper losses [W]	2.1	2.7
Stator iron losses [W]	7	4.27
Rotor core iron losses [W]	1.36	0.79
Motor mass [kg]	2.6	2.04
Copper material cost [$]	3.86	3.43
Lamination material cost [$]	5.29	3.93
PM material cost [$]	2.12	0.78
Rotor shaft material cost [&]	0.13	0.11
Active material cost [$]	11.4	8.25
Total motor cost [$]	15.82	11.73
Average torque penalty cost [$]	2.75	1.8
Minimum torque penalty cost	447.17	0
Energy penalty cost	67	4
Demagnetization penalty cost	0	0
Stator outer diameter sDo [mm]	107	98
Stator inner diameter sDi [mm]	57	48
Stator yoke height shy [mm]	7.8	8
Stator yoke height shy1 [mm]	5.6	6.6
Stator tooth span α_{ST} [rad]	1.09	1.25
Stack length [mm]	35.5	31.5
PM height	6.6	3
Smaller airgap part hag [mm]	0.45	0.45
Larger airgap height hag1 [mm]	0.7	0.9
Rotor pole span coefficient α_{RT} [p.u.]	0.53	0.57
Stator pole width [mm]	22.2	22.6

Although the rated stator current amplitude decreased during the optimization process, the copper losses increased in the final solution because of the increase in winding resistance (increase in the number of turns per coil concomitantly with the reduction of the wire gauge, to be able to accommodate the coil in the stator slot available room. However, the iron losses decrease due to smaller magnetic loading improved the efficiency to 2.8%, raising it close to the 88% requirement value.

A major improvement is the minimum torque value, increased to 0.1 Nm and the motor material cost of 11.73$ (74.1% of the initial cost). These improvements were achieved by reducing the stack length, stator and rotor diameter and PM height, while increasing the airgap height, the stator and rotor pole spans (Fig. 4.9) and the number of turns per coil.

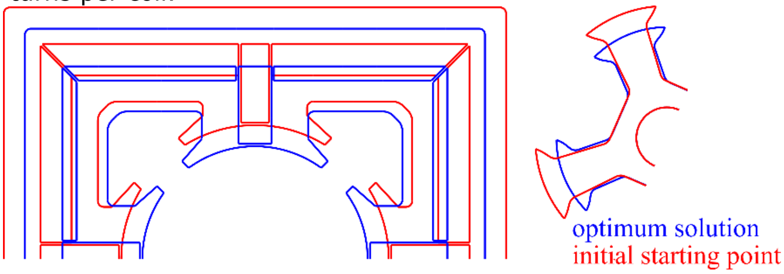

Fig. 4.9 Motor geometry cross-section comparison: initial starting point versus the optimum solution

Fig. 4.10 a shows the evolution of the main motor performance indexes, electric parameter and design variables throughout the optimization process. The objective function cost value (Fig. 4.10 a) was reduced from 532 $ to 17.49 $. Since the motor total materials cost of the final solution is 11.7 $, the 5.79 $ difference constitutes the penalty costs for non-achievement of the penalty conditions, which breaks down to (Fig. 4.10 b): 3.99 $ for efficiency value lower than 88% and 1.8 $ for average torque value below 2.7Nm. The demagnetization and minimum torque penalty costs are 0. The evolution of the penalty costs also shows that the optimization effort was mostly oriented towards increasing the minimum torque value to 0.1Nm (also visible in Fig. 4.10 d).

The copper and core lamination costs are similar, while the PM cost is significantly smaller (Fig. 4.10 c).

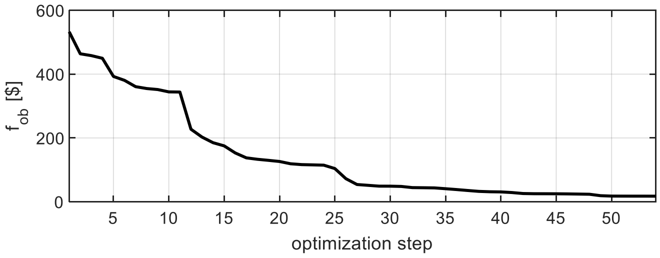

a)

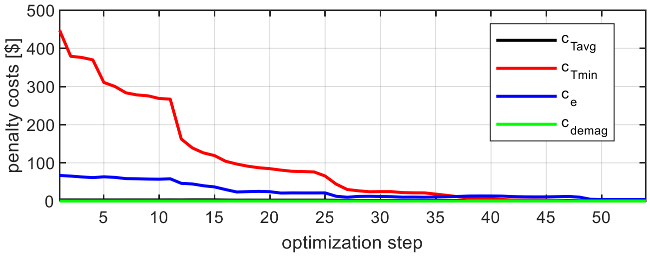

b)

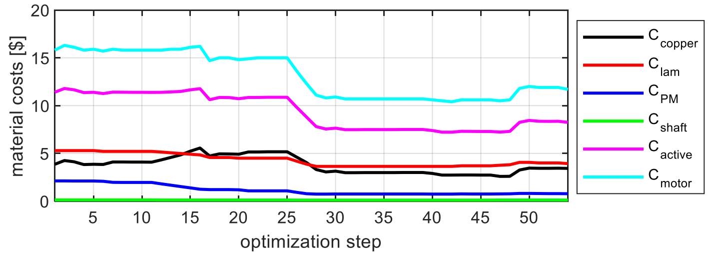
material costs [$]
20
15
10
5
0
5
10
15
20
25
30
35
40
45
50
optimization step
C_{copper}
C_{lam}
C_{PM}
C_{shaft}
C_{active}
C_{motor}

c)

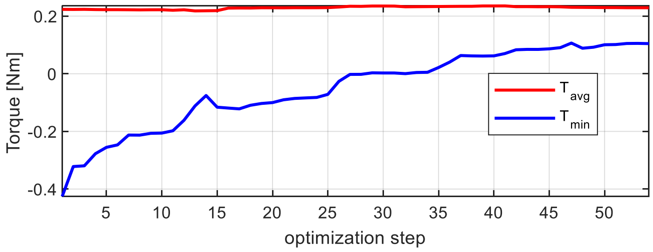
Torque [Nm]
0.2
0
-0.2
-0.4
5
10
15
20
25
30
35
40
45
50
optimization step
T_{avg}
T_{min}

d)

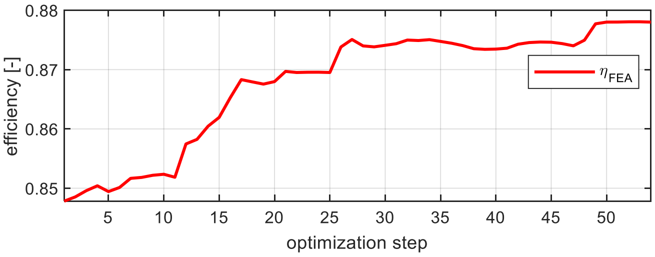
efficiency [-]
0.88
0.87
0.86
0.85
5
10
15
20
25
30
35
40
45
50
optimization step
η_{FEA}

e)

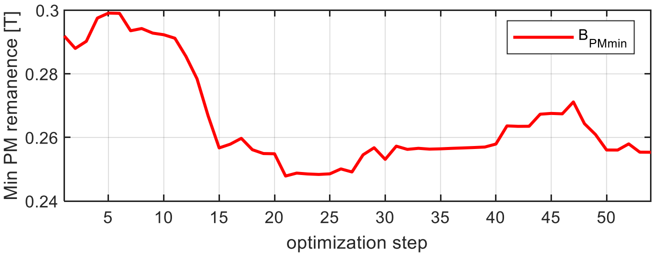
Min PM remanence [T]
0.3
0.28
0.26
0.24
5
10
15
20
25
30
35
40
45
50
optimization step
B_{PMmin}

f)

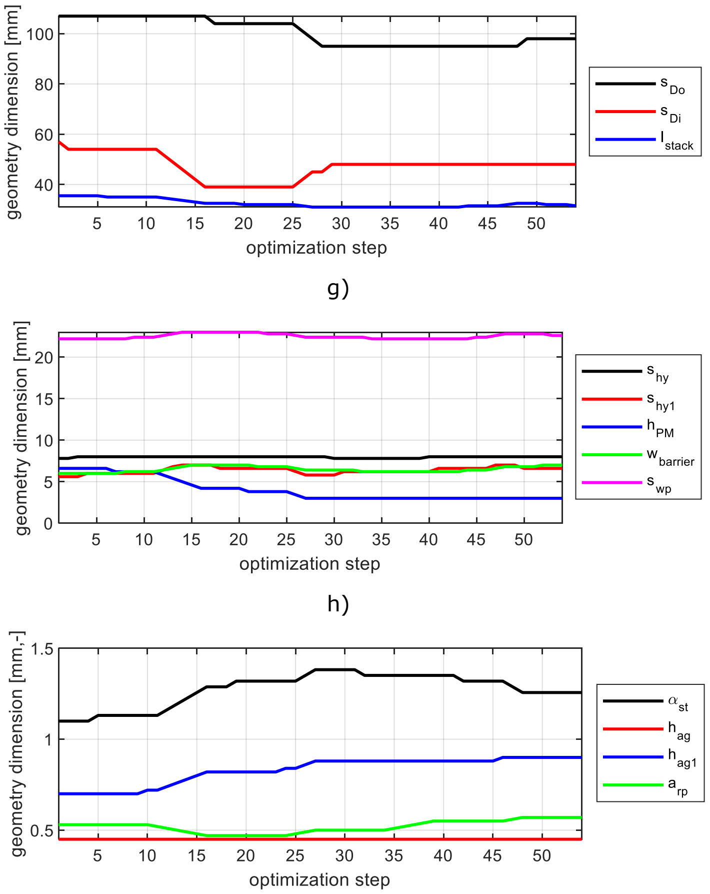

g)

h)

i)

Fig. 4.10 Evolution during the optimization process of: a) objective function, b) penalty costs, c) material costs, d) minimum torque value over an electric period and the average torque value, e) efficiency, f) minimum PM normal flux density component at 1.5 times rated current overload, g, h, i) optimal design variables.

The next set of optimization results in Fig. 4.11 show a comparison between the initial point (start of the optimization process) versus the optimization final solution for a set of FEA extracted values for successive rotor positions over an electric period. Cogging torque shape comparison shows a large reduction in the pulsation’s amplitude. The flux linkage per 1 turn/coil is slightly smaller, caused by the reduction of PM surface (due to reduction of outer diameter and stack length). Additionally, as a measure to reduce to total torque pulsation (for flat trapezoidal current reference) the bemf coefficient became symmetric in the optimization results.

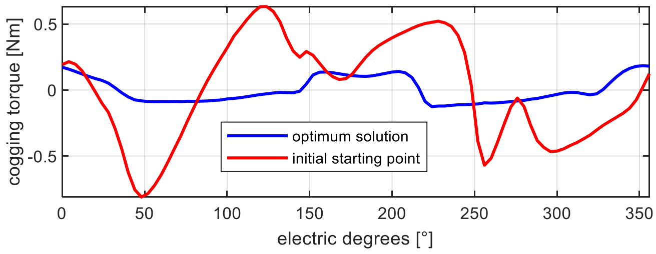
cogging torque [Nm]
0.5
0
-0.5
0
50
100
150
200
250
300
350
electric degrees [°]
optimum solution
initial starting point

a)

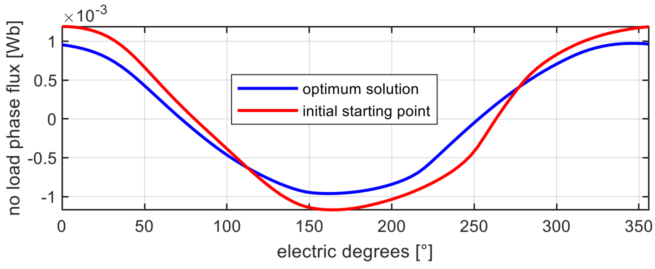
×10^-3
no load phase flux [Wb]
1
0.5
0
-0.5
-1
0
50
100
150
200
250
300
350
electric degrees [°]
optimum solution
initial starting point

b)

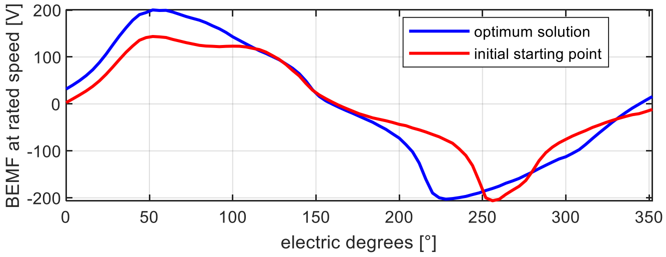
BEMF at rated speed [V]
200
100
0
-100
-200
0
50
100
150
200
250
300
350
electric degrees [°]
optimum solution
initial starting point

c)

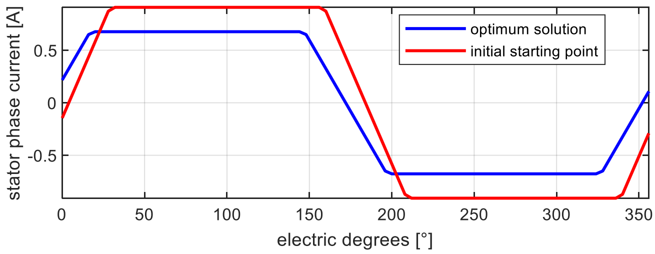
stator phase current [A]
0.5
0
-0.5
0
50
100
150
200
250
300
350
electric degrees [°]
optimum solution
initial starting point

d)

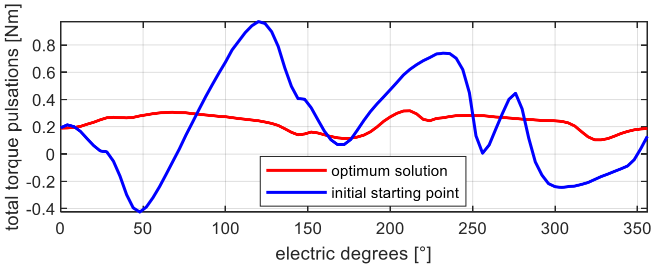

e)

Fig. 4.11 Initial optimization point versus optimal design solution comparison for: a) cogging torque, b) 1 magnetic flux for 1 turn per coil winding, c) BEMF coefficient, d) current waveform e) total torque waveform

As for the load torque pulsations, the pulsation amplitudes are also greatly reduced, for the same average value of 0.22 Nm (Fig. 4.11 e).

A final set of comparative results for a few performance parameters versus the load torque (for $0.5-2\cdot I_N$ load current) is presented in Fig. 4.12. The performance of the optimization result is generally better, for efficiency, minimum normal flux density value along the PM width and core losses.

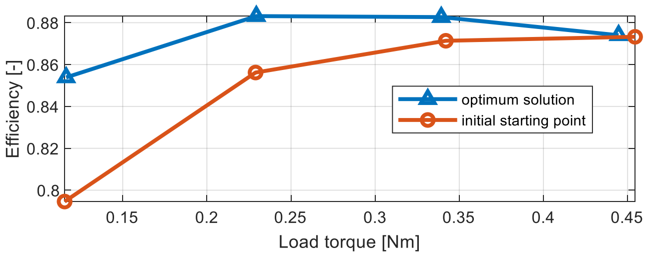

a)

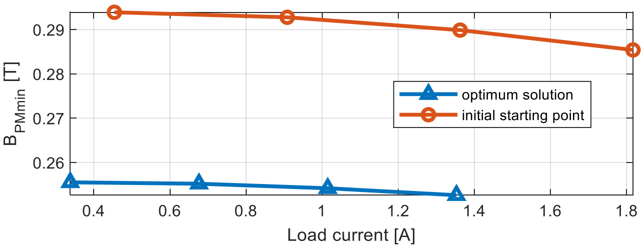

b)

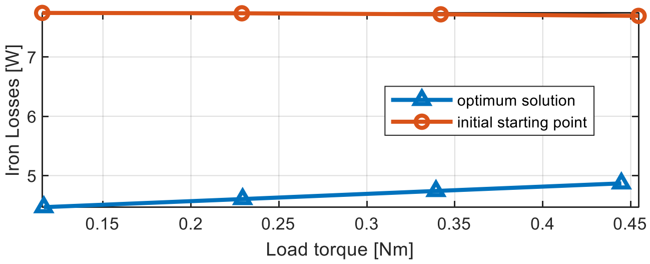

c)

Fig. 4.12 Initial vs. optimum motor comparison for different load values: a) efficiency, b) minimum normal flux density in PMs, c) iron losses

4.4 Dynamic operation simulation of the optimization result

Like the analysis in Chapter 3, the dynamic performance is checked via Simulink digital simulation for the same closed loop control strategy: a PI controller-based closed loop speed control and a hysteresis controller-based current control. The reference current for the inner current control loop is calculated based on the speed controller output, which is modulated by a trapezoidal shape signal, based on the rotor position (Fig. 4.13).

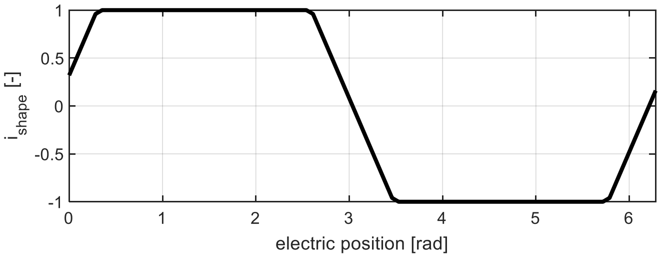

Fig. 4.13 Current imposed shape

The motor parameters are listed in Table 4.3.

Table 4.3 Four stator poles single phase motors: motor parameters

Parameter	Value
V_{DC} (DC rated voltage [V]):	280
n_N (rated speed [RPM]):	3000
R_s (phase resistance [Ω]):	7.98
J (inertia constant [kg·m2]):	5.2 x10^{-5}
Number of poles:	4

The motor model uses FEA extracted values to model the rotor dependency of cogging torque, bemf constant and stator inductance (Fig. 4.14).

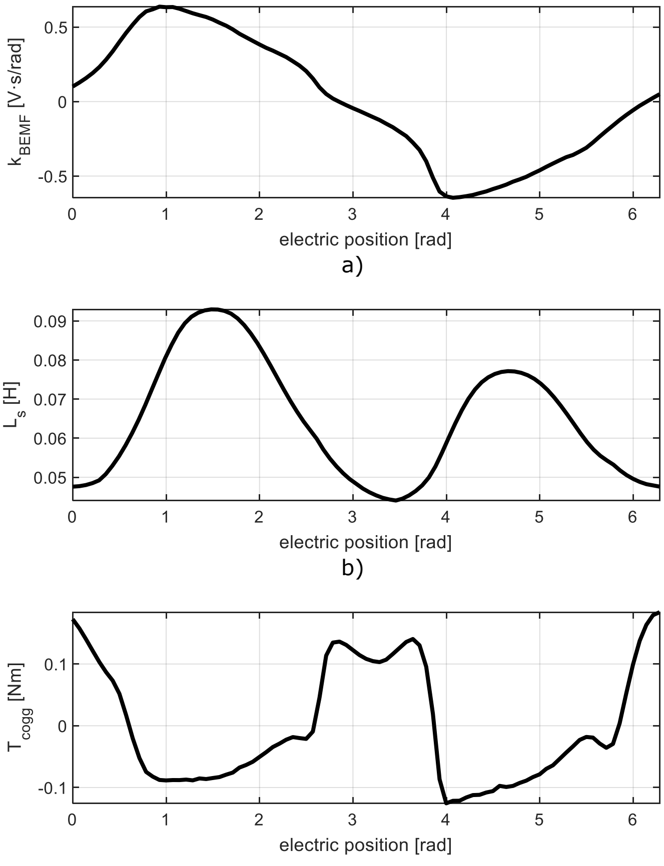

c)

Fig. 4.14 FEA extracted parameters, used for machine model, versus the rotor position: a) BEMF coefficient, b) stator winding inductance, c) cogging torque

The controller's speed PI proportional gain value is set to 0.1, the speed integrator gain value is set to 1, the reference current maximum value is limited to 1.5 A and current controller hysteresis band is set to 0.02 A.

To test the control strategy effectiveness, a reference step speed of 0 to 1500rpm (50% of the rated speed) is prescribed, followed by a step change to 3000rpm. Two operation modes are considered: operation under constant load torque and operation under a reciprocating compressor characteristic load torque.

4.4.1 Constant ideal step load torque

A constant load T_L=0.27 T (rated torque) is applied within 0.5-1.5s time frame. (Fig. 4.15). The motor can reach the rated speed at rated torque load (Fig. 4.15 a). The speed change rate is imposed by controller output limitation, set to 1.5A (approx. 2 times the rated current). Operating at rated speed and torque pushes the operation towards this current limitation (Fig. 4.15 b).

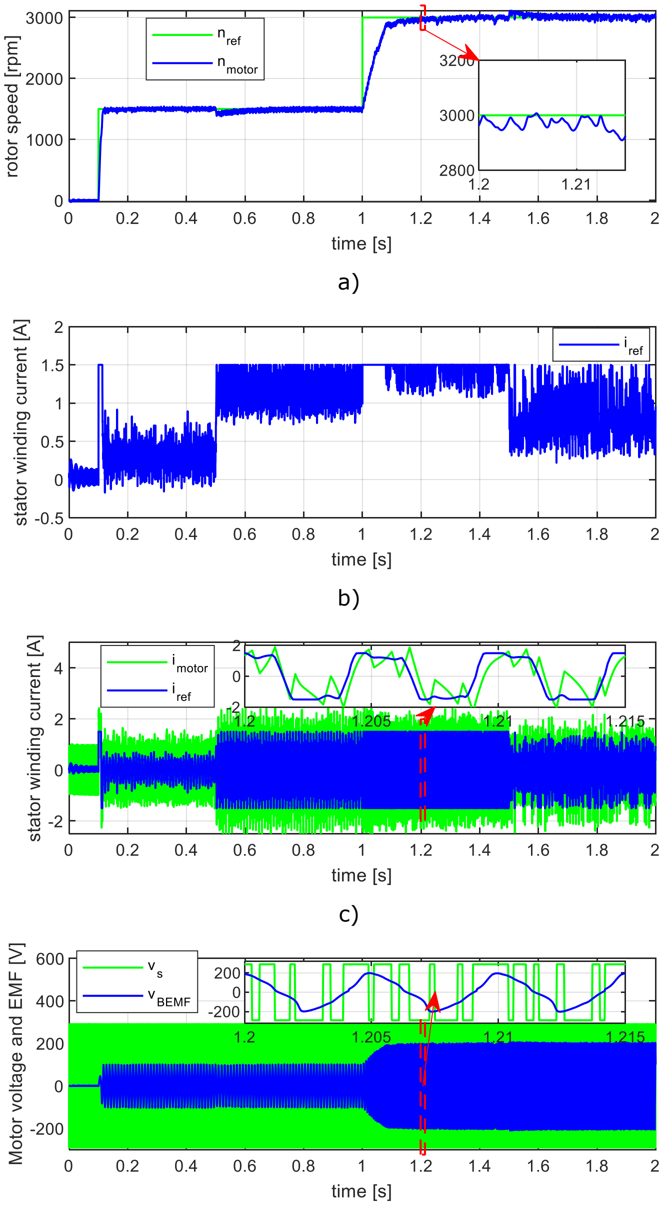
rotor speed [rpm]
3000
2000
1000
0
n_{ref}
n_{motor}
3200
3000
2800
1.2
1.21
0
0.2
0.4
0.6
0.8
1
1.2
1.4
1.6
1.8
2
time [s]
stator winding current [A]
2
1.5
1
0.5
0
-0.5
i_{ref}
time [s]
stator winding current [A]
4
2
0
-2
i_{motor}
i_{ref}
1.2
1.205
1.21
1.215
time [s]
Motor voltage and EMF [V]
600
400
200
0
-200
v_s
v_{BEMF}
200
0
-200
1.2
1.205
1.21
1.215
time [s]

a)

b)

c)

d)

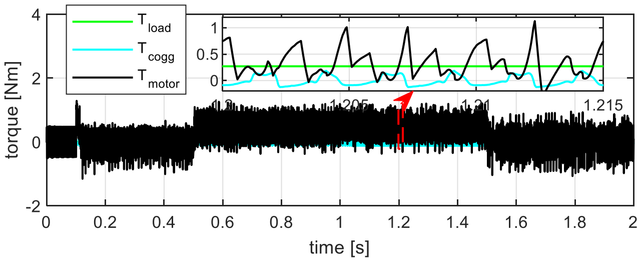

e)

Fig. 4.15 Simulation results for step acceleration setpoint and step load

As enforced through optimization process, the load torque has only positive values (Fig. 4.15 e). Its high pulsation amplitude is caused by the current ripples, inherent for a hysteresis controller.

4.4.2 Operation under reciprocating compressor torque load

The second simulation set uses the same speed reference, but the load torque profile of the compressor model presented in Chapter 2. Due to compressor load torque characteristics, the speed pulsations are large, reaching approx. 400rpm, being amplified by the speed controller saturation due to reference current limitation. However, the simulation shows the motor capable to drive the compressor at its rated speed.

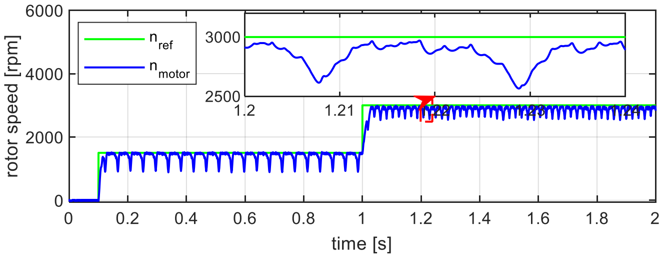

a)

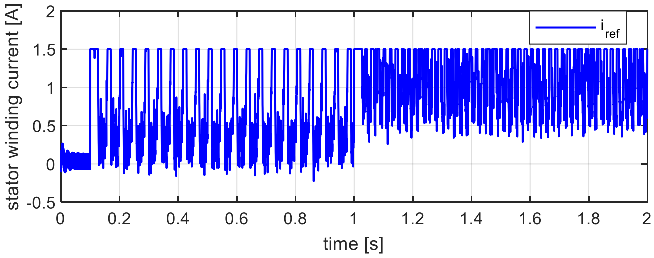

b)

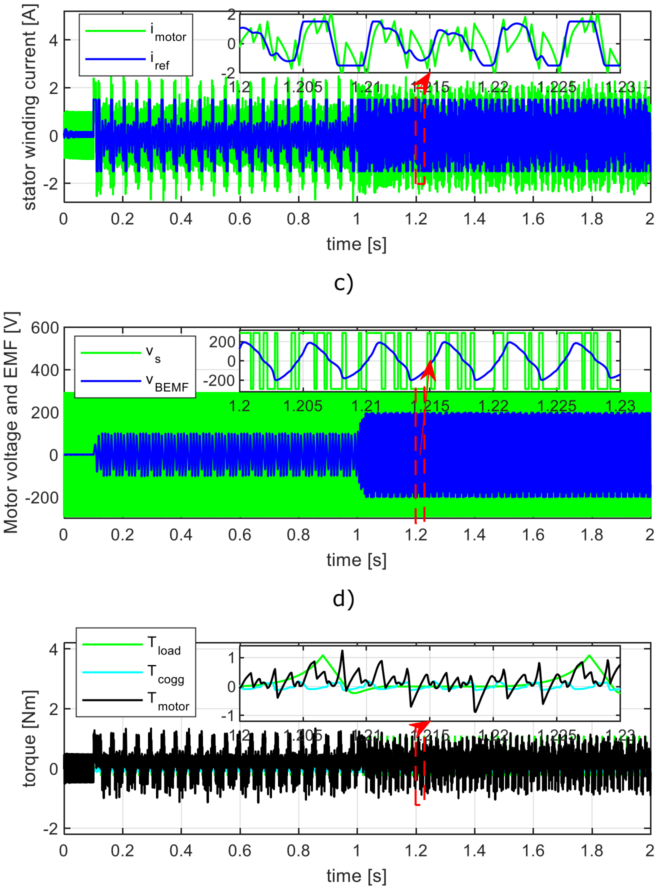

c)

d)

e)

Fig. 4.16 Simulation results for compressor load torque

4.5 Conclusions

This chapter presented a new topology of single-phase doubly salient flux reversal machine. With four stator poles, it represents a good alternative to the single-phase machine presented in Chapter 3, by having the advantage of better utilization of the PMs and of the winding mmf. An optimization routine designed for minimizing the material usage (cost), maximizing the efficiency at rated operation and reduce the total torque pulsations (minimum torque value higher than 0.1Nm) was used for optimizing the motor, for a case study targeting a compressor drive motor application with the requirement to develop 85 W at 3000 rpm. The dynamic digital simulation proved the optimum solution capable to produce the rated torque at rated speed.

CHAPTER 5. DESIGN AND ANALYSIS OF SALIENT SINGLE PHASE FOUR POLE MOTOR WITH PM IN ROTOR

Abstract

This chapter introduces and analyses a new single-phase motor PM topology, contra-candidate for the single phase four stator poles machine presented in Chapter 4. Its main feature is the placement of the PMs in the rotor, in a V-shape arrangement for flux concentration. The particularities of this new topology are investigated and a full comparative analysis versus the stator PM single phase motor is done for an optimally designed motor based on same requirements.

5.1 Introduction

Placing the main torque producing permanent magnets the rotor (which now has only two pole pairs) reduces the supply frequency required to operate the motor at given speed to half, thus reducing the core losses to a quarter. Tapered airgap is used for securing the self-starting and, in addition, two stator teeth equipped with permanent magnets are added, to provide the stop position and to modify the airgap flux density and cogging torque, to smoothen the toque shape (Fig. 5.1). By having the PM placed on the rotor, this motor topology falls within the flux switching single phase motor category.

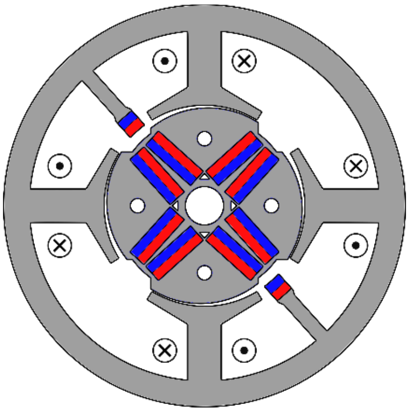

Fig. 5.1 Doubly salient single phase

The most studied motors under this category represent the motors having the permanent magnets placed on the rotor surface. The rotor can be either interior [52] or exterior [49] [53]. Secured starting is ensured via tapered airgap (on stator teeth side), via stepped airgap, or via notches in stator [54]. Another category includes the u-shape stator core motors. Double salient motors with rotor embedded PMs were also investigated for small power home appliance in [55] [56], by analytic and finite element methods, with good dynamic performance results.

The design of this motor category is usually done via parametric analysis [49] [52]- [54], where a selected parameter (a geometry dimension, usually) is varied in several steps and the best outcome is selected. Another approach is to use optimal design, by employing an automated routine to find the best solution for the corresponding parameter. The optimal design objective can include cogging torque minimization, with efficiency and torque average value constraints [54].

To improve the operation of single-phase motor, auxiliary magnets placed in the stator have been proposed for use. [57] proposed adding auxiliary magnets at the stator core end, in the extension of the stator lamination stack, over the prolonged rotor to improve the starting torque and reduce the torque ripple. The additional PMs serve for rotor parking [58] or for shaping of the cogging torque.

5.2 Machine finite element model

As for the previous studied motors, a FEMM4.2 FEM motor model was built. The parametrized model is presented in Fig. 5.2 (and Table 5.1). The geometry parameters (diameter, width, and height dimensions) will be used within the optimal design process. Fixed values were assigned for the geometry dimensions considered not to have an important influence in machine performance improvement (e.g., rotor yoke height, flux barriers width, rotor holes diameter, etc.). The size of these geometry elements was set to: 3mm diameter for the rotor holes used for rotor stack fixture, 0.5 mm for the iron bridge in the lower side of rotor PMs.

Table 5.1 Rotor PMs single phase motor: initial point versus optimum point versus optimum point

Parameter	Description [unit]
s_{Do}	stator outer diameter [mm]
s_{Di}	Stator inner diameter [mm]
s_{hy}	stator yoke height [mm]
r_{hy}	rotor yoke height [mm]
l_{stack}	Stator core stack length [mm] – not shown in Fig. 4.2
h_{pm}	rotor PM height (thickness) [mm]
s_{wp}	stator tooth width [mm]
h_{ag}	minimum airgap height [mm]
h_{ag1}	larger airgap height [mm]
r_{wp}	rotor pole width [mm]
α_{st}	stator tooth span relative to stator pole span [-]
w_{pmst}	stator PM width [mm]
α_{shst2}	Shift angle for the stator PM tooth relative to the stator main teeth inter-equidistant position

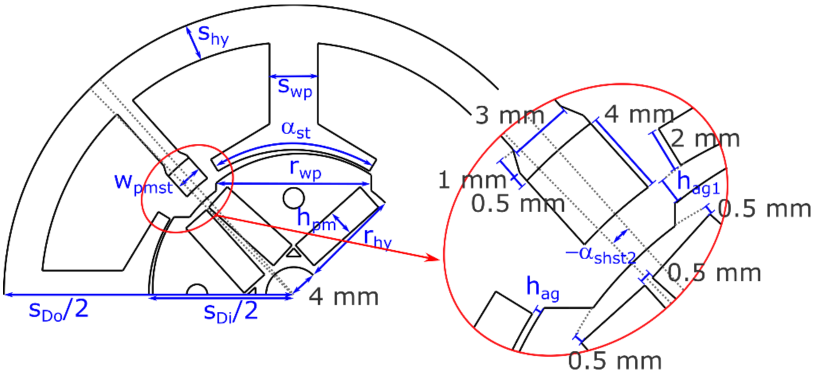

Fig. 5.2 Geometry dimensions parametrization for the new motor

The same materials as for the other previously analyzed motors were used for the finite element model (introduced in Chapter 2). Both the stator and the rotor are made of 0.18 mm steel laminated sheet, the stator and the rotor PMs are made of sintered Ferrite, having 0.45 T remanent flux density, while cooper is used for the stator winding. The four coils are connected in series. The rotor shaft is made of magnetic iron (pure iron material). However, the PM magnetic flux crossing is prevented by using Dirichlet boundary conditions (A = 0) on the shaft boundary. The rotor circular fixing holes and triangular flux barrier holes are filled by air. The meshing size was automatically selected by the FEA software. Fig. 5.3 a shows a pre-processor stage of machine model, with the generated mesh, while Fig. 5.3 b shows the postprocess stage for the no load analysis (0 A current through the stator windings). With the additional stator pair of PM teeth, the machine cannot be divided in symmetrical parts and, therefore, it needs to be fully modeled.

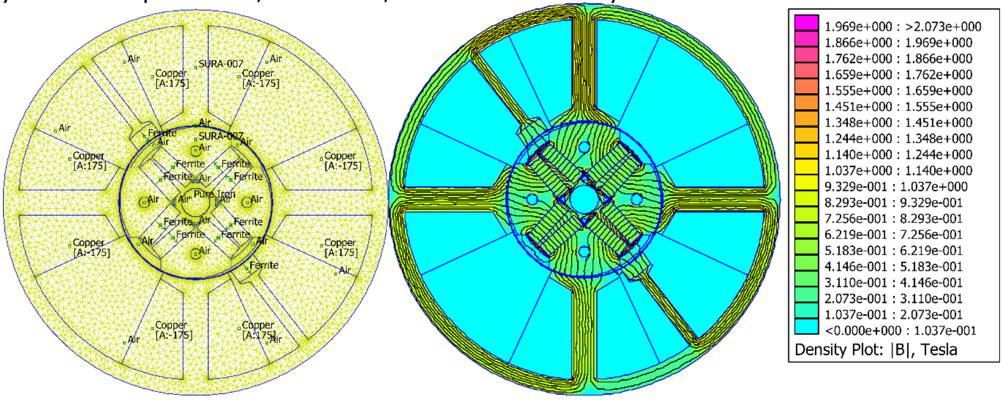

Fig. 5.3 Motor FEM model

The rationality of selecting the additional PM assisting stator set of teeth is explained below. The desired situation is to have the cogging torque pulsations compensate for the 0 values of the electromagnetic torque, during current polarity change. This reduces the torque pulsations amplitude and thus vibrations during operation. Moreover, the minimum torque value during load amplitude is desired to be at least 0.1 Nm – design conditions enforced for the previous studied motors, too.

Preliminary analysis of this new motor performance showed that the minimum torque condition is not achievable by using four stator teeth/four rotor poles configuration, even with tapered airgap. After additional topology improvement attempts (not shown here), involving adding additional notches in stator teeth, additional flux barriers in the rotor poles, creating asymmetry by shifting the rotor poles, adding two extra stator teeth with surface Ferrite PMs differently facing the airgap was found as the best solution.

To showcase the benefits of tapered airgap and assisting stator PM teeth, three motor configurations shown in Fig. 5.4 are comparatively analyzed, the first two being intermediary solutions leading to the 3rd, final motor configuration (right side).

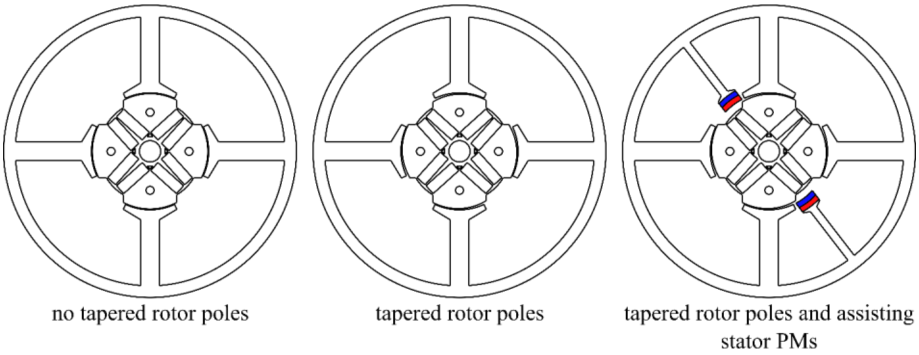

Fig. 5.4 Studied intermediary motor geometries

The left side motor has constant airgap, while the middle motor has tapered airgap produced by uneven rotor diameter along rotor teeth span. The 3rd motor (right side) contains the extra stator PM teeth. A comparison of these motor performance obtained via FEA is shown in Fig. 5.5 (the motor configurations being in Fig. 5.5 labeled - from left to right- as v.1, v.2 and v.3, respectively).

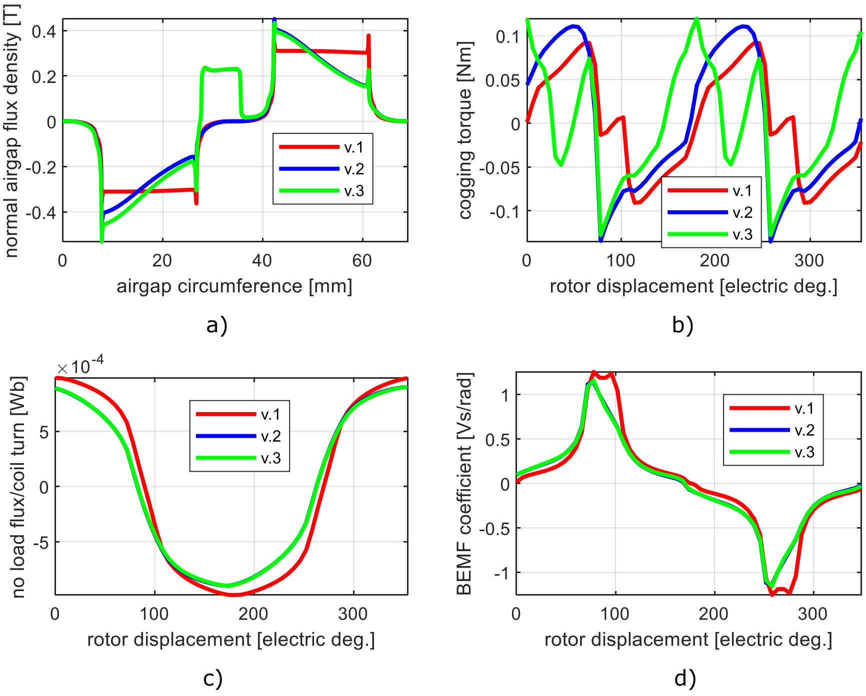

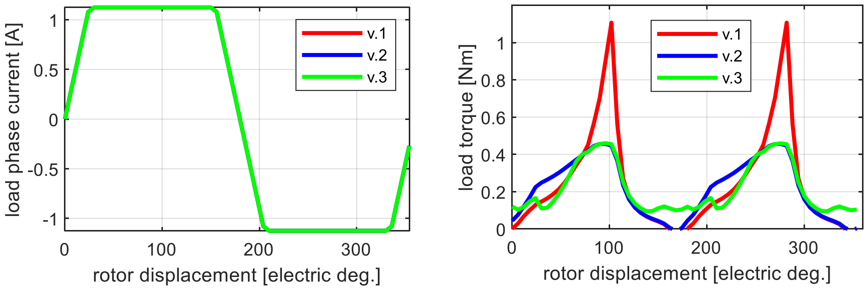

e) f)

Fig. 5.5 FEA analysis for the three studied intermediary motor geometries in Fig. 4.4, versus the rotor position: a) radial component of the flux density produced by the PMs (no stator current), b) cogging torque, c) PM flux linkage for 1 turn per coil (operation as open load generator), d) BEMF coefficient (EMF for 1 turn per coil, at rated speed of 3000 rpm operation and open load generator), e) stator current shape, imposed during load operation, f) total torque pulsations during load operation

The tapered airgap influence is visible on the flux density shape below stator teeth (Fig. 5.5 a - the airgap flux density corresponding to the rotor position in Fig. 5.4). The main influence of the tapered airgap and additional stator teeth pair is visible in the cogging torque shape (Fig. 5.5 b). Here, the extra stator PMs shift the positive cogging torque peaks towards 0° and 180° electric rotor positions, which, according to BEMF waveform in Fig. 5.5 d, correspond to the positions of 0 electromagnetic torque (current polarity change). Additionally, they increase the cogging torque pulsations amplitude and separates them into multiple pulsations, which introduce additional potential rotor stop positions (rotor positions where the cogging torque changes its polarity from positive values to negative values).

The PM linkage flux is bipolar (Fig. 5.5 c), justifying the use of a bipolar current in the motor control strategy. By departing from the ideal trapezoidal shape and being further worsen by the airgap tapering and adding stator PMs, the BEMF coefficient shape predicts large torque pulsations during load.

For the load analysis, an ideal trapezoidal current shape is fed to the motors (Fig. 5.5 e). The resulted torque pulsations are shown in Fig. 5.5 d. Tapering the airgap reduces the extremely large torque positive peaks caused by the EMF shape, while the use of stator PMs increases the minimum torque values from 0 Nm to close to 0.1 Nm.

The load torque pulsations amplitude is still large, relative to the pulsation amplitude of the Chapter 4 single phase four stator poles motor. This torque shape can be further improved by shaping the current. For example, Fig. 5.6 shows the torque pulsations for a winding current shaped in such way to exhibit lower amplitude for the rotor positions of maximum EMF peaks. The current shape was calculated as a linear function of BEMF shape, cogging torque shape and torque pulsations for trapezoidal feeding current. The torque pulsation amplitude is reduced to 41%. However, enforcing this current profile might be difficult due to large winding inductance and could also require phase advance control technique.

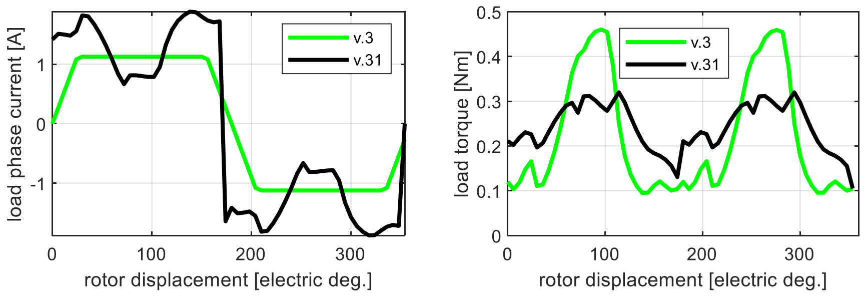

a) b)

Fig. 5.6 Torque pulsation reduction by appropriate current shaping: a) current shape, b) torque pulsations

5.3 Optimal design program and optimization results

Having the motor model defined, the Hooke Jeeves based optimization routine was adapted to accommodate it. Same design requirements, design procedure and objective function were used as for the four stator poles stator PM double salient single-phase motor (Chapter 4), reiterated below, for convenience:

- design requirements:85 W mechanical output rated power developed at the rated speed of 3000 rpm.
- supply: full bridge single phase inverter, supplied from a 290 V DC power source.
- Fitness (objective function): minimum motor material cost (minimum material use), with the additional penalty costs for:
    - Energy additional consumption due to operating at rated condition with an efficiency lower than 88% over the expected operation lifetime (10 years)
    - Average output torque below the rated torque value (0.27 Nm)
    - Minimum torque value below 0.1 Nm
    - Demagnetization susceptibility: minimum normal flux density within the rotor PMs below 0.2 T at 1.5 times the rated load operation
- Hooke Jeeves optimization algorithm is used (Chapter 2)
- FEA based motor design, following the design routine presented in Chapter 3 (Fig. 3.9). The no load / load analysis is done for iterative rotor displacement covering 180 mechanical degrees, with an analysis step of 3° mechanical. An additional FEA run is done for checking the demagnetization risk (for a single rotor position). This results in 60 x 2 + 1= 121 FEA runs for calculating the objective function for a given optimization step (candidate solution).
- 13 design variables were used, all geometry parameters (shown in Fig. 5.2). The exploration interval and minimum objective function step are given in Table 5.2. The initial optimization staring point, randomly selected within the multidimensional search domain is also given here, as "Optimization starting point".

Table 5.2 Rotor PMs single phase motor: optimal design variables and their initial values and limits

Parameter	Optimization start point	Min values	Max values	Minimum step
s_{Do}	84	80	110	1
s_{Di}	42	40	65	1
s_{hy}	5.4	4	8	0.2
r_{hy}	14	11	20	0.2
l_{stack}	30	25	40	0.5
h_{pm}	4	3	7	0.2
s_{wp}	7	7	20	0.5
h_{ag}	0.32	0.3	0.7	0.01
h_{ag1}	1.3	0.6	1.4	0.01
r_{wp}	22.5	12	25	0.5
α_{st}	0.7	0.4	0.9	0.01
w_{pmst}	4	3	9	0.2
α_{shst2}	-3	-12	12	0.2

An optimum solution was found after 67 intermediary steps (counting both exploratory and gradient descending successfully steps). The total runtime of the optimization process was several days on a regular desktop computer. In the following paragraphs the optimization results will be presented extensively (labeled as "*rotor PM motor*", for notation simplification) by comparing them against the optimization results for the four stator poles stator PM doubly salient single-phase motor (labeled "*stator PM motor*").

Table 5.3 presents the optimization results in comparison to the results for the randomly chosen initial starting point. The optimization process led to a solution close to the optimization targets. The final motor cost is slightly larger than the cost of the *stator PM motor*, at similar efficiency and lower total motor mass. The current amplitude is significantly larger and the number of turns per coil is also larger, compensating for the smaller number of PMs use. The copper losses are significantly larger, too, being however compensated by the twice as small iron losses (also due to the rated frequency which is only half).

Table 5.3 Rotor PMs single phase motor: optimization results comparison

Parameter	rotor PM motor – initial starting point	rotor PM motor – optimum solution	stator PM motor – optimum solution
Stator outer diameter [mm]	84	110	98
Stator inner diameter [mm]	42	45	48
Stack length [mm]	30.5	40	31.5
PM height [mm]	4	7	3
Minimum airgap height [mm]	0.3	0.3	0.45
Maximum airgap height [mm]	1.3	0.91	0.7
Output power [W]	72.63	68.47	72
Average torque value [Nm]	0.23	0.217	0.22
Minimum torque value [Nm]	0.01	0.08	0.1
Rated current amplitude [A]	0.95	1.11	0.67
Number of turns per coil	337	171	142
Copper cost [$]	1	2.47	3.43
Lamination cost [$]	2.8	6.29	3.93

Rotor shaft material cost [$]	0.04	0.06	0.11
PM cost [$]	0.39	0.57	0.78
Active material cost [$]	4.23	9.39	8.25
Motor mass [kg]	0.842	1.39	2.04
Copper losses [W]	28.18	5.79	2.76
Iron losses [W]	1.77	2.51	5.06
Efficiency [-]	0.7	0.8799	0.878
Energy penalty cost [$]	451.6	0.1	3.99
Minimum torque penalty cost [$]	84.14	6.93	0
Average torque penalty cost [$]	0.82	2.29	1.79
PM demagnetization penalty cost [$]	0	0	0
Objective function [$]	542	21.08	17.09

The FEM models of the initial optimization point, and final solution are shown in Fig. 5.7. The stator outer diameter was considerably increased to fit the large number of turns per coil and reduce the winding resistance. Additionally, due to low flux density in stator core material (low magnetic load and risk for saturation), the stator teeth and yoke width were reduced, to reduce the core material cost.

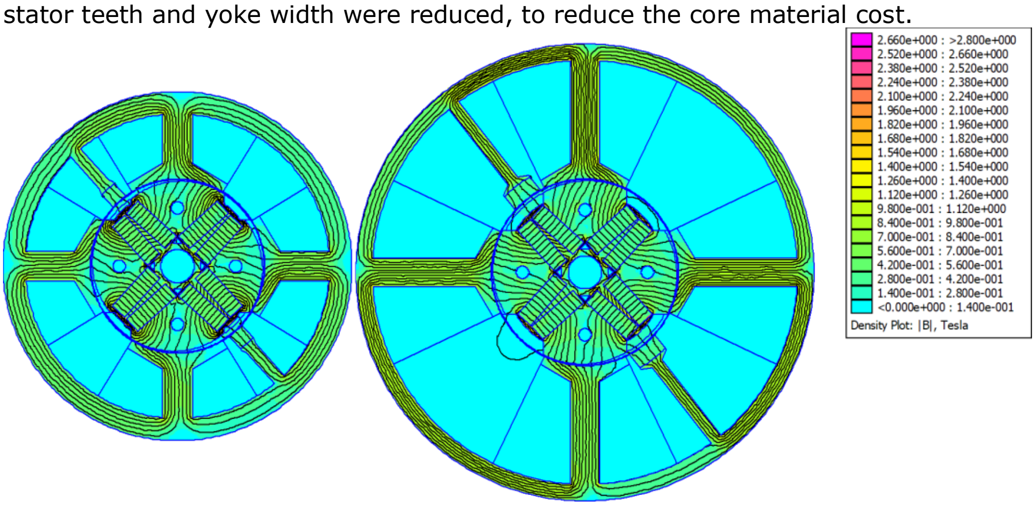

Fig. 5.7 Optimization process initial (left side) versus final solution FEM models (right side - same scale)

The next set of comparative optimization results present the evolution of main parameters, geometry dimensions and performance index during the optimization process. Fig. 5.8 shoes the evolution of the objective function and of the penalty costs. The final objective (fitness) function values are: 21.08 / 17.49 $ for the *rotor PM motor / stator PM motor*. Except for the PM demagnetization cost, all other penalty costs have non-null values, the optimization constraints expressed through the penalty costs not being 100% achieved (Table 5.3 – last rows).

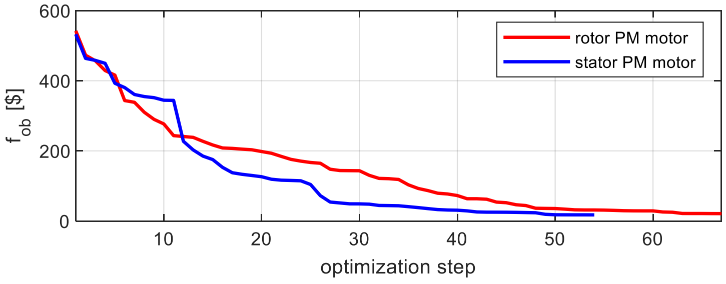
600
400
200
0
f_{ob} [$]
10
20
30
40
50
60
optimization step
rotor PM motor
stator PM motor

a)

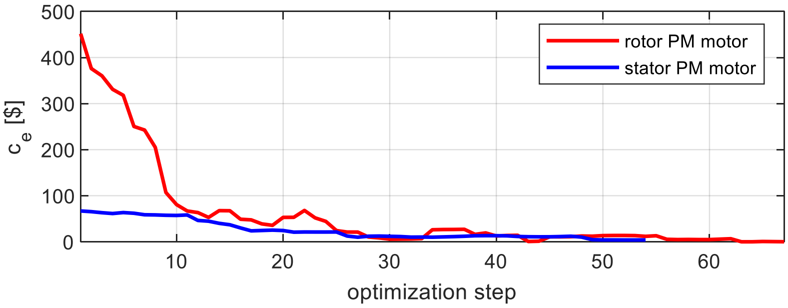
500
400
300
200
100
0
c_e [$]
10
20
30
40
50
60
optimization step
rotor PM motor
stator PM motor

b)

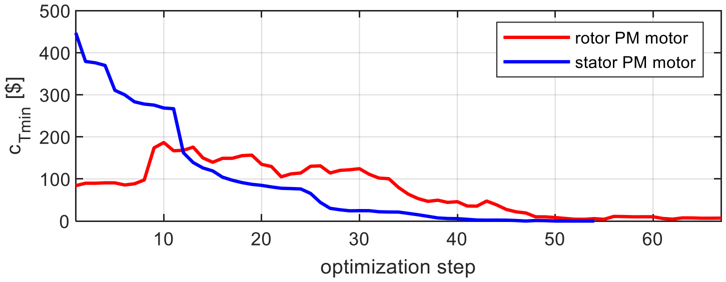
500
400
300
200
100
0
c_{Tmin} [$]
10
20
30
40
50
60
optimization step
rotor PM motor
stator PM motor

c)

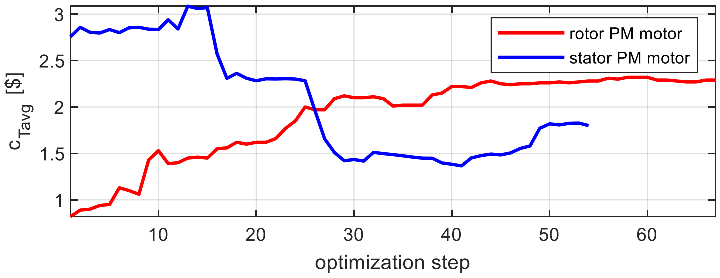
3
2.5
2
1.5
1
c_{Tavg} [$]
10
20
30
40
50
60
optimization step
rotor PM motor
stator PM motor

d)

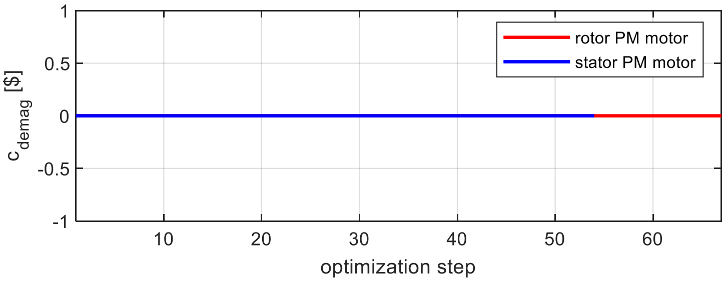

e)

Fig. 5.8 Objective function and penalty costs evolution – comparative optimization results: a) objective function, b) energy penalty cost, c) minimum torque penalty cost, d) average torque penalty cost, e) PMs demagnetization penalty cost

Fig. 5.8 also shows that, due to the characteristics of the randomly selected starting optimization point, the main challenge thorough the optimization process of the *rotor PM motor* was improving the motor efficiency, while the challenge during the *stator PM motor* optimization was increasing the minimum torque value. The next set of comparative optimization results in Fig. 5.9 present the materials comparative cost evolution. Although the number of turns per coil is larger, the *rotor PM motor* is characterized by a lower use of copper quantity, due to shorter coil turns. On the other hand, the lamination stack cost, consisting of the non-stamped square lamination stack cost is significantly larger, due to both larger outer diameter and longer core stack length. The PM quantity is smaller for the *rotor PM motor*, even with the additional stator PM pieces.

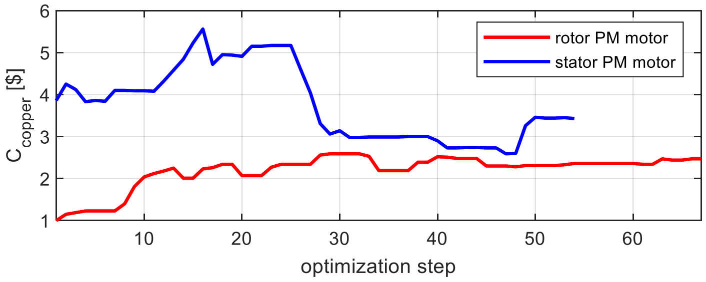

a)

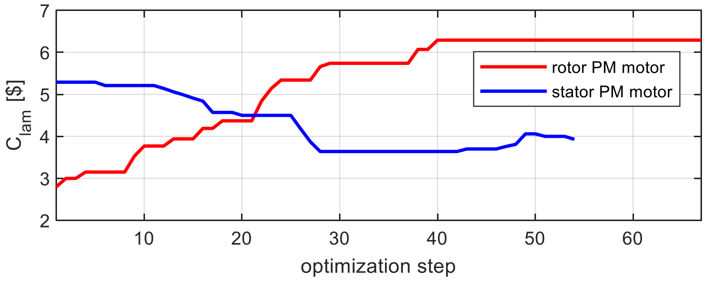

b)

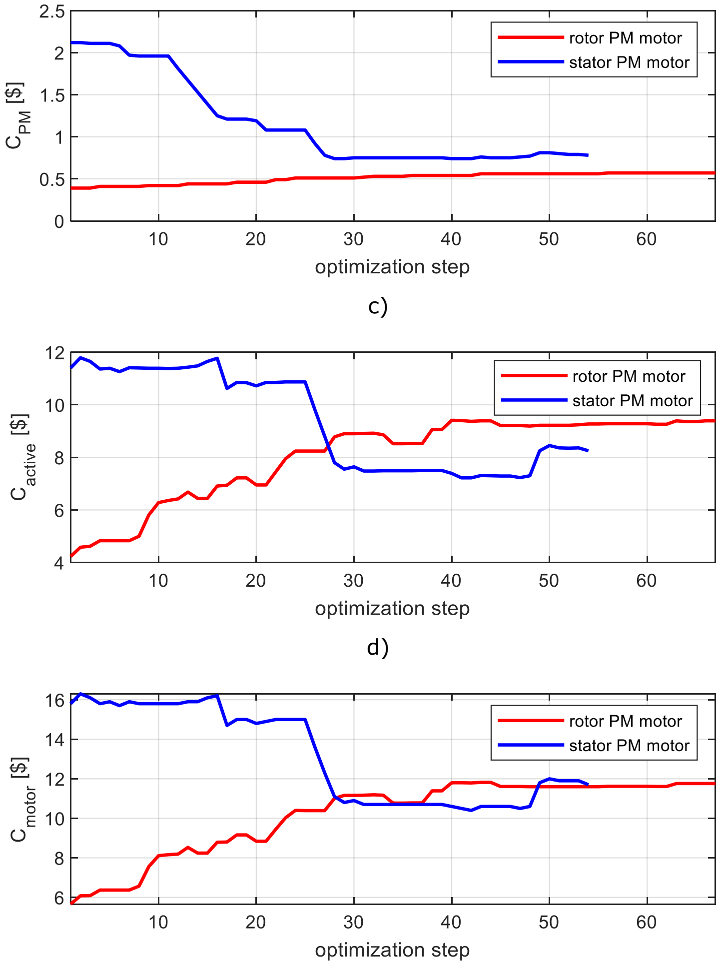

c)

d)

e)

Fig. 5.9 Material costs evolution – comparative optimization results: a) copper cost, b) lamination stack cost, c) PM cost, d) active material cost, e) total motor material cost

The total active material cost is 1.14 $ larger for the *rotor PM motor*. However, the total motor cost (which considers additionally the passive material cost, proportional with motor mass, which compensates the cost difference in the active material cost) is equal for the two motors.

The average torque value is smaller than the rated requested torque value of 0.27 Nm (Fig. 5.10 a). The small penalty cost for the torque non-realization suggests that the selected penalty coefficient of 1 is not strong enough to enforce the torque increase. On the other hand, the minimum torque value is visibly improved throughout the optimization process. According to the results in Fig. 5.10 c, the *rotor PM motor* is less susceptible to demagnetization during overloading (the analysis includes only the rotor PMs and not the two stator PM pieces).

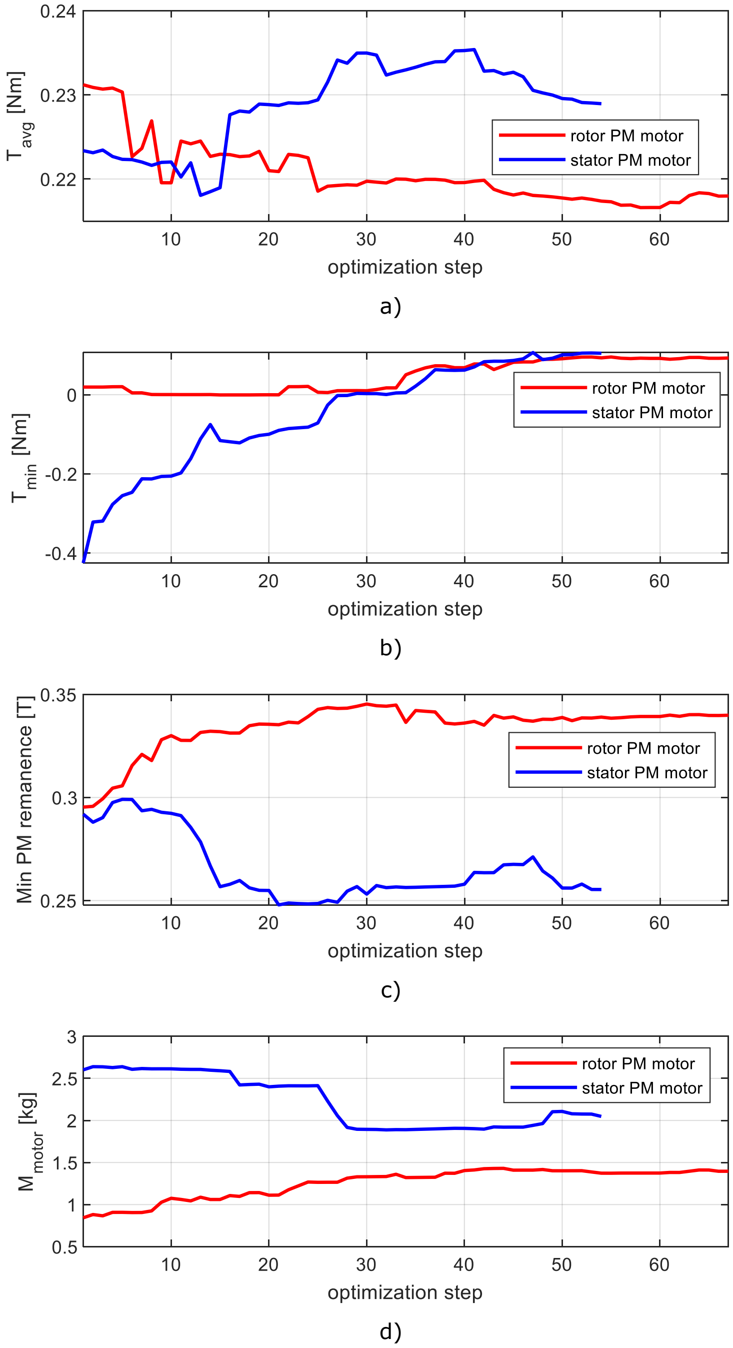

a)

b)

c)

d)

Fig. 5.10 Performance related parameters evolution – comparative optimization results: a) average torque value, b) minimum torque value, c) minimum PM remanence for 1.5 times rated load d) motor mass

One of the clear improvements in the *rotor PM motor* is its smaller weight (68% of the *stator PM motor* weight). This difference is mainly caused by the smaller core material use (large stator diameters, but thin stator teeth and yoke). However, considering that the un-stamped lamination core price is higher for the *rotor PM motor*, this indicates a better usage of the paid lamination stack material for the *stator PM motor*.

The optimization comparative set below (Fig. 5.11) presents the efficiency related data. The core losses are significantly larger for the *stator PM motor*, mainly

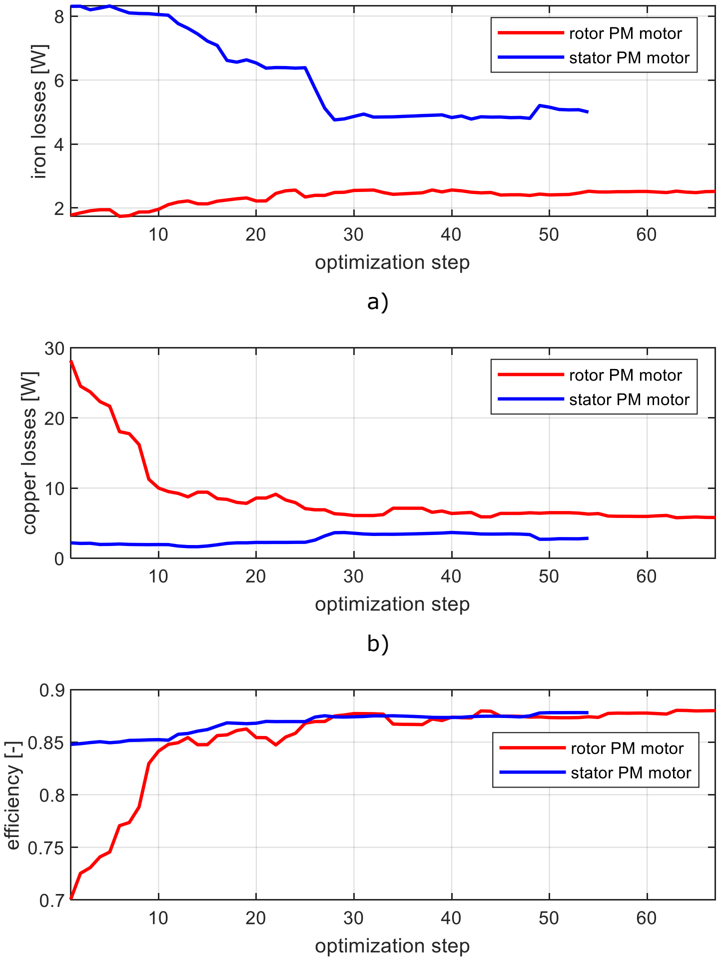

a)

b)

c)

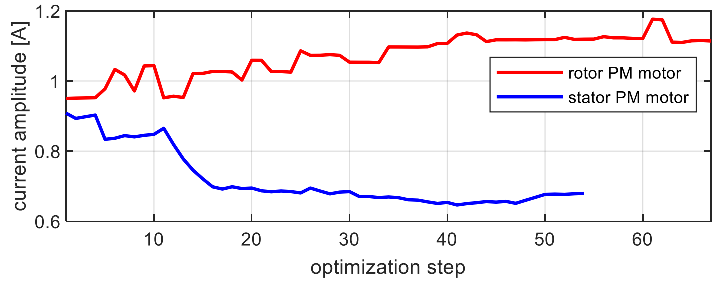

d)

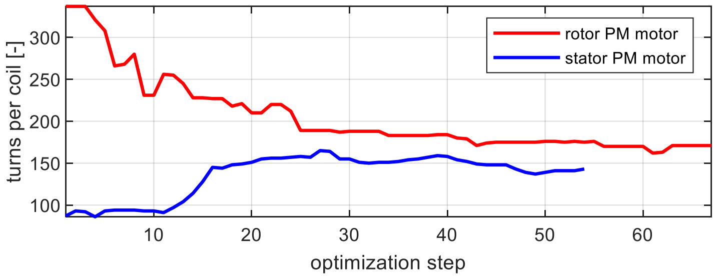

Fig. 5.11 Performance related parameters evolution – comparative optimization results: a) iron losses, b) copper losses, c) efficiency d) stator rated current amplitude, e) number of turns per coil

due to the electric frequency difference (for the same number of rotor teeth, the number of poles pairs is four, whereas the number of pole pairs for the *rotor PM motor* is two, due to the PM magnets, which also reduces the required current frequency needed to drive the motor at a given speed to half). On the other hand, the copper losses are larger, due to larger rated current amplitude, which brings the motor efficiency at approximately same value.

The last set of optimization process comparative results presented in Fig. 5.12 deals with the evolution of few selected optimal design variables. The stator outer diameter and stack length of the *rotor PM motor* already reached the maximum allowed values before optimization process end. This suggests that another optimal solution could be available for reaching by expanding these search limits (if the target application volume constrains allows it). The minimum airgap height also reached the minimum allowed value of 0.3mm, which represents a technological manufacturing limitation that cannot be extended, in this case.

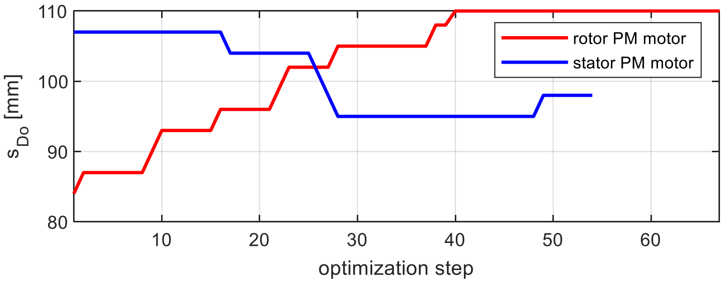

a)

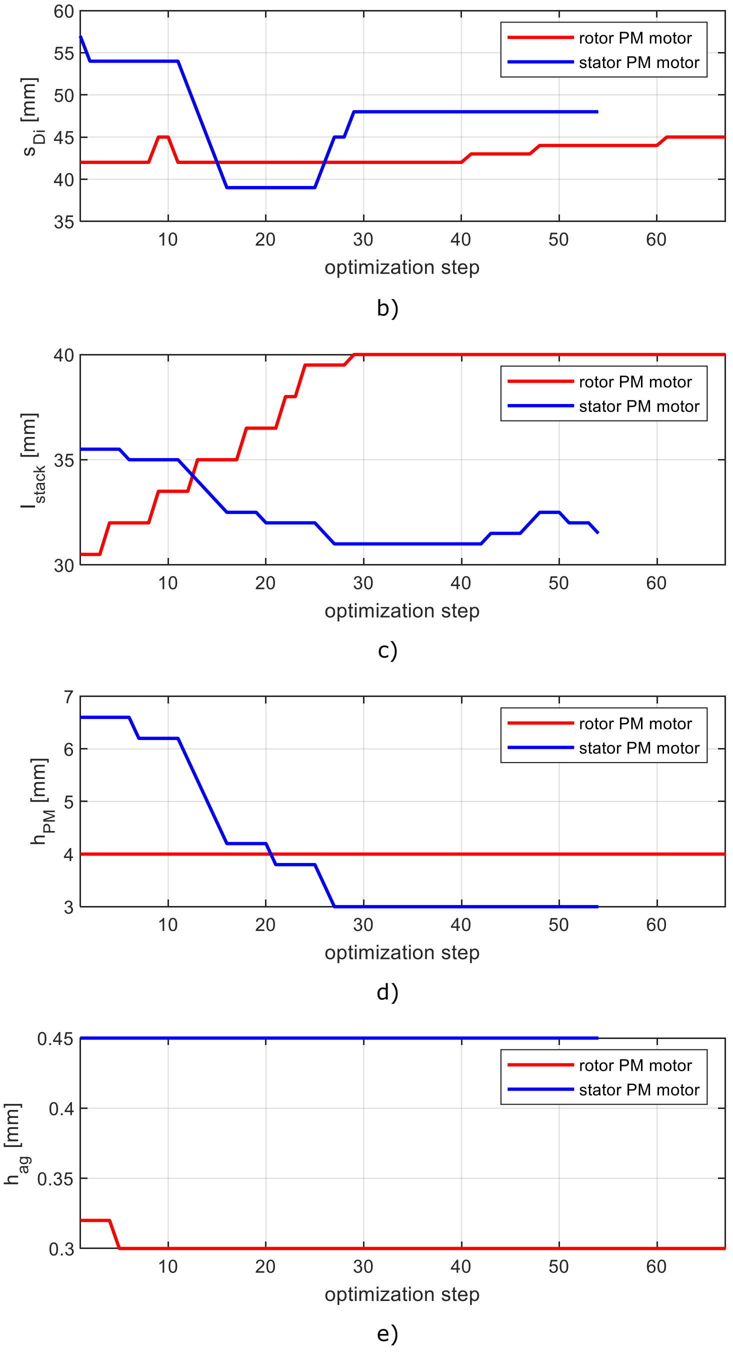
s_{Di} [mm]
60
55
50
45
40
35
rotor PM motor
stator PM motor
10
20
30
40
50
60
optimization step
l_{stack} [mm]
40
35
30
rotor PM motor
stator PM motor
10
20
30
40
50
60
optimization step
h_{PM} [mm]
7
6
5
4
3
rotor PM motor
stator PM motor
10
20
30
40
50
60
optimization step
h_{ag} [mm]
0.45
0.4
0.35
0.3
rotor PM motor
stator PM motor
10
20
30
40
50
60
optimization step

b)

c)

d)

e)

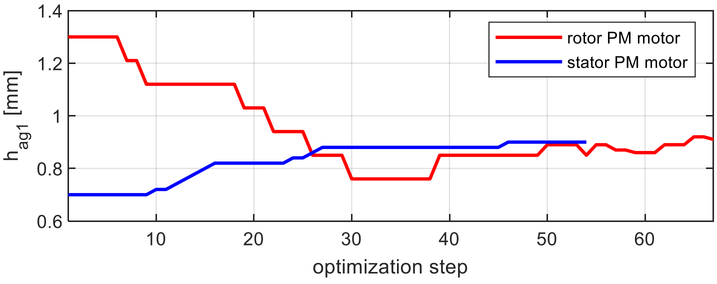

f)

Fig. 5.12 Selected optimal design variables evolution – comparative optimization results: a) stator outer diameter, b) stator inner diameter, c) stack length d) PM height, e) airgap minimum height, f) airgap larger height

As the optimization results show relative similar performance for the two motor topologies, the motivation for choosing one over another might reside in another application related factors and constraints: e.g., manufacturing difficulties, available room for installing the motor or mass limitation.

5.4 FEM analysis results

The next section will present FEA comparative results for no load and load analysis for the rotor displacement over an electric period. Fig. 5.13 presents the no-load analysis; the cogging torque pulsations have similar amplitude, with the most important feature being the positive 0.1 Nm min. torque values at 0 and 180 deg. rotor displacement.

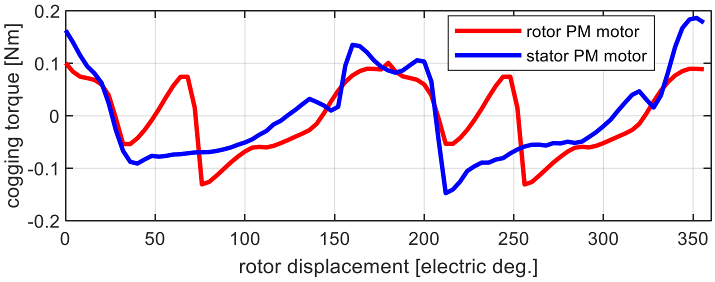

a)

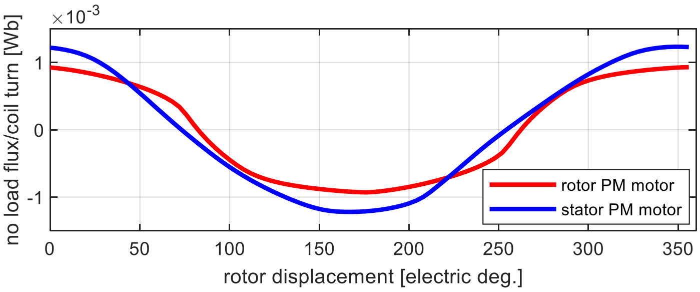

b)

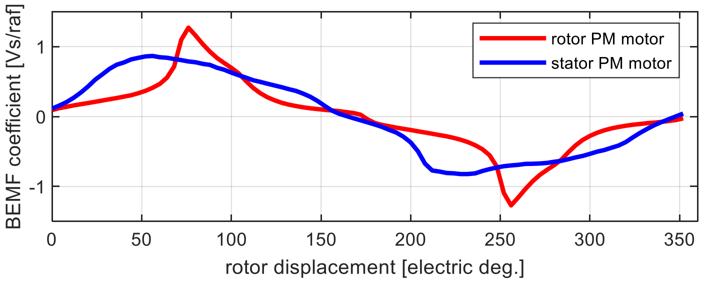

c)

Fig. 5.13 No load analysis results a) cogging torque, b) flux linkage for 1 turn per coefficient, c) bemf coefficient

Although the PM flux linkage has relatively close amplitudes, high variation during polarity change causes high amplitude peaks in the emf voltage.

The load analysis was performed by feeding the motors with trapezoidal shape currents of amplitude equal to the rated current (Fig. 4.15 a), in phase with the EMF. The *rotor PM motor* torque peaks are larger in amplitude, due to the EMF shape. They can be reduced by current shaping, as shown in Fig. 4.6.

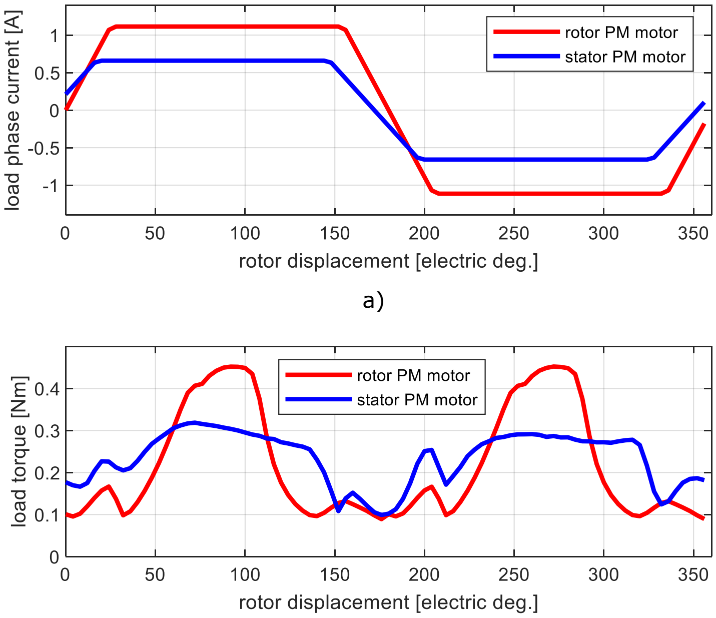

a)

b)

Fig. 5.14 On-load analysis results: a) load current profile b) total torque pulsations

As predicted by the optimization results, the FEM analysis resulted performance is also relatively similar for the two motors.

5.5 Dynamic operation digital simulation

The dynamic performance is checked via a Simulink digital simulation, as in the case of the previously studied motors. The machine model and the control strategy were presented in Section 3.2.1. The motor parameters are listed in the Table 5.4.

Table 5.4 Rotor PMs single phase motor: motor parameters used in dynamic simulation

Parameter	Value
V_{DC} (DC rated voltage [V]):	280
n_N (rated speed [rpm]):	3000
R_s (Phase resistance [Ω]):	4.6732
J (Inertia Constant [kg·m^2]):	8.69 x10-5
p (number of pole pairs)	2

The machine model uses FEA extracted values to model the rotor dependency of cogging torque, BEMF constant and stator inductance (Fig. 4.16):

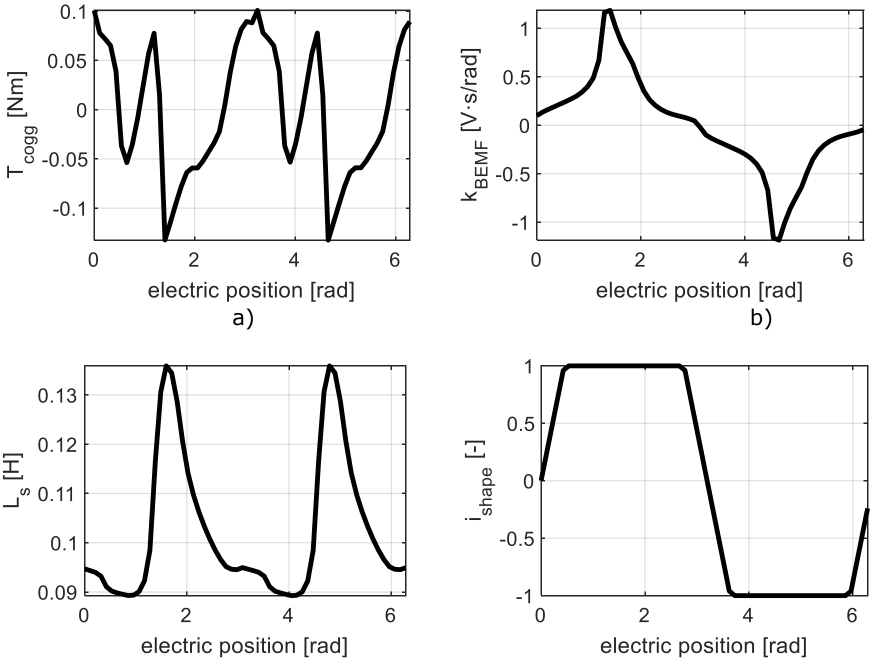

a)

b)

c)

d)

Fig. 5.15 FEA extracted parameters, used for machine model, versus the rotor position: a) cogging torque, b) BEMF coefficient, c) stator winding inductance, d) stator current imposed shape

Same as for the other studied single-phase motors, the closed loop control strategy consists of a speed PI based control and a current hysteresis control. The reference current for the inner current control loop is calculated based on the speed controller’s output, modulated by the trapezoidal shape signal in Fig. 4.16 d (current shape also used in the optimization process).

The control loops parameters values are speed PI controller proportional gain: 0.1, speed integrator gain: 1, reference current maximum limit 2.5 A and current controller hysteresis band: 0.02 A.

The simulation inputs consist of a reference step speed of 0 to 1500 rpm (50% of the rated speed) followed by a step change to 3000 rpm. Two operation modes were considered here, too: constant load and compressor torque profile load. The simulation results (denoted by *rt_PM_motor* label) are compared against the simulation results for the four stator poles doubly salient single-phase motor, presented in Chapter 4 (denoted by *st_PM_motor* label).

5.5.1 Constant ideal step load torque

A constant load T_L=0.26 T (rated torque value) is applied within 0.5 - 1.5 s time frame. Fig. 5.16 shows the simulation results. The motor can reach the rated speed at rated torque load (Fig. 5.16 a). The speed change rate is imposed by controller output limitation, set to 2.5A (approx. 2 times the rated current). Operating at rated speed and torque pushes the operation towards this current limitation (Fig. 5.16 b). The acceleration to rated speed (under rated load) is slower for the *st_PM_motor* because of the reference current limitation to 1.5A (two times the rated current), visible in Fig. 5.16 b. The speed pulsation amplitudes are relative similar.

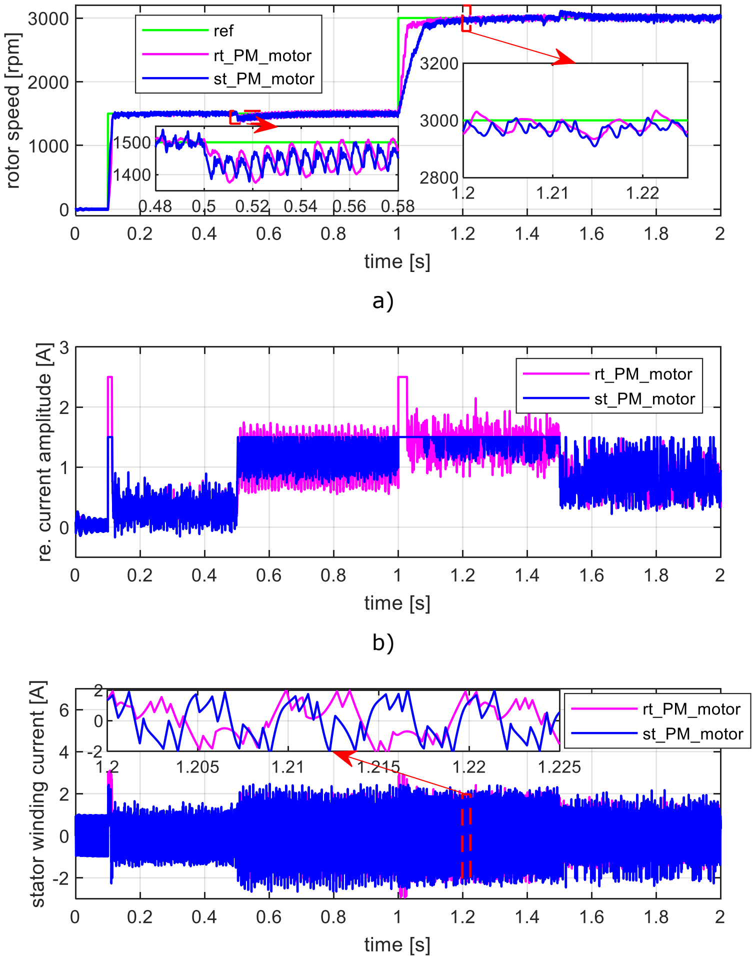

a)

b)

c)

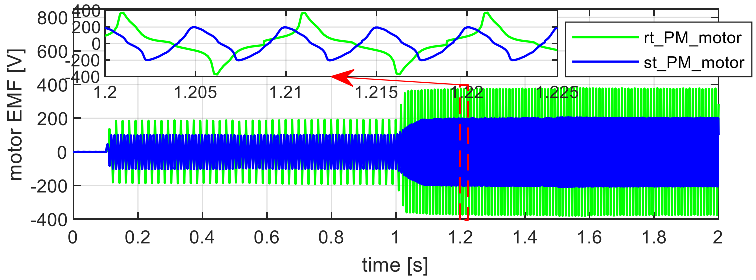

d)

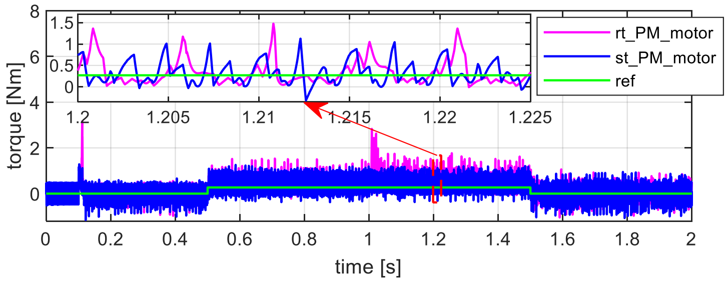

e)

Fig. 5.16 Simulation results for step acceleration setpoint and step load

Under full load, the current amplitude peaks reach 2 A for both motors. The EMF amplitude peaks are significantly higher for the *rt_PM_motor*, exceeding the DC voltage level. This suggest that the operation at rated speed might be affected by the insufficient voltage reserve.

As enforced through optimization process, the load torque has positive values (Fig. 5.16 e) during rated load operation. The high torque pulsation amplitudes are caused by the current pulsations, inherent for a hysteresis controller.

5.5.2 Operation under reciprocating compressor torque load

The second simulation set uses the same speed reference, but the load from the compressor model presented in Chapter 2. The results are shown in Fig. 5.17. Due to compressor torque characteristics pulsations reaching 1 Nm in amplitude for short time, the speed pulsations are larger, reaching approx. 400 rpm. The significantly larger pulsations amplitude present in the speed of the *st_PM_motor* is caused by the speed controller output limitation.

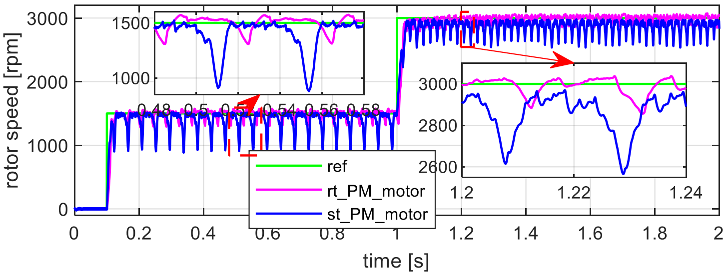

a)

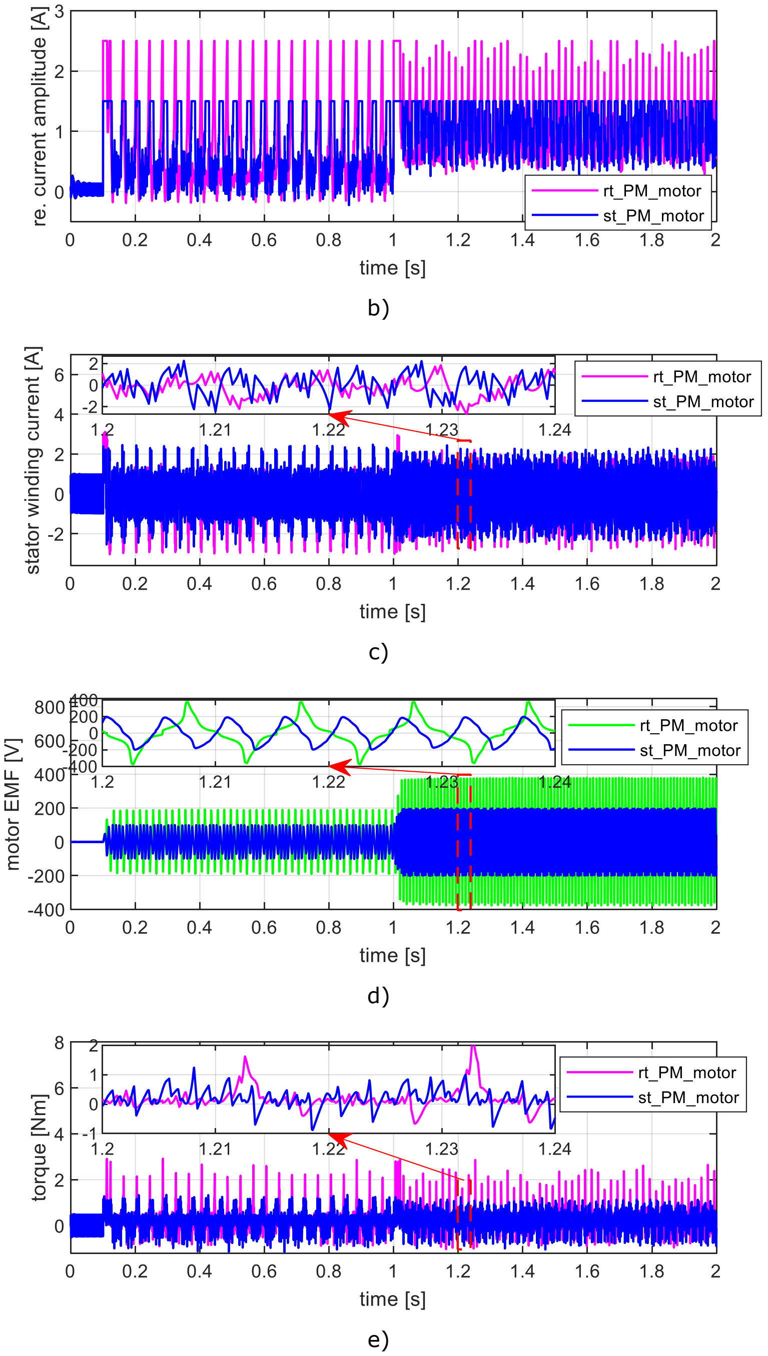

b)

c)

d)

e)

Fig. 5.17 Simulation results for compressor load torque

The dynamic simulation results confirm that the two motors exhibit relatively similar performances.

5.6 Conclusions

A novel single phase doubly salient flux switching rotor permanent magnet motor was introduced, designed, and investigated in this chapter. The motor uses Ferrite PMs in the rotor, arranged in star-shape and tapered airgap. Two additional assisting stator teeth containing surface Ferrite PMs are used, for torque shaping and rotor parking. A FEM model was built and embedded into a Hooke Jeeves based optimal design routine, with the purpose of minimizing the total material cost, including penalty costs for minimum torque, average torque, minimum efficiency, and demagnetization. To make the performance assessment easier, same design requirements were used as for the single-phase motor topology introduced in Chapter 4. Deploying the optimal design process, a solution was found after 64 steps. Comparative optimal design, FEM analysis and dynamic simulation results show the motor performance is relatively similar to the performance of four stator poles single phase motor, at a slightly higher material cost and higher torque pulsations.

CHAPTER 6. DESIGN AND ANALYSIS OF OUTER-FERRITE-PM-ROTOR BLAC MOTOR

Abstract

This chapter presents a FEM-assisted optimal design methodology for a 9 stator slots/8 rotor poles 3 phase outer Ferrite PM rotor BLAC motor. The design methodology uses an electromagnetic analytic machine model, iteratively corrected during optimization process by two FEA calculated coefficients K_E and K_L. These coefficients, calculated based on analytic/FEA model differences, multiply the analytic expression of magnetic flux per pole (accounting for complex distribution of the airgap flux density not considered in the analytic model) and the expression of stator winding synchronous inductance (accounting for saturation nonlinearity effects). With the finite element corrective intervention limited to specific moments during optimization process, a compromise between computation time and accuracy is obtained. The corrected analytic model is embedded in an optimization algorithm used for optimizing the cost of the motor under overtemperature and minimum efficiency constraints.

6.1 Introduction

Exterior rotor motors present a few characteristics which makes them attractive for compressor and pump application: e.g., higher inertia and coping well with the high torque pulsations of a load [59]. Additional advantages include shorter coil lengths which translates into lower copper use and lower copper losses [60] and better fixing for surface PMs due to centrifugal forces [61] [62], compensating the electromagnetic forces they are exposed to.

One of the main applications (but not excluding small compressors) for the external rotor motors are the in-wheel hub in traction applications [63] [64] allowing for vehicle torque vectoring and providing more free space by concentrating the motor part in the wheel itself, while bringing the challenge of dealing with unspring mass and motor protection from environment influences [65]. The design targets for this application are flux weakening capability and high torque density. To achieve constant power/speed range and allow for flux weakening, the magnets are usually placed inside the rotor, in different configurations. But external rotor motors have also been reported for use in home appliances. [66] designs a switch reluctance motor for a direct drive washing machine application.

Literature reports different methodologies for designing the outer rotor motor models with different design goals based on the specific requirements of the targeted applications. Several examples are: cogging torque and net torque ripples minimization [67], increase the efficiency in operation under the speed/torque profile corresponding to a given urban driving cycle [68], maximize the torque per volume [69], increase efficiency and reduce the motor weight [70] [71]. Correspondingly, various analytic models have been proposed and employed in the design process: lumped parameter models [72] [63] [64], 2D analytic models [73] and conformal mapping [74].

Employing these design algorithms and motor models into optimization routines where they are being executed numerous times poses the challenge of finding a compromise between model accuracy and reduced computation effort (or reduced optimization run-time). This compromise excludes the use of finite element based models (limiting their use only for optimization results validation [69]) or minimizes their use (e.g., by using computation efficient FEA analysis [75]), favoring the use of combined analytic/numerical models by e.g.: combining a magnetic equivalent circuit model with a FEM-based model to ensure precision of the airgap flux density calculations [70], or by using a field-circuit coupled optimal design method, which combines a magnetic circuit model for partial optimization with finite element analysis, used for global optimization [76].

This chapter investigates an analytic/FEM combined design model for an outer rotor BLAC motor, proposed as a solution to this accuracy/runtime compromise.

6.2 Motor topology and design requirements

The selected motor configuration is a 3 phase, 9 stator teeth/8 rotor poles surface Ferrite PM synchronous motor (Fig. 6.1). The 9/8 ratio provides a compromise between the fundamental frequency (300 Hz) which influences the core losses, motor size (influenced by the number of rotor pole pars) and the copper material cost (influenced by the copper used, dependent also on the number of stator teeth).

The motor uses factionary concentrated windings (q = 0.375 coils/poles/ phase), known for their high-power density, lower copper use (shorter coil endings) and easier manufacturing. The phase coils are distributed in adjacent slots, configuration which does introduce unbalanced radial forces in operation [62], but it represents an acceptable compromise, considering the compressor high mechanical load pulsation (for example, the case of a reciprocating compressor).

The Ferrite PMs are placed on the inner surface of the solid back iron (facing the airgap). Placing the Ferrite PMs on the rotor surface, facing the airgap has both benefits, such as: manufacturing simplicity, reduced use of iron material, good fixing due to centrifugal forces, but also disadvantages, such as: increased airgap height and increased risk of demagnetization (due to low coercive field of Ferrite PMs which are usually buried inside the iron core).

The solid cup-like shape of the back iron rotor also brings cost reduction by eliminating the need of an external motor frame, at the disadvantage of increased iron losses (due to the stator MMF harmonics produced by concentrated stator winding) which are present even in surface PM motor configurations [68] [77].

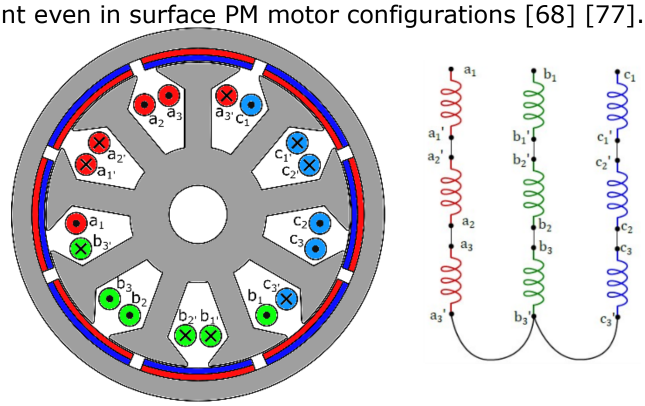

a) b)

Fig. 6.1 Three phase outer Ferrite PM motor: a) topology; b) winding connections

6.3 Analytic design model

An analytic design model is built in the following subsections, to be used in an optimization design routine. A common approach in the design of a motor is to start from electromagnetic design: determine the main geometry dimensions from electromagnetic loading, by employing a simplified magnetic circuit model [3]. This method is also applied here.

A set of parameters, consisting of geometrical dimensions are initially selected, as starting point for the machine design. These parameters, which will also serve as optimal design variables, are shown in Fig. 6.2.

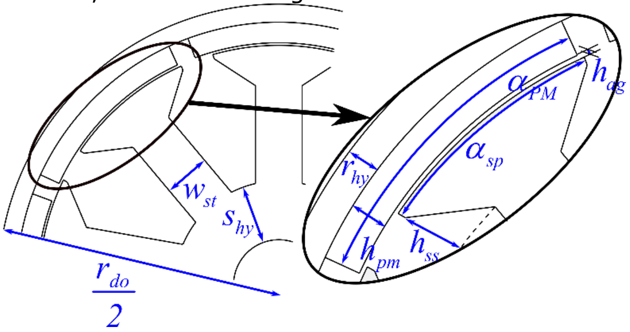

Fig. 6.2 Design initial variables

The description and the initial values of the variables is shown in Table 6.1.

Table 6.1 Outer rotor BLAC motor: initial values for the optimal design variables

Design variable	Value [mm]	Description
r_{do}	124	rotor outer diameter [mm]
l_{stack}	30	core stack length [mm] (not shown in Fig. 4.4)
h_{ag}	0.7	airgap height [mm]
h_{pm}	4	PM height [mm]
w_{st}	7.4	stator tooth width [mm]
r_{hy}	6	rotor yoke height [mm]
s_{hy}	7.5	stator yoke height [mm]
h_{ss}	3.5	stator pole top height [mm]
α_{PM}	0.73	PM width span relatively to the rotor pole span [mm]
α_{sp}	0.83	stator tooth tip span relatively to the stator pole span [mm]

6.3.1 Geometry dimensions calculations

The initial set of analytic calculations consists of computing the main geometric dimensions based on the optimal design variables selected values. The stator outer diameter and the rotor inner diameter are calculated as:

$$\begin{aligned} s_{do} &= r_{do} - 2 \cdot \left(r_{hy} + h_{ag} + h_{PM} \right) \\ r_{di} &= s_{do} + 2 \cdot h_{ag} \end{aligned} \tag{6.1}$$

The stator and rotor pole span are calculated as:

$$\begin{aligned} \tau_s &= \frac{\pi \cdot s_{do}}{N_s} \\ \tau_r &= \frac{\pi \cdot r_{di}}{2 \cdot p} \end{aligned} \tag{6.2}$$

The actual stator tooth and rotor PM's span values are determined based on the span coefficients:

$$\begin{aligned} w_{ts} &= \tau_s \cdot \alpha_{sp} \\ w_{pm} &= \tau_r \cdot \alpha_{pm} \end{aligned} \tag{6.3}$$

The stator slot height, top and bottom width are calculated as (Fig. 6.3):

$$h_{st} = \frac{s_{do} - s_{di}}{2} - s_{hy} \tag{6.4}$$

$$w_{s1} = \pi \frac{s_{do} - 2 \cdot (h_{ss} + h_{sw})}{H_s} - \left(\frac{s_{do}}{2} - h_{ss} - h_{sw}\right) \cdot \sin^{-1}\left(\frac{w_{st}}{\frac{s_{do}}{2} - h_{ss} - h_{sw}}\right) \tag{6.5}$$

$$w_{s2} = \pi \cdot \frac{s_{do} - 2 \cdot h_{st}}{N_s} - \left(\frac{s_{do}}{2} - h_{st}\right) \cdot \sin^{-1}\left(\frac{w_{st}}{\frac{s_{do}}{2} - h_{st}}\right) \tag{6.6}$$

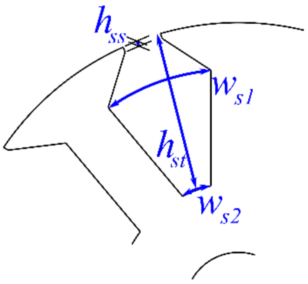

Fig. 6.3 Stator slot geometry dimensions

The slot useful area (area which can be filled by winding) is:

$$A_s = (h_{st} - h_{ss} - h_{sw}) \frac{w_{s1} + w_{s2}}{2} \tag{6.7}$$

The length of one turn per coil calculation is simplified to:

$$l_{turn} = 2 \cdot (l_{stack} + 0.8 \cdot \tau_s) \tag{6.8}$$

With the slot fully filled by the winding (for a slot filling factor k_{fill} of 0.4), the current density through the winding wire is:

$$j_{co} = \frac{2 \cdot mmf}{A_s \cdot k_{fill}} \tag{6.9}$$

The mmf value will be determined later, with (6.26).

Having these dimensions determined, the quantity of the materials used is further calculated as:

$$m_{co} = N_s \cdot l_{turn} \cdot A_{st} \cdot k_{fill} \cdot \rho_{co} \tag{6.10}$$

The stator core mass, used for core losses calculation is determined as:

$$m_{st} = \left[\pi \frac{s_{do}^2 - s_{di}^2}{4} - N_s \left(A_{st} + w_{ss} + h_{sw} + h_{ss} \frac{w_{s1} + w_{s2}}{2}\right)\right] \cdot l_{stack} \cdot \rho_{lam} \tag{6.11}$$

However, the laminated material cost calculation is based on the unstamped lamination sheets mass:

$$m_{lam} = s_{do}^2 \cdot l_{stack} \cdot \rho_{lam} \tag{6.12}$$

The PM mass is calculated as:

$$m_{PM} = 2 \cdot p \cdot h_{PM} \cdot w_{PM} \cdot l_{stack} \cdot \rho_{PM} \tag{6.13}$$

The rotor mass has three components associated with main core, the shaft, and the cup-end part:

$$m_{rt1} = \pi \frac{\left(r_{do}^{2} - \left(r_{do} - r_{hy}\right)^{2}\right)}{4} \cdot l_{stack} \cdot \rho_{fe} \qquad (6.14)$$

$$m_{rt2} = r_{hy} \cdot \pi \cdot \frac{r_{do}^{2} - s_{di}^{2}}{4} \qquad (6.15)$$

$$m_{rt3} = \pi \cdot \left(l_{stack} \cdot k_{os} \cdot \frac{s_{di}^{2}}{4} + r_{hy} \cdot \frac{s_{do}^{2}}{4} \right) \cdot \rho_{fe} \qquad (6.16)$$

where k_{os} is the over-shaft factor. The final rotor mass results:

$$m_{rt} = m_{rt1} + m_{rt2} + m_{rt3} + m_{PM} \qquad (6.17)$$

The winding mass is calculated as:

$$m_{co} = N_{s} \cdot l_{turn} \cdot \frac{A_{s} \cdot k_{fill}}{2} \cdot \rho_{co} \qquad (6.18)$$

The final motor active material mass (no frame, bearings, connection box mass included) is:

$$m_{motor} = m_{st} + m_{co} + m_{rt} \qquad (6.19)$$

Knowing the mass of each material, the material cost can be easily determined by using the material cost (material prices in $/kg are given in Chapter 2).

The rotor moment of inertia is estimated using the expression:

$$J_{r} = \frac{r_{do}^{2} - \left(r_{do} - 2 \cdot r_{hy}\right)^{2}}{8} \cdot m_{rt1} + \frac{\left(r_{do} - 2 \cdot r_{hy}\right)^{2} - r_{di}^{2}}{8} \cdot m_{PM} + \frac{r_{do}^{2} - s_{di}^{2}}{8} \cdot m_{rt2} \qquad (6.20)$$

6.3.2 Simplified magnetic circuit

The second part of the analytic model uses a simplified linear magnetic circuit model (Fig. 6.4) for the electromagnetic design, for determining the required mmf to operate under rated conditions. The circuit models the path for a flux line which passes through the rotor yoke, rotor PM, airgap stator tooth (and stator coil) and stator yoke.

The main circuit components are the PM and airgap reluctance (the core reluctance being neglected). The magnetic flux sources (magnetomotive forces - *mmf*) are the PM and the stator coil.

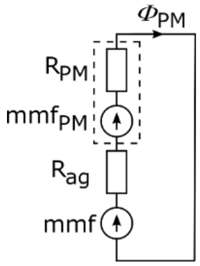

Fig. 6.4 External rotor model: simplified magnetic circuit model

Using Ampere law, the airgap magnetic flux density produced by the rotor PM can be expressed as:

$$B_{g} = B_{rPM} \cdot \frac{h_{PM}}{h_{PM} + h_{ag}} \qquad (6.21)$$

with B_{rPM} – the PM remanence, h_{PM} – PM height and h_{ag} – airgap height. It is considered that the PM permeability is close to the air relative permeability ($\mu_{rPM} \simeq \mu_{r0}$).

Using the magnetic flux definition, the amplitude of the fundamental component of airgap magnetic flux per pole is expressed as:

$$\Phi_{PM_{max}} = \frac{4}{\pi} B_g \cdot w_{PM} \cdot l_{stack} \cdot \sin\left(\frac{\pi}{2} \cdot \alpha_{PM}\right) \frac{1}{k_{fringe}} \tag{6.22}$$

where k_{fringe} – coefficient accounting for the airgap flux fringing.

The magnetic flux density within the stator tooth is expressed as:

$$B_{st} = 2 \frac{B_g \cdot w_{ts}}{\pi \cdot w_{st}} \tag{6.23}$$

The electromagnetic torque expression for pure i_q control ($i_d = 0$ – MTPA condition for non-salient, non-saturated synchronous motors) is:

$$\begin{aligned} T_e &= \frac{3}{2} p \cdot \lambda_{PM} \cdot i_{s\,max} \\ &= \frac{3}{2} p \cdot \left(3 \cdot N \cdot \Phi_{PM\,max} \cdot k_{w1}\right) \cdot i_{s\,max} \\ &= \frac{9}{2} p \cdot \Phi_{PM\,max} \cdot k_{w1} \cdot mmf \end{aligned} \tag{6.24}$$

where N is the number of turns per coil and k_{w1} – the winding factor and the $mmf = N \cdot I_q$ represents the magnetomotive force per coil. The number of turns per coil is not known yet. If the rotor losses and mechanical friction losses are neglected, the electromagnetic torque can be equated to the output mechanical torque. The rated output torque for given output power and speed requirements is:

$$T_m = \frac{P_N}{2 \cdot \pi \cdot f_N \cdot p} \tag{6.25}$$

Combining (6.24) and (6.25), the mmf necessary to produce the rated torque is expressed as:

$$mmf = \frac{T_m}{\frac{9}{\sqrt{2}} \cdot \Phi_{PM} \cdot p \cdot k_{w1}} \tag{6.26}$$

6.3.3 Winding parameters

Because the number of turns per coil is not known yet, the winding resistance and inductance cannot be determined. However, their values normalized to the N^2 can be calculated, being useful later in determining the number of turns per coil.

The stator inductance is calculated as the sum of main and leakage inductance:

$$\begin{aligned} L_s &= \left(L_m + L_\sigma\right) \\ &\approx 1.3 \cdot \frac{3 \cdot N^2}{R_{PM} + R_{ag}} \\ &\approx 1.3 \cdot 3 \cdot \mu_0 \cdot N^2 \cdot k_{w1} \cdot \frac{w_{PM} \cdot l_{stack}}{h_{ag} + h_{PM}} \end{aligned} \tag{6.27}$$

where R_{PM} and R_{ag} are PM and airgap magnetic reluctances in Fig. 6.4. The 0.3 coefficient assumes that the leakage component of the stator inductance L_{σ} is approximatively equal to 30% of the main inductance L_m value. Therefore, the stator inductance per number of turns per coil squared yields:

$$\frac{L_s}{N^2} = 3.9 \cdot \mu_0 \cdot k_{w1} \cdot \frac{w_{PM} \cdot l_{stack}}{h_{ag} + h_{PM}} \tag{6.28}$$

The stator resistance can be written as:

$$\begin{aligned} R_s &= \rho_{co} \cdot \frac{l_{turn} \cdot N \cdot 3}{A_s \cdot k_{fill}} \\ &= \rho_{co} \cdot \frac{l_{turn} \cdot N \cdot 3}{A_s \cdot k_{fill}} \\ &= \rho_{co} \cdot \frac{3 \cdot l_{turn} \cdot N^2}{mmf} \cdot j_{co} \end{aligned} \tag{6.29}$$

Similarly, the stator resistance per number of turns per coil squared yields:

$$\frac{R_s}{N^2} = \rho_{co} \cdot \frac{3 \cdot l_{turn}}{mmf} \cdot j_{co} \tag{6.30}$$

6.3.4 Losses and efficiency

The copper losses (joule losses) are obtained from the mmf and stator resistance coefficient:

$$p_{co} = 3 \cdot R_s \cdot I_s^2 = 3 \cdot \frac{R_s}{N^2} \cdot mmf^2 \tag{6.31}$$

The iron core losses for operation at rated speed (rated frequency) are calculated based on core specific losses and magnetic loading ($p_{fe_{1T400Hz}}$ = 14.3W/kg specific losses for 400Hz frequency and 1T magnetic load [19]):

$$p_{fe} = k_{p_{fe}} \cdot p_{fe_{1T400Hz}} \left(B_{st} \cdot \frac{f_N}{400} \right)^2 \cdot m_{st} \tag{6.32}$$

where $k_{p_{fe}} = 1.45$ represents a safety coefficient added to represent the mechanical core processing losses. Since the rotor back-iron flux density shows a significantly less variation with rotor position and because the thickness of magnets/main flux space harmonics pole pitch is large, the stator was considered as the only region for the core losses calculation.

Finally, the efficiency for operation at rated conditions is determined as:

$$\eta_N \approx \frac{P_N}{P_N + p_{co} + p_{fe} + p_{mec}} \tag{6.33}$$

where the mechanical losses p_{mec} are taken as fix percentage value of 1.5% of output rated power.

6.3.5 Number of turns per coil determination

The third part of the model uses the stator voltage equation for steady state operation. Written for the main harmonic component, the equation yields:

$$\bar{V}_s = R_s \cdot \bar{I}_s + j\omega\bar{\lambda}_s \tag{6.34}$$

$$\bar{\lambda}_s = \bar{\lambda}_{PM} + L_s \cdot \bar{I}_s \tag{6.35}$$

$$\lambda_{PM} = 3 \cdot \Phi_{PM} \cdot N \cdot k_{w1} \tag{6.36}$$

The electromotive force (emf) RMS value at rated speed operation is written as a function of number of turns per coil N:

$$\begin{aligned} E &= \omega_N \cdot \lambda_{PM} \\ &= 3 \cdot 2 \cdot \pi \cdot f_N \cdot N \cdot \frac{\Phi_{PM}}{\sqrt{2}} \cdot k_{w1} \end{aligned} \tag{6.37}$$

By assuming that the pure I_q control is used (usually employed for unsaturated surface PM synchronous motors), the phasor diagram associated to the Eq (6.34) - (6.36) can be represented as in Fig. 6.5:

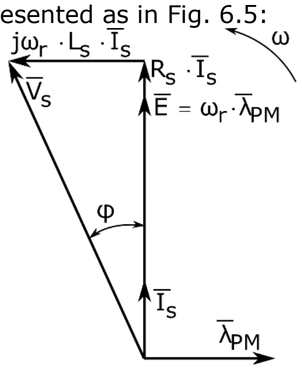

Fig. 6.5 External rotor model: steady state phasor diagram

According to the phasor diagram, the voltage phasor RMS value can be written as:

$$V_s = \sqrt{\left(R_s I_s + E\right)^2 + \left(\omega_r L_s I_s\right)^2} \tag{6.38}$$

This equation can be used to calculate the number of turns per coil.

$$V_s = N\sqrt{\left(\frac{R_s}{N^2} \cdot mmf + \frac{E}{N}\right)^2 + \left(\omega_r \frac{L_s}{N^2} \cdot mmf\right)^2} \tag{6.39}$$

Based on the DC bus voltage level, the maximum phase voltage RMS value is:

$$V_s = \frac{4}{\pi} \cdot \frac{V_{DC}}{\sqrt{2}} \cdot \frac{1}{\sqrt{3}} \cdot sin\left(\frac{2\pi}{3}\right) \cdot k_{safety} \tag{6.40}$$

where k_{safety} is a sub-unitary coefficient of 0.7 which artificially decreases the available phase voltage with 30% to provide the designed machine with a safety margin for reaching the rated speed. Finally, with all other terms on the right side of the (6.39) already known, the number of turns per coil can be extracted:

$$N = \frac{V_s}{\sqrt{\left(\frac{R_s}{N^2} \cdot mmf + \frac{E}{N}\right)^2 + \left(\omega_r \frac{L_s}{N^2} \cdot mmf\right)^2}} \tag{6.41}$$

With the number of turns per coil N determined, the motor parameters: stator resistance R_s, the stator winding inductance L_s, the permanent magnet flux linkage λ_{PM} can be determined. Additionally, the rated stator current RMS value is calculated as:

$$I_N = I_s = \frac{mmf}{N} \tag{6.42}$$

The flow diagram of the analytic model presented above is shown in Fig. 6.6. The blocks represent the quantities expressed by the equations above, while the arrows denote their dependencies and the direction of calculation flow. The model inputs (marked with blue) are the design requirements, the optimal design variables and the materials electric/magnetic/mechanical properties and cost, while the model output quantities, expressing the motor performance and fitness are the motor efficiency and total material cost. These quantities will be used in the optimal design's objective function to determine the motor fitness.

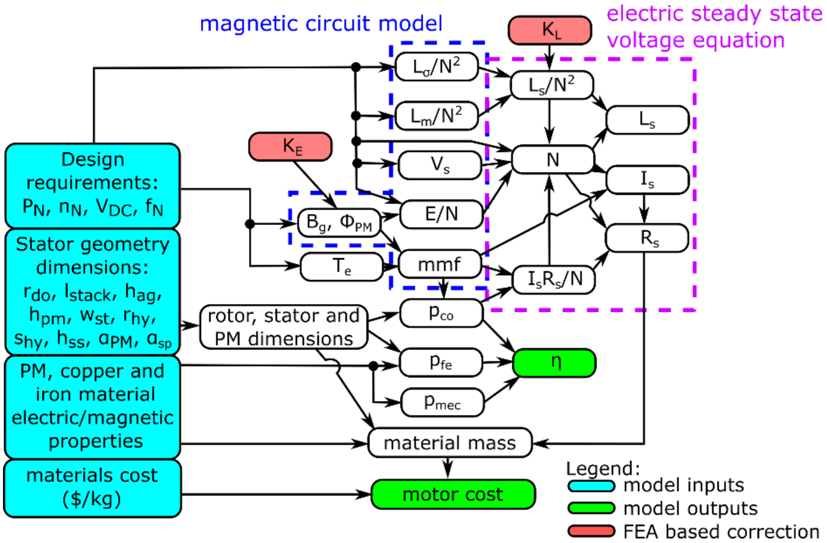

Fig. 6.6 Analytic model used in the optimization process

While being simple and fast to execute, good features for a model which is iteratively executed in an optimization routine, this analytic model is not very precise, its accuracy being reduced as a tradeoff to simplicity. The main simplifications were done in the magnetic circuit model, where the saturation and flux leakage accurate calculation were not considered. This can lead to designing a machine which will not meet the design requirements in real operation (being able to operate at rated speed and rated load torque). One approach in improving the analytic model would be the embedding of a nonlinear magnetic circuit model. Another option would be to change the model to a more accurate one, such as finite element-based model. However, this leads to a prohibitive calculation effort (as seen in previous chapter where FEA based optimization was implemented). A new approach is proposed here as a compromise between the reduced optimization time and model accuracy: iteratively correct the analytic model via specific FEA validation until the analytic model's results converge to the FEA model's results.

6.3.6 FEA based correction coefficients

One of the main sensitive part of the analytic model is the PM magnetic flux. The inaccuracies in its calculation influence directly the mmf and emf calculation, affecting the motor capability to produce the rated torque at rated speed.

An overestimate of the stator PM flux (the real value is smaller than the value calculated by design) will limit the possibility to achieve the load torque for the designed rated current. On the other hand, if the PM flux is underestimated (the real PM flux is larger than the calculated value by design) the motor will not be able to reach the rated speed under rated load (due to high emf value). In both cases, the effect is visible in the torque produced by the motor operating at rated current. Therefore, checking the electromagnetic torque value via FEA at the end of the optimization process for rated current load is a good indicator for the accuracy of the PM flux estimation. The deviation between the analytic electromagnetic torque value and FEA electromagnetic torque value can be expressed as:

$$K_E = 1 + \frac{T_{FEM} - T_e}{T_e} \tag{6.43}$$

where T_e is the electromagnetic torque calculated with the (6.24) and the T_{FEM} represents the electromagnetic torque extracted via FEA analysis of the designed motor. The K_E coefficient is used then for correcting the analytic model's Equ. (6.44). as shown in the analytic model diagram:

$$\Phi_{PM_{max}} = K_E \cdot \frac{4}{\pi} B_g \cdot w_{PM} \cdot l_{stack} \cdot \sin\left(\frac{\pi}{2} \cdot \alpha_{PM}\right) \frac{1}{k_{fringe}} \tag{6.44}$$

With the PM flux equation corrected, the analytic design is deployed again. Because the PM flux correction will lead to a different design result, the correction factor will be adjusted recurrently until the FEA – analytic torque difference converges to 0:

$$K_E = K_{E_{(n-1)}} + \frac{T_{FEM} - T_e}{T_e} \cdot k_E \tag{6.45}$$

where K_E is the previous value of the correction coefficient and k_E is a sub-relaxation factor which controls the corrected value's convergence speed. Since this operation requires more FEA check – analytic design successive steps, the total computation effort is higher than the computation effort of directly using FEA for the electromagnetic design, especially in an optimal design routine where the design algorithm is successively applied for each candidate. **To avoid this, the FEA based check is used only at the end of the optimization process** (done only based on the analytic model) and a next analytic model-based optimization process is started from the current optimum results, with the model corrected. A detailed overview of the optimization process is done in the next subchapter.

In a similar way, the stator inductance is corrected via FEM analysis. The Equ. (6.28) provides a rough approximation of the stator inductance as it considers the leakage inductance and end-coil inductance to equal 30% of the main inductance. The K_L inductance correction coefficient is calculated in a similar way:

$$K_L = K_{L_{(n-1)}} + \frac{L_{FEM} - L_s}{L_s} \cdot k_L \tag{6.46}$$

and applied to the stator inductance analytic formula:

$$L_s = K_L \cdot 1.3 \cdot 3 \cdot \mu_0 \cdot N^2 \cdot k_{w1} \cdot \frac{w_{PM} \cdot l_{stack}}{h_{ag} + h_{PM}} \tag{6.47}$$

The two coefficients are marked in the algorithm flow diagram with red.

6.4 Optimal design routine

The optimization routine uses the set of 10 optimal design variables shown in Table 6.1. Their search domain (minimum - maximum interval along each dimension) is shown in Table 6.2.

Table 6.2 Outer rotor BLAC motor: optimal design variables exploration range

Design variable	Min. value [mm]	Max. value [mm]	Description
r_{do}	115	124	rotor outer diameter [mm]

l_{stack}	20	30	core stack length [mm] (not shown in Fig. 4.4)
h_{ag}	0.5	1	airgap height [mm]
h_{PM}	2	7	PM height [mm]
w_{st}	5	15	stator tooth width [mm]
r_{hy}	4	15	rotor yoke height [mm]
s_{hy}	4	15	stator yoke height [mm]
h_{ss}	2	8	stator pole top height [mm]
α_{PM}	0.5	0.9	PM width span relatively to the rotor pole span [mm]
α_{sp}	0.8	0.9	stator tooth tip span relatively to the stator pole span [mm]

6.4.1 The multi-objective fitness function

As for the previous designed motors, the optimal design routine employs an objective function or fitness function expressed in cost, to be minimized. The optimization process targets multiple outcomes, embedded in the optimization function by penalty functions expressing their fulfillment in terms of cost. The main objective function component is the material cost C_{mat} composed by active and passive material cost. The active material cost includes the stator stack core cost, PM cost, rotor material cost and winding copper cost, while the passive material cost includes motor frame, insulation sheets, bearings, etc.

$$f_{ob} = C_{mat} + c_{temp} + c_e \tag{6.48}$$

The two sets of constraints written in terms of penalty costs concern overtemperature rise during rated operation and energy consumption.

The stator heat extraction due to joule and iron losses represents a challenge for the interior stator PMSM motors, which should be considered in the electromagnetic design [78]. The heat buildup inside the motor is reduced in a refrigerator compressor application, due to the intermittent operation (in case of no-variable speed drive) or operation at a lower power in majority of the time. Increasing the temperature above the insulation class rated temperature will cause the reduction of the insulation life and performance degradation. The c_{temp} objective function cost component represents the penalty cost applied only if the winding temperature exceeds the maximum temperature given by the material insulation grade (155 °C). The penalty cost varies linearly with the over-temperature multiplied by the material cost and by a weighting factor. The winding temperature is calculated based on the core and iron losses, considering the convection heat transfer coefficient from the stator core side surface to the ambient.

$$c_{temp} = max\left(T_W - T_{W_{max}}, 0\right) \cdot k_{ctemp} \cdot C_{mat} \tag{6.49}$$

$$T_W = \frac{p_{co} + p_{fe}}{\alpha_t \cdot S_{side\_stator}} + T_{amb} \tag{6.50}$$

$k_{ctemp} = 10$ is the over temperature penalty function coefficient, T_{amb} is the ambient temperature, α_t represents the equivalent heat transmission coefficient and S_{side_stator} is the areas of the stator surface which exchanges heat with the environment.

The efficiency can be improved during the optimization process by imposing an electric energy consumption cost which covers the motor losses during the machine total expected run time t_1, expressed as:

$$c_e = P_N\left(\frac{1}{\eta} - 1\right) \cdot t_1 \cdot p_e \tag{6.51}$$

with P_N - machine rated power, η – rated efficiency for a candidate, t_1- machine expected run time (10 years), p_e - energy price per kW/h.

A modified version of the efficiency penalty cost is used here (6.52), which accounts only for the energy consumption caused by operation characterized by an efficiency below the η_{min} minimum efficiency-imposed value.

Additionally, it is assumed that the motor operation will not always take place at rated speed (operation characterized by efficiency η_N), but most of the time it will operate at a lower speed and load (operation characterized by a lower efficiency η_1). Therefore, the η_1 efficiency is also included in the energy penalty cost.

$$c_e = \begin{cases} 0, \eta_N > \eta_1 > \eta_{min} \\ P_N \cdot k_{n1} \cdot \left(\dfrac{1}{\eta_1} - \dfrac{1}{\eta_{min}} \right) \cdot t_1 \cdot p_e, \eta_N > \eta_{min} > \eta_1 \\ P_N \cdot \left(\dfrac{k_{n1}}{\eta_1} + \dfrac{1 - k_{n1}}{\eta_N} - \dfrac{1}{\eta_{min}} \right) \cdot t_1 \cdot p_e, \eta_{min} > \eta_N > \eta_1 \end{cases} \tag{6.52}$$

with k_{n1} = 85% represents the percentage of time the motor operates at 44% of the rated speed.

6.4.2 Optimization process

The machine analytic design routine introduced in sections 6.3.1 - 6.3.5 is integrated into Hooke Jeeves optimal design algorithm. To make sure the optimum solution fulfills the design requirements, i.e., the analytic model is accurate enough to predict the motor performance, the iterative FEA based model correction mechanism presented in section 6.3.6 is additionally implemented. Fig. 6.7 presents the optimization process, which consists of the following steps:

Step 1: Analytic model-based optimal design run

An initial Hooke Jeeves algorithm-based optimization process takes place using the analytic outer rotor PMSM model in (6.1) – (6.42), for a randomly selected starting point, which leads to an optimum solution in terms of minimum cost.

Step 2: Optimum result FEA validation

A finite element model of the optimum solution is built and used for calculation of the following two parameters:

- T_{FEM} - the average electromagnetic torque value for rated load
- L_{FEM} - stator winding apparent inductance in rotor coordinates.

Using the analytically calculated values: T_a - based on (6.24), respectively L_a - based on (6.27), the recursive correction coefficients are calculated as:

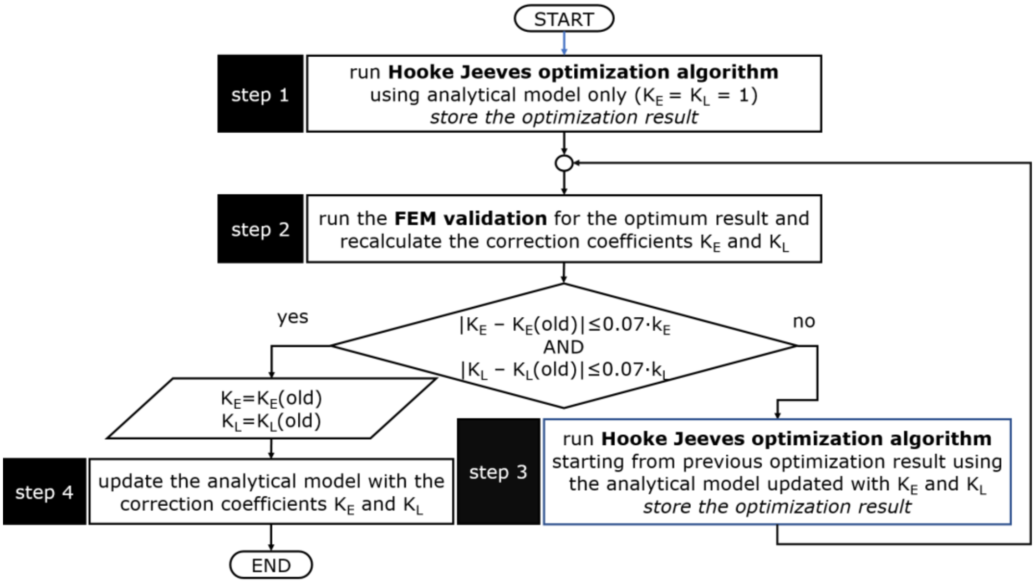

Fig. 6.7 The external rotor BLAC optimization process

$$K_E = K_{E(old)} + \frac{T_{FEM} - T_a}{T_a} \cdot k_E$$
$$K_L = K_{L(old)} + \frac{L_{FEM} - L_a}{L_a} \cdot k_L \qquad 6.53)$$

where "(old)" represents the older values, and k_E, k_L represent sub-relaxation factors, calibrated to a value of 0.3 (by trial and error) to control the correction convergence speed. The initial (old) value of the K_E and K_L correction coefficients is 1.

The rate of change of the correction coefficients provides an information on the mismatch between analytic/FEA values:

$$\left|K_E - K_{E(old)}\right| \leq 0.07 \cdot k_E$$
$$\left|K_L - K_{L(old)}\right| \leq 0.07 \cdot k_L \qquad (6.54)$$

If (6.54) conditions are true, i.e., the analytic/FEA values difference is equal to or below 7%, the analytic model is considered to be accurate enough and the optimization process is ended (Step 4). Otherwise, Step 3 is deployed.

The T_{FEM} calculation is done assuming a pure I_q vector control method. To further reduce the computation effort, the torque is calculated as an average value of FEA extracted torque values for only two rotor positions: $\theta_{rT_{min}}, \theta_{rT_{max}}$ corresponding to the maximum and minimum values of the total torque pulsations. These two rotor positions expressed as values within an electric period are selected from a lookup table as a function of current values of stator tooth span a_{sp} and rotor pole span a_{PM} design variables (the two design variables were observed to have the main impact on torque pulsation shape and min/max values position). The lookup table (Fig. 6.8) is constructed offline, prior to the optimization process by calculating the total torque pulsations by FEA for the entire exploratory range of α_{sp} and α_{PM} .

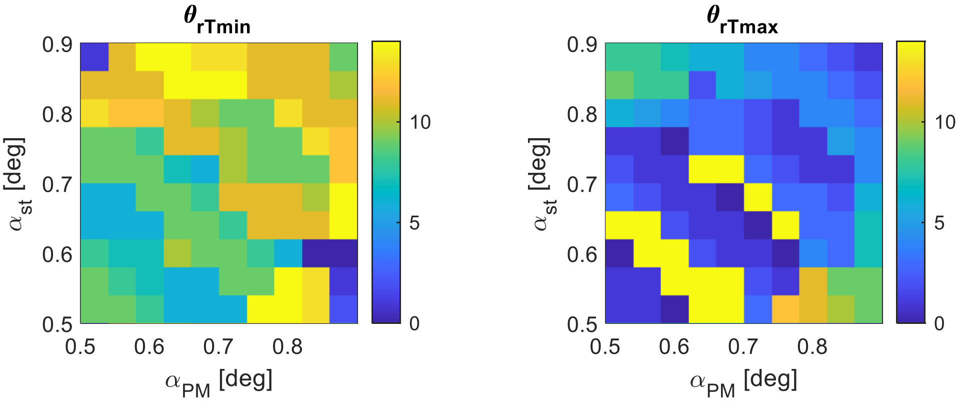

Fig. 6.8 The rotor positions withing an electric period corresponding to the minimum and maximum torque peaks

6.4.2.1 *Step 3: re-run the Hooke Jeeves algorithm with the corrected analytic model*

The analytic model-based Hooke Jeeves optimization is started again, with the previous optimum solution used as initial point. This time, the analytic values of the fundamental component of airgap flux per pole and stator inductance (6.22) and (6.28) are corrected as shown in section 6.3.6, using the updated FEM correction coefficients (6.53). After a new optimum solution is obtained, the optimization process returns to Step 2.

After a finite number of Step 2 - Step 3 iterations, the analytic model's results are expected to converge to the FEA calculated values, fulfilling the (6.54) conditions and ending the optimization process.

6.4.3 Optimization results

The design requirements for the outer-rotor PMSM motor are to maximize efficiency at rated 4500 rpm and 1 kW (targeting a household refrigerator compressor drive application) and to minimize the material cost. The continuous operating point for the motor is considered 2000 rpm, operating point which is also considered in objective function through the energy penalty cost. Additional constraints given by the compressor housing are imposed through the design variables limits (maximum rotor outer diameter and core stack length). No operation above the rated speed is required, therefore no flux weakening capabilities are needed.

The optimal design process presented in Fig. 6.7 was ran 20 times [79] (to ensure a better coverage of the searching space and increase the change of finding the global minimum). The total computation time is 176.7 minutes, which results in an average of 8.8 minutes per optimization process.

A short overview of the objective function evolution, optimization time duration per optimization step and the number of objective function evaluations per optimization step for the 20 optimization process deployments is shown in Fig. 6.9. Due to a few orders of magnitude differences within data, a part of the values is displayed on a different scale, having the axis placed on the right side of the graphics. The legend has the following meaning:

- *Initial:* f_{ob} value evaluated for the initial randomly chosen optimization starting point

- *Step: 1:* f_{ob} value, optimization time and number of f_{ob} evaluation for the initial analytic model-only optimization process.
- *Step:4:* f_{ob} value for the final optimum result
- *Step: 2/3:* run-time and number of f_{ob} evaluations during the iteratively FEA check - corrected analytic model-based optimization.

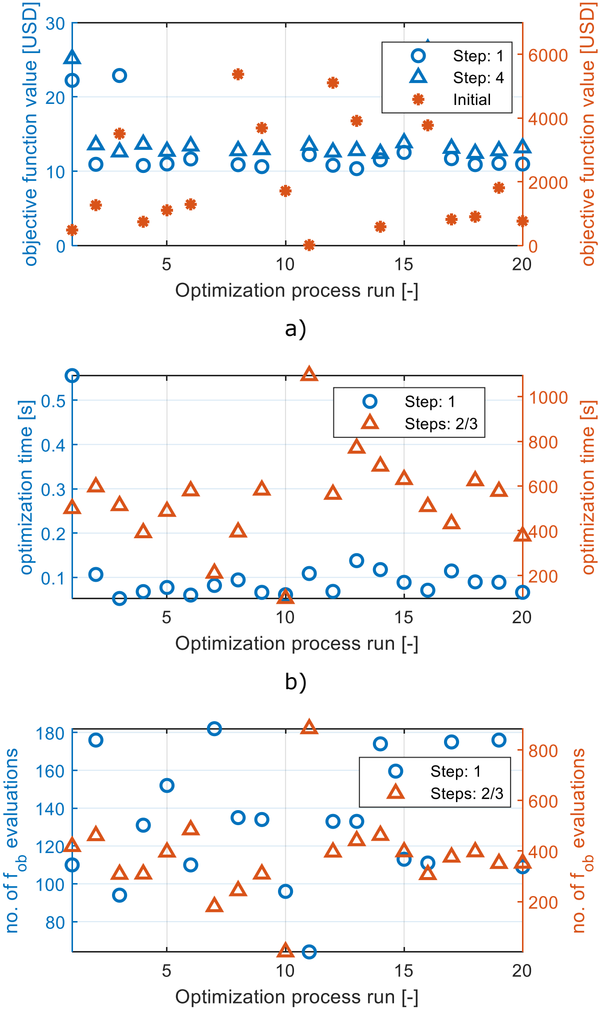

a)

b)

c)

Fig. 6.9 Results for the 20 runs of the optimization process, in terms of: a) objective function evolution per step, b) optimization time per step; c) number of objective function evaluations per step.

The objective function value after the Step 1 (analytic model optimization) is few orders of magnitude smaller than the objective function value for the starting candidate (randomly selected), proving the optimization algorithm effectiveness. However, after applying the analytic model correction, the final value of the objective function (Step 4, in Fig. 6.7, Fig. 6.9 a) shows a generally small increase in cost. The reasons are explained below.

The 13th optimization process run provides the best candidate after the optimization Step 1 stage (f_{ob} value: 10.34 \$). However, the 14th optimization process run (who's objective function value after the Step 1 was 11.52 \$ –Fig. 6.9) provides the best result for the objective function, after FEM correction (Step 4 stage): 12.38 \$ (whereas the final objective function value for the 13th candidate is 12.76 \$). This disproves the incorrect assumption in [80] that the best solution found by running multiple times the optimization process based only on the analytic model (Step 1) remains the best solution also after the correction of the analytic model. Therefore, the result of the 14th optimization process is considered the optimum solution.

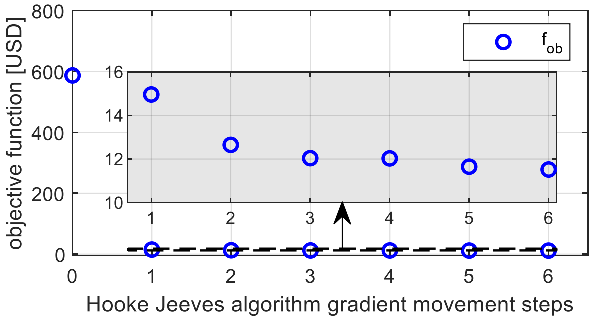

Fig. 6.10 Objective function evolution for the 14th optimization process run during analytic mode optimization (Step 1)

A detailed evolution of the optimal design variables and main electric/magnetic parameters values for the 14th candidate is presented in Fig. 6.11 and Table 6.3. The vertical dashed line separates the optimum result obtained by running the Hook Jeeves using analytic model only (Step 1 result - on the left side) from the successive optimization results obtained by running the Hooke Jeeves algorithm during FEM correction of the analytic mode (successive Step 3 results - on the right side).

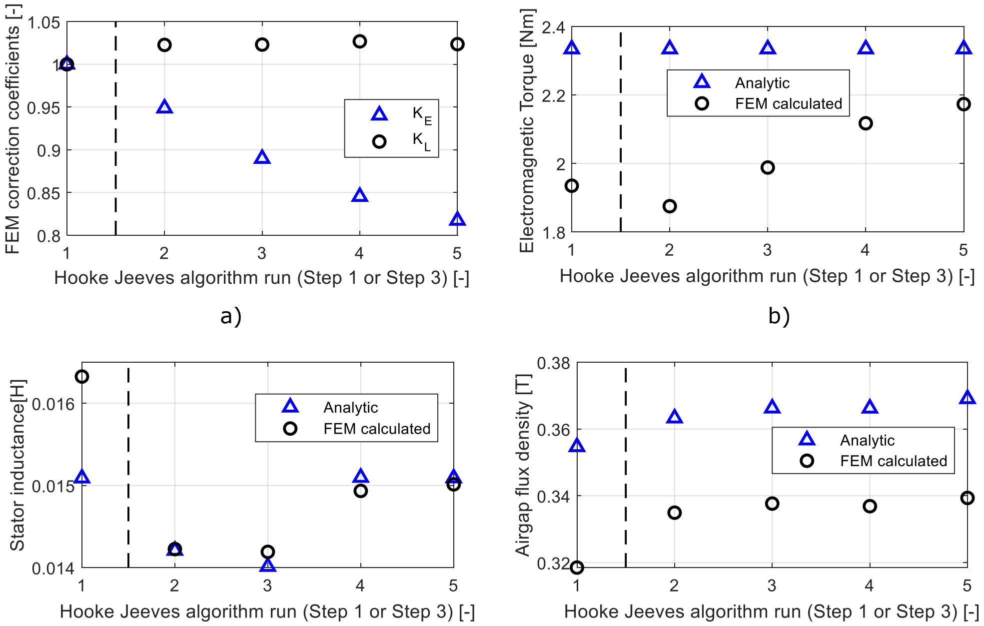

a) b)

c) d)

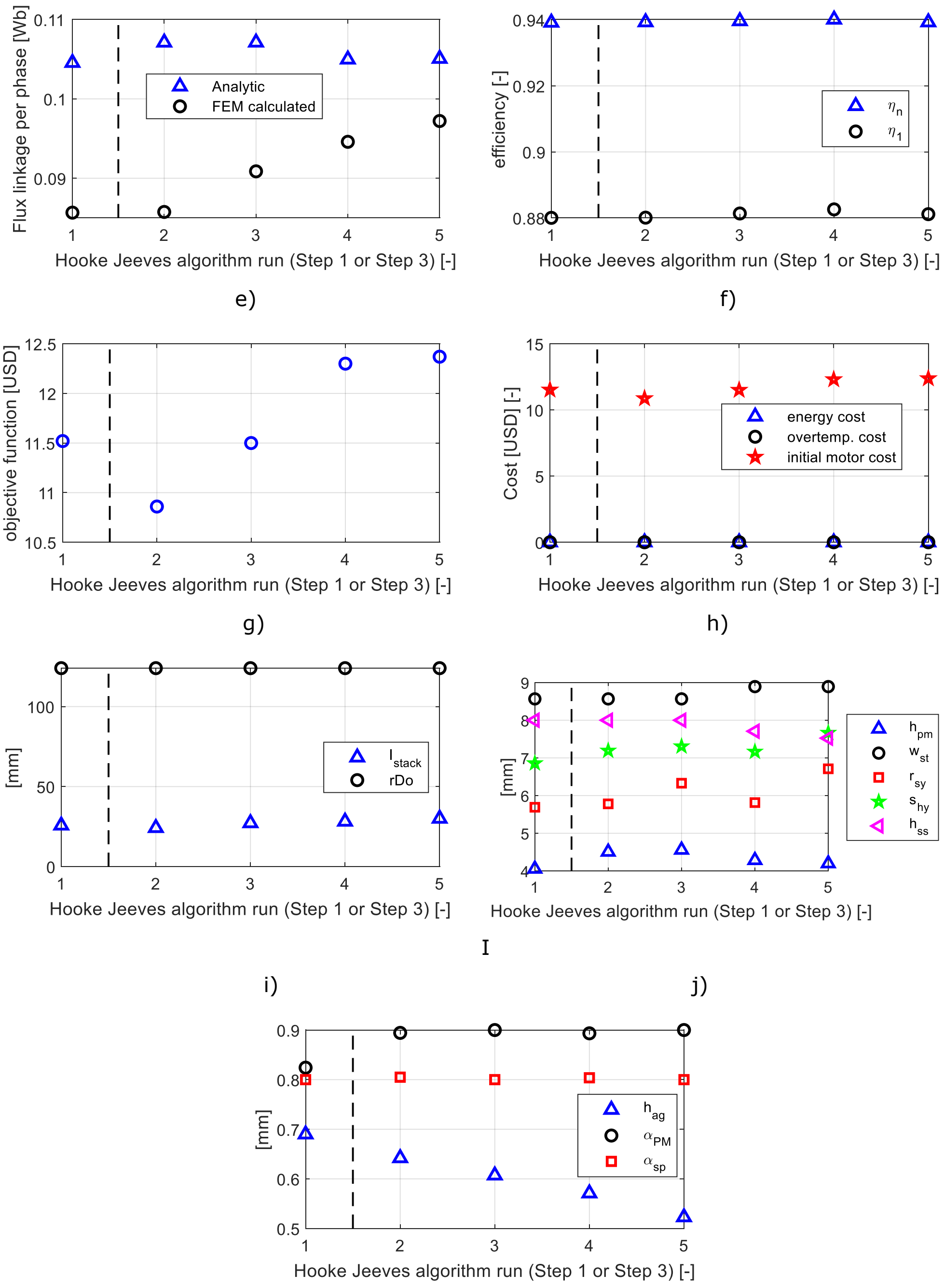

e) f)

g) h)

I

i) j)

k)

Fig. 6.11 Optimization process evolution of: a) FEM correction coefficients, b) electromagnetic torque, c) stator inductance, d) airgap flux density amplitude, e) flux linkage per phase, f) efficiency at rated load and rated speed and at low speed (0.44 p.u.), g) objective function, h) objective function components, i, j, k) optimal design variables

As expected, the differences between the analytic and FEA calculated values of stator winding inductance and electromagnetic torque value after initial optimization step were large enough to enable the iterative analytic model correction Fig. 6.11 b, c). After 5 Step 2 – Step 3 optimization iterations, this difference decreased below 7%, ending the optimization process. The evolution of the correction coefficients, displayed in Fig. 6.11 a, shows that:

- The PM flux per pole was largely overestimated in the analytical model leading to an initial optimum solution which could not produce the rated torque while being fed with the rated current. The K_E coefficient reduced the flux per pole amplitude in (6.44), forcing the design algorithm to find a solution for increase the analytic torque value, by reducing the airgap height h_{ag} value and by increasing the PM width a_{PM}, the stack length l_{stack} and the stator and rotor yokes: s_{hy}, rhy. These changes and few other increased the material cost with 0.86 \$ (7.3 %) and the motor mass with 0.3 kg.
- The stator winding inductance value calculated with the analytic model was only slightly underestimated.

Being placed in the airgap, the Ferrite PMs face the risk of demagnetization, due to their low coercive field. During optimization process, this risk was evaluated by analytically checking the airgap flux density for twice the rated current load.

$$B_g(2I_N) = \mu_0 \frac{2 \cdot mmf \cdot \sqrt{2}}{h_{ag} + h_{PM}} \tag{6.55}$$

The results (listed as $B_g(2I_N)$ values in Table 6.3), show no risk of demagnetization.

Table 6.3 Results for the 14th optimization process run

Parameter	Initial values	Best analytic model result (Step 1)	Final optimi-zation result (Step 4)	Description
E [Vrms]	106.25	131.68	132.33	EMF at rated speed
I_N [Arms]	3.45	2.68	2.77	rated current
λ_{PM} [Wb]	0.084	0.104	0.105	PM flux per phase
L_s [H]	0.017	0.015	0.015	winding total inductance
p_{co} [W]	54.78	44.48	43.7	rated copper loss
p_{fe} [W]	6.18	5.28	5.92	rated iron loss
η_N [-]	0.92	0.93	0.93	rated efficiency
η_1 [-]	0.86	0.88	0.88	efficiency at rated torque and 0.44 pu speed
B_g [T]	0.33	0.35	0.37	air-gap PM flux density
B_g ($2I_N$) [T]	0.316	0.221	0.204	airgap flux density for twice the rated current
r_{Do} [mm]	124	124	124	rotor outer diameter
s_{hy} [mm]	11.3	6.85	7.66	stator yoke width
r_{hy} [mm]	8.11	5.69	6.71	rotor yoke width
w_{st} [mm]	10.62	8.56	8.89	stator tooth width
h_{ag} [mm]	0.50	0.68	0.52	air-gap height
h_{PM} [mm]	3.66	4.05	4.19	PM height

l_{stack} [mm]	28.19	25.72	30	core stack length
h_{ss} [mm]	2.09	8	7.52	stator pole top height
α_{PM} [-]	0.9	0.82	0.9	PM width span relatively to the rotor pole span
a_{sp} [-]	0.8	0.8	0.8	stator tooth tip span relatively to the stator pole span
m_{motor} [kg]	1.46	1.40	1.55	motor total mass
c_e [\$]	100	0	0	energy loss cost
c_t [\$]	474.12	0	0	overtemperature cost
f_{ob} [\$]	586.89	11.52	12.38	objective function
t_{run} [s]	-	0.11	688	computation time
n_{fob_eval} [-]	1	174	462	number of objective function evaluations

6.5 FEM validation of the optimization results

The optimally designed motor was further analyzed using a finite element model (Fig. 6.12) under both no-load and on-load analysis. The cogging torque (Fig. 6.13 a) has a small amplitude, of less than 1% of the rated torque.

The EMF shape is closer to a trapezoidal shape, characteristic for concentrated windings, which suggests that trapezoidal current control is also be feasible. For obtaining best performance under sinusoidal control, additional PM skewing might have to be considered (e.g., by using segmented shifted PM pieces).

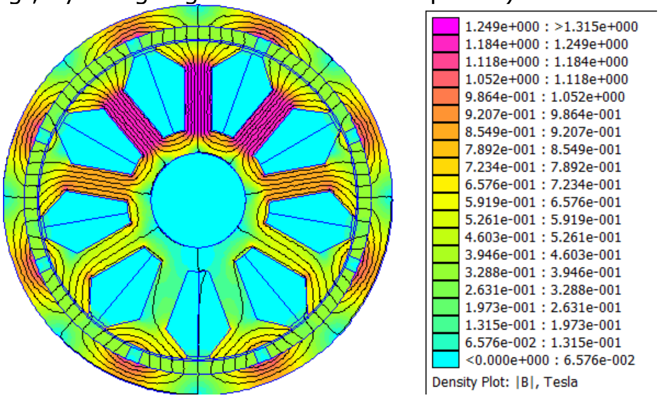

Fig. 6.12 Outer Ferrite PM rotor BLAC-motor FEM model: flux distribution under no load

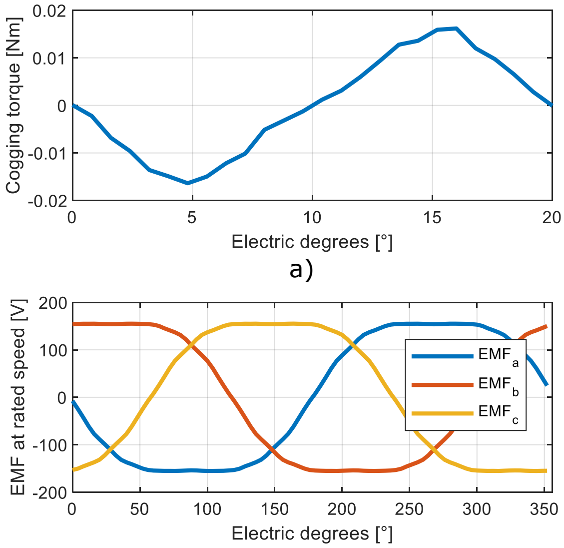

a)

b)

Fig. 6.13 No load finite element analysis results: a) cogging torque versus rotor position, b) EMF value per phase at rated speed versus rotor position

A sinusoidal control strategy was simulated for the load analysis, by imposing an I_q current equal to the rated current (2.77 A). Fig. 6.14 shows the total torque pulsations. The average value of 2.17 Nm is close to the T_{FEM} final value in Fig. 6.11 b, confirming the torque calculation method used during optimization Step 2.

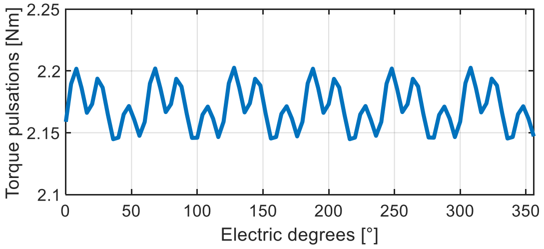

Fig. 6.14 Total torque pulsations for rated load

6.6 Experimental results

A few experimental results extracted from [79] are presented in this section, obtained by testing a prototype built based on former optimal design results. Fig. 6.15 shows the cup-like rotor, the stator core, and the assembled motor. Each rotor pole consists of two glued magnet pieces. Lower performance magnets, with a remnant flux density of 0.33 T were used for the prototype, whereas the design specifications considered $B_{r_{PM}}$ =0.45 T.

Fig. 6.15 BLAC exterior rotor prototype

The experimental results were checked against finite element analysis. To make the comparison possible, the finite element model's PM flux density was lowered to 0.33 T. The no load line to line back-EMF waveform for operation at 2000 rpm results show good agreement (Fig. 6.16).

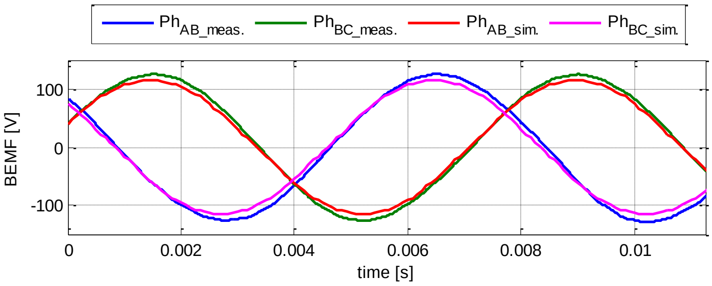

Fig. 6.16 Line to line EMF at 2000rpm: measured vs. FEA extracted values

The efficiency of the motor versus load torque was also analyzed via the analytic model, for several operating speeds and compared against the measured values, available only for operation at 2000 rpm. Additional torque/speed maps for calculated iron, copper losses and efficiency are displayed in Fig. 6.17. At 1.8 Nm (85% of the rated torque) the measured efficiency is 88.2%, while the calculated value is 1% less. The difference decreases as the load decreases. The following loss components were considered in the analytic calculation of the motor efficiency:

$$\eta = \frac{P_{out}}{P_{out} + p_{fe} + p_{co} + p_s + p_{mec}} \tag{6.56}$$

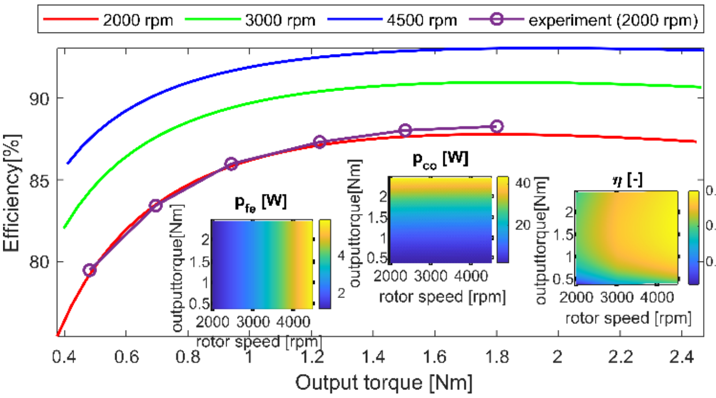

Fig. 6.17 Efficiency vs. torque

The mechanical losses were estimated to be 2% of the output rated power Pout (1000W at 4500rpm). An additional source of losses was included in efficiency calculation (Fig. 6.17), namely stray losses p_S, which were approximated to 1.5% of the output mechanical power. The eddy current losses in PM were neglected, given the higher resistivity of Ferrite and because the PMs have been segmented axially (further reducing these losses). Also, the skin effect was neglected in the calculation of the copper losses.

6.7 Conclusions

This chapter presented the optimal design for a 1 kW, 4500 rpm 3 phase outer rotor PMSM motor. An analytic model was built for electromagnetic design of the motor. To improve the model accuracy two key FEA based corrections were added, which iteratively correct the stator phase inductance and airgap flux analytic values during optimization process until the FEA and analytically computed values converge. The FEA use within the optimization process is reduced, keeping the optimization time to an acceptable value (approx. 8 minutes). A material cost objective function was used for design, with embedded penalty cost for overtemperature and small efficiency (operating at rated and reduced 0.44p.u. speed and load). Deployed 20 times from randomly selected initial points, the optimization process found an optimum meeting the penalty const constraints with a material cost of 12.57 $, FEA validation proving the motor's performance.

A few experimental results done on a previously designed prototype and published in [79] were presented. The FEA analysis matches rather well the measured data.

CHAPTER 7. V/F WITH STABILIZING LOOPS AND MTPA VERSUS SENSORLESS FOC FOR 3 PHASE PMSM DRIVES

Abstract

This chapter comparatively implements two sensorless control strategies for interior permanent magnet synchronous motor. The scalar V/f control strategy with stabilizing loops for voltage vector amplitude (based on d-axis current control for MTPA operation, expressed using magnetic energy formulation) and for voltage vector phase (based on active power oscillations) is presented and compared against the standard field-oriented control strategy. Both strategies use active flux-based position observer. The active flux observer is introduced and compared against other model-based position estimation strategies. Both control strategies are comparatively investigated by digital simulation and experimental test. It is shown that, while not matching the field-oriented control in terms of dynamic response and current control capabilities, the benefits brought by the stabilization loops and the easier implementation make scalar control a good candidate strategy for applications with less dynamic response requirements such as compressor pumps or fans motor applications.

7.1 Introduction

Permanent magnet synchronous motors (PMSMs) gained an important role in the industry due to their well-known advantages of high-power density, high efficiency, and due to advances in power electronics.

To operate at different rotor speeds throughout the operating range, variable speed drives are required for changing both the frequency and amplitude of the voltage supply.

The most common three phase variable speed drive topology uses a voltage source inverter composed by 3 half-bridge legs, each connecting one motor phase to either DC voltage (through the high-side power switch) or to ground (through the low side power switch).

Several strategies can be used to command of the voltage source inverters, to synthetize the reference voltages: space vector modulation (SVM), space PWM modulation (SPWM). Their output is a synchronized PWM command for the six power switches. The switching is done either at fixed frequency (PWM modulation – most common technique) or variable frequency (frequency modulation – optimizes the switching losses but introduces EMC related issues).

A variable speed drive control strategy produces a voltage reference (at given amplitude and frequency) with the purpose of controlling the motor speed or/and the torque. The PMSM control structures can be grouped in two major categories:

- **scalar control (V/f control or I-f control):** lower performance control strategy, mainly used for variable speed drives applications intended to operate at steady state most of their time. In its basic structure, it is an open loop control strategy, having the advantage of simplicity, at the cost of poor dynamic performance and instable operation. Due to its low complexity and lower computation requirements, it represents a good solution for driving pumps, fans and for refrigerating applications.
- **vector control**, which can be further split in:
    - the field-oriented control (FOC) or current vector control
    - the direct torque and flux control (DTFC) [81] [82]

The FOC and DTFC strategies are used in high-performance PMSMS drives which have high requirements on reference tracking and disturbance rejection. Their high performance comes with higher computation resources requirements and higher complexity, due to their higher number of parameters requiring tuning.

By not being subjected to fast reference or load changes and operating most of the time under steady state, the household refrigerator or air conditioning compressor applications are not demanding in terms of fast dynamic response. Therefore, with improvements in efficiency and stability, the scalar control strategies represent a good candidate for such applications.

7.2 Spoke-PMSM Mathematical Model

The Spoke-permanent magnet synchronous machine is an interior permanent magnet synchronous machine which has the permanent magnets distributed radially in the rotor core, in a star shape, bringing the benefit of flux concentration (as there are two permanent magnets to contribute to the magnetic flux per pole).

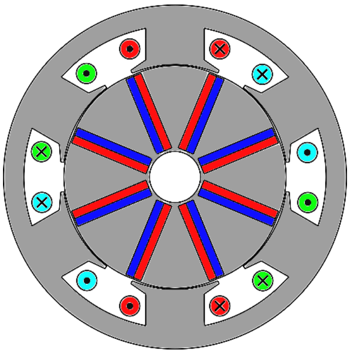

Fig. 7.1 Spoke-PMSM

By considering the following simplifications: only fundamental component is considered, thermal effect and saturation are neglected, influence of stator tooth slot, anisotropy is neglected, iron losses are neglected, the stator voltage equation in stator coordinates (denoted as $\alpha\beta$), in complex phasor representation writes as (Fig. 7.2):

$$\bar{v}_s^s = R_s \bar{i}_s^s + \frac{d\bar{\lambda}_s^s}{dt} \tag{7.1}$$

where:

$$\bar{v}_s^s = v_\alpha + jv_\beta = v_s \cdot \left(cos(\omega_e t + \theta_{v_s}) + j \cdot sin\left(\omega_e t + \theta_{v_s}\right)\right) \tag{7.2}$$

$$\bar{i}_s^s = i_\alpha + ji_\beta = i_s \cdot \left(cos(\omega_e t + \theta_{i_s}) + j \cdot sin\left(\omega_e t + \theta_{i_s}\right)\right) \tag{7.3}$$

$$\bar{\lambda}_s^s = \lambda_\alpha + j\lambda_\beta = \lambda_s \cdot \left(cos(\omega_e t + \theta_{\lambda_s}) + j \cdot sin\left(\omega_e t + \theta_{\lambda_s}\right)\right) \tag{7.4}$$

$$\theta_{v_s} = \theta_{i_s} + \varphi \tag{7.5}$$

's' subscript denotes stator winding related electric variables, while 's' superscript denotes fixed, stator reference system. j represents the complex unit and ω_e represents the angular speed of the phasor quantities.

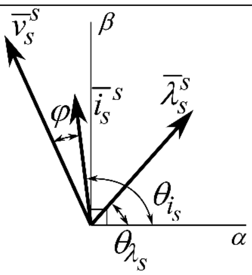

Fig. 7.2 Stator voltage equation phasors in complex reference frame

The stator magnetic flux, stator coordinates can be break-down into:

$$\bar{\lambda}_s^s = \bar{L}_s \cdot \bar{i}_s^s + \bar{\lambda}_{PM}^s \tag{7.6}$$

where the $\bar{L}_s$ represents a complex inductance term and $\bar{\lambda}_{PM}^s$ represents flux component produced by the permanent magnet placed in the rotor. Both terms are dependent on rotor position.

Since all the electric signals have a sinusoidal variation (of ω_e angular velocity) and also since the motor winding inductance and PM flux show a variation dependent to rotor position (also sinusoidal, or including a sinusoidal component, for constant rotor speed), it is convenient to translate them in a reference system which rotates synchronously with the rotor electric speed (the so-called dq reference system).

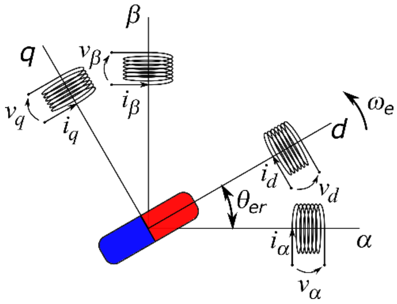

Fig. 7.3 The fixed αβ coordinate system versus the rotating dq coordinate system

By defining the rotor electric position as:

$$\theta_{er}(t) = \int \omega_e \cdot dt + \theta_{e_0} \tag{7.7}$$

where θ_{e_0} represents the initial position (the initial angle between axis d and axis α), the translation of the space phasors from fixed stator coordinates to rotating rotor synchronous coordinates is done as follows ('r' superscript denotes the rotor reference system):

$$\begin{aligned} \bar{i}_s^r &= \bar{i}_s^s \cdot e^{-j\theta_e} = i_d + j \cdot i_q \\ \bar{v}_s^r &= \bar{v}_s^s \cdot e^{-j\theta_e} = v_d + j \cdot v_q \\ \bar{\lambda}_s^r &= \bar{\lambda}_s^s \cdot e^{-j\theta_e} = \lambda_d + \lambda \cdot i_q \end{aligned} \tag{7.8}$$

The coordinate system translation preserves the current amplitude and number of turns per coil ($\left|\bar{i}_s^s\right| = \left|\bar{i}_s^r\right|$).

Thus, in the rotating coordinate frame, the stator voltage equation expression simplifies:

$$\bar{v}_s^r = R_s \cdot \bar{i}_s^r + \frac{d\bar{\lambda}_s^r}{dt} + j\omega_e \cdot \bar{\lambda}_s^r \tag{7.9}$$

Where the stator linkage phasor is expressed as:

$$\bar{\lambda}_s^r = L_d \cdot i_d + \lambda_{PM} + j \cdot L_q \cdot i_q \tag{7.10}$$

L_d represents the d-axis winding inductance, L_q – represents the q-axis winding inductance and λ_{PM} represents the PM flux linkage amplitude. Fig. 7.4 shows the phasor diagram of the stator voltage equation in rotor reference system, relevant for steady state operation $\left(\frac{d\bar{\lambda}_s^r}{dt} = 0\right)$.

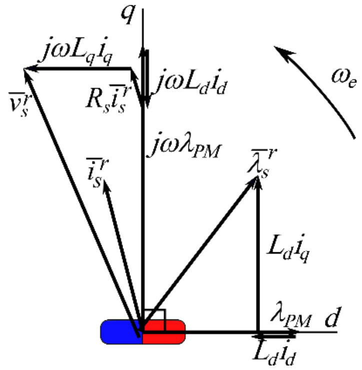

Fig. 7.4 PMSMS stator voltage equation phasor diagram in rotor reference system

The electromagnetic torque is defined as [36]:

$$\begin{aligned} T_e &= \frac{3}{2} p \cdot Im\left\{\bar{i}_s^r \cdot \bar{\lambda}_s^{r*}\right\} \\ &= \frac{3}{2} p \cdot \left(\lambda_d i_q - \lambda_q i_d\right) \\ &= \frac{3}{2} p \left(\lambda_{PM} + \left(L_d - L_q\right) i_d\right) i_q \end{aligned} \tag{7.11}$$

where p represents the number of rotor pole pairs, $Im\{x\}$ is the imaginary part of x complex number and '*' superscript denotes the conjugate of a complex number. (7.11) shows that there are two torque producing components: the PM flux component, and the reluctance component (which varies linearly to the $L_d - L_q$ difference). For the spoke-PMSM motor, $L_q > L_d$, therefore, to benefit of torque increase due to machine saliency, a negative d-axis current must be prescribed by the control algorithm.

7.3 Strategies for estimating the rotor position

The topic of estimating the rotor position and speed received much attention in the last three decades, as these strategies can either replace mechanical/electronic sensor in not very-high performant drive application, for benefits such as cost reduction and downsizing. For high performance drives, the position/speed estimation strategies provide plausibility and redundancy for encoder/resolver/hall sensors.

These position estimation strategies fall under two main categories [83] [84]: fundamental model-based methods and saliency-based methods (signal injection-based methods). The first group will be detailed in the following section.

7.3.1 Fundamental model-based observer methods

These methods are used at medium-high speeds [83] [84] [85] [86] [87] [88] [89] [90] and employ the machine mathematical model to estimate the rotor position. The model can be expressed either in stationary frame or in synchronous frame (estimated rotor position frame) [91]. D. Xu et al [84] divided the general structure of model-based position estimation algorithms into the following parts (Fig. 7.5)

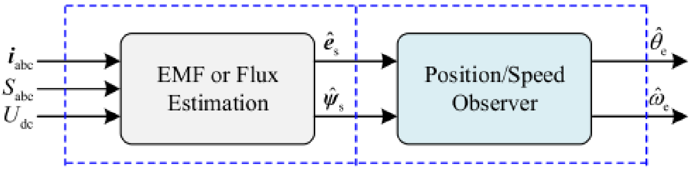

Fig. 7.5 Generic structure of model-based position estimation algorithms [84]

The first part makes use of the machine model to estimate the stator EMF or stator magnetic flux. The right-side part extracts the position information from the estimated flux or EMF vectors.

A short introduction of two of the most common model-based observers is presented below.

a) Active Flux based method

The "active flux" or torque producing flux concept was developed and introduced by Boldea et al [92] for all ac drives. It is a fictitious flux quantity which is always oriented along the rotor d-axis. This reduces the problem of estimating the rotor position to the problem of determining the active flux phasor position.

The active flux is defined as the quantity which multiplies the q-axis current in the electromagnetic torque expression (7.11). For an IPMSM, the expression of the active flux amplitude is:

$$\lambda_a = \lambda_{PM} + \left(L_d - L_q\right) \cdot i_d \tag{7.12}$$

Using active flux, the torque expression for an IPMSM becomes similar to the torque expression of a SPMSM, that is the machine "loses its salient feature" and gains the advantage of SPMSM in simplicity of rotor position estimation.

$$T_e = \frac{3}{2} p \lambda_a \cdot i_q \tag{7.13}$$

In stator coordinates, the phasor expression of the active flux is:

$$\bar{\lambda}_a^s = \bar{\lambda}_s^s - L_q \cdot \bar{i}_s^s \tag{7.14}$$

As shown in Fig. 7.6, $\bar{\lambda}_a^s$ is positioned along the rotary reference system's d-axis. Therefore, its position θ_{λ_a} is at the same time the rotor electric position θ_{er} .

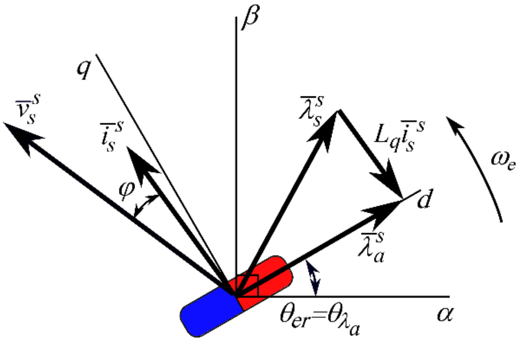

Fig. 7.6 Active flux observer phasor vector calculation and position relative to stationary/rotary coordinates

A straightforward way to calculate the active flux phasor is to determine the stator flux in stator coordinates using stator voltage equation (7.1), followed by the active flux calculation using (7.15). The main issue with this method resides in using the voltage discrete integration operation, necessary for calculating the stator magnetic flux phasor, which can lead to offset accumulation, especially due to offset presence in measured current and motor parameter estimation inaccuracies. To overcome these problems, the active flux observer has been enhanced with a compensation feedback mechanism (Fig. 5.9), which combines a “voltage model” with a “current model” in similar fashion to the Gopinath observers, proposed for induction motor rotor flux estimation [93]. The active flux phasor expression becomes:

$$\hat{\bar{\lambda}}_a^s = \int\left(\bar{v}_s^{s*} - R_s \cdot \bar{i}_s^s - \bar{v}_{comp}^s\right)\cdot dt - L_q \cdot \bar{i}_s^s = \bar{\lambda}_s^s - L_q \cdot \bar{i}_s^s \tag{7.15}$$

where $\bar{v}_s^{s*}$ is the stator voltage reference value in stator coordinates and $\bar{v}_{comp}^s$ is the voltage compensation value of the active flux observer.

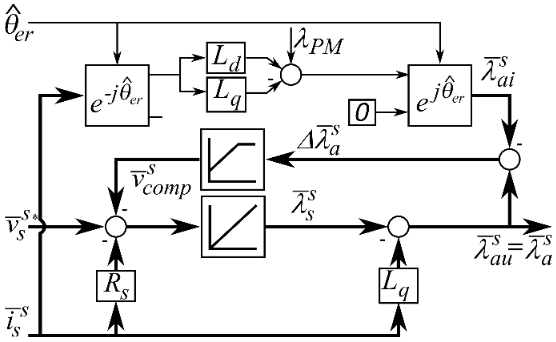

Fig. 7.7 Active flux observer (the parallel model)

The compensation voltage is calculated using a proportional-integrator compensator, which is fed by the difference between the active flux calculated using the “voltage model” (7.15) – lower part in Fig. 7.7- and the active flux calculated using the “current mode” (active flux calculated in rotor coordinates and then translated to stator coordinates using rotor estimated position) – upper part in Fig. 7.7:

$$\bar{v}_{comp}^s = \left(k_p + k_i \cdot \frac{1}{s}\right)\left(\bar{\lambda}_{au}^s - \bar{\lambda}_{ai}^s\right) \tag{7.16}$$

k_p and k_i are the proportional integrator compensator coefficients.

The compensator coefficients values can be calculated using pole placing method:

$$\begin{aligned} k_{pc} &= \omega_1 + \omega_2 \\ k_{ic} &= \omega_1 \cdot \omega_2 \end{aligned} \tag{7.17}$$

They characterize the observer frequency behavior, which depends on the chosen poles ω_1, ω_2 ($\omega_1 \le \omega_2$) as follows. At low speeds ($\omega < \omega_1$), the active flux estimation based on the current model becomes dominant, whereas the voltage model dominates and at medium-high speeds ($\omega > \omega_2$).

b) Emf based method

This method estimates the extended EMF vector position (a fictitious voltage quantity, with similar properties as the fictitious active flux quantity), which is then used for determining the rotor position. The concept will be presented using the matrix form of PMSM model, for simplicity. Expanding (7.8) into matrix form (an equation for each axis), the PMSM model can be written as:

$$\begin{bmatrix} v_d \\ v_q \end{bmatrix} = \begin{bmatrix} R_s + pL_d & -\omega_e L_q \\ -\omega_e L_d & R_s + pL_q \end{bmatrix} \begin{bmatrix} i_d \\ i_q \end{bmatrix} + \begin{bmatrix} 0 \\ \omega_e \lambda_{PM} \end{bmatrix} \tag{7.18}$$

where $\omega_e \cdot \lambda_{PM}$ term represents the EMF value. This model cannot be used, as the rotor position and speed are presumably not known. Rewritten into stationary αβ coordinates, (7.18) translates into:

$$\begin{bmatrix} v_\alpha \\ v_\beta \end{bmatrix} = \begin{bmatrix} R_s + p\left(L_0 + L_1 \cos(2\theta_{er})\right) & p\left(L_1 \sin(2\theta_{er})\right) \\ p\left(L_1 \sin 2(\theta_{er})\right) & R_s + p\left(L_0 - L_1 \cos(2\theta_{er})\right) \end{bmatrix} \begin{bmatrix} i_\alpha \\ i_\beta \end{bmatrix} + \omega_e \lambda_{PM} \begin{bmatrix} -\sin(\theta_{er}) \\ \cos(\theta_{er}) \end{bmatrix} \tag{7.19}$$

$$L_0 = \frac{L_d + L_q}{2}; L_1 = \frac{L_d - L_q}{2}$$

where p represents the differential operation (applied on both motor parameter matrix and stator currents i_α, i_β). Is visible in (7.19) that the rotor position information is present in both the inductance values and EMF term. However, using this model for extracting the position information is not straightforward, due to the presence of $2\theta_{er}$ terms in the stator winding inductance terms. For a non-salient machine, where $L_d = L_q = L_s$, the model greatly simplifies to:

$$\begin{bmatrix} v_\alpha \\ v_\beta \end{bmatrix} = \begin{bmatrix} R_s + pL_s & 0 \\ 0 & R_s + pL_s \end{bmatrix} \begin{bmatrix} i_\alpha \\ i_\beta \end{bmatrix} + \omega_e \lambda_{PM} \begin{bmatrix} -\sin(\theta_{er}) \\ \cos(\theta_{er}) \end{bmatrix} \tag{7.20}$$

Using (5.13), and reference voltages phasor $\bar{v}_s^{s*} = v_\alpha^* + j \cdot v_\beta^*$, instead of the actual phase voltage phasor $\bar{v}_s^s$, together with measured current value $\bar{i}_s^s$, the EMF calculation is straightforward.

For the salient PMSMs, the model can be mathematically manipulated in such way to eliminate the $2\theta_{er}$ terms. By defining the following fictive voltage quantity:

$$E_{ex} = \omega_r \left(\lambda_{PM} + \left(L_d - L_q\right) i_d\right) + \frac{di_q}{dt}\left(L_d - L_q\right) \tag{7.21}$$

and introducing it into (7.19), the model in stationary coordinates greatly simplifies to a form which resembles the synchronous coordinates form (7.20):

$$\begin{bmatrix} v_\alpha \\ v_\beta \end{bmatrix} = \begin{bmatrix} R_s + pL_d & -\omega_e\left(L_q - L_q\right) \\ -\omega_e\left(L_d - L_q\right) & R_s + pL_d \end{bmatrix} \begin{bmatrix} i_\alpha \\ i_\beta \end{bmatrix} + E_{ex} \begin{bmatrix} -\sin\left(\theta_{er}\right) \\ \cos\left(\theta_{er}\right) \end{bmatrix} \tag{7.22}$$

The E_{ex} term is called extended emf. Its phasor is aligned with the EMF phasor (90 electrical degrees in advance to permanent magnet axis) and can be used to determine the rotor position [94] [95].

$$\bar{e}_{ex}^{s} = E_{ex}\left(-\sin\left(\theta_{er}\right) + j\cos\left(\theta_{er}\right)\right) = E_{ex}.e^{j\left(\theta_{er}+\frac{\pi}{2}\right)} \tag{7.23}$$

The same substitution can be performed also on the machine model expressed in rotor coordinates system yielding:

$$\begin{bmatrix} v_d \\ v_q \end{bmatrix} = \begin{bmatrix} R_s + pL_d & -\omega_e Lq \\ -\omega_e Lq & R_s + pL_d \end{bmatrix} \begin{bmatrix} i_d \\ i_q \end{bmatrix} + E_{ex} \begin{bmatrix} 0 \\ 1 \end{bmatrix} \tag{7.24}$$

Although this model cannot be used directly, since it needs the knowledge of rotor position θ_{er} a different rotating coordinate system can be considered: $\gamma\delta$ (Fig. 7.8), which rotates with $\hat{\omega}_e$ estimated speed and it is phase shifted to dq frame by $\Delta\theta_{er} = \theta_{er} - \hat{\theta}_{er}$ - the position estimation error (where $\hat{\theta}_{er}$ is the estimated position) [96].

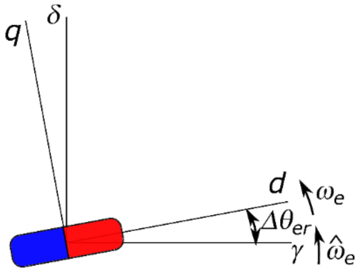

Fig. 7.8 γδ rotating reference system (estimated position frame)

The PMSM mathematical model in $\gamma\delta$, using the extended EMF can be written as:

$$\begin{bmatrix} v_\gamma \\ v_\delta \end{bmatrix} = \begin{bmatrix} R_s + pL_d & -\omega_e L_q \\ -\omega_e L_q & R_s + pL_d \end{bmatrix} \begin{bmatrix} i_\gamma \\ i_\delta \end{bmatrix} + \begin{bmatrix} e_\gamma \\ e_\delta \end{bmatrix}$$
$$\begin{bmatrix} e_\gamma \\ e_\delta \end{bmatrix} = E_{ex} \begin{bmatrix} -\sin\left(\Delta\theta_{er}\right) \\ \cos\left(\Delta\theta_{er}\right) \end{bmatrix} + \left(\hat{\omega}_e - \omega_e\right) L_d \begin{bmatrix} -i_\delta \\ i_\gamma \end{bmatrix} \tag{7.25}$$

The second term in definition of extended EMF, which depends on speed estimation error is usually neglected, as it is considered that the estimated speed is close to the real one. In this case, the EEMF phasor in $\gamma\delta$ is written as:

$$\bar{e}_{es}^{\hat{r}} = e_\gamma + je_\delta = \bar{e}_{es}^{r} \cdot e^{j\Delta\theta_e} \tag{7.26}$$

The extended emf estimation strategies deal with the estimation of $\bar{e}_{es}^{\hat{r}}$, for estimators in rotating frame, respectively $\bar{e}_{es}^{s}$, for estimators expressed in stator frame.

Several methods have been proposed for the estimation of the EEMF: based on disturbance observer in rotating frame [96] or in stator frame [94], based on state filter, using current error-based compensator [95], based on sliding mode observer [97] [98], strategy which can use reduced or full order observer models.

A disturbance observer-based estimation of the EEMF is shown in Fig. 7.9 [96]. The observer inputs are the reference voltage command and the measured current. The EEMF is considered the system disturbance to be estimated. For this, the voltage drop on the stator winding is computed ("process" inverse transfer function). The "s" derivative operation can be replaced by a high pass filter, to remove sharp changes (especially during sudden load changes). The extended emf phasor is filtered using a low pass filter. The filter gain must be selected according to the desired observer's bandwidth.

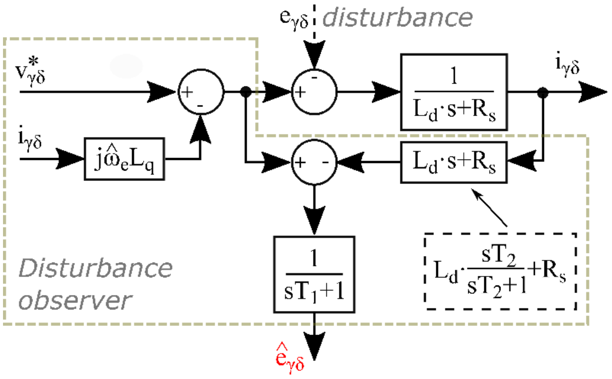

Fig. 7.9 Disturbance observer (based on [96])

Being expressed in rotor estimated coordinates, the output of this estimator is the EEMF phasor in real rotor coordinated system, phase shifted by the rotor position estimation error.

c) Position-Speed Estimators

Beside flux or emf estimators, the other important component of a model-based rotor position observer is the mechanical observer, or position/speed tracker. Its inputs are the emf (extended) in stator/estimated rotor coordinates or the active flux in stator coordinates, while its outputs are the rotor speed and position. There are several methods of tracking the rotor position:

d)Direct calculation

The phasor's position can then be extracted using inverse tangent trigonometric function, for extended emf estimator

$$\hat{\theta}_{er} = tan^{-1}\left(-\frac{e_\alpha}{e_\beta}\right) \tag{7.27}$$

and for active flux estimator:

$$\hat{\theta}_{er} = tan^{-1}\left(\frac{\lambda^s_{a\beta}}{\lambda^s_{a\alpha}}\right) \tag{7.28}$$

The rotor speed can be calculated by taking the derivative of the rotor position (by differentiation of the inverse tangent function, using the quotient rule for the active flux components ratio differentiation). For the active flux observer:

$$\hat{\omega}_r = \frac{d\hat{\theta}_{er}}{dt} = \frac{\lambda^s_{a\alpha[n-1]} \cdot \lambda^s_{a\beta[n]} - \lambda^s_{a\beta[n-1]} \cdot \lambda^s_{a\alpha[n]}}{h \cdot \left(\left(\lambda^s_{a\alpha[n]} \right)^2 + \left(\lambda^s_{a\beta[n]} \right)^2 \right)} \tag{7.29}$$

where h is the sampling period, $\left[n\right]$ index denotes the current values while $\left[n-1\right]$ denotes the previous calculated value.

The main advantages of this method are simplicity and the no-delay added to the speed signal. The main disadvantage is the noise it introduced by differentiation operation (a low pass filter is needed to attenuate it, which cancels the second benefit).

e) PLL mechanical tracking observer

Another widely used option is the phase look loop observer. Its inputs are the active flux/extended emf components in $\alpha\beta$ coordinates, normalized, or the extended emf error in estimated rotor coordinates (Fig. 7.10):

$$\Delta\theta_{er} = \tan^{-1}\left(-\frac{e_\gamma}{e_\delta} \right) \tag{7.30}$$

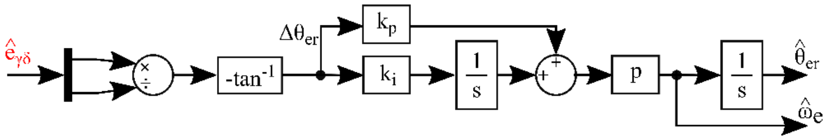

Fig. 7.10 PLL structure for estimating the rotor position and speed from the extended emf vector

Having the structure of a filter, it inherently introduces a delay in the observed position and speed. Observer structures including mechanical equation-based angle tracker [89] [99], capable of estimating the load torque and load disturbance rejection were also proposed in the literature.

7.3.2 Simulation of the speed/position estimators

The active flux observer in Fig. 7.7 was simulated, using an encoder based close loop field-oriented control strategy, which will be presented later. The IPMSM motor parameters are introduced in Table 7.1. Simplified MATLAB Simulink models for the active flux observer (AFO) and extended EMF observer (EEMFO) are shown in Fig. 7.11, respectively Fig. 7.12. The disturbance observer based extended emf observer in Fig. 7.9 is coupled with the PLL rotor position/speed tracker in Fig. 7.10, whereas the active flux observer uses direct position calculation, based on inverse tangent method. Both models are fed with the stator reference voltage and currents, in stator coordinates $\alpha\beta$, shown in Fig. 7.13. The field-oriented control uses the encoder provided position information; the two position observers not being involved in the close loop control.

Table 7.1 Parameters of the Spoke-PMSM

Parameter	Value
DC voltage V_{DC} [V]	280
output power P_n [W]	1000
rated current I_n [A]	3.4
pole pairs p	4
rated speed ω_N [rpm]	4500
d-axis inductance L_d [H]	0.013
q-axis inductance L_q [H]	0.016

stator phase resistance R_s [Ω]	1
PM flux λ_{PM} [Wb]	0.06
Rotor moment of inertia J [kg·m^2]	0.0017
Viscous friction coefficient B	0.0015

An operation profile consisting of acceleration to 2000 rpm, followed by step load to 1 Nm, at t = 0.55 s is prescribed. The sample time for both motor model and control model are $10\mu s$. Fig. 7.14 shows the simulation results.

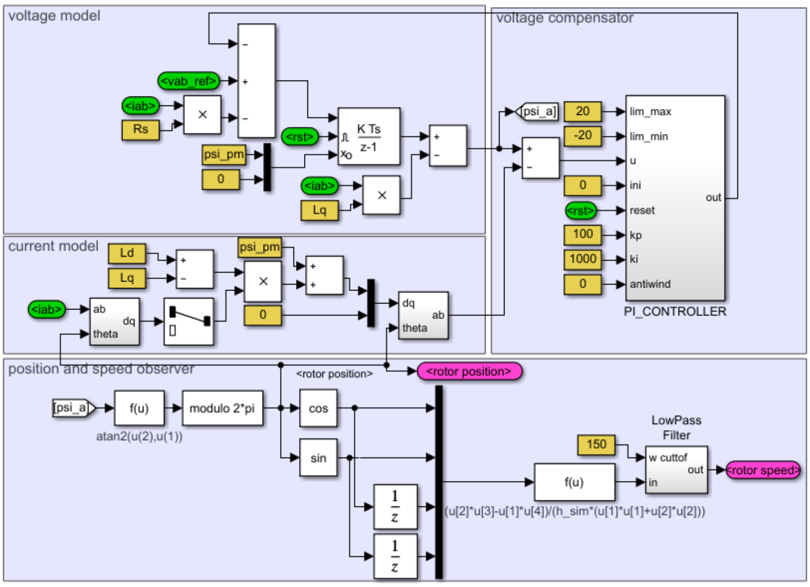

Fig. 7.11 Active flux observer model

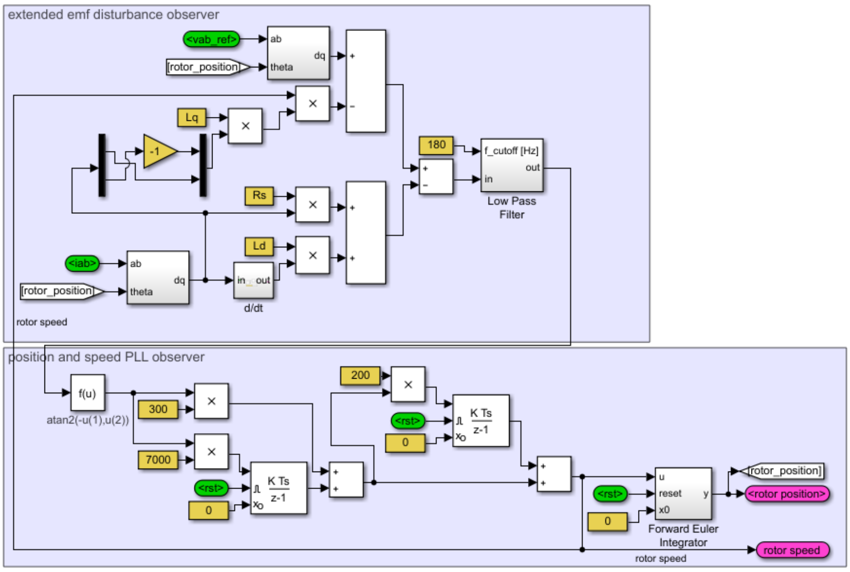

Fig. 7.12 Extended emf observer model

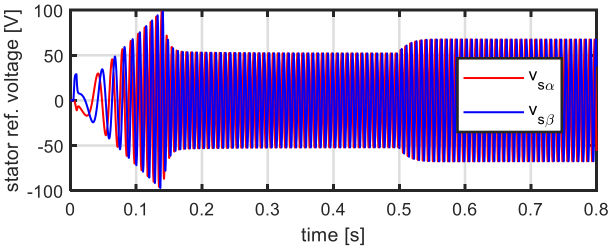

a)

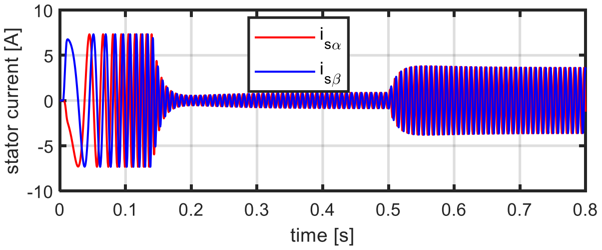

b)

Fig. 7.13 Inputs for the observers simulation: a) stator reference voltage, b) stator current, in stator coordinates

The estimates of the speed follow the real speed (denoted with ENC, in Fig. Fig. 7.14 a), the active flux observer response to speed variation being sensibly slower. The maximum position estimation error is larger for the EEMFO, the AFO the position estimation being less affected by load changes, with respect to EEMFO, which shows a transient deviation of 1.5° electric. Both observers show a constant position estimation error of less than 1° electric.

As visible in Fig. 7.14 e, the extended emf phasor is aligned along δ rotating axis, the role of the PLL observer being to force the γ phasor component to 0. Although not implemented here, real application implementations of the EEMFO can use a high pass filter instead of the differentiation operation, which can have the same cutoff frequency as the low-pass filter filtering the observed $\hat{e}_{\gamma\delta}$. Using a differentiation operator amplifies the current oscillations, introducing noises in the estimated voltage.

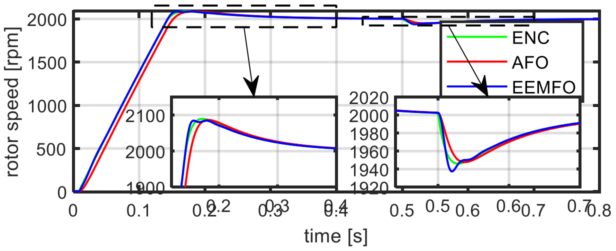

a)

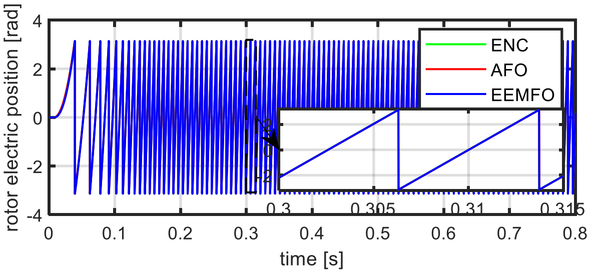
rotor electric position [rad]
4
2
0
-2
-4
0
0.1
0.2
0.3
0.4
0.5
0.6
0.7
0.8
time [s]
ENC
AFO
EEMFO
0.3
0.305
0.31
0.315

b)

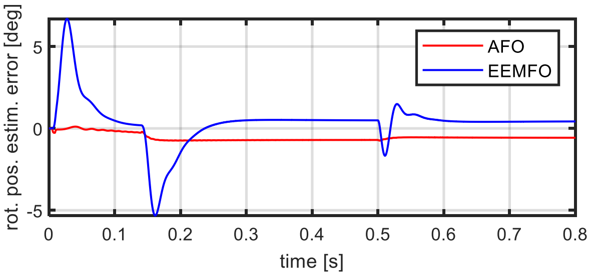
rot. pos. estim. error [deg]
5
0
-5
0
0.1
0.2
0.3
0.4
0.5
0.6
0.7
0.8
time [s]
AFO
EEMFO

c)

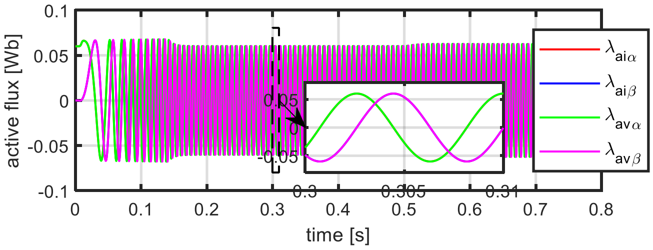
active flux [Wb]
0.1
0.05
0
-0.05
-0.1
0
0.1
0.2
0.3
0.4
0.5
0.6
0.7
0.8
time [s]
0.05
0
-0.05
0.3
0.305
0.31
$\lambda_{ai\alpha}$
$\lambda_{ai\beta}$
$\lambda_{av\alpha}$
$\lambda_{av\beta}$

d)

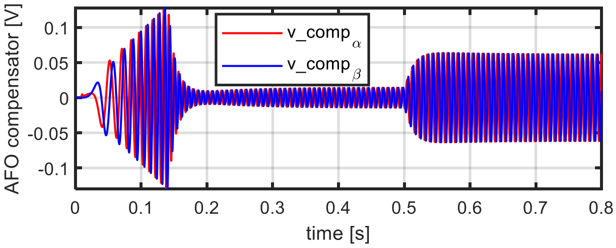
AFO compensator [V]
0.1
0.05
0
-0.05
-0.1
0
0.1
0.2
0.3
0.4
0.5
0.6
0.7
0.8
time [s]
v_comp$_\alpha$
v_comp$_\beta$

e)

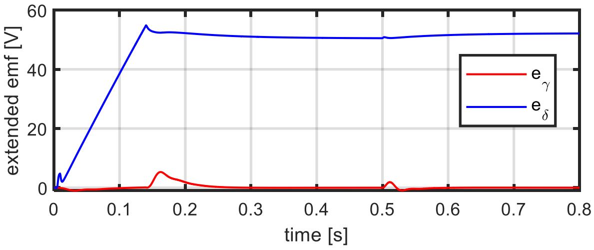

f)

Fig. 7.14 Simulation results: a) rotor speed, b) rotor position, c) rotor position estimation error, d) active flux components in stator coordinates for both current and voltage models, e) active flux observer compensator model, f) extended emf components in γδ rotating frame

7.4 Sensorless control of the IPMSM

Two control strategies were studied and implemented for sensorless speed control of the spoke-IPMSM: a V/f scalar control strategy, coupled with stabilizing loop and the classic rotor field-oriented control. Both are presented in the following subsections.

7.4.1 Scalar V/f control with stabilizing loops

The scalar V/f control for PMSMs represents a sensorless open loop control strategy which feeds the motor with a 3-phase voltage system whose amplitude linearly varies with its frequency, ensuring in this way a constant stator magnetic flux amplitude, necessary for maintaining the load capability through the entire speed range. Fig. 7.15 show a simplified control scheme, employed for PMSMs control. The PM flux linkage represents the proportionality constant between the reference speed and reference voltage. To avoid synchronization loss, a reference speed change rate limitation is needed. A small voltage offset value V_0 is added to the reference voltage amplitude to compensate the voltage drop on winding resistance. The reference voltage angle is directly calculated by integrating the rate limited reference speed. Finally, polar-to-cartesian coordinate translation is used for calculating the reference voltage in stator coordinates.

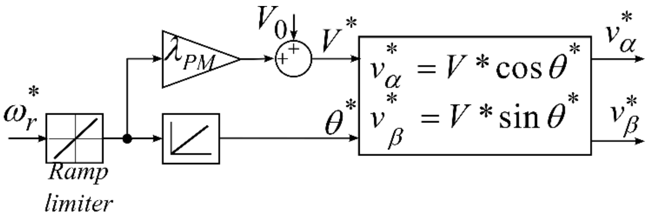

Fig. 7.15 Standard V/f control scheme

While the simplicity and low implementation cost represent its main advantage (no rotor position information is not needed and no AC or DC current controllers or reference system transformation are required), the open loop nature of the standard V/f control shows low dynamic performance and unstable operation during reference speed change or load perturbations, especially when it is employed for controlling PMSMs. To improve these shortcomings, the standard control strategy has been enhanced with stabilizing (or correction or compensation) loops, for both reference voltage amplitude V^* and reference voltage angle θ^* [82] [100] [101] [102] [103] [104] [105] [106]. While the main approach in stabilizing loops implementation is to use the instantaneous active and reactive power to correct the reference voltage angle, respectively the reference voltage amplitude, several other compensating strategies were proposed in the literature, such as:

- use the reactive power close loop control for both reference voltage amplitude and angle correction [101].
- use of active power variation for correcting the reference voltage speed (angle), while the reactive power-based power factor close loop control provides the voltage amplitude correction [102].
- MTPA operation-based correction of the reference voltage amplitude with a single current sensor [103], for energy saving.
- use of active flux loop for correcting the reference voltage amplitude, while the active flux speed loop corrects the reference voltage angle [104].
- use of direct current MTPA control loop, using load angle calculation, for both reference voltage amplitude and angle correction [105].

The V/f control strategy proposed in this chapter employs two correction loops which serve the following purpose (Fig. 7.16):

- a closed loop control of d-axis current ensures the operation under MTPA and provides the reference voltage amplitude correction.
- the instantaneous active power variation information provides the reference voltage angle correction.

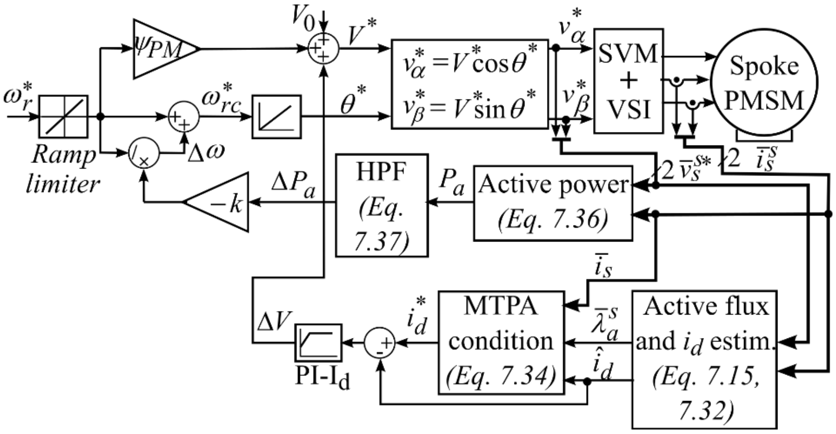

Fig. 7.16 Proposed V/F control with two stabilizing loops

No position information is needed (the motor can start from any position). The principles behind both correction loops are explained below.

7.4.1.1 Voltage amplitude correction loop

The reference voltage amplitude correction loop provides a voltage quantity ΔV added to the reference voltage which is produced by a close loop d-axis current controller.

$$\Delta V = \left(k_{p\_id} + k_{i\_id}\frac{1}{s}\right)\left(i_d^* - \hat{i}_d\right) \qquad (7.31)$$

The d-axis current $\hat{i}_d$ is estimated using the active flux amplitude $\left|\bar{\lambda}_a^s\right|$ and the *magnetic energy* expression based on stator flux $\bar{\lambda}_s^s$, both flux quantities being provided by the active flux observer:

$$\hat{i}_d = \frac{\lambda_{s_\alpha} i_\alpha + \lambda_{s_\beta} i_\beta - L_q i_s^2}{\left|\bar{\lambda}_a^s\right|} \tag{7.32}$$

$$\left|\bar{\lambda}_a^s\right| = \sqrt{\lambda_{a_\alpha}^2 + \lambda_{a_\beta}^2}\,; i_s^2 = i_{s_\alpha}^2 + i_{s_\beta}^2 \tag{7.33}$$

The reference d-axis current i_d^* is determined based on MTPA condition which is also expressed using the active flux amplitude:

$$i_d^* = \frac{\hat{i}_q^2 \left(L_d - L_q\right)}{\left|\bar{\lambda}_a^s\right|} < 0 \tag{7.34}$$

$$\hat{i}_q^2 = i_s^2 - \hat{i}_d^2 \tag{7.35}$$

The MTPA based correction strategy was selected for improving the operation efficiency, by adjusting the reference voltage to the motor loading. It acts by reducing the reference voltage amplitude in case the d-axis current needs to be reduced and vice-versa. Because the accuracy of the computed d-axis current reference and estimated values is affected by speed transients, the correction loop is enabled only in speed steady state operation (acting mainly during torque load change).

7.4.1.2 Voltage angle (speed) correction loop

The sudden changes in PMSM supply frequency (due to reference speed change) or load torque produce rotor speed oscillations which can lead to loss of synchronism. The purpose of the voltage angle correction loop is to detect these transient operations and adjust the reference voltage phasor's speed accordingly, to damp the speed oscillations and improve the stability [100], [103].

With no information on actual rotor position or speed, the rotor speed oscillations caused by speed/load transients are detected by monitoring the oscillations in the instantaneous active power P_a (calculated based on stator currents and reference voltages):

$$P_a = \frac{3}{2} \cdot \left(v_{s_\alpha}^* i_{s_\alpha} + v_{s_\beta}^* i_{s_\beta}\right) \tag{7.36}$$

As there are similarities between the rotor speed oscillations and the active power oscillations, the reference voltage phasor speed correction $\Delta\omega$ is determined based on the active power variation ΔP_a extracted using a high pass filter. The speed correction has the opposite sign of the active power variation and it is added to the reference voltage vector speed ω_r^*.

$$\begin{aligned} \Delta P_a &= \frac{sT}{1 + sT} \cdot P_a \\ \Delta\omega &= -\frac{k}{\omega_r^*} \Delta P_a\,; \omega_{rc}^* = \omega_r^* + \Delta\omega \end{aligned} \tag{7.37}$$

As the active power variation in steady state is null, the correction acts only during transient operation and it has the following effect: if the rotor speed decreases during load increase, the active power increases: $\Delta P_a > 0$, determining the application of a negative speed correction $\Delta\omega < 0$ which decreases the speed of the reference voltage vector, to maintain the synchronism. The amplitude of the speed correction depends on the reference speed ω_r^* and on a parametrizable factor k.

7.4.2 Sensorless field-oriented control (FOC)

The classic field-oriented control strategy, shown if Fig. 7.17 is investigated and implemented in this chapter. It uses a speed PI controller (PI-ω), and two current PI controllers which operate in synchronous reference frame (PI-I_d, PI-I_q). The rotor position information required for coordinate translation is either estimated via active flux observer or measured (via an encoder, or a resolver).

$$\begin{aligned} i_q^* &= \left(k_{p\_\omega} + k_{i\_\omega}\frac{1}{s}\right)\left(\omega_m^* - \omega_m\right) \\ V_d^* &= \left(k_{p\_id} + k_{i\_id}\frac{1}{s}\right)\left(i_d^* - i_d\right) \\ V_q^* &= \left(k_{p\_iq} + k_{i\_iq}\frac{1}{s}\right)\left(i_q^* - i_q\right) \end{aligned} \tag{7.38}$$

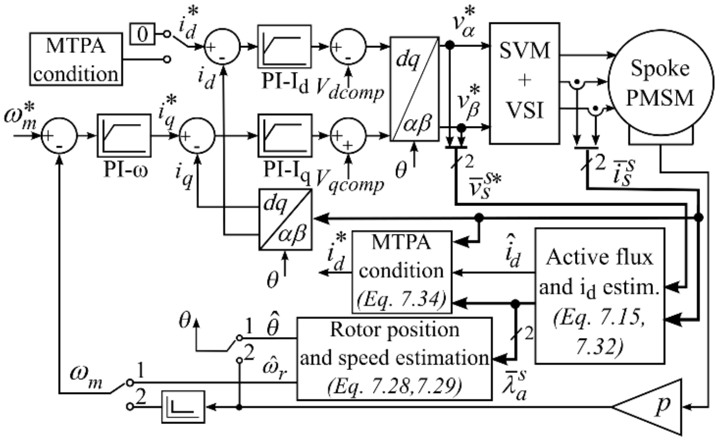

Fig. 7.17 Field-Oriented Control scheme: 1- sensorless, 2 -with position sensor

The control strategy also includes axes decoupling, to allow for independent control of the two stator currents:

$$\begin{aligned} v_{dcomp} &= \hat{\omega}_r \cdot L_q i_q \\ v_{qcomp} &= \hat{\omega}_r \cdot \left(\lambda_{PM} + L_d i_d\right) \end{aligned} \tag{7.39}$$

The resulted reference voltage vector $\bar{v}_s^r$ is translated to stator coordinates $\bar{v}_s^s$ using inverse Park transformation, where it will be used for PWM command calculation via SVM (listed in the Appendix).

$$\bar{v}_s^{s*} = \bar{v}_s^{r*} \cdot e^{j\hat{\theta}_{er}} \tag{7.40}$$

The introduction of deadtime in the PWM command and the voltage drop on power converter switching components distort the inverter output voltage, effect which becomes prominent at lower motor speeds. Compensation techniques consisting of including additional voltage components in the reference voltage $\bar{v}_s^{s*}$, to neutralize or mitigate the voltage distortion were proposed in the literature [107] [108] [109]. The inverter nonlinearities compensation is also considered here by adding a $\bar{v}_{s_{inv}}^{s}$ voltage compensation component to the reference stator voltage $\bar{v}_s^s$, calculated based on phase current amplitude and sign [108].

$$\bar{v}^s_{s_{abc}} = \bar{v}^s_s + \bar{v}^s_{s_{inv}} \tag{7.41}$$

The deadtime effect compensation is included in the space vector modulation strategy (listed in the Appendix).

The *dq* stator currents are calculated via Park transformation:

$$\bar{i}^r_s = \bar{i}^s_s \cdot e^{-j\hat{\theta}_{er}} \tag{7.42}$$

The i_d^* current reference can be either calculated based on MTPA condition (7.34) or set to zero, to reduce the computation effort for the case of small or no saliency. For the case of the spoke-PMSM motor investigated in this chapter, the ratio L_q/L_d *is 1.23* (Table 7.1).

7.4.3 Digital simulation results

Simulations have been carried out for the two control strategies and are presented below, for providing an insight on their performance.

7.4.3.1 V/f control with stabilizing loops

The control scheme in Fig. 7.16 was implemented and simulated. The controller calculations part is executed at 10 kHz while the motor (plant) model part is executed at 100 kHz. A rotor reference speed step change to 2000 rpm (0.44 p.u.) is prescribed at t=0.1 s, followed by a step load to 1.06 Nm (0.5 p.u.) over the t= 2..3 s interval. Both compensation loops are enabled. The simulation results are presented in Fig. 7.18 and the control parameters are listed in Table 7.2.

Table 7.2 Parameters of the V/f control with stabilizing loops

Parameter	Value
i_d controller proportional gain k_{p_id}	0.5
i_d controller integrator gain k_{i_id}	8
maximum/minimum i_d controller output value [V]	± 25
voltage amplitude correction loop coefficient k	80
active power high pass filter time constant T [s]	0.125
V/f boost voltage V_0 [V]	1
active flux observer controller proportional gain k_{p_afo}	100
active flux observer controller integrator gain k_{i_afo}	1000
maximum/minimum active flux observer controller output V_{comp} [V]	± 20
maximum speed difference (reference-estimated value) at which the voltage amplitude correction loop is still enabled [rad/s]	5

Due to the 250Hz/s speed rate limiter, the acceleration time to 2000rpm is 0.6 s (Fig. 7.18 a). The speed disturbances during load and unload exceed 100 rpm, but the operation is stable, even under step load.

Although not directly used in the control loop, the estimated active flux observer estimated speed (AFOBS, in Fig. 7.18 a, follows closely the actual rotor speed, denoted by ENC).

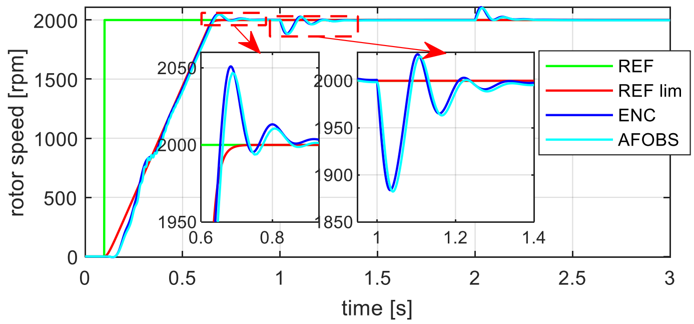
rotor speed [rpm]
2000
1500
1000
500
0
time [s]
0
0.5
1
1.5
2
2.5
3
2050
2000
1950
0.6
0.8
2000
1950
1900
1850
1
1.2
1.4
REF
REF lim
ENC
AFOBS

a)

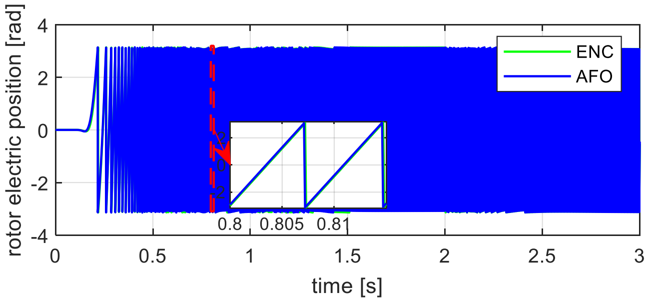
rotor electric position [rad]
4
2
0
-2
-4
time [s]
0
0.5
1
1.5
2
2.5
3
0.8
0.805
0.81
ENC
AFO

b)

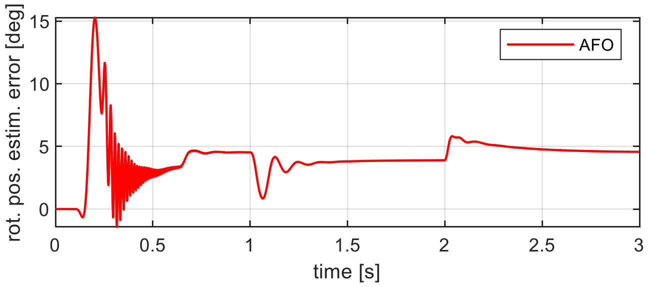
rot. pos. estim. error [deg]
15
10
5
0
time [s]
0
0.5
1
1.5
2
2.5
3
AFO

c)

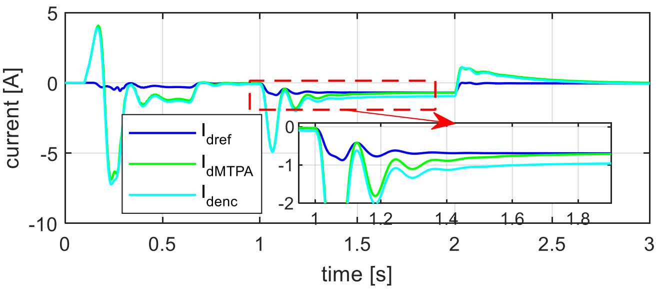
current [A]
5
0
-5
-10
time [s]
0
0.5
1
1.5
2
2.5
3
I_dref
I_dMTPA
I_denc
0
-1
-2
1
1.2
1.4
1.6
1.8

d)

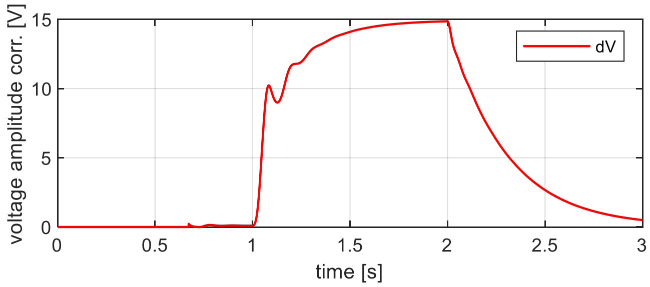
voltage amplitude corr. [V]
15
10
5
0
0
0.5
1
1.5
2
2.5
3
time [s]
dV

e)

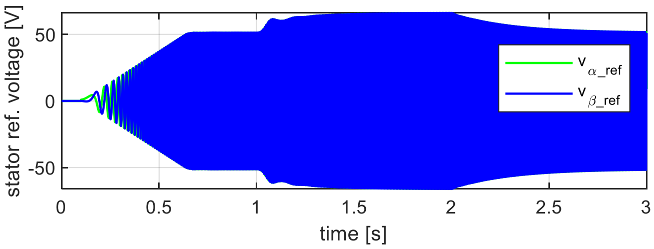
stator ref. voltage [V]
50
0
-50
0
0.5
1
1.5
2
2.5
3
time [s]
v_{α_ref}
v_{β_ref}

f)

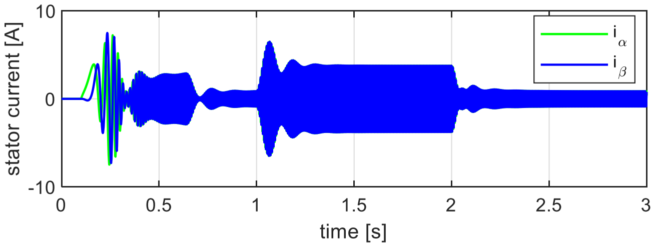
stator current [A]
10
0
-10
0
0.5
1
1.5
2
2.5
3
time [s]
i_α
i_β

g)

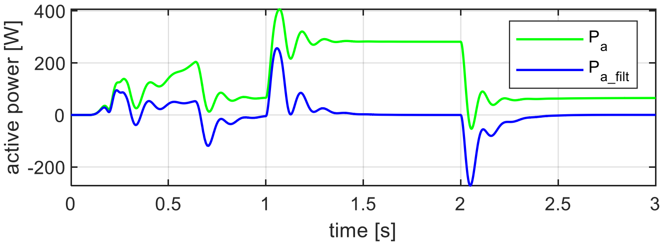
active power [W]
400
200
0
-200
0
0.5
1
1.5
2
2.5
3
time [s]
P_a
P_{a_filt}

h)

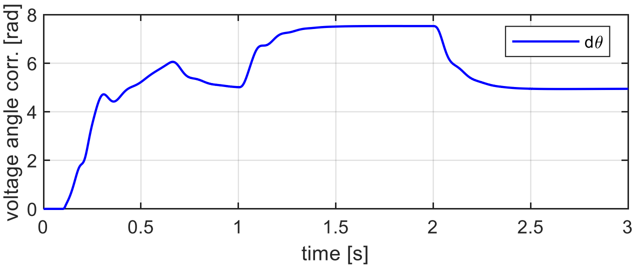

i)

Fig. 7.18 V/f with stabilizing loops simulation results: a) rotor speed, b) rotor position, c) rotor position estimation error, d) d-axis current, e) stator voltage amplitude correction, f) reference voltage in stator coordinates, g) reference current in stator coordinates, h) active power and its oscillations, i) voltage angle correction

The estimated speed has a maximum error of 20° el., during speed transient change and a constant error of approx. 5° el. This error offset seems to vary with the calculation rate (e.g., at observer model calculation rate of 100kHz – Fig. 7.18 c the simulation error is less than 1° electric). Fig. 7.18 d shows the voltage amplitude correction loop effectiveness in controlling the reference d-axis current for MTPA operation, while Fig. 7.18 e shows the voltage amplitude correction. The difference between the estimated d-axis current and the actual d-axis current of 1 A during load is attributed to the position estimation error. The voltage angle correction is shown in Fig. 7.18 g.

As shown in Fig. 7.18 f, the stator current reaches high amplitude values during transient operation of approx. two times the rated value. This represents one of the shortcomings of the V/f control method.

7.4.3.2 Sensorless field-oriented control, based on active flux observer

The sensorless field-oriented control in Fig. Fig. 7.17 was simulated under the same conditions as V/F control strategy. The active flux observer was used for estimating the rotor position, the control parameters being presented in Table 7.3.

Table 7.3 Parameters of the FOC sensorless control

Parameter	Value
i_d (and i_q) controllers proportional gain k_{p_id} (and k_{p_iq})	20
i_d (and i_q) controllers integrator gain k_{i_id} (and k_{i_iq})	50
maximum/minimum i_d (i_q) controller output [V]	±100
speed controller proportional gain k_{p_ω}	0.04
speed controller integrator gain k_{i_ω}	10
maximum/minimum speed controller output [A]	±5.5
maximum speed difference (reference - estimated value) at which the MTPA i_d* is calculated [rpm]	50

The results presented in Fig. 7.19 show that the rotor acceleration to 2000 rpm occurs in a much shorter time, being limited by the q-axis reference current limitation. Additionally, even if the same observer structure and parameters were used, the estimation position error is lower than in the case of V/f control (Fig. 7.19 c). The d-axis real current presents oscillations during rotor acceleration, caused by the active flux observer estimation errors (which also impacts the d-axis reference current calculation for MTPA operation). However, the operation becomes smooth after the speed transients.

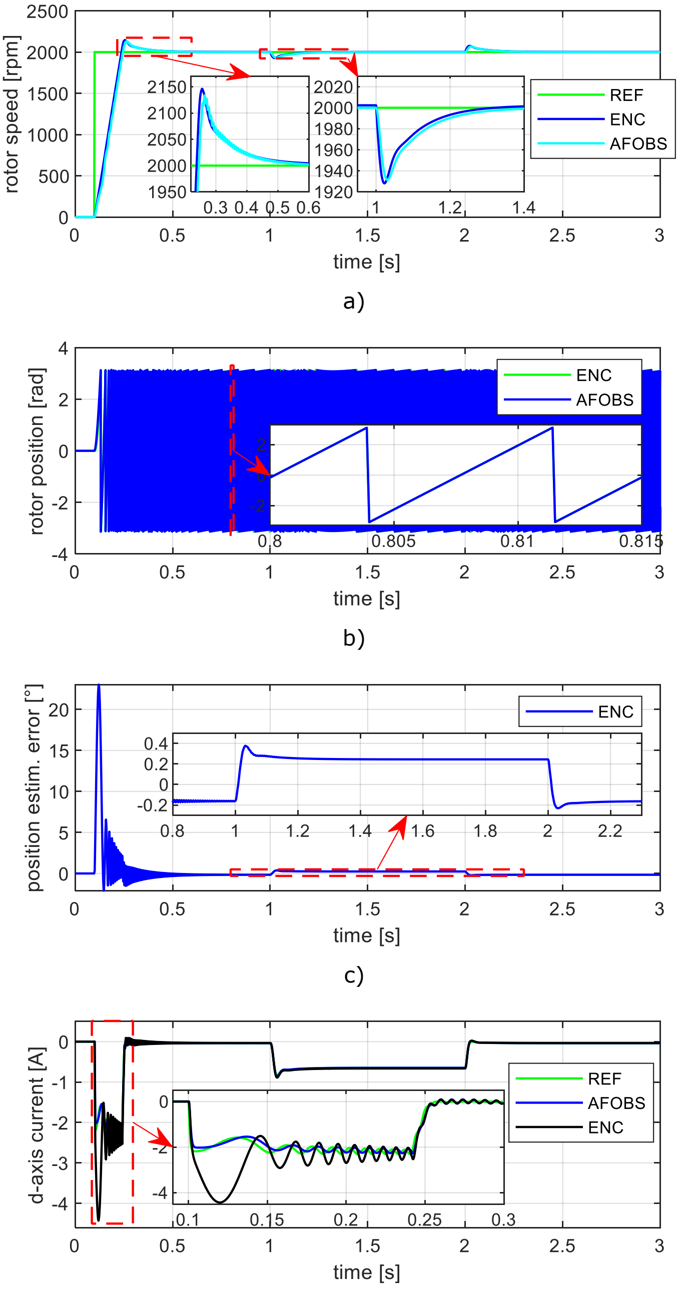
rotor speed [rpm]
2500
2000
1500
1000
500
0
REF
ENC
AFOBS
2150
2100
2050
2000
1950
0.3 0.4 0.5 0.6
2020
2000
1980
1960
1940
1920
1
1.2
1.4
rotor position [rad]
4
2
0
-2
-4
ENC
AFOBS
0.8
0.805
0.81
0.815
position estim. error [°]
20
15
10
5
0
ENC
0.4
0.2
0
-0.2
0.8
1
1.2
1.4
1.6
1.8
2
2.2
d-axis current [A]
0
-1
-2
-3
-4
REF
AFOBS
ENC
0.1
0.15
0.2
0.25
0.3
0
0.5
1
1.5
2
2.5
3
time [s]

a)

b)

c)

d)

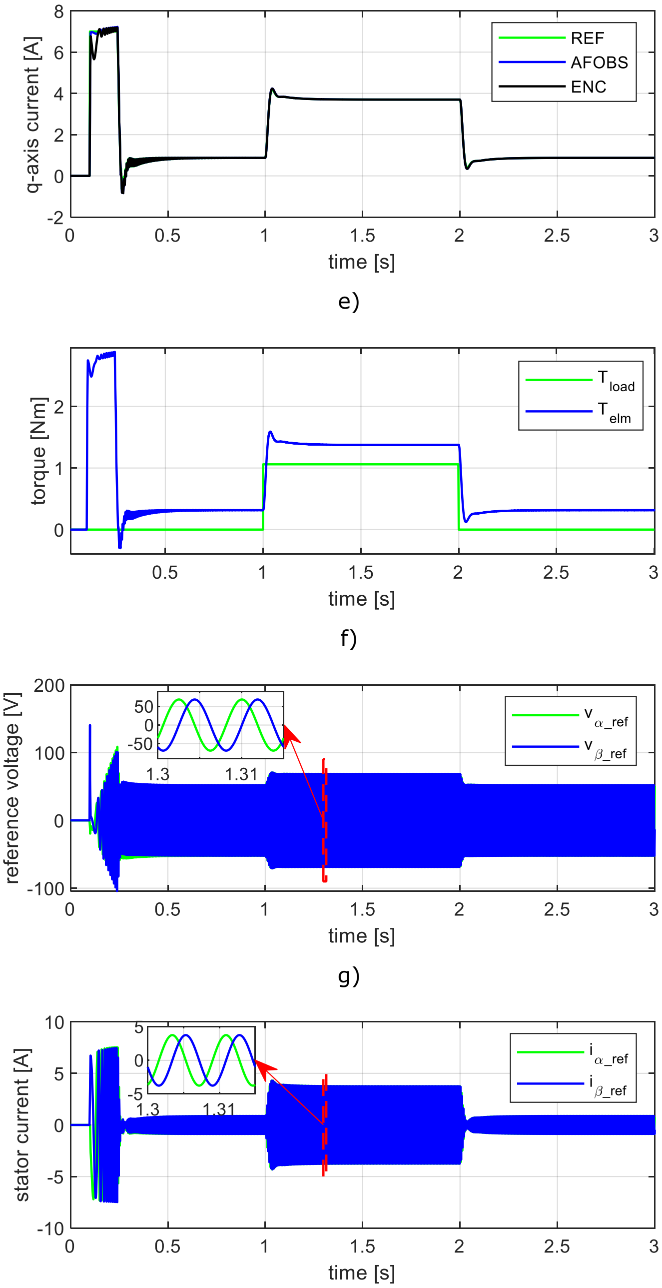

e)

f)

g)

h)

Fig. 7.19 Active flux observer sensorless field-oriented control simulation results: a) rotor speed, b) rotor position, c) position estimation error, d) d-axis current, e) q-axis current, f) load/electromagnetic torque, g) reference voltage in stator coordinates, h) stator current in stator coordinates

Overall, as expected, the field-oriented control provides a better performance in terms of dynamic operation. However, for targeted applications of pumps, compressors and fans, the scalar control dynamic performance is considered satisfactory.

7.4.3.3 Parameter variation influence on position estimation (digital simulation study)

The active flux observer relies on a model of the machine stator winding electric circuit, making the accuracy of the position estimation dependent on the accuracy of the estimated electric machine parameters values. The real values change in time, due to temperature or magnetic saturation, and affect the quality of the position estimation (if the observer's model does not include built-in strategies to compensate for such effects).

The impact of machine parameter changes from the rated values (listed in Table 7.1) on the estimated rotor position is studied by simulation for operation at 2000 rpm under no load, and partial 50% load (1.06 Nm). The results are shown in Fig. 7.20, for both sensorless control strategies.

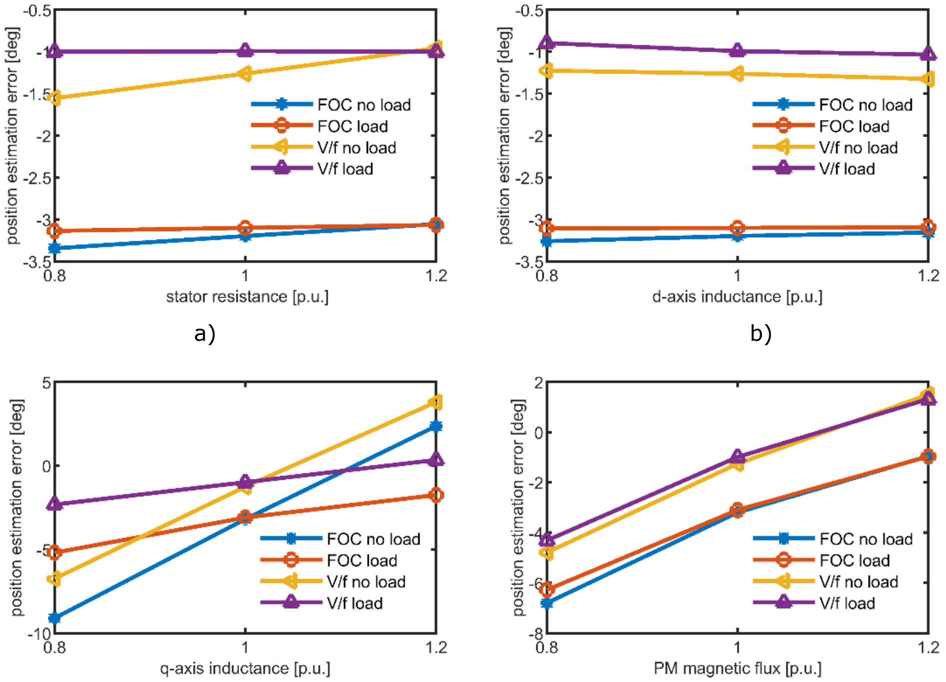

a) b)

c) d)

Fig. 7.20 Position estimation error versus motor parameters variation of: a) stator resistance, b) d-axis inductance, c) q-axis inductance, d) PM flux

The position estimation seems to be less affected by the stator resistance and d-axis inductance change (the impact is larger at lower operating speeds), whereas a 10% change in q-axis inductance or PM flux has a major impact in position estimation error.

Overall, FOC sensorless control operation is less influenced by parameter changes than V/f with stabilizing loops. For parameter variation of higher amplitude, the V/f control strategy becomes unstable and, thus, requires parameter value compensation strategies.

7.5 Experimental results

This section presents experimental results performed on a spoke-IPMSM prototype motor shown in Fig. 7.15 a, manufactured based on the design procedure presented in [110]. The design requirements were: 1 kW at 4500 rpm, fed by a voltage source inverter connected to a 380 V_{DC} source. However, due to the use of lower performance PM magnets and a larger airgap height, the resulted prototype machine can produce an output power only in the range of few hundreds of Watts. The test rig fixing platform also limits the speed operation to 2000 rpm. For this reason, the experimental results presented in this chapter were carried out at maximum 2000 rpm rotor speed and less that the rated load (2.12 Nm). A comparison of design machine parameters versus the measured ones is also presented in the next subsections.

7.5.1 Experimental platform

The experimental platform depicted in Fig. 7.21 b consists of the spoke-IPMSM prototype, coupled via Magtrol TM307 torquemeter to the 1.63kW, 2000 rpm BSM90N-2150AF ABB BLDC motor. The load motor is powered by a MintDrive II which is programmed to operate in torque closed loop control mode.

The prototype motor is fed by a Danfoss VLT®Automation Drive FC 302 3 phase voltage source inverter connected through an autotransformer to the 400V grid supply. 3 LA 55-P LEM current sensors are used for acquiring the 3 phase currents, while the inverter DC bus voltage is acquired using a LEM LV-25p based custom voltage sensor box.

The dSpace 1103 control board is used for control strategy implementation, optically connected to the Danfoss inverter via a custom interface card. The rotor position acquired with an incremental encoder mounted on the load motor is routed via MintDrive II to the dSpace interface card. An additional connection between the dSpace control board and MintDrive II is used for providing the analog load torque reference for the load motor.

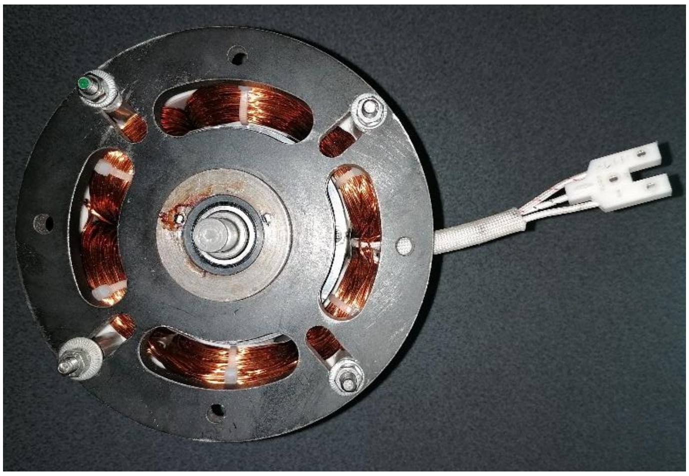

a)

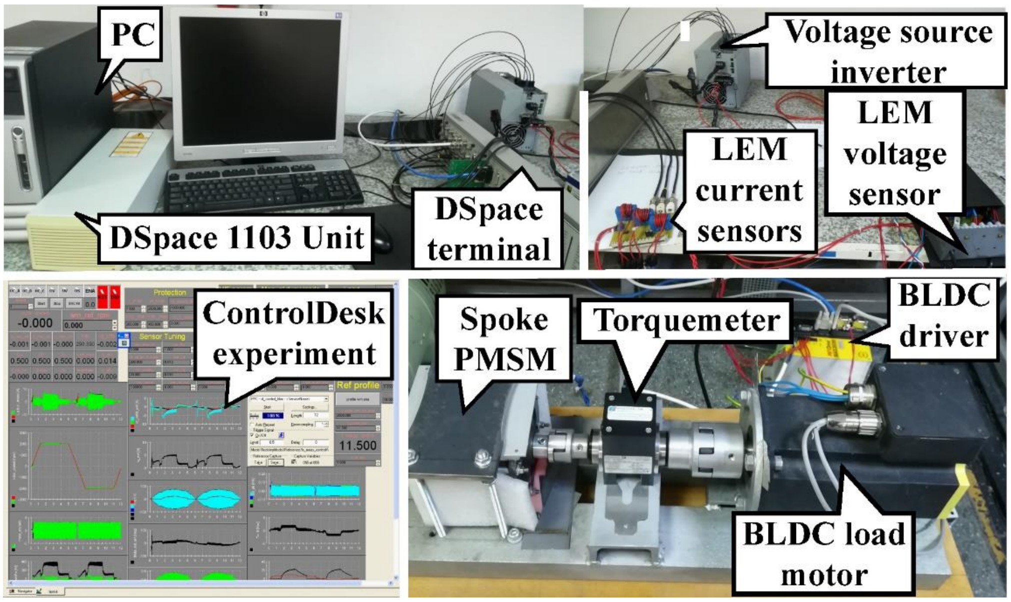

b)

Fig. 7.21 Experimental platform: a) spoke-PMSM, b) test rig

MATLAB Simulink, Real-Time Interface and Target Link are used for motor control strategies implementation, while the Control Desk experiment is used for measurements and instrumentation.

7.5.1.1 Machine parameter determination

The motor parameters are presented in Table 7.1. Part of them were determined experimentally using both static and dynamic tests. The procedure is presented in the next subsections.

7.5.1.2 PM flux linkage

The PM flux linkage was calculated using the EMF value measured during an open load generator test (Fig. 7.22). With the spoke-IPMSM motor rotated at a constant speed, the EMF line value waveform was captured with an oscilloscope. As it can be observed, the EMF waveform is not close to a sinusoidal shape, the FFT transformation showing a rather large value of the 5’th harmonic (10% of the fundamental harmonic amplitude – Fig. 7.23).

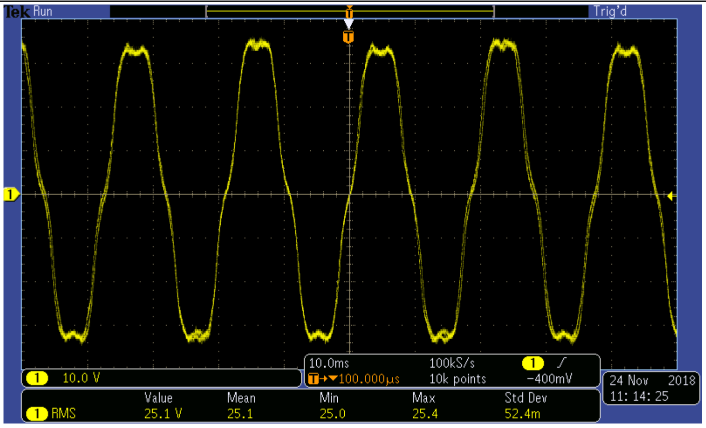

```
1   10.0 V                 10.0ms          100kS/s      1  ⁄
                           T→▾100.000µs    10k points   -400mV     24 Nov   2018
                                                                   11: 14: 25
          Value     Mean     Min     Max     Std Dev
1 RMS     25.1 V    25.1     25.0    25.4    52.4m
```

Fig. 7.22 EMF line voltage for open loop generator mode at 700 rpm

Using the measured EMF, the PM flux linkage amplitude was determined as:

$$E=\frac{d\bar{\lambda}_{PM}^{s}}{dt}=\frac{d\bar{\lambda}_{PM}^{s}}{d\theta_{er}}\cdot\frac{d\theta_{er}}{dt}=\frac{d\bar{\lambda}_{PM}^{s}}{d\theta_{er}}\cdot\omega_{er}$$
$$\Rightarrow\lambda_{PM}=\frac{E}{\omega_r}=\frac{E}{2\pi\frac{n_m}{60}\cdot p}\qquad(7.43)$$

where n_m is the rotor speed in rpm and p is the number of pole pairs. For a 1500 rpm rotor speed open loop generator operation, the value of $\lambda_{PM}=0.06Wb$ was obtained.

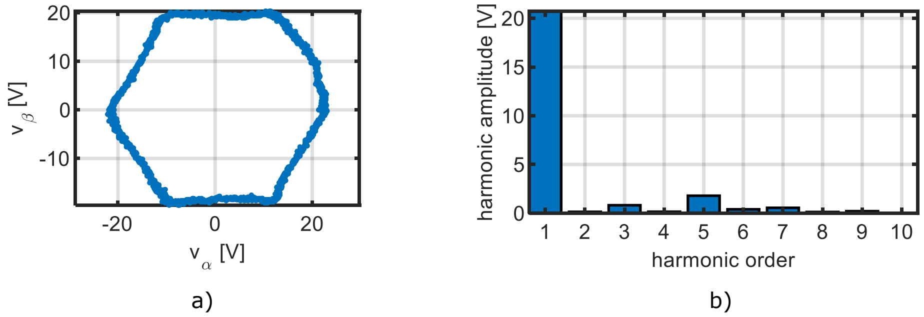

Fig. 7.23 EMF of Spoke-PMSM for 700 rpm, generator mode in open loop: a) stator voltage vector trajectory in αβ coordinates; b) harmonic component of Vα

Due to airgap PM flux density distribution, the EMF is not sinusoidal, containing a set of harmonics, the most prominent being the 5th harmonic These EMF harmonic components inevitably produce current harmonics whose effect is seen in the torque pulsations.

7.5.1.3 Estimation of inductances along d and q-axis

The synchronous inductances were calculated during a standstill test. The rotor was mechanically fixed in a position with the d axis aligned to the stator phase a axis. The stator phases, connected in a special way to exhibit the properties of synchronous inductances, were fed through an autotransformer which had its AC voltage varied to produce a phase current variation from close to 0 A to the rated current amplitude.

Using the voltage and current RSM values, the inductances is estimated as follows:

$$L_d = \sqrt{\frac{\left(\frac{2}{3}\frac{V_{d(rms)}}{I_{d(rms)}}\right)^2 - R_S^2}{(2 \cdot \pi \cdot f)^2}}; L_q = \sqrt{\frac{\left(\frac{1}{2}\frac{V_{q(rms)}}{I_{q(rms)}}\right)^2 - R_S^2}{(2 \cdot \pi \cdot f)^2}} \tag{7.44}$$

where f is the grid frequency of 50Hz, and R_S is the phase resistance. The measured currents and estimated inductances variation with current is depicted in Fig. 7.24. The saturation effect is not visible because the test was performed for current values up to the rated current (2.44 Arms).

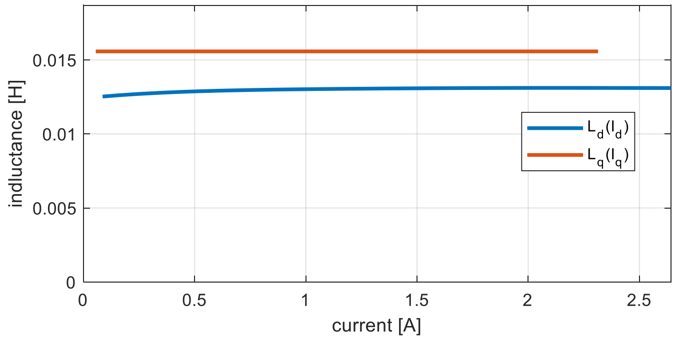

Fig. 7.24 Stator dq axes inductances

Finally, Table 7.4 shows a summary of the measured parameters, in comparison with the design values [110]. The stator winding resistance was determined using Ohm law (by feeding the stator winding with a DC voltage source).

Table 7.4 Design versus measured parameters of 6/8 pole Ferrite spoke PMSM

Parameter	Design values	Measured values
PM flux [Wb]	0.107	0.06
stator resistance (Ω)	1.36	0.85
d-axis inductance [mH]	14.2	13
q-axis inductance [mH]	13.8	15.6

7.5.2 Motor control test results

The two sensorless control strategies presented in section 7.4 were implemented and comparatively tested [106] [111]. To facilitate the results interpretation and evaluation, the experimental tests were ran using same reference speed and load torque profiles:

- reference speed change from 0 rpm to ω_r^* at t = 0.1 s, followed by operation at constant speed and reversal to $-\omega_r^*$ at t = 5s and deceleration to 0 rpm at t =11 s.
- reference load torque T_L^* applied during 1.5 - 3.5 s time interval and negative torque reference $-T_L^*$ is applied during 7.5 - 9.5 s time interval.

"enc" suffix denotes the signals whose calculation was done based on encoder provided position information, the encoder being used only as a witness, to assess the performance of the active flux observer-based rotor position estimation.

7.5.2.1 *Sensorless V/f control with stabilizing loops*

The first set of tests investigates the benefits added by the stabilizing loops to the scalar V/f control. Tree cases were checked for a reference speed ω_r^* of 700rpm and a load torque T_L^* of 0.95Nm: operation with both stabilizing loops enabled (case$_1$) versus operation with voltage amplitude correction loop disabled (case$_2$) versus operation with no correction loops enabled (case$_3$). Fig. 7.25 shows the results for rotor speed, d and q axis currents. The benefits of the correction loops are evident in case$_1$, as the case$_3$ operation becomes unstable after loading, while case$_2$ operation shows a large d-axis current value during motor loading.

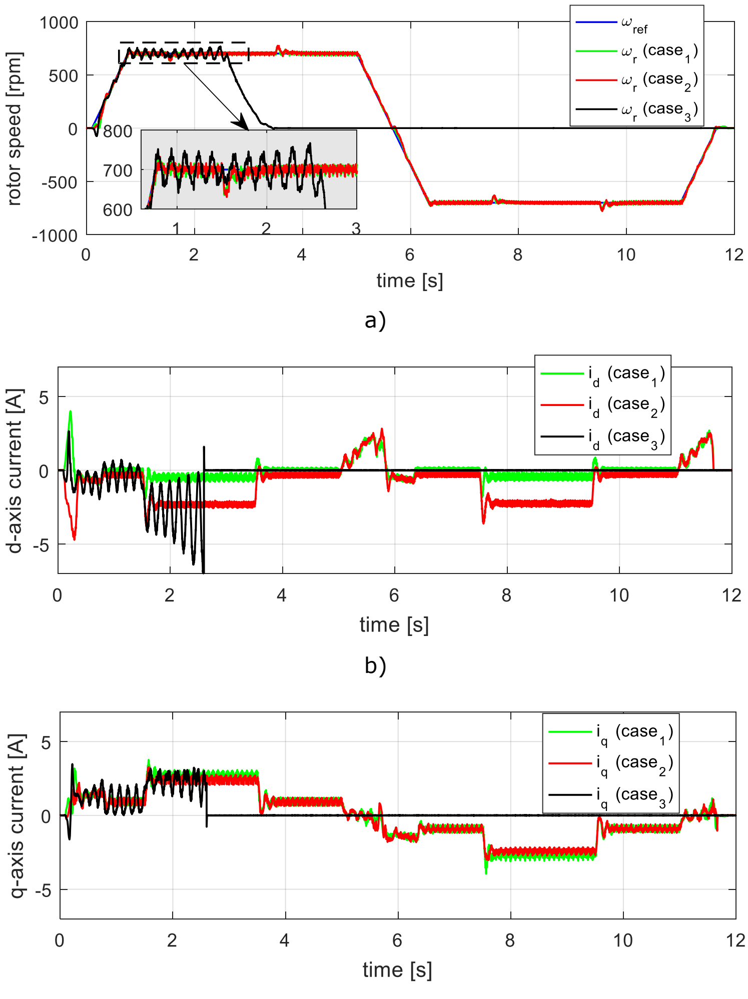

a)

b)

c)

Fig. 7.25 V/f with stabilizing loops: study of stabilizing loops contribution on a) rotor speed, b) d-axis current, c), q-axis current (experimental results)

The next set of experimental test results in Fig. 7.26 present the performance of the V/f scalar control strategy for $\omega_r^* = 1000rpm$ (with the reference frequency slope limited to $125\,Hz/s$) and $T_L^* = 1.7Nm$ operation. The parameters of the control are listed in Table 7.2.

The motor operation is stable, the control strategy being able to cope with the load torque disturbance. The rotor position becomes correctly estimated after approx. 5 electrical rotations from startup (Fig. 7.26 e), the average rotor position estimation error being approx. 4°. As the voltage amplitude correction loop operation is disabled during speed transients, the d-axis current shows high amplitude pulsations in these cases. However, the benefic influence of the voltage amplitude correction is visible during loading, where the d-axis current is visibly reduced (Fig. 7.26 b) by increasing the reference voltage amplitude with approx. 12 V (Fig. 7.26 i).

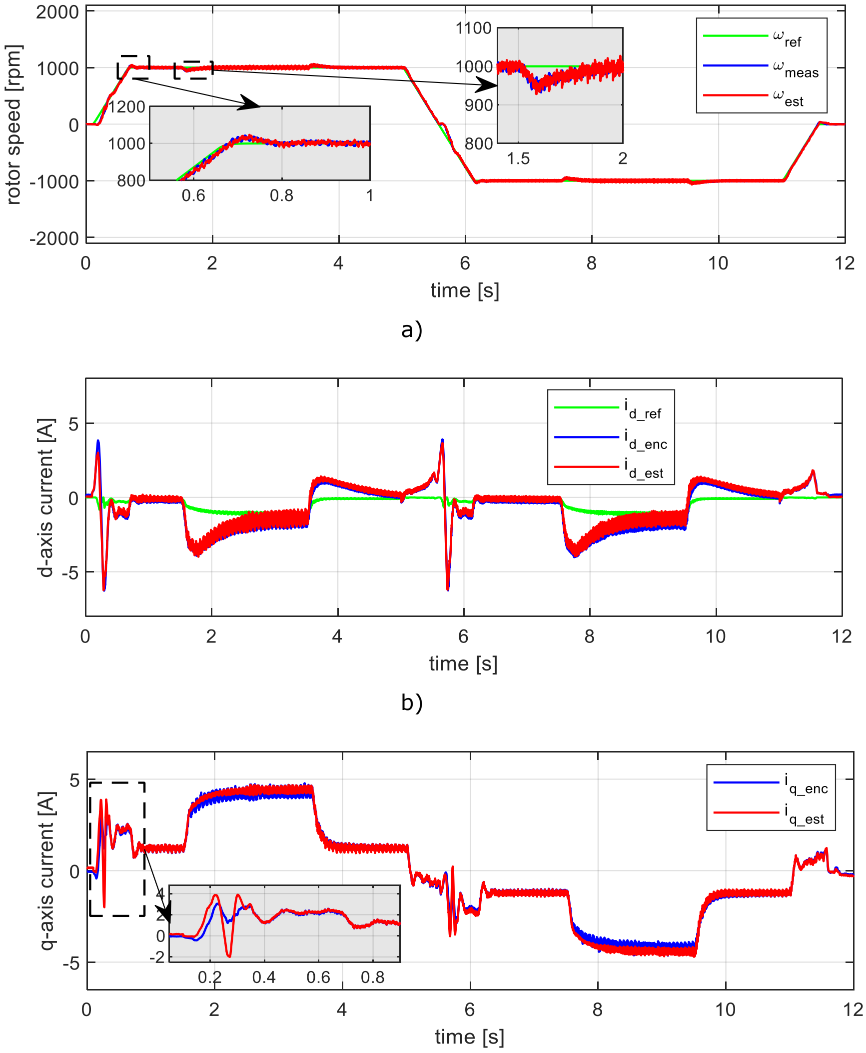

a)

b)

c)

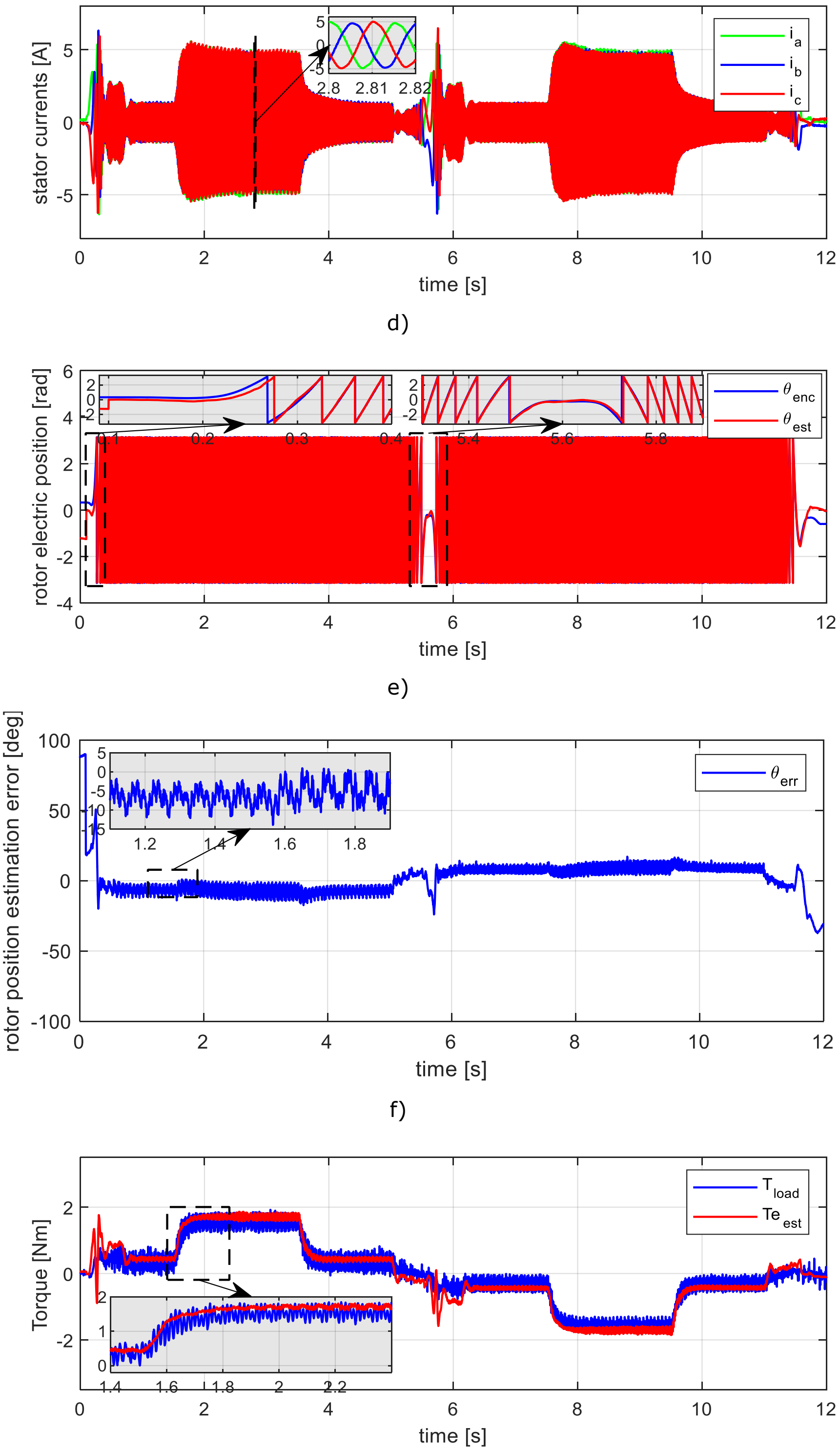
stator currents [A]
time [s]
i_a
i_b
i_c
2.8 2.81 2.82
d)
rotor electric position [rad]
time [s]
θ_{enc}
θ_{est}
0.1 0.2 0.3 0.4
5.4 5.6 5.8
e)
rotor position estimation error [deg]
time [s]
θ_{err}
1.2 1.4 1.6 1.8
f)
Torque [Nm]
time [s]
T_{load}
Te_{est}
1.4 1.6 1.8 2 2.2

g)

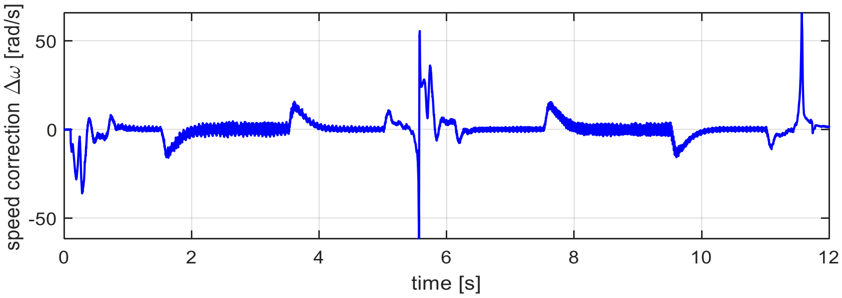

h)

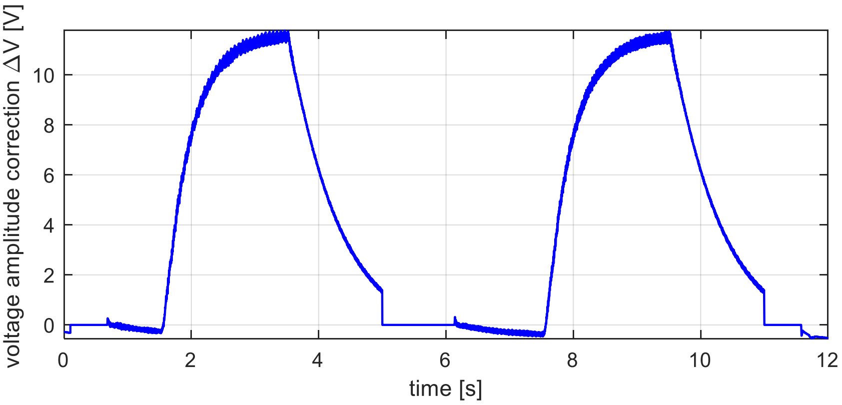

i)

Fig. 7.26 V/f control with stabilizing loops: experimental results at ±1000 rpm: a) rotor speed, b) d-axis current, c) q-axis current, d) current amplitude, e) rotor position, f) rotor position estimation error, g) load and electromagnetic torque, h) voltage angle correction, i) voltage amplitude correction

The machine cogging torque, and possibly the mechanical coupling, motor axe imperfect alignment and spoke-IPMSM motor fixing system are responsible for the high measured load torque pulsations (Fig. 7.26 g).

7.5.2.2 Sensorless FOC with Active Flux Observer

Same conditions were used for testing the implementation of the sensorless FOC control strategy. The control parameters are listed in the Table 7.3 (chosen by trial and error). The experimental test results are depicted in Fig. 7.27. With no knowledge of the initial rotor position, a starting routine must be used, consisting of prescribing the voltage vector V_1 for 0.5 s (determining the rotor to align its d-axis to the phase A axis), followed by resetting the rotor position value to 0, as well as resetting the accumulators for all integrator components.

Being limited by the q-axis reference current limitation, the rotor acceleration time is twice as fast compared to the scalar control acceleration time. The response to load changes is also faster, the d-axis current controller keeping the transient current amplitude at low values. The position estimation error has similar value (same position observer is used), the offset being probably introduced by an incorrect encoder initialization during the initialization phase.

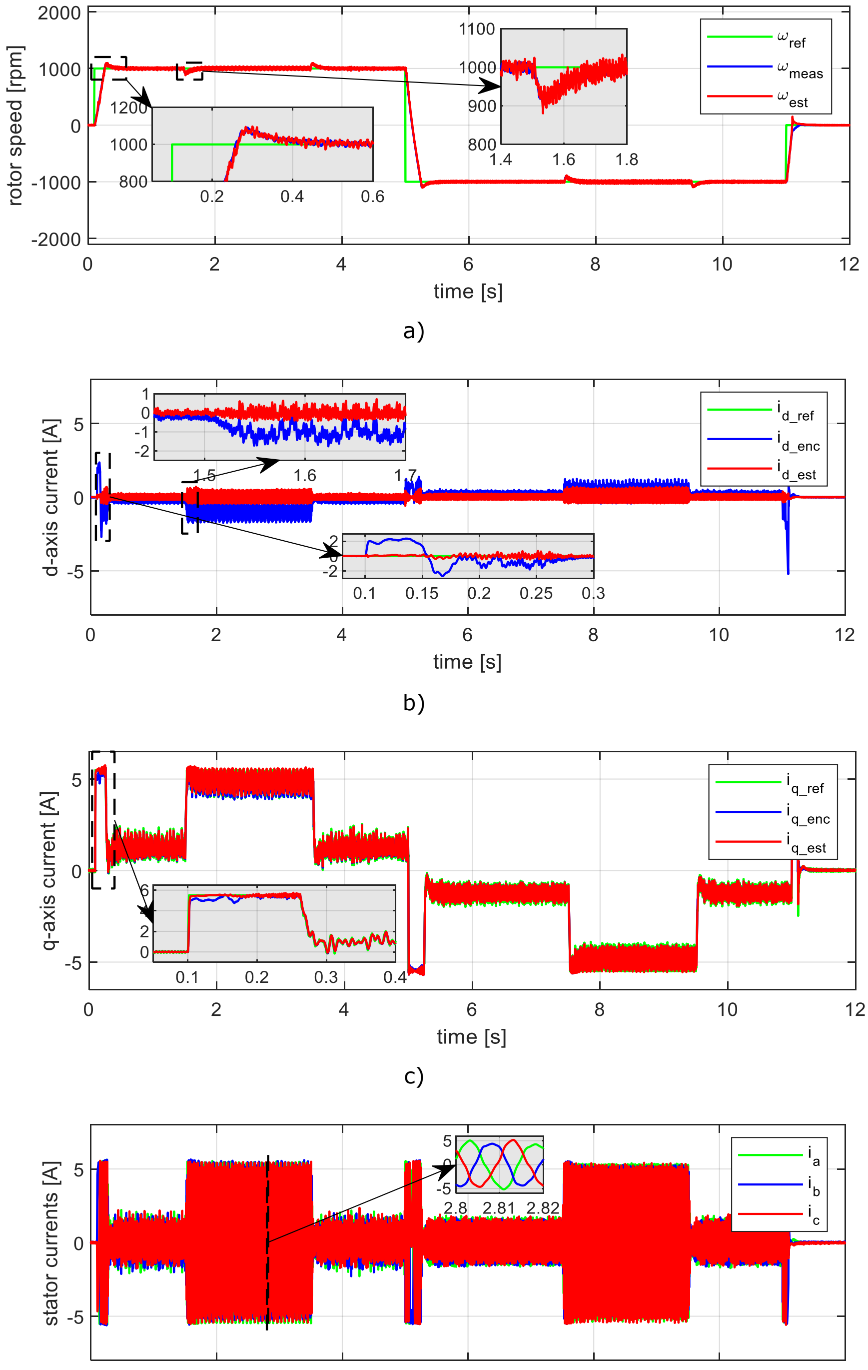
rotor speed [rpm]
2000
1000
0
-1000
-2000
time [s]
0
2
4
6
8
10
12
ω_{ref}
ω_{meas}
ω_{est}
1200
1000
800
0.2
0.4
0.6
1100
1000
900
800
1.4
1.6
1.8
d-axis current [A]
5
0
-5
i_{d_ref}
i_{d_enc}
i_{d_est}
1
0
-1
-2
1.5
1.6
1.7
2
0
-2
0.1
0.15
0.2
0.25
0.3
q-axis current [A]
i_{q_ref}
i_{q_enc}
i_{q_est}
6
4
2
0
0.1
0.2
0.3
0.4
stator currents [A]
i_a
i_b
i_c
5
0
-5
2.8
2.81
2.82

a)

b)

c)

d)

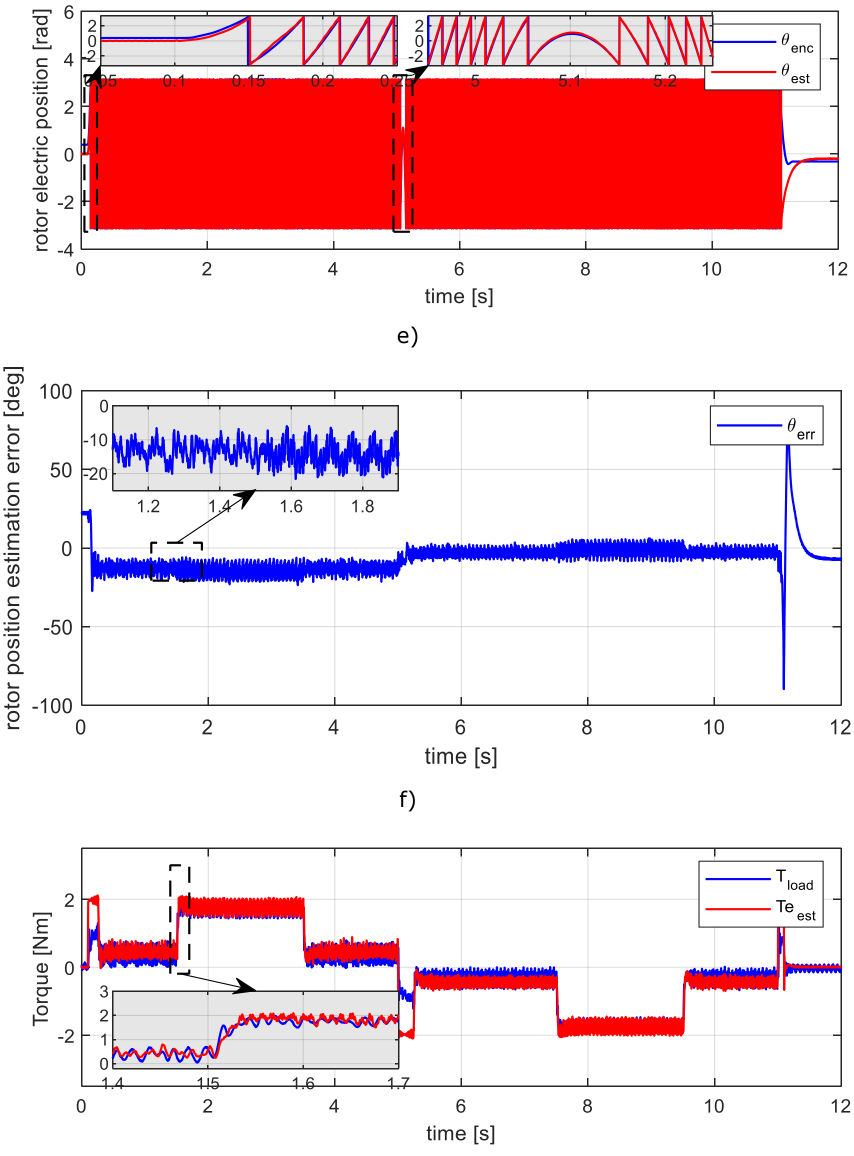

e)

f)

g)

Fig. 7.27 Field oriented control (FOC): experimental results at 1000 rpm: a) rotor speed, b) d-axis current, c) q-axis current, d) current amplitude, e) rotor position, f) rotor position estimation error, g) load and electromagnetic torque

7.5.2.3 Sensorless V/f with two stabilizing loops versus sensorless FOC – results comparison

To better asses the performance differences, a comparison of two control strategies is presented in Fig. 7.28 and Fig. 7.29 for two operation conditions:

a) high-speed operation: $\omega_r^* = 2000\,rpm, T_L^* = 1.42\,Nm$ load

b) *low speed operation:* $\omega_r^* = 100\,rpm, T_L^* = 0.82\,Nm$ load

While the vector control response is generally faster at higher operating speeds, the control performance at low speed is similar (except for higher current peaks at the beginning of the transient phases, present during V/f-controlled operation).

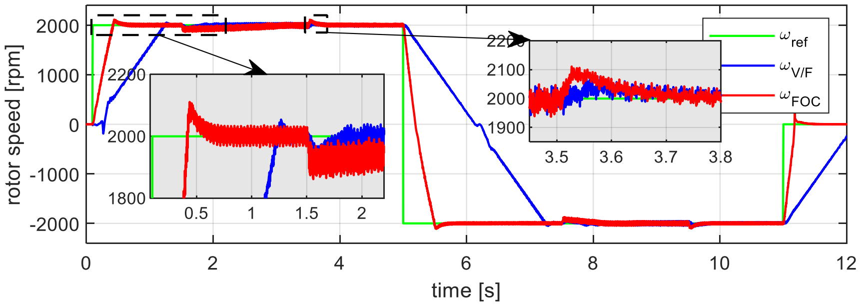

a)

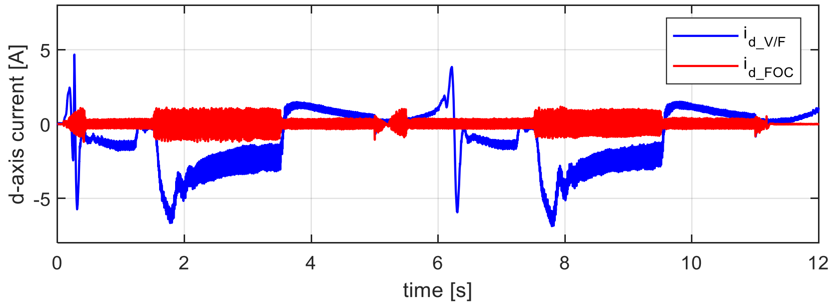

b)

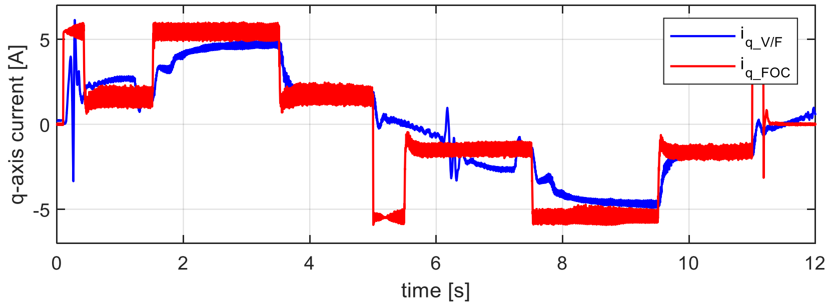

c)

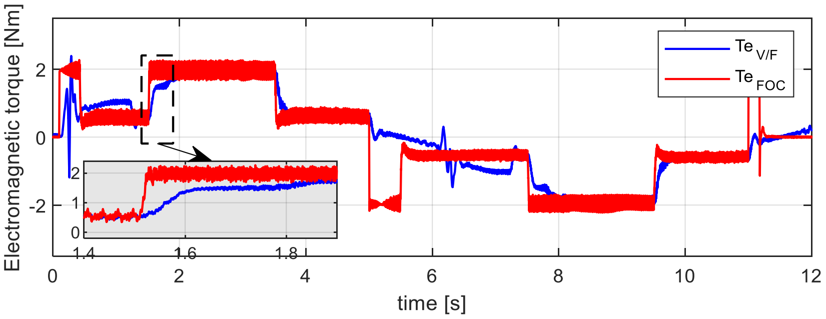

d)

Fig. 7.28 Sensorless V/f control with stabilizing loops versus FOC sensorless control at ±2000 rpm: a) estimated speed, b) estimated d-axis current, c) estimated q-axis current, d) estimated electromagnetic torque

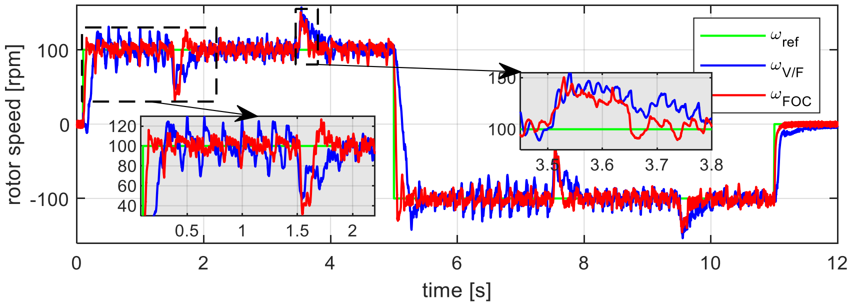

a)

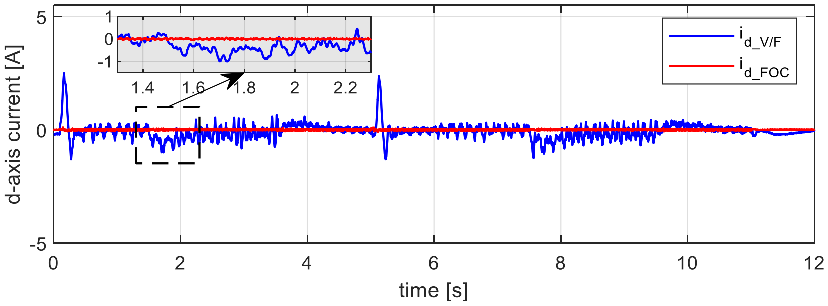

b)

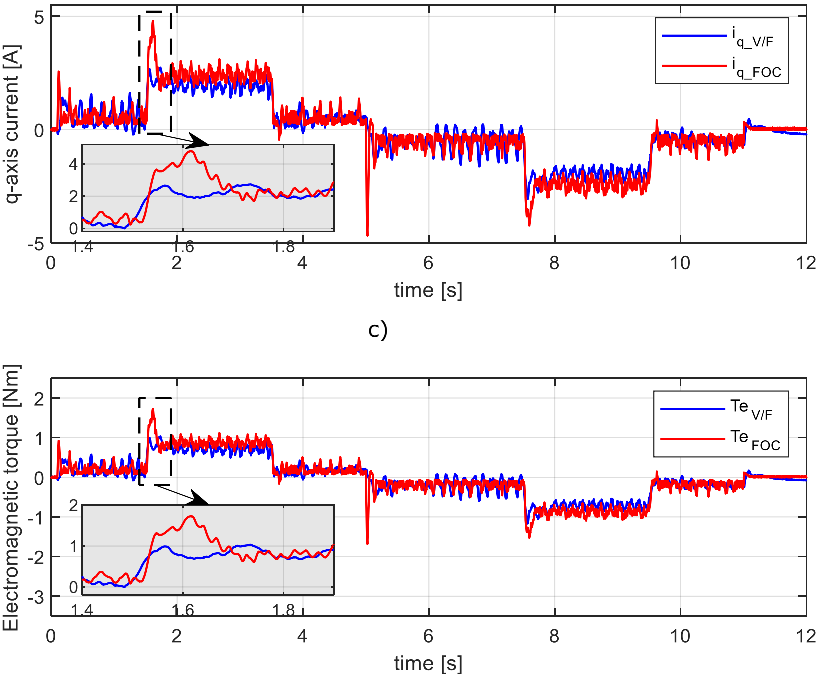

c)

d)

Fig. 7.29 Sensorless V/f control with stabilizing loops versus FOC sensorless control at ±100 rpm: a) estimated speed, b) estimated d-axis current, c) estimated q-axis current, d) estimated electromagnetic torque

Operation at lower than 100rpm is possible in steady state, but becomes problematic during reference speed and load changes, due to uncertainties in motor parameter values used by the active flux observer and the inverter nonlinearities, whose effect becomes visible, even with the compensation strategy in (7.41) applied.

While showing a slower dynamic response, the overall V/f control strategy is shown to be acceptable and stable enough to be used in compressor drive applications.

7.6 Conclusion

This chapter investigated through digital simulation and experimental tests two sensorless control strategies: V/f with stabilizing loops versus sensorless field-oriented control, intended for controlling a spoke-PMSM prototype for use in a compressor application. Both strategies employ the active flux observer for rotor speed and position estimation as well as for estimating the active flux amplitude. The novelty proposed here is the enhancement of the scalar V/f control strategy with an amplitude correction loop based on d-axis current control, where both d-axis current reference and estimated values are expressed based on active flux amplitude.

The performance of both control strategies was compared in detail based on extensive experimental results covering 100 – 2000 rpm (0.022 – 0.44 p.u.) speed range and 0.82 – 1.7 Nm (0.38 p.u. – 0.8 p.u.) load torque range. Relatively good performance was obtained for both control strategies, the sensorless FOC exhibiting higher dynamic response and showing less influence on motor parameters variation.

The stabilizing loops were shown to improve the scalar control’s both stability and efficiency in operation - by enforcing operation under MTPA.

Adding the benefit of being able to start form any position, with no need for initial rotor position information or start-up strategy and the easier commissioning due to the smaller number of tuning parameters, the performance of the V/f control with correction loops is considered satisfactory for driving fans, pumps and for compressor applications.

CHAPTER 8 CONCLUSIONS, CONTRIBUTIONS AND FUTURE WORK

The research in the present thesis is focused on the study (design, analysis, and control) of small Ferrite permanent magnet synchronous motors intended for driving compressors in low power home appliances such as refrigerators or air conditioning systems, within power ranges of 35-1000W and speed ranges of 1600-4500rpm. Several new motor topologies are analyzed and optimally designed, the targeted results of the design being low material cost (motivation in using Ferrite PMs), high (88 - 94%) efficiency and simple and performantly enough control strategy for the intended application. FEA-assisted / FEA only design methods are built, employed in a pattern search optimal design routine, which uses the motor cost as fitness function.

For this, three new single phase permanent magnet motor topologies are proposed and thoroughly investigated. A FEA based optimal design methodology is built and applied to design the motors according to several case study requirements. 88% efficiency at rated load and speed is obtained as well as motor material costs of 16$ and smaller. The optimized motors performances are further investigated and validated via finite element analysis and dynamic operation simulations.

A new FEA assisted optimal design methodology is built for an outer rotor PMSM motor. It consists of an analytic model corrected iteratively in two key points (airgap flux density and stator inductance) by finite element analysis, to ensure required model accuracy while keeping the computation time low. The optimal design strategy is used for optimizing the outer rotor motor for compressor drive application requirements. Greater than 90% efficiency is obtained for rated operation at a 12.32$ material cost. The design is validated via FEA analysis and few experimental results on a previous designed prototype are presented.

Sensorless control of 3 phase PMSM motors is investigated, based on active flux model-based observer. The V/f scalar control strategy with stabilizing looks is thoroughly checked and compared against sensorless field-oriented control through digital and experimental simulation. While not having the same dynamic response, the results show the scalar control stable and fast enough for compressor driving applications.

The author’s main original research contributions are:

- Presentation of an overview of the permanent magnet solutions used in low power compressor applications and their main requirements.
- Proposal and analysis of three new topologies of single-phase Ferrite permanent magnet motors.
- Development of FEA/analytic model based optimal design methodologies which can be employed in motor design, with focus on minimizing the material cost and maximizing the efficiency and improving the starting torque.
- Study and implementation via digital simulation of control strategies for single/3 phase permanent magnet synchronous motors.
- Comparative study and implementation via digital and experimental simulation of two sensorless control strategy for 3 phase motors (based on active flux observer). The novelty of the studied control strategies is represented by using the voltage amplitude correction loop based on d-axis

current control for operation under MTPA (condition expressed using magnetic energy and active flux amplitude).

Several topics related to the thesis's work are open for improvement, such as:

- Improve the single-phase motor analytic calculation of the number of turns per coil to ensure during optimal design stage that the design motor has enough voltage reserve for operating at rated speed and load.
- Further in-depth analysis of the rotor PM's single-phase motor investigated in Chapter 5, including thorough dynamic digital simulations.
- Investigate and implement sensorless control strategies for the studied single-phase motors.
- Improve the Chapter 7 studied sensorless control strategies operation at low speeds by adding a saliency-based position estimation method or including a position close loop control strategy.

APPENDIX

Both V/f with stabilizing loops and FOC control implementations presented in Chapter 7 used the space vector modulation module, implemented by Assoc. Prof. Cristian Lascu. The implementation is listed below:

svmtmpl.c

```
/********************************************************\
*           Space Vector Modulation S-Function Template          *
*                                                                *
* Proiect: PMSM Sensorless DTC drive                             *
* Autor:   Cristian Lascu, 2004                                  *
*                                                                *
* Continut: Space Vector Modulation S-Function template for Simulink *
*          Input:  Us.alfa, Us.beta, Vdc                         *
*          Output: Da, Db, Dc                                    *
\********************************************************/

#define S_FUNCTION_NAME  svmtmpl
#define S_FUNCTION_LEVEL 2

#include "simstruc.h"

#include "svm.c"


static void mdlInitializeSizes(SimStruct *S)
{
   ssSetNumSFcnParams(S, 1);  /* Number of expected parameters */
   if (ssGetNumSFcnParams(S) != ssGetSFcnParamsCount(S)) {
      /* Return if number of expected != number of actual parameters */
      return;
   }

   ssSetNumContStates(S, 0);
   ssSetNumDiscStates(S, 0);

   if (!ssSetNumInputPorts(S, 2)) return;
   ssSetInputPortWidth(S, 0, 3);
   ssSetInputPortDirectFeedThrough(S, 0, 1);
   ssSetInputPortWidth(S, 1, 3);
   ssSetInputPortDirectFeedThrough(S, 1, 1);

   if (!ssSetNumOutputPorts(S, 2)) return;
   ssSetOutputPortWidth(S, 0, 3);
   ssSetOutputPortWidth(S, 1, 2);

   ssSetNumSampleTimes(S, 1);

   /* Take care when specifying exception free code - see sfuntmpl.doc */
   ssSetOptions(S, SS_OPTION_EXCEPTION_FREE_CODE);
//    ssSetOptions(S, 0);
}

static void mdlInitializeSampleTimes(SimStruct *S)
{
//    ssSetSampleTime(S, 0, CONTINUOUS_SAMPLE_TIME);
```

```
    ssSetSampleTime(S, 0, INHERITED_SAMPLE_TIME);
    ssSetOffsetTime(S, 0, 0.0);

}

static void mdlOutputs(SimStruct *S, int_T tid)
{
    InputRealPtrsType uPtr = ssGetInputPortRealSignalPtrs(S,0);
    InputRealPtrsType iPtr = ssGetInputPortRealSignalPtrs(S,1);
    real_T              *d = ssGetOutputPortRealSignal(S,0);
    real_T              *y = ssGetOutputPortRealSignal(S,1);
    real_T              *k = mxGetPr(ssGetSFcnParam(S,0));
    real_T u[3],i[3];
    u[0]=*uPtr[0];
    u[1]=*uPtr[1];
    u[2]=*uPtr[2];
    i[0]=*iPtr[0];
    i[1]=*iPtr[1];
    i[2]=*iPtr[2];
    SVM(u,i,d,y,k);
}

static void mdlTerminate(SimStruct *S)
{
}

#ifdef  MATLAB_MEX_FILE    /* Is this file being compiled as a MEX-file? */
#include "simulink.c"      /* MEX-file interface mechanism */
#else
#include "cg_sfun.h"       /* Code generation registration function */
#endif
```

svm.c

```
/**********************************************\
*                 Space Vector Modulation              *
*                                                      *
* Proiect: PMSM Sensorless DTC drive                   *
* Autor:   Cristian Lascu, 2004                        *
*                                                      *
* Continut: Space Vector Modulation                    *
*          Input:  Us.alfa, Us.beta, Vdc               *
*          Output: Da, Db, Dc                          *
\**********************************************/

#include <math.h>
#include "vector.h"


#define R3 1.732051
#define Dmax 0.98
#define Dmin 0.02


// Space Vector Modulation

void SVM(real_T *u, real_T *i, real_T *d, real_T *y, real_T *k)
{
```

```
struct Vector{float alfa,beta;} Us;
float K=(*k)*tdead/h;
float Umax=R3/u[0];
float Da,Db,Dc;
float T1,T2;
int sector;

Us.alfa = R3*Umax*u[1]; //normalizare - Holtz
Us.beta = Umax*u[2];


// Sectorul tensiunii si timpii de modulare
if (Us.beta>0)
     if (Us.alfa>Us.beta)
    {
        sector=0;
        T1=0.5*(Us.alfa-Us.beta);
        T2=Us.beta;
    }
    else if (-Us.alfa<Us.beta)
    {
        sector=1;
        T1=0.5*(Us.alfa+Us.beta);
        T2=0.5*(Us.beta-Us.alfa);
    }
        else
    {
        sector=2;
        T1=Us.beta;
        T2=-0.5*(Us.alfa+Us.beta);
    }
else if (Us.alfa<Us.beta)
    {
        sector=3;
        T1=0.5*(Us.beta-Us.alfa);
        T2=-Us.beta;
    }
    else if (-Us.alfa>Us.beta)
    {
        sector=4;
        T1=-0.5*(Us.alfa+Us.beta);
        T2=0.5*(Us.alfa-Us.beta);
    }
        else
    {
        sector=5;
        T1=-Us.beta;
        T2=0.5*(Us.alfa+Us.beta);
    }


// Supramodularea Holtz
if (T1>1.0) T1=1.0,T2=0.0;  //bang-bang
else if (T2>1.0) T2=1.0,T1=0.0; //bang-bang
else if (T1+T2>1.0) if (T1>T2) T2=1.0-T1; else T1=1.0-T2;//OVM
```

```
   // Factorii de umplere - SVM
   switch (sector) {
   case 0: Da=0.5*(1.0+T1+T2);
      Db=0.5*(1.0-T1+T2);
      Dc=0.5*(1.0-T1-T2);
      break;
   case 1: Da=0.5*(1.0+T1-T2);
      Db=0.5*(1.0+T1+T2);
      Dc=0.5*(1.0-T1-T2);
      break;
   case 2: Da=0.5*(1.0-T1-T2);
      Db=0.5*(1.0+T1+T2);
      Dc=0.5*(1.0-T1+T2);
      break;
   case 3: Da=0.5*(1.0-T1-T2);
      Db=0.5*(1.0+T1-T2);
      Dc=0.5*(1.0+T1+T2);
      break;
   case 4: Da=0.5*(1.0-T1+T2);
      Db=0.5*(1.0-T1-T2);
      Dc=0.5*(1.0+T1+T2);
      break;
   case 5: Da=0.5*(1.0+T1+T2);
      Db=0.5*(1.0-T1-T2);
      Dc=0.5*(1.0+T1-T2);
      break;
   default:
      Da=0.0;Db=0.0;Dc=0.0;
   }

   // Stator voltage
   y[0] = u[0]*(2.0*Da-Db-Dc)/3.0;
   y[1] = u[0]*(Db-Dc)/R3;

   // Dead-time compensation
   Da = Da + K*sat(i[0],zone);
   Db = Db + K*sat(i[1],zone);
   Dc = Dc + K*sat(i[2],zone);

   // Pulse drop
   if (Da>Dmax) Da=1.0; else if (Da<Dmin) Da=0.0;
   if (Db>Dmax) Db=1.0; else if (Db<Dmin) Db=0.0;
   if (Dc>Dmax) Dc=1.0; else if (Dc<Dmin) Dc=0.0;

   // Duty cycles
   d[0] = Da;
   d[1] = Db;
   d[2] = Dc;
}
```

vector.h

```
/************************************************\
*          Global Variables and Constant Definitions          *
*                                                              *
* Proiect: PMSM Sensorless DTC drive                           *
* Autor:   Cristian Lascu, 2004                                *
*                                                              *
* Continut: Global Variables and Constant Definitions          *
```

```
\*************************************************/


#ifndef VECTOR
#define VECTOR

// Sampling time
const float h=0.000125;       //              [s]

// SVM parameters
const float tdead = 2e-6;   // dead time    [s]
const float zone = 1.0;     // linear zone  [A]

// Constante matematice
const float pi=3.1415926;

// Saturation function
float sat(real_T x, real_T z)
{
   if (x>z) return 1.0;
   else if (x<-z) return -1.0;
   else return x/z;
}

#endif
```

REFERENCES

[1] B. C. Mecrow and A. G. Jack, "Efficiency trends in electric machines and drives," *Elsevier, Energy Policy,* vol. 36, no. 12, pp. 4336-4341, 2008.

[2] D. M. Ionel, "High-efficiency variable-speed electric motor drive technologies for energy savings in the US residential sector," in *2010 12th International Conference on Optimization of Electrical and Electronic Equipment*, Brasov, 2010.

[3] I. Boldea and L. N. Tutelea, Electric machines: steady state, transients, testing &design, with MatLab, New York: CRC Press, Taylor&Francis Group, 2009.

[4] S. Musuroi and D. Popovici, Actionari electrice cu servomotoare, Timisoara: Editura Politehnica, 2006.

[5] C. Chabu, V. C. Silva, S. I. Nabeta, M. A. M. Afonso and J. R. Cardoso, "Axial flux concentration technique applied to the design of permanent magnet motors: theoretical aspects and their numerical and experimental validation," in *IEEE International Conference on Electric Machines and Drives*, San Antonio, TX, 2005.

[6] D. Kamalakannan, V. Mariappan, V. Narayanan and N. S. Ramanathan, "Energy efficient appliances in a residential building," in *2016 First International Conference on Sustainable Green Buildings and Communities (SGBC)*, Chennai, 2016.

[7] A. H. Sabry and P. J. Ker, "DC Environment for a Refrigerator With Variable Speed Compressor; Power Consumption Profile and Performance Comparison," *IEEE Access,* vol. 8, pp. 147973-147982, 2020.

[8] W. J. Yoon, K. Seo and Y. Kim, "Development of an optimization strategy for insulation thickness of a domestic refrigerator-freezer," *International Journal of Refrigeration,* vol. 36, no. 3, pp. 1162-1172, 2013.

[9] H. P. Bloch and J. J. Hoefner, Reciprocating compressors, Operation Maintenance, Houston: Gulf publishing Company, 1996.

[10] J. F. Gieras, Permanent magnet motor technology, 3 ed., Boca Raton: CRC Press, Taylor&Francis Group, 2010.

[11] D. Kim, K. Lee, B. Kim and B. Kwon, "A Novel Starting Method of the SPM-type BLDC Motors without Position Sensor for Reciprocating Compressor," in *Conference Record of the 2006 IEEE Industry Applications Conference Forty-First IAS Annual Meeting*, Tampa, FL, 2006.

[12] Danfoss, HG-EA (https://www.secop.com), "Compressor design mechanical and electrical," September 1974. [Online]. Available: https://www.secop.com/fileadmin/user_upload/technical-literature/danfoss-lectures/compressor_design_mechanical_and_electrical.pdf. [Accessed 12 12 2020].

[13] F. Parasiliti, M. Villani and M. Castello, "PM Brushless DC Motor with exterior rotor for high efficiency household appliances," in *2014 International Conference on Electrical Machines (ICEM)*, Berlin, 2014.

[14] "State of the Art Survey of Motor Technology Applicable to Hermetic Compressors for Domestic Refrigerator/Freezers," United States Environmental Protection Agency, 1993.

[15] G. Feng, W. Qi, B. Zhang and C. Li, "Analysis and comparison of three-phase variable frequency PMSM with single-phase induction motor in household appliances," in *2011 International Conference on Electrical Machines and Systems*, Beijing, 2011.

[16] M. A. Rahman and et al, "Advances on Single-Phase Line-Start High Efficiency Interior Permanent Magnet Motors," *IEEE Transactions on Industrial Electronics,* vol. 59, no. 3, pp. 1333-1345, 2011.

[17] S. Kikuchi and et al., "Development of self-starting permanent magnet synchronous motors for compressor drives," in *2009 International Conference on Electrical Machines and Systems*, Tokyo, 2009.

[18] K. Kurihara and M. A. Rahman, "High-efficiency line-start interior permanent-magnet synchronous motors," *IEEE Transactions on Industry Applications,* vol. 40, no. 3, pp. 789-796, 2004.

[19] F. J. H. Kalluf, L. N. Tutelea, I. Boldea and A. Espindola, "2/4-POLE Split-Phase Capacitor Motor for Small Compressors: A Comprehensive Motor Characterization," *IEEE Transactions on Industry Applications,* vol. 50, no. 1, pp. 356-363, 2014.

[20] Z. Wu, J. Wang, J. Ying and J. Zeng, "Sensorless brushless DC motor drive for air-conditioner compressor," in *ICEMS'2001. Proceedings of the Fifth International Conference on Electrical Machines and Systems (IEEE Cat. No.01EX501)*, Shenyang, China, 2001.

[21] Y. Kano, T. Kosaka and N. Matsui, "Optimum Design Approach for Two-Phase Switched Reluctance Compressor Drive," in *IEEE International Electric Machines & Drives Conference*, Antalya, 2007.

[22] V. Gradinaru, L. Tutelea and I. Boldea, "Hybrid analytical/FEM optimization design of SPMSM for refrigerator compressor loads," in *International Aegean Conference on Electrical Machines and Power Electronics and Electromotion, Joint Conference*, Istambul, 2011.

[23] M. Chiu, J. Chiang and C. Lin, "Design and Optimization of a Novel V-Type Consequent-Pole Interior Permanent Magnet Synchronous Motor for Applying to Refrigerant Compressor," in *2018 21st International Conference on Electrical Machines and Systems (ICEMS)*, Jeju, 2018.

[24] Y. Hu, B. Chen, Y. Xiao, Q. Li and L. Li, "Topology Optimization of an Interior PM Motor for Applying to Refrigerant Compressor," in *2019 22nd International Conference on Electrical Machines and Systems (ICEMS)*, Harbin, China, 2019.

[25] L. N. Tutelea, M. C. Kim, M. Topor, J. Lee and I. Boldea, "Linear Permanent Magnet Oscillatory Machine: Comprehensive Modeling for Transients With Validation by Experiments," *IEEE Transactions on Industrial Electronics,* vol. 55, no. 2, pp. 492-500, 2008.

[26] H. K. Lee, G. Y. Song, J. S. Park, E. P. Hong, W. H. Jung and K. B. Park, "Development of the Linear Compressor for a Household Refrigerator," in *Proceedings of International Compressor Engineering Conference*, 2000.

[27] "Small compressor electric motor technologies: EMBRACO's perspective," in *2008 11th International Conference on Optimization of Electrical and Electronic Equipment*, Brasov, 2008.

[28] D. Meeker, "FEMM 4.2 - Full-featured finite element package for the solution of 2D planar and axisymmetric problems in low frequency magnetics under Windows," [Online]. Available: www.femm.info.

[29] "Electrical Steel Thin Non-Oriented Grades American version," [Online]. Available: http://www.polarislaserlaminations.com/Cogent.pdf. [Accessed 12 12 2020].

[30] C. P. Steinmetz, "On the Law of Hysteresis," *Transactions of the American Institute of Electrical Engineers,* vol. IX, no. 1, pp. 1-64, Jan 1892.

[31] M. Ibrahim and P. Pillay, "Core Loss Prediction in Electrical Machine Laminations Considering Skin Effect and Minor Hysteresis Loops," *IEEE Transactions on Industry Applications,* vol. 49, no. 5, pp. 2061-2068, Sept.-Oct 2013.

[32] D. Ionel, M. Popescu, S. J. Dellinger, T. J. Miller, R. J. Heideman and M. I. McGilp, "Computation of core losses in electrical machines using improved model for laminated steel," *IEEE Transactions on Industry Appl,* vol. 43, no. 6, pp. 1554-1564, Nov/December 2007.

[33] A. Boglietti, A. Cavagnino, M. Lazzari and M. Pastorelli, "Predicting iron losses in soft magnetic materials with arbitrary voltage supply: an engineering approach," *IEEE Transactions on Magnetics,* vol. 39, no. 2, pp. 981-989, March 2003.

[34] R. Hooke and T. A. Jeeves, "Direct search solution of numerical and statistical problems," *Journal of ACM,* vol. 8, no. 2, pp. 212-229, 1961.

[35] S. Wang, X. Da, M. Li and T. Han, "Adaptive backtracking search optimization algorithm with pattern search for numerical optimization," *Journal of Systems Engineering and Electronics,* vol. 27, no. 2, pp. 395-406, April 2016.

[36] L. Tutelea and I. Boldea, "Induction motor electromagnetic design optimization: Hooke Jeeves method versus genetic algorithms," in *2010 12th International Conference on Optimization of Electrical and Electronic Equipment*, Brasov, 2010.

[37] R. P. Deodhar, S. Andersson, I. Boldea and T. J. E. Miller, "The flux-reversal machine: a new brushless doubly-salient permanent-magnet machine," in *IAS '96. Conference Record of the 1996 IEEE Industry Applications Conference Thirty-First IAS Annual Meeting*, San Diego, CA, 1996.

[38] M. Cheng, W. Hua, J. Zhang and W. Zhao, "Overview of Stator-Permanent Magnet Brushless Machines," *IEEE Transactions on Industrial Electronics,* vol. 58, no. 11, pp. 5087-5101, Nov 2011.

[39] M. Cheng, K. T. Chau, C. C. Chan and Q. Sun, "Control and operation of a new 8/6-pole doubly salient permanent-magnet motor drive," *IEEE Transactions on Industry Applications,* vol. 39, no. 5, pp. 1363-1371, Sept.-Oct. 2003.

[40] E. Binder, "Magnetoelectric rotary machine (magnetelektrische schwungradmaschine in german)". Germany Patent 741163, 16 September 1943.

[41] K. B. Jang, S. H. Won, T. H. Lim and J. Lee, "Starting and high-speed driving of single-phase flux-reversal motor for vacuum cleaner," *IEEE Transactions on Magnetics,* vol. 41, no. 10, pp. 3967-3969, 2005.

[42] V. A. Prakht, V. A. Dmitrievskii, V. M. Kazakbaev and S. F. Sarapulov, "Mathematical Modelling and Optimization of Single-Phase High-Speed Flux Reversal Motor," in *2018 XIII International Conference on Electrical Machines (ICEM)*, Alexandroupoli, 2018.

[43] T. H. Kim and J. Lee, "A study of the design for the flux reversal machine," *IEEE Transactions on Magnetics,* vol. 40, no. 4, pp. 2053-2055, July 2004.

[44] I. Boldea, J. Zhang and S. A. Nasar, "Theoretical characterization of flux reversal machine in low-speed servo drives-the pole-PM configuration," *IEEE Transactions on Industry Applications,* vol. 38, no. 6, pp. 1549-1557, Nov.-Dec. 2002.

[45] D. S. More, H. Kalluru and B. G. Fernandez, "Outer Rotor Flux Reversal Machine for Rooftop Wind Generator," in *2008 IEEE Industry Applications Society Annual Meeting*, Edmonton, AB, 2008.

[46] A. S. Isfanuti and et al., "Small single-phase two pole Ferrite-PM-stator double-saliency motor: Optimal design and experimental characterization," in *2016 XXII International Conference on Electrical Machines (ICEM)*, Lausanne, 2016.

[47] F. J. H. Kalluf, A. D. P. Juliani, I. Boldea, I. Tutelea, A. Isfanuti and A. R. Laureano, "Single-phase stator-ferrite PM double saliency motor performance and optimization," in *2015 Intl Aegean Conference on Electrical Machines & Power Electronics (ACEMP), 2015 Intl Conference on Optimization of Electrical & Electronic Equipment (OPTIM) & 2015 Intl Symposium on Advanced Electromechanical Motion Systems (ELECTROMOTION)*, Side, 2015.

[48] M. Fazil and K. R. Rajagopal, "A Novel Air-Gap Profile of Single-Phase Permanent-Magnet Brushless DC Motor for Starting Torque Improvement and Cogging Torque Reduction," *IEEE Transactions on Magnetics,* vol. 46, no. 11, pp. 3928-3932, 2010.

[49] C. Chiu, Y. Chen and W. Jhang, "Properties of Cogging Torque, Starting Torque, and Electrical Circuits for the Single-Phase Brushless DC Motor," *IEEE Transactions on Magnetics,* vol. 44, no. 10, pp. 2317-2323, 2008.

[50] D.-R. Huang and et al., "Cogging torque reduction of a single-phase brushless DC motor," *IEEE Transactions on Magnetics,* vol. 34, no. 4, pp. 2075-2077, 1998.

[51] A. Isfanuti, L. N. Tutelea, I. Boldea and T. Staudt, "Small-power 4 stator-pole stator-ferrite PMSM single-phase self-starting motor drive: FEM-based optimal design and controlled dynamics," in *2017 International Conference on Optimization of Electrical and Electronic Equipment (OPTIM) & 2017 Intl Aegean Conference on Electrical Machines and Power Electronics (ACEMP)*, Brasov, 2017.

[52] S. Bentouati, Z. Q. Zhu and D. Howe, "Influence of design parameters on the starting torque of a single-phase PM brushless DC motor," *IEEE Transactions on Magnetics,* vol. 36, no. 5, pp. 3533-3536, Sept. 2000.

[53] L. I. Iepure, L. Tutelea and I. Boldea, "FEM analysis and control of a tapered airgap single phase PMSM," in *2008 11th International Conference on Optimization of Electrical and Electronic Equipment*, Brasov, 2008.

[54] D. Kim, Y. Park and J. Cho, "Cogging torque reduction of single-phase brushless DC motor with a tapered air-gap using optimizing notch size and position," in *2014 IEEE Energy Conversion Congress and Exposition (ECCE)*, Pittsburgh, PA, 2014.

[55] M. M. Radulescu, C. Martis and K. Biro, "A new electronically-commutated doubly-salient permanent-magnet small motor," in *1995 Seventh International Conference on Electrical Machines and Drives*, Durham, UK, 1995.

[56] C. Martis, M. M. Radulescu and K. Biro, "On the dynamic model of a doubly-salient permanent-magnet motor," in *9th Mediterranean Electrotechnical Conference. Proceedings (Cat. No.98CH36056)*, Tel-Aviv, Israel, 1998.

[57] M. Andriollo, G. Martinelli and A. Tortella, "Torque improvement of single phase brushless PM motors by auxiliary magnets," in *2011 IEEE International Electric Machines & Drives Conference (IEMDC)*, Niagara Falls, ON, 2011.

[58] G. Iliescu, L. Tutelea and I. Boldea, "Performance of a Single-Phase Self-Starting PM Brushless Motor Fed by a Chopper-Controlled Current-Source Thyristor Inverter," in *OPTIM*, Brasov, 2006.

[59] M. A. Raj and A. Kavitha, "Effect of Rotor Geometry on Peak and Average Torque of External-Rotor Synchronous Reluctance Motor in Comparison With Switched Reluctance Motor for Low-Speed Direct-Drive Domestic Application," *IEEE Transactions on Magnetics,* vol. 53, no. 11, pp. 1-8, Nov. 2017.

[60] S. S. R. Bonthu, S. Choi, A. Gorgani and K. Jang, "Design of permanent magnet assisted synchronous reluctance motor with external rotor architecture," in *2015 IEEE International Electric Machines & Drives Conference (IEMDC)*, Coeur d'Alene, ID, 2015.

[61] S. Zuo, F. Lin and X. Wu, "Noise Analysis, Calculation, and Reduction of External Rotor Permanent-Magnet Synchronous Motor," *IEEE Transactions on Industrial Electronics,* vol. 62, no. 10, pp. 6204-6212, Oct. 2015.

[62] J. Krotsch and B. Piepenbreier, "Radial Forces in External Rotor Permanent Magnet Synchronous Motors With Non-Overlapping Windings," *IEEE Transactions on Industrial Electronics,* vol. 59, no. 5, pp. 2267-2276, May 2012.

[63] M. Z. Islam and S. Choi, "Design of rare-earth free five-phase outer-rotor IPM motor drive for electric bicycle," in *2016 IEEE Applied Power Electronics Conference and Exposition (APEC)*, Long Beach, CA, 2016.

[64] Y. Feng, F. Li, S. Huang and N. Yang, "Variable-flux outer-rotor permanent magnet synchronous motor for in-wheel direct-drive applications," in *Chinese Journal of Electrical Engineering*, 2018.

[65] K. Reis and A. Binder, "Development of a permanent magnet outer rotor direct drive for use in wheel-hub drives," in *2014 International Conference on Electrical Machines (ICEM)*, Berlin, 2014.

[66] S. M. Castano, R. Yang, C. Mak, B. Bilgin and A. Emadi, "External-Rotor Switched Reluctance Motor for Direct-Drive Home Appliances," in *IECON 2018 - 44th Annual Conference of the IEEE Industrial Electronics Society*, Washington, DC, 2018.

[67] D. Shin and B. Kwon, "Multi-objective optimal design for in-wheel permanent magnet synchronous motor," in *2009 International Conference on Electrical Machines and Systems*, Tokyo, 2009.

[68] Q. Li, T. Fan, Y. Li, Z. Wang, Z. Wen and J. Guo, "Optimization of external rotor surface permanent magnet machines based on efficiency map over a target driving cycle," in *2017 20th International Conference on Electrical Machines and Systems (ICEMS)*, Sydney, NSW, 2017.

[69] W. Chu, Z. Zhu and Y. Shen, "Analytical optimisation of external rotor permanent magnet machines," *IET Electrical Systems in Transportation,* vol. 3, no. 2, pp. 41-49, June 2013.

[70] G. Cvetkovski and L. Petkovska, "Multi-objective optimal design of permanent magnet synchronous motor," in *2016 IEEE International Power Electronics and Motion Control Conference (PEMC)*, Varna, 2016.

[71] X. Jannot, J. Vannier, C. Marchand, M. Gabsi, J. Saint-Michel and D. Sadarnac, "Multiphysic Modeling of a High-Speed Interior Permanent-Magnet Synchronous Machine for a Multiobjective Optimal Design," *IEEE Transactions on Energy Conversion,* vol. 26, no. 2, pp. 457-467, June 2011.

[72] S. S. R. Bonthu and S. Choi, "Design procedure for multi-phase external rotor permanent magnet assisted synchronous reluctance machines," in *IEEE Applied Power Electronics Conference and Exposition (APEC)*, Long Beach, CA, 2016.

[73] H. Moayed-Jahromi, A. Rahideh and M. Mardaneh, "2-D Analytical Model for External Rotor Brushless PM Machines," *IEEE Transactions on Energy Conversion,* vol. 31, no. 3, pp. 1100-1109, Sept. 2016.

[74] K. Boughrara, R. Ibtiouen, D. Zˇarko, O. Touhami and A. Rezzoug, "Magnetic Field Analysis of External Rotor Permanent-Magnet Synchronous Motors Using Conformal Mapping," *IEEE Transactions on Magnetics,* vol. 46, no. 9, pp. 3684-3693, Sept. 2010.

[75] G. Y. Sisov, D. M. Ionel and A. O. Demerdash, "Modeling and Parametric Design of Permanent-Magnet AC Machines Using Computationally Efficient Finite-Element Analysis," *IEEE Transactions on Industrial Electronics,* vol. 59, no. 6, pp. 2403-2413, June 2012.

[76] F. Yaojing, H. Shoudao, Y. Kai and W. Xuan, "Research on optimal design of permanent magnet synchronous motors based on field-circuit coupled method," in *2014 17th International Conference on Electrical Machines and Systems (ICEMS)*, Hangzhou, 2014.

[77] I. Petrov, M. Niemelä, P. Ponomarev and J. Pyrhönen, "Rotor Surface Ferrite Permanent Magnets in Electrical Machines: Advantages and Limitations," *IEEE Transactions on Industrial Electronics,* vol. 64, no. 7, pp. 5314-5322, July 2017.

[78] A. Tovar-Barranco, F. Briz, A. López-de-Heredia and I. Villar, "Reduced lumped parameter thermal model for external rotor permanent magnet motor design," in *2017 IEEE Energy Conversion Congress and Exposition (ECCE)*, Cincinnati, OH, 2017.

[79] A. S. Isfanuti, L. N. Tutelea, I. Boldea, T. Staudt and P. Ely da Silva, "Outer Ferrite-PM-Rotor BLAC Motor Characterization: FEM-Assisted Optimal Design and Preliminary Experiments," *IEEE Transactions on Industry Applications,* vol. 56, no. 3, pp. 2580-2589, May-June 2020.

[80] A. Isfanuti, L. N. Tutelea, I. Boldea, T. Staudt and P. Ely da Silva, "Outer-Ferrite-PM-Rotor BLAC Motor Characterization: FEM Assisted Optimal Design," in *2018 XIII International Conference on Electrical Machines (ICEM)*, Alexandroupoli, 2018.

[81] G. S. Buja and M. P. Kazmierkowski, "Direct torque control of PWM inverter-fed AC motors - A survey," *IEEE Trans. Ind. Electron,* vol. 51, no. 4, p. 44–757, April 2004.

[82] I. Boldea, A. Moldovan and L. Tutelea, "Scalar V/f and I-f control of AC motor drives: An overview," in *2015 Intl Aegean Conference on Electrical Machines & Power Electronics (ACEMP), 2015 Intl Conference on Optimization of Electrical & Electronic Equipment (OPTIM) & 2015 Intl Symposium on Advanced Electromechanical Motion Systems (ELECTROMOTION)*, Side, Turkey, 2015.

[83] G. Wang, M. Valla and J. Solsona, "Position Sensorless Permanent Magnet Synchronous Machine Drives—A Review," *IEEE Transactions on Industrial Electronics,* vol. 67, no. 7, pp. 5830-5842, July 2020.

[84] D. Xu, B. Wang, G. Zhang, B. Wang and Y. Yu, "A review of sensorless control methods for AC motor drives," *CES Transactions on Electrical Machines and Systems,* vol. 2, no. 1, pp. 104-115, March 2018.

[85] Y. Zhao, C. Wei, Z. Zhang and W. Qiao, "A review on position/speed sensorless control for permanent-magnet synchronous machine-based wind energy conversion systems," *IEEE Journal of Emerging and Selected Topics in Power Electronics,* vol. 1, no. 4, pp. 203-216, Dec. 2013.

[86] S. K. Sul, Y. C. Kwon and Y. Lee, "Sensorless control of IPMSM for last 10 years," *CES Trans. Electrical Machines and Systems,* vol. 1, no. 2, p. 91–99, Jun 2017.

[87] S. Morimoto, M. Sanada and Y. Takeda, "Mechanical sensorless drives of IPMSM with online parameter identification," *IEEE Trans. Ind. Applicat.,* vol. 42, no. 5, p. 1241–1248, Sep.-Oct. 2006.

[88] Y. Tang, Y. He, F. Wang, D. H. Lee, J. W. Ahn and R. Kennel, "Back-EMF-based sensorless control system of hybrid SRM for high-speed operation," *IET Electric Power Applic.,* vol. 12, no. 6, pp. 867-873, Jul. 2018.

[89] Y. Lee and S. K. Sul, "Model-based sensorless control of an IPMSM with enhanced robustness against load disturbances based on position and speed estimator using a speed error," *IEEE Trans. Ind. Appl.,* vol. 54, no. 2, p. 1448–1459, Mar.-Apr. 2018.

[90] A. T. Nguyen, M. S. Rafaq, H. H. Choi and J. W. Jung, "A model reference adaptive control based speed controller for a surface-mounted permanent magnet synchronous motor drive," *IEEE Trans. Ind. Electron.,* vol. 65, no. 12, p. 9399–9409, Dec. 2018.

[91] Y. Lee, Y. Kwon and S. Sul, "Comparison of rotor position estimation performance in fundamental-model-based sensorless control of PMSM," in *2015 IEEE Energy Conversion Congress and Exposition (ECCE)*, Montreal, QC, 2015.

[92] I. Boldea, C. M. Paicu and G. D. Andreescu, "Active flux concept for motion-sensorless unified AC drives," *IEEE Trans. Power Electron.,* vol. 23, no. 5, p. 2612–2618, May 2008.

[93] P. L. Jansen and R. D. Lorenz, "A physically insightful approach to the design and accuracy assessment of flux observers for field oriented induction machine drives," *IEEE Transactions on Industry Applications,* vol. 30, no. 1, pp. 101-110, Jan.-Feb. 1994.

[94] Z. Chen, M. Tomita, S. Doki and S. Okuma, "An extended electromotive force model for sensorless control of interior permanent-magnet synchronous motors," *IEEE Transactions on Industrial Electronics,* vol. 50, no. 2, pp. 288-295, April 2003.

[95] H. Kim, M. C. Harke and R. D. Lorenz, "Sensorless control of interior permanent-magnet machine drives with zero-phase lag position estimation," *IEEE Transactions on Industry Applications,* vol. 39, no. 6, pp. 1726-1733, Nov.-Dec. 2003.

[96] S. Morimoto, K. Kawamoto, M. Sanada and Y. Takeda, "Sensorless control strategy for salient-pole PMSM based on extended EMF in rotating reference frame," *IEEE Transactions on Industry Applications,* vol. 38, no. 4, pp. 1054-1061, July-Aug. 2002.

[97] G. Wang, H. Zhan, G. Zhang, X. Gui and D. Xu, "Adaptive Compensation Method of Position Estimation Harmonic Error for EMF-Based Observer in Sensorless IPMSM Drives," *IEEE Transactions on Power Electronics,* vol. 29, no. 6, pp. 3055-3064, June 2014.

[98] Y. Zhao, Z. Zhang, W. Qiao and L. Wu, "An Extended Flux Model-Based Rotor Position Estimator for Sensorless Control of Salient-Pole Permanent-Magnet Synchronous Machines," *IEEE Transactions on Power Electronics,* vol. 30, no. 8, pp. 4412-4422, Aug. 2015.

[99] G. D. Andreescu,, Estimatoare în conducerea acționărilor electrice. Aplicații la mașini sincrone cu magneți, Timisoara: Editura Orizonturi Universitare (EOU), 1999.

[100] P. D. C. Perera, F. Blaabjerg, J. K. Perdersen and P. Thogersen, "A sensorless, stable V/f control method for PMSM drives," *IEEE Trans. Ind. Applicat.,* vol. 39, no. 3, p. 783–791, May-Jun. 2003.

[101] R. Ancuti, I. Boldea and G. D. Andreescu, "Sensorless V/f control of high-speed surface permanent magnet synchronous motor drives with two novel stabilising loops for fast dynamics and robustness," *IET Electric Pow. Appl.,* vol. 4, no. 3, p. 149–157, Mar. 2010.

[102] S. C. Agarlita, C. E. Coman, G. D. Andreescu and I. Boldea, "Stable V/f control system with controlled power factor angle for permanent magnet synchronous motor drives," *IET Electric Power Applications,* vol. 7, no. 4, p. 278–286, Apr. 2013.

[103] A. Consoli, G. Scelba, G. Scarcella and M. Cacciato, "An effective energy-saving scalar control for industrial IPMSM drives," *IEEE Trans. Ind. Electron.,* vol. 60, no. 9, p. 3658–3669, Sep. 2013.

[104] I. Boldea, A. Moldovan-Popa, V. Schramel-Coroban, G. D. Andreescu and L. N. Tutelea, "A class of fast dynamics V/f sensorless AC general drives with PM-RSM as a case study," in *2010 12th International Conference on Optimization of Electrical and Electronic Equipment*, Brasov, 2010.

[105] Z. Tang, X. Li, S. Dusmez and B. Akin, "A New V/f-Based Sensorless MTPA Control for IPMSM Drives," *IEEE Transactions on Power Electronics,* vol. 31, no. 6, pp. 4400-4415, June 2016.

[106] A. S. Isfanuti, M. C. Paicu, L. N. Tutelea, T. Staudt and I. Boldea, "V/f with stabilizing loops versus FOC of Spoke-PM rotor SM drive: Control with experiments," in *2018 IEEE 18th International Power Electronics and Motion Control Conference (PEMC)*, Budapest, 2018.

[107] H. Ge, Y. Miao, B. Bilgin, B. Nahid-Mobarakeh and A. Emadi, "Speed range extended maximum torque per ampere control for PM drives considering inverter and motor nonlinearities," *IEEE Transactions on Power Electronics,* vol. 32, no. 9, pp. 7151-7159, Sept. 2017.

[108] J. Holtz and J. Quan, "Drift- and parameter-compensated flux estimator for persistent zero-stator-frequency operation of sensorless-controlled induction motors," *IEEE Trans. Ind. Applicat.,* vol. 39, no. 4, p. 1052–1060, Jul.-Aug. 2003.

[109] Y. Park and S. -K. Sul, "A novel method utilizing trapezoidal voltage to compensate for inverter nonlinearity," *IEEE Trans. Power Electron.,* vol. 27, no. 12, p. 4837–4846, Dec. 2012.

[110] F. J. H. Kalluf, A. Isfanuti, L. N. Tutelea, A. Moldovan-Popa and I. Boldea, "1-kW 2000–4500 r/min ferrite PMSM drive: Comprehensive characterization and two sensorless control options," *IEEE Trans. Ind. Applicat.,* vol. 52, no. 5, p. 3980–3989, Sep.-Oct. 2016.

[111] A. Isfanuti, M.-C. Paicu, G. D. Andreescu, L. N. Tutelea, T. Staudt and I. Boldea, "V/f with Stabilizing Loops and MTPA versus Sensorless FOC for PMSM Drives," *Electric Power Components and Systems,* 2020.

[112] "www.st.com," [Online]. Available: https://www.st.com/resource/en/application_note/cd00236479-singlephase-induction-motor-drive-for-refrigerator-compressor-application-formerly-an1354-stmicroelectronics.pdf. [Accessed 12 12 2020].